DOE/NASA/0342-2
NASA CR-175072

NASA-CR-175072
19860015119

Methods for Heat Transfer and Temperature Field Analysis of the Insulated Diesel

Phase II—Progress Report

Thomas Marel, Rifat Keribar,
Edward F. Fort, and Paul N. Blumberg
Integral Technologies Incorporated

September 1985

Prepared for
NATIONAL AERONAUTICS AND SPACE ADMINISTRATION
Lewis Research Center
Under Contract DEN 3-342

for
U.S. DEPARTMENT OF ENERGY
Conservation and Renewable Energy
Office of Vehicle and Engine R&D

DISCLAIMER

Printed in the United States of America

Available from
National Technical Information Service
U.S. Department of Commerce
5285 Port Royal Road
Springfield, VA 22161

NTIS price codes[1]
Printed copy: A14
Microfiche copy: A01

[1]Codes are used for pricing all publications. The code is determined by the number of pages in the publication. Information pertaining to the pricing codes can be found in the current issues of the following publications, which are generally available in most libraries: *Energy Research Abstracts (ERA); Government Reports Announcements* and Index (*GRA* and I); *Scientific and Technical Abstract Reports (STAR);* and publication, NTIS-PR-360 available from NTIS at the above address.

DOE/NASA/0342-2
NASA CR-175072

Methods for Heat Transfer and Temperature Field Analysis of the Insulated Diesel

Phase II—Progress Report

Thomas Marel, Rifat Karibar,
Edward F. Fort, and Paul N. Blumberg
Integral Technologies Incorporated
Westmont, Illinois 60559

September 1985

Prepared for
National Aeronautics and Space Administration
Lewis Research Center
Cleveland, Ohio 44135
Under Contract DEN 3-342

for
U.S. DEPARTMENT OF ENERGY
Conservation and Renewable Energy
Office of Vehicle and Engine R&D
Washington, D.C. 20545
Under Interagency Agreement DE-AI01-80CS50194

TABLE OF CONTENTS

SUMMARY

This report presents the results of Phase II of a three-phase program sponsored by DOE and administered by NASA. The program was initiated in June 1983. The objective of the program is to develop a methodology for the analysis of insulated diesel engine concepts, validate it with experiments, and to use the methodology to address significant issues related to optimization of the concepts. The progress made on the program during the first year has been described in the Phase I Report issued in August 1984 (DOE/NASA/0342-1, NASA CR-174783).

During the first year of the program, work concentrated on the development of a new convective heat transfer model based on fluid flow calculations including swirl, squish and turbulence. Another task that was fully completed was a method for studying surface temperature transients fully coupled with the in-cylinder gas-phase heat transfer and with steady-state conduction through the engine structure. Preliminary work was carried out in areas of heat radiation (completed during Phase II), analysis of insulated diesel engine conccepts (continued in Phase II), single cylinder engine installation (completed in Phase II) and development of experimental techniques (continued in Phase II).

During the second year of the program, progress was made in a number of areas. In the area of heat radiation a comprehensive model was developed, that represents the key phenomena and processes which affect radiation heat transfer in diesel engines. The absorption and emission of radiation by soot is treated by a kinetics-based model which calculates the soot formation and burnup. The geometrical description of the process, which is essential to calculation of spatial distribution, uses a zonal approach capable of treating surface radiation and multiple reflections. Predictions were made of heat radiation as a function of speed and load, and it was found that for a heavy duty highway truck engine, radiation accounts for five to twenty-five percent of the total in-cylinder heat transfer. Under insulated conditions this fraction increases, and ranges from ten to over forty percent. This means that correct representation of radiative heat transfer is essential in insulated engine studies.

A methodology was developed for coupling the multi-dimensional heat conduction calculations to cycle thermodynamics and in-cylinder heat transfer. This methodology can use network-type representations of the structure, as well as detailed finite element models (FEM). Further, a rigorous mathematical procedure was developed for the treatment of the piston-liner interface, accounting for the piston motion and the resulting thermal interactions. Using NASTRAN FEM code, finite element representation of the baseline metallic Cummins NH engine was constructed.

The model was then employed in a parametric study of the effects of engine load at rated speed. Detailed results for heat flux and temperature distributions as a function of load were obtained including the details on the piston-ring-liner interface. Using the simpler network representation, parametric studies were carried out to demonstrate the applicability of the integrated heat transfer methodology and to document some important effects of speed, load and insulation level on component temperatures and main heat paths.

Studies were carried out of some of the key issues in low heat rejection engines using the developed heat transfer methodology including convective and radiative gas-phase heat transfer, multi-dimensional heat conduction and cyclic heat conduction transients. A wide-ranging design analysis matrix was covered, including seven different heat rejection configurations, and three different engine operating conditions. These studies led to the identification and definition of an important insulation parameter labeled retained-heat-conversion-efficiency (RHCE), which is the efficiency with which in-cylinder heat retained in the gases by insulation is converted directly into work. For a typical turbocharged intercooled highway truck engine at rated conditions RHCE is near 35-40 percent. This RHCE level is higher than that predicted by previous models due to differences in heat transfer models, specifically due to differences in spatial and temporal distribution of the heat transfer. As a result, the predicted thermal efficiency benefits of insulation are greater than previously reported by others, especially for engines with no exhaust heat recovery. Insulation of cylinder liner was found to bring only

marginal efficiency benefits, offset by the negative effects of lower volumetric efficiency, lower power and higher piston-ring-liner temperatures. A practical zirconia-coated configuration with a cooled metal liner, intercooled, with combined turbocompounding and Rankine cycle exhaust heat recovery, provided a 26 percent increase in thermal efficiency over a metallic cooled turbocharged intercooled baseline engine. Non-intercooled diesel engines have an even larger percentage increase in thermal efficiency, but since they start with a lower efficiency in their cooled baseline configuration, this larger increase only serves to close the gap between the non-intercooled and intercooled engines.

The analytical methodology is being supported by engine experiments carried out at Purdue University on a single-cylinder engine. The purpose of these experiments is to provide experimental data for calibration and validation of the methods. The single cylinder test engine installed at Purdue University is a Cummins NH engine, provided by the Cummins Engine Co. During the second year this engine was brought to operational status including super-charging and air heating equipment necessary to duplicate the in-cylinder conditions found in turbocharged highway truck diesels. A special test cylinder head with access ports for the required instrumentation was fabricated and installed as part of this effort. In order to provide a suitable access port for the gas radiation probe, one intake valve was replaced by a special sleeve. Since the engine breathes quite freely through the remaining valve, the reduction in air flow can be offset by additional boost from the supercharger. Special rocker arm and crosshead components insure normal timing and lift for the one operational intake valve.

The experimental data will be acquired using specialized instrumentation capable of measuring heat radiation, total surface heat flux and accurately phased cylinder pressure. Radiation heat flux is determined from a signal collected by a paired fiber-optic bundle protected from direct gas impingement by a sapphire window. The paired bundle splits the radiation signal into two channels and conducts each one to its own filter/detector system which is responsive to one specific wavelength.

Germanium (1.5 μm) and silicon (0.9 μm) photodiodes are used for the two detectors. The system has been constructed and tested in the single cylinder engine and is now ready for calibration prior to use in experimental segment of the program. Total heat flux is measured by an iron-nickel fast-response surface thermocouple installed in the cylinder head. Initial designs failed in service and so two alternative designs were substituted. Neither has reached the test stage yet. In addition, backup probes were ordered from a commercial source. Pressure-crank-angle data is measured by a commercial water-cooled pressure transducer, used throughout the diesel industry, combined with a precision angle encoder rigidly mounted to the engine crankshaft. Top dead center reference is determined by the optical proximeter described in the first year report.

ACKNOWLEDGEMENTS

The work reported herein has benefited from the contributions of many individuals and organizations.

The authors wish to thank Messrs. James C. Wood and George M. Prok, Project Managers at NASA-Lewis, for their constant interest and support, and for their valuable suggestions during the course of the program. ITI wishes to acknowledge the highly supportive role of Messrs. Albert A. Chesnes, Edward W. Gregory and Stephen Goguen of DOE staff in Washington, DC, contributing to the early integration of the ITI work into the overall Heavy Duty Transport and Ceramic Technology programs. In the materials area, the suggestions provided by Mr. Anthony C. Schaffhauser and Dr. David L. McElroy of Oak Ridge National Laboratory regarding the behavior of zirconia ceramics were very valuable.

The Purdue University subcontract effort has laid, despite many experimental difficulties, a foundation for the engine experimental program. Cummins Engine Company continued to be a very active voluntary industrial participant in this program giving generously of their time and material resources. Dr. S. M. Shahed and Messrs. Michael Brands, Kevin Hoag and Roy Primus have been very constructive in their technical liaison role, providing data for model development and application, and consultation with respect to the single cylinder engine Cummins has donated to Purdue University for this work.

INTRODUCTION

A technological thrust is currently in progress to develop insulated, low heat rejection diesel engines which exhibit higher thermal efficiency than current state-of-the-art diesel engines. Both industrial and government funded programs of significant magnitude are in place to develop the high temperature materials, lubricants and technical know-how required to achieve this potential.

Integral Technologies Incorporated (ITI) is carrying out a three year, three phase program, funded by the U.S. Department of Energy and administered by NASA-Lewis Research Center, aimed at developing a comprehensive heat transfer and thermal analysis methodology oriented specifically to the design requirements of insulated diesel engines. The technology developed in this program will make possible a quantitative analysis of the low heat rejection concept, including the determination of the degree of heat transfer reduction and performance improvement that may be realistically achieved, the identification of design strategies that may be adopted toward that end, and a detailed characterization of the thermal environment in which new materials, lubricants and lubricant concepts will have to exist.

The program is comprehensive in that it addresses all of the heat transfer issues that are critical to the successful development of the low heat rejection diesel engine, i.e.:

1) in-cylinder convective and radiative heat transfer;
2) cyclic transient heat transfer in thin solid layers at component surfaces adjacent to the combustion chamber;
3) heat transfer and heat flux paths to the moving interface between the piston, rings and liner;
4) steady-state heat conduction in the overall engine structure;
5) "slow" transients in the engine structure resulting from warmup or changes in speed and load.

Heat transfer data for development and validation of the metholodogy are being acquired at Purdue University under subcontract. In order that practical considerations are adequately taken into account in the development of the analytical methods, the program is structured around a commercial, state-of-the-art, heavy-duty diesel engine. Early in the program, NASA approved ITI's request to involve a major diesel engine manufacturer in the program on a voluntary, non-funded basis. As a result, the Cummins Engine Company and ITI have reached an agreement along these lines and Cummins' extensive design and testing experience in this field is available to the program.

The ITI program is comprised of a set of integrated analytical and experimental tasks. This Phase II report provides a detailed review of the ITI program approach, including the technical issues which underlie it, a summary of the methods that have been developed and the results which have been obtained in the second year of the contract effort. Results obtained during the first Phase of the program have been presented in the Phase I Report -- NASA CR-174783.

TECHNICAL ISSUES UNDERLYING ITI PROGRAM

A controlled amount of heat transfer is incorporated by design in current metal engines to assure adequate cooling of internal surfaces even at the highest thermal loadings, i.e. at the highest fuel flow rates occurring at the rated speed and load. The result is that a substantial amount of fuel energy is carried away from the combustion chamber, reducing the in-cylinder cycle efficiency and the energy availability of the exhaust gases. Based on ITI's calculations, for typical Class 8 highway truck diesel engines the heat transfer from the combustion chamber gases ranges from over 10 to 30 percent of the fuel energy depending on the operating conditions.

In order to reduce the rate of in-cylinder heat transfer substantially, it is necessary to increase the temperature of in-cylinder surfaces from current values near 500°K to well over 1000°K. Since the current levels

of heat transfer are near the lowest achievable with practical metal components, efforts are concentrated on the design of components using high temperature materials which would require less engine cooling. For a number of reasons, cost being prominent among them, ceramics appear to be the most likely candidates to satisfy the requirements set by practical considerations. However, their use as engine structural materials introduces a multitude of materials-oriented, engine design considerations. Some of the more prominent of these are:

1. material strength, toughness and stability at elevated temperatures;
2. thermal conductivity of high temperature, high strength, durable materials;
3. fatigue due to high cyclical thermal loading;
4. thermal expansion matching for ceramic and metallic materials;
5. lubricant stability and performance at high temperatures;
6. friction and wear characteristics with new structural materials and lubricants, which should be at least comparable to current technology engines.

As a result, sizable programs to evaluate insulated engine materials and designs and exhaust energy recovery methods (e.g., power turbine, organic Rankine cycle) are currently in progress, supported by both the industry and by the government. To be most effective, these efforts should be grounded in a comprehensive system analysis, which combines thermodynamic and heat transfer considerations and is designed to fully assess the implications of the concept as well as its feasibility and benefits in practical terms. The need for such an analysis becomes apparent once one considers some basic facts about the engine heat transfer process:

1. Combustion gas temperatures (spatially averaged) may be expected to reach values of up to 1800-2000°K at the highest thermal loading, which corresponds to a cycle-averaged temperature of 1300-1400°K. Therefore, in order to eliminate or substantially reduce the convective heat transfer, the average

wall temperature must be allowed to rise up to or near these levels.

2. Materials available for combustion chamber application appear to be limited to about 1400°K, which is close to the value estimated above for the desired average wall temperature. However, the materials limitations are accentuated by the fact that the wall temperature is non-uniform spatially as well as temporally.

3. Some of the heat transfer is due to heat radiation, which is cited in the literature to be on the order of 20-30% of the total heat rejected (see Chapter I). This radiation emanates from the hottest portions of the flame (on the order of 2500°K) which are well above any envisioned wall temperatures. Consequently, it is likely that in insulated engines with low convective heat transfer, a much higher percentage of the heat transfer will be through the radiation mechanism.

4. There is a complex interaction between the piston, piston rings, lubricants and the cylinder liner surface which determines the amount of energy (approximately three percent of the fuel energy) which is dissipated into heat at the interfaces and the direction of the resulting heat flow. At these interfaces issues of adequate lubricant life must be balanced against heat rejection paths created by lubricant cooling.

Therefore, due to fundamental physical phenomena (i.e., radiation, piston ring friction and limitations posed by currently envisioned materials), some engine heat transfer to coolant will have to be permitted. Additional limitations on maximum permissible temperatures may also be imposed by the lubricant properties. Beyond these, there are numerous other considerations, such as the magnitude of wall temperature swings and their impact on thermal stress fatigue, temperature limitations deriving from the large expansions to which the hot components will be subjected, and special cooling that may have to be provided for injectors and exhaust valves.

OUTLINE OF THE ITI PROGRAM

It is apparent that the task of development of the low heat rejection engine is a multifaceted one, and it requires a synergistic approach combining a number of engineering disciplines and technologies. Prominent among these are: heat transfer, thermodynamics, engine design and development, high temperature structural materials, and high temperature lubrication. All of these issues are coupled and need to be assessed and ultimately solved together. They are linked together by what might be termed the "engine environment," i.e., gas temperatures and pressures, wall surface temperatures, transient and steady state thermal profiles within the walls, etc. This environment has impact on engine heat transfer and thermodynamic efficiency and at the same time is a key input into the selection of materials and high temperature lubricants. The constraints that derive from the ranges of applicability of practical and forthcoming materials and lubricants must serve to keep specific designs for reduced heat rejection engines within realistic bounds. For cost effective development of this technology one must be able to assess the merits of different approaches in achieving significant reductions in heat rejection without compromising engine durability.

In view of all the technical issues discussed previously, the ITI program is structured around the development of an integrated methodology which can address the special design considerations inherent in the insulated engine concept. The general objectives of the program are:

1. Development of a systematic methodology for quantitative assessment of heat transfer and thermal processes in insulated engines which can serve as a tool for concept optimization;

2. Validation of the methodology with experimental data;

3. Application of the resulting methods to a comprehensive analysis of insulated engine design and operation, including evaluation of temperature fields in structure materials and temperature of lubricated surfaces.

To achieve these objectives, a number of closely related program elements or task areas have been defined. These are:

1) development of spatially and temporally resolved convection and radiation heat transfer submodels,
2) analysis of conductive heat transfer during fast and slow engine transients,
3) analysis of multi-dimensional steady state conduction heat transfer,
4) thermodynamic cycle analysis,
5) baseline cooled engine experiments and calibration of heat transfer models,
6) insulated engine experiments and code validation,
7) comprehensive analysis of the insulated engine concept and of materials implications.

These elements are described in more detail below.

Heat Transfer Models. Because they lack the basic physics of the convective process, the engine heat transfer correlations available in the literature are not applicable to detailed studies of heat transfer such as those needed in insulated engine analysis. New correlations were developed in the ITI program for convective heat transfer for bowl-in piston geometries, which include the effects of actual gas velocity, turbulence and zoned combustion. At the same time a sophisticated model was developed for heat radiation, which includes features such as the use of flame temperature instead of average chamber temperature, extinction coefficients based on soot concentration, and zonal geometrical model accounting for geometrical details of the combustion chamber and of the burned zone. Both of these correlations predict heat transfer in a spatially resolved fashion as well as time resolved.

Transient Conduction. The heat flux to the wall is highly transient with concentrated bursts of high heat flux followed by relatively long periods of low heat flux rates. This pattern produces temperature

transients in thin layers adjacent to the combustion wall surfaces. This dynamic heat conduction through the chamber walls is being analyzed by a transient one-dimensional heat conduction code which includes the effects of finite wall heat capacity. The model can handle layered or laminated walls, and this is an important capability, permitting studies of unconventional materials. Of interest are the surface temperature dynamics (time-varying wall temperature can reduce heat transfer) as well as thermal stress and fatigue produced by the temperature waves in the thin layer near the surface.

Steady State Conduction. The heat flux from the gases to the surfaces of the combustion chamber passes through the thin transient layer into the structure below. There the temperature field is steady-state (at fixed engine speed and load). It may be solved for by a network representation of the structure or by finite-element methods. Such a solution provides information about the temperature distribution produced in the structure by the engine combustion process. The calculated details of surface temperatures in the piston, along the head and in valves and along the liner set boundary conditions for the one-dimensional transient heat transfer calculations and feed back into the gas-wall heat transfer calculations. In this manner, the whole heat transfer/thermal problem is closed, and may be solved by appropriate analytical techniques.

Thermodynamic Analysis. The entire heat transfer problem is driven by the engine air flow and combustion phenomena. Thus, the central element within which an advanced heat transfer the methodology must be implemented is a reliable, detailed model of the engine operation. This model has to provide time resolved information about combustion chamber pressure, temperature and thermodynamic properties (separately for burned and unburned bases), flow velocities and mass flow through valves, intake angular momentum flux, details of the injection process, as well the instantaneous piston location and chamber geometry. The heat transfer calculations in turn feed back into the thermodynamic analysis and they have an effect on the instantaneous energy balance which ultimately determines the piston work done and exhaust temper-

atures. The engine thermodynamic cycle code used in this work is described in the Phase I Report. In addition to the capability to describe the in-cylinder processes, it also treats the engine as a system, including the turbocharger, aftercooler and power turbine. This allows prediction of the effects of insulation on the ultimate performance objective -- i.e., the overall system thermal efficiency.

Baseline Engine Experiments. Experiments are being carried out on the Cummins single cylinder engine based on the 14 liter NH series, representing a typical state-of-the-art (non-insulated) DI diesel engine. The engine test matrix includes a wide range of speeds and loads to provide an essential data base for subsequent analyses. This includes measurements of combustion chamber pressure and also the development and application of a technique for measurements of radiative heat transfer. The acquired data will be used to test and calibrate the new correlations for convection and radiation heat transfer developed in this program, using the thermodynamic cycle analysis in the pressure-time mode. In order to obtain the highest quality experimental data, state-of-the-art techniques and instrumentation for accurate pressure-time data acquisition are being developed. This includes accurate calibration of pressure transducers and the development of a precise method of crank angle indication based on an optical proximeter approach. A multiple-color method described in Chapter V will be applied to obtain accurate measurement of heat radiation in the engine environment, supported by an in-depth analytical study of heat radiation from sooting flames.

Insulated Engine Experiments. The baseline engine will be converted to an insulated engine by implementation of substitute materials. The main objective of these experiments will be to generate a reliable data base for testing and validation of the heat transfer and thermal methodology developed in this program. Accordingly, in choosing the locations and methods of insulation, use will be made of the methodology to produce meaningful changes in heat rejection, but at the same time every effort will be made to insure that the insulation applied does not interfere with the ability to acquire accurate data. The experience of Cummins

Engine Company, available to the program, is expected to be a very valuable resource during this portion of the work. The baseline data obtained in the initial set of experiments (see above) will provide a reference for before-and-after comparisons. In preparation for the experimental evaluation, instrumentation for temperature, heat flux and pressure measurements is being developed. These have to be suitable for high temperature operation, and in addition, techniques for their correct implantation into the ceramic components have to be found. The acquired data on temperatures, heat fluxes and engine performance will feed back into the thermodynamic cycle analysis and will be used to validate the design methods and concepts developed in the course of this project. Thus, a solid foundation for the refinement of the heat rejection strategies and for amplifying the design insights obtained in the analytical part of this program will be established.

Heat Rejection Analysis. Using the complete methodology, i.e., the thermodynamic cycle code, heat transfer submodels, one-dimensional heat conduction model for the near surface layers, the multi-dimensional heat conduction model for the surrounding structure and engine system model including turbocharger, power turbine and Rankine bottoming cycle, studies of heat rejection and engine performance are being made. The studies include baseline cooled engine, superinsulated limiting case, and span a whole range of intermediate insulating strategies utilizing spray coatings and monolithic ceramics. The engine conditions include rated speed/load, peak torque and rated speed/part load. The addition of the turbocharger, power turbine and Rankine bottoming cycle to the model provides a meaningful assessment of efficiency gains and also of materials requirements for these components.

One of the key outputs of the calculations will be the definition of the operating dynamic thermal environment of an insulated engine, knowledge of which is an essential input not only for selection and application of high temperature structural materials and lubricants but is also critically important in guiding the extensive research and development efforts that are underway in these fields. In this context different

strategies of heat rejection with different degrees of insulation are being investigated, weighing the growing severity of problems arising from increasing degree of insulation against the well-known benefits of increased thermodynamic efficiency, greater available energy in the exhaust and reduced or eliminated cooling system.

I. HEAT RADIATION IN D.I. DIESEL ENGINES

I. HEAT RADIATION IN D.I. DIESEL ENGINES

INTRODUCTION

A significant portion of in-cylinder heat transfer in diesel engines is due to heat radiation. Its importance relative to the convective heat transfer increases with increasing engine load and it will further increase as a result of evolutionary developments towards low heat rejection engine concepts.

In this chapter we address the in-cylinder heat transfer process from the modeling point of view. A complementary experimental program is underway at Purdue University, carried out on a single cylinder Cummins engine, whose objective is to provide heat radiation measurements for model validation. The present work extends the previous modeling effort carried out by the authors (Phase I Report, NASA CR-174783) which concentrated on modeling of the convective heat transfer. Similarly, as in that work, the emphasis is placed here on description of the key physical mechanisms involved, and on spatial resolution, extending the treatment of both beyond the previous state of the art.

Radiation heat transfer in internal combustion engines is produced by soot particles (if present during the combustion process) and by carbon dioxide and water molecules. Radiation is also emitted by many of the intermediate chemical species formed during combustion, but their concentration levels are small, and their effect is less important. Unlike soot, whose radiation is broad band, radiation from gaseous species is concentrated in narrow spectral bands, and its total magnitude is substantially smaller than that produced by soot.

In spark ignition engines, where the combustion is relatively soot free, the radiation heat transfer is always small compared to the convection heat transfer. By contrast, in diesel engines the radiation heat transfer during the combustion process can be of the same order of magnitude as the convection heat transfer. The relative magnitude of

these two components for the overall cycle is a point argued about in the literature, which tends to place the radiation magnitude at between 10 and 40 percent of the convection heat transfer magnitude. The uncertainty about this stems mainly from the fact that the split between radiation and convection heat transfer is highly dependent upon the engine design and operating characteristics. Other contributing factors are the difficulties of making such measurements, as well as the particular arrangement and location of the viewing port used to measure the radiation, which can significantly affect the collected radiation intensity. However, it seems to be well established that in state of the art metallic engines the heat transfer from gases to wall is dominated by convection, and radiation adds a smaller contribution. Thus, it has been considered acceptable until recently to treat radiation heat transfer in a rudimentary fashion or to lump it together with convection.

A special impetus for efforts to understand and quantify radiation heat transfer comes from the trend towards the development of low heat rejection (insulated) diesels. By applying insulating materials to diesel engines, one may expect to reduce the convective heat transfer more than the radiation heat transfer, making the latter the dominant source of gas-to-wall heat transfer. Thus, whereas the heat radiation has been a relatively minor element in studies of conventional diesel engines, its role in insulated engines is much more pronounced and of critical importance to assessments of the effects of insulation on engine heat transfer and performance. In consideration of the recent improvements in the detailed description of convective heat transfer (Phase I Report, NASA CR-174783), it became essential that parallel improvements be made in the modeling of radiation heat transfer.

EXPERIMENTAL STUDIES OF DIESEL HEAT RADIATION

A number of experimental studies have concentrated on diesel engine heat radiation over the past two decades. The observations made in these experiments provide an important source of data needed for validation of radiation models, giving an insight to the trends and magnitudes of radiation heat fluxes under typical engine conditions. In this section we review the experimental evidence to which references will be made in a later section dealing with model predictions. It should also be pointed out, that an experimental program is under way which will provide additional data for validation of the present model.

The first of the experimental studies in diesel heat radiation apparently was the work of Ebersole et al (1963) who used a fast response thermocouple located in the head behind a removable window. The engine used was a supercharged (pressure ratio, PR=2.3) two-cycle DI diesel engine. By measuring the surface temperature with and without the window, they deduced the ratio of radiant to total heat transfer as a function of engine load at a contant engine speed. The results were plotted as percent of maximum indicated horsepower and they showed that cycle-averaged radiant heat transfer increased from 5 to 45% of the total heat transfer, as load increased from 10 to near 100% of the rated load.

Flynn et al (1972) used a multi-color optical technique in which a detector was placed behind a window, viewing into the combustion chamber radially from the side near the head/cylinder interface. To provide access to the combustion gases inside the piston cup, a passage was cut across the piston top. The probe thus measured radiation along a line extending through the cut passage and across the cup diameter. The engine used in this work was a DI diesel operated in a supercharged mode (PR=2). The radiation was measured by a mono-chromator at seven discrete wavelengths from 1 to 4 μm. By fitting the seven readings, they obtained the spectrum of the radiation from which they deduced the apparent radiant temperature and emissivity. From these they calculated the radiant heat flux per unit area as

$$\dot{q} = \varepsilon_a \sigma T_a^4$$

This expression is strictly valid only for an infinite wall adjoining a medium with uniform properties (temperature and emissivity), and it is a good approximation if the entire volume of the engine were filled with uniformly distributed and strongly absorbing/emitting gas. From the spectrum of the radiation they also determined that Hottel's suggestion regarding the variation of soot emissivity with wavelength

$$\varepsilon = 1 - \exp(-kL/\lambda^{0.95})$$

was well supported by their data. The peak apparent radiant temperature they deduced, was about 2300°K, producing a peak radiant flux of 1.3 MW/m^2. By comparison to some earlier data taken on the same engine they concluded that the time-average radiant heat transfer accounted for about 20% of the total heat transfer at their standard operating point.

Their data also indicated a delay between the start of heat release and the start of radiant emission (4-6 CA degrees), indicative of reduced or no soot production during the premixed burn period. A no-boost run simulating naturally aspirated operation having a pronounced premixed burn, had no radiant emission during the premixed burn period. A further indication of these trends came from a run with a large injection advance and also from a run with lower cetane number fuel, both of which again had an extensive premixed burn with no associated radiation. In summary, the data form a very consistent picture which strongly supports their statement that there is no significant soot production during the premixed burn.

Oguri and Inaba (1972) studied two DI engines, one naturally aspirated (engine A) and one turbocharged (engine B); in addition, some limited data were obtained in a third engine. The total heat transfer was measured by a surface thermocouple, and the radiation heat transfer was measured by the same technique as used by Ebersole et al, i.e. a thermocouple behind a window. The radiation flux probe was located in the head at a radial location near the edge of the piston cup. The peak

radiation fluxes were lower than those measured by Flynn et al, about 0.42 MW/m^2 for engine A, and 1.1 MW/m^2 for engine B. The ratio of radiation to total heat transfer was found to depend on engine load, reaching values around 17% for engine A and 33% for engine B.

Sitkei (1974) also measured radiation in a DI diesel, but his description of the technique and results is not detailed enough to allow deduction of general results.

Dent and Suliaman (1977) used a fast response pyroelectric thermal detector to measure radiation, and a thin film thermocouple to measure the total heat flux. The engine used was a naturally aspirated DI diesel with deep cup and swirl combustion system. The measurements were taken at two locations on the head, one near the center and one above the piston crown. The center detector showed highly peaked emissions with maxima near TDC, increasing in intensity with speed and load from 0.09 to 0.55 MW/m^2. The outside detector showed lower peaks and broader, longer emission curves, reflecting the fact that the detector was shielded by the piston crown near TDC, and that the flame expanded outward into the squish zone and into the detector view on the power stroke at which time flame temperatures were already below peak levels. The overall level of emission agreed with the results obtained by Oguri and Inaba in their naturally aspirated engine, but was much lower than that measured by Flynn et al under no-boost conditions.

PRIOR MODELING APPROACHES TO DIESEL HEAT RADIATION

To calculate radiation heat transfer, one has to first address several key issues which have a direct impact on the calculated radiation level and on the spatial distribution of the radiation along the combustion chamber surfaces. These issues are:

1. Soot temperature
2. Absorption and emission of heat by soot
3. Geometrical representation and viewing factors

All of these parameters depend on engine speed and load and vary with crankangle as well. In this section we shall review literature dealing with modeling of diesel engine radiation heat transfer, and indicate how the above three issues have been addressed by others in prior investigations.

The earliest models of radiation heat transfer are typified by the model proposed by Annand (1963)

$$\dot{q} = C \sigma (T_g^4 - T_W^4) \tag{1}$$

where T_g is the mass averaged gas temperature from a one-zone model. The constant C lumps the effects of gas and wall emissivity. According to Annand, its value is greater than unity (1.5-3.0), which quite obviously is an artifice compensating for the use of the mass average temperature instead of the much higher soot temperature. In these early models, there were no attempts to determine the crankangle variation of the absorption coefficients or to account for flame/combustion chamber geometry.

Sitkei and Ramanaiah (1972) addressed these issues and proposed the use of experimentally obtained flame temperatures and of soot emissivity in the form

$$\dot{q} = \varepsilon \sigma (T_f^4 - T_w^4) \tag{2}$$

where

$$\varepsilon = 1 - \exp(-kp\ell) \tag{3}$$

where p is combustion chamber pressure, ℓ is a mean beam length defined as

$$\ell = 3.6\ V/A$$

where V is combustion chamber volume and A its surface. The absorption factor k in equation (3) was deduced by them from their experiments and was presented as a function of crank angle and excess air ratio.

Kunitomo et al (1975) proposed a model similar to that of Sitkei, complemented by a soot emissivity correlation. This correlation linked soot emissivity to gas emissivity (CO_2 and H_2O)--an implausible proposition.

More recently, Chang and Rhee (1983) calculated soot emissivity from an expression involving soot volumetric fraction. In that approach they used Rayleigh-limit expression ratio for the very small diesel soot particles. However, the model did not include calculation of the requisite soot volumetric fraction or radiation temperature, nor did they consider a realistic flame/combustion chamber geometry. In addition, they applied their emissivity model within the context of a highly idealized representation of the in-cylinder processes rather than to actual diesel engine conditions.

Chapman et al (1983) have recently contributed to the modeling effort by inclusion of spatial resolution through geometrical modeling. They modeled the radiating soot volume as opaque conical jets emanating from the injector, and solved for spatial distribution of the resulting heat flux by considering all direct viewing areas between the conical jet envelopes and the surrounding walls. It should be pointed out that treating the burned zone as being opaque implies that the absorption coefficient is always very high with emissivity of the burned zone equal to unity. However, literature shows that this limit is only approached in the middle of the combustion period in highly loaded turbocharged engines. Most of the time the burned zone is partially transparent and it must be treated by a volume rather than surface approach.

After the present work was completed, a parallel development appeared in the literature, the work of Whitehouse and Shahad (1984), who applied a zonal approach to geometrical representation of heat radiation between gas and surface elements. The combustion chamber content was divided into seven zones and to each of these were attributed the time variations of gas temperature and emissivity. Their model did not calculate these two quantities, however, and values obtained from experiments were used instead.

In summary, the literature shows a gradual development of the various elements required to construct a comprehensive heat radiation model. However, a complete model accounting for all of the key parameters has been lacking.

PRESENT APPROACH

In this chapter we shall describe our approach to the construction of a comprehensive heat radiation model applicable to diesel engines.

The heat radiation model which will be described here is imbedded in a general I.C. engine simulation code IRIS, which is currently being used to study a wide range of engine processes and design configurations. The present model seeks to describe the in-cylinder heat radiation process in a comprehensive way, subject to the constraint that the numerical burden introduced by the model on the overall engine simulation is not excessive so as not to compromise the capability to carry out extensive parametric studies at acceptable costs.

As a result, the radiation model has been constructed on a level consistent with that used to represent the combustion process. The combustion chamber is divided into two zones, burned and unburned, and the carbon particles (soot) produced by the combustion are assumed to remain confined within the burned zone. The radiation produced by the gas species is small and is neglected in our approach, although its inclusion would not be a major complication. The error introduced by this neglect is

likely to be most important during the latter portion of the combustion when soot levels decrease rapidly due to soot burnup, but during the early portions of combustion the soot absorption dominates the radiation process and the error is very small. The conditions within the burned zone are assumed to be spatially uniform, specifically the soot concentration, absorption coefficient and temperature. Further, the soot-laden gas is assumed to be gray, although in calculation of the total effective absorption coefficient the actual spectral variation of the absorption coefficient is taken into account. The surrounding surfaces are assumed to be diffuse.

The method used in our approach required work in six separate areas, which form the key complementary elements of the radiation model:

1. Combustion model
2. Geometrical description of the burned zone as a function of crankangle
3. Radiation temperature
4. Absorption coefficient
5. Soot concentration model
6. Spatial distribution of radiation heat flux.

The modeling approaches employed in these areas are described in the subsections which follow.

Combustion Model. During the combustion period the content of the combustion chamber is divided into two parts: unburned and burned. The burned products of air and fuel are thermodynamically treated as a mixture of 11 species representing the key combustion products.

During each time step, a portion of mass in the unburned zone is transferred to the burned zone according to the combustion rate. This rate is calculated from a combustion correlation which accounts for premixed combustion, diffusion burning, and a slow mixing "tail" burning region which becomes increasingly important at rich overall equivalence ratios.

Geometrical Description. The burned zone is assumed to be located in the central portion of the combustion chamber, surrounded by the unburned zone. The volume of the burned zone is calculated from its mass and density, available from a two-zone thermodynamic model. Its shape is obtained from a geometrical model which calculates the thickness of the surrounding unburned zone. Near TDC, all of the burned volume lies inside the piston bowl and, as the piston descends, this volume expands into the squish region and eventually fills the whole combustion chamber (Figure 1-1). This geometrical model is the same as that already introduced in the convective heat transfer model (Phase I Report, NASA CR-174783).

Radiation Temperature. The radiating soot temperature has always been an issue in engine radiation modeling, because it is difficult to predict. Previous investigations used, for example, the mean gas temperature (recognized now to be much too low) and adiabatic flame temperature. In the present model we link the radiation temperature to the average temperature of the burned zone (T_b). After the start of combustion, T_b at first gradually increases from its initial value, reaching a maximum shortly after TDC, and then decreases rather rapidly towards the end of combustion due to rapid entrainment of air from the unburned zone and volume expansion. Up to the point of the maximum, the model sets $T_{rad} = 0.9\ T_b$. This is done to account for the preferential radiant heat transfer from the soot particles which are thus cooler than the surrounding burned gases. After the burned zone temperature maximum has been reached, the soot radiation temperature is obtained from

$$T_{rad} = 0.9\ (r_b\ T_b + (1-r_b) T_{b,max})$$

where r_b increases from zero to unity during the tail end of the combustion period as a function of the ratio of burned mass to total cylinder mass. This particular form of the radiation temperature was adopted in order to reflect the fact that due to the fourth power temperature dependence the effective soot radiating temperature is dominated by the actively burning flame front, whose temperature is

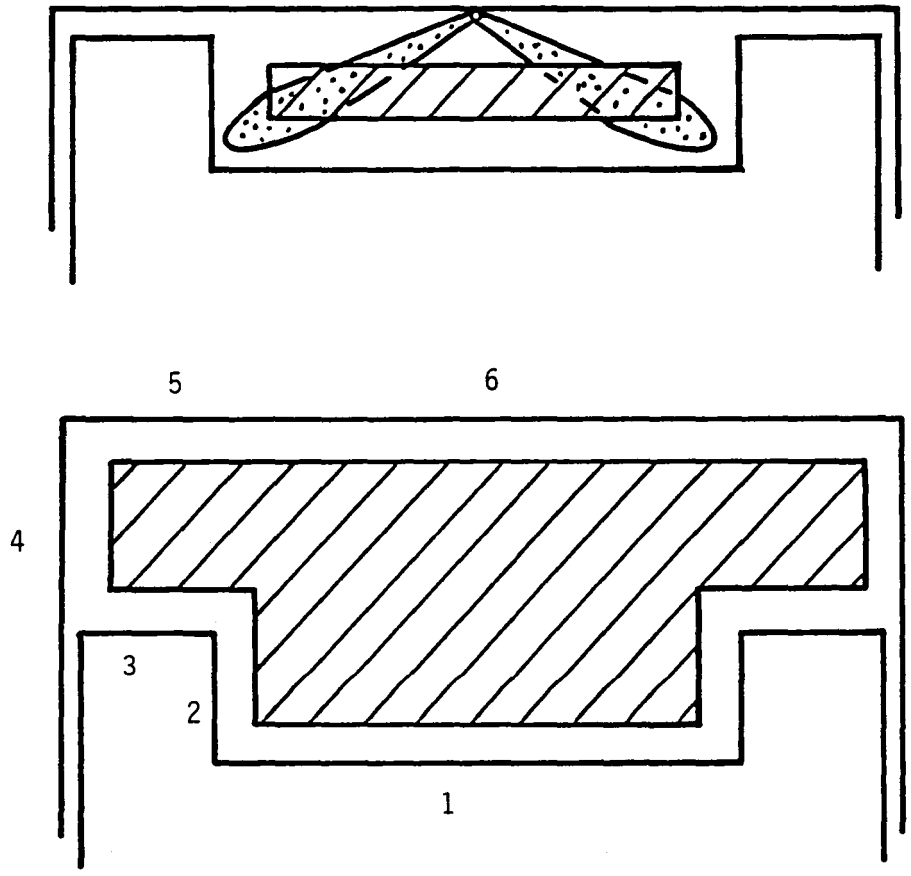

Figure 1-1 Geometrical model representing the unburned and burned (shaded) gas zones. Numbers refer to individual surface zones.

higher than the average of the burned zone (which includes actively burning species as well as burned-out products and which is being diluted by entrained air). Also, since the soot is produced in the flame itself, its concentration is the highest in these hottest parts of the burned zone. Better radiating temperature prediction could probably be obtained from a more detailed burned zone model tracking 3 or more zones during combustion, but that would require a substantial increase in the model complexity impacting also the thermodynamic model and the geometric zonal model described below.

Absorption Coefficient. As already mentioned, the soot is considered to be uniformly distributed over the burned zone. The absorption coefficient produced by this soot concentration can be calculated using the wealth of experimental and analytical studies of radiation soot laden gases available in the literature.

Radiation from soot depends on its spatial distribution, particle sizes and their refractive indices. For the small sizes encountered in diesel combustion an approximation known as the Rayleigh limit applies. From the Mie theory (van de Hulst, 1957), the absorption coefficient can be written

$$a_{\lambda s} = \frac{36\pi f_v}{\lambda} \quad \frac{nk}{(n^2-k^2+2)^2 + (2nk)^2} = \frac{f_v}{\lambda} g(n,k) \qquad (1\text{-}1)$$

where f_v is the volume fraction of soot in the gas and n and k are the refraction and absorption index, respectively, both of which are functions of the particular fuel properties and of λ. It should be noted that in this limit of small particle sizes, absorption coefficient a is independent of the actual particle size. Based on experimental data, Hottel (1954, p. 100) shows that the spectral distribution of $a_{\lambda s}$ is broadband with a shape

$$a_{\lambda s} \sim f_v/\lambda^n$$

where n is close to unity in the infrared region and approaches 1.4 in the visible range. The experimental results of Flynn et al (1972) confirm this dependence with $n \sim 0.95$. As a result, the function g(n,k) in equation (1-1) is approximately independent of the wavelength.

For a volume with uniform temperature and composition, one can calculate spectral emittance of soot for a layer of thickness L from

$$\varepsilon_{\lambda s} = 1 - \exp(-a_{\lambda s} L) \qquad (1\text{-}2)$$

Assuming that g(n,k) is indeed independent of wavelength, and substituting equation (1-1) into (1-2), and integrating over the entire wavelength space the product of ε_λ and the blackbody thermal spectrum to obtain the average soot emittance, one obtains a solution that can be expressed as (Yuen and Tien, 1977)

$$\varepsilon_s = 1 - 15/\pi^4 \, \Psi^{(3)}(1 + f_v g T/C_2 L) \qquad (1\text{-}3)$$

where T is the soot temperature and where $\Psi^{(3)}$ is the pentagamma function, and C_2 is a constant in Planck's spectral energy distribution.

Close approximations to the above equation are expressions

$$\varepsilon_s = 1 - \exp(-3.6 \, f_v g T/C_2 L) \qquad (1\text{-}4)$$

and

$$\varepsilon_s = 1 - 1/(1+f_v g T/C_2 L)^4 \qquad (1\text{-}5)$$

Experimental data (Gray and Mueller, 1974, p. 69) show that the function g has values that depend on the fuel hydrogen-to-carbon ratio. For oil flames they quote $g \sim 6.3$.

Substituting for g and C_2 into equation (1-4) yields

$$\varepsilon_s = 1 - \exp(-1575\ f_v\ TL)$$

or $$a = 1575\ f_v\ T \qquad (1\text{-}6)$$

Therefore, to calculate the soot absorption coefficient it is necessary to have the value of soot concentration. This concentration can be obtained from a soot model which tracks the instantaneous rates of soot production and oxidation and integrates them in time.

The absorption coefficient described above is strictly applicable only to radiation from the soot laden gases and to soot radiation reflected off the walls. Radiation emitted by the walls themselves is attenuated in the sooting volume with an absorption coefficient which is different due to different spectral content of this radiation. However, since this component of radiation is the smallest of all those considered, it was decided to minimize the model complexity and use the same absorption coefficient even for this portion of the radiation.

Soot Concentration Model. Soot formation is intrinsic to the diesel diffusion combustion process, and it stems from burning occurring in oxygen-poor regions surrounding the fuel droplets. The physical processes involved are very complex, as they depend on:

chemistry of precursor reactions,
coagulation and particle growth processes,
carbon oxidation chemistry,

which in turn depend on:

fuel composition,
pressure,
temperature,
local fuel and oxygen concentrations.

The final tailpipe soot level is a small quantity, being the result of two large and essentially cancelling processes of formation and burn up. Thus, prediction of the exhaust level is subject to substantial uncer-

tainty. Fortunately, in this work we are much less concerned about the residual level than about the much larger levels occurring during the combustion.

The initial thrust of this work concentrated on review of available empirical models in the literature which describe the rates of soot formation and of subsequent burnup. The review showed two models for soot production, one due to Khan et al (1973)

$$\frac{ds}{dt} \sim \phi_F^3 \quad p_f \exp(-20000/T)$$

where s is soot mass, ϕ_F is equivalence ratio in the formation zone, p_f is partial pressure of fuel in the formation zone and T is the unburned temperature. Another model is that due to Hiroyasu and Kadota (1976)

$$\frac{ds}{dt} \sim P \exp\ (-10000/T_b)$$

where T_b is the burned zone temperature.

As for soot burn up, there are four prior models. Nagle and Strickland-Constable proposed

$$\frac{ds}{dt} \sim - \frac{6s}{\rho_s d_s} P_{02}\ f(T,P_{02})$$

where P_{02} is partial pressure of oxygen, and function f is a complex Arrhenius-type expression. Fenimore and Jones suggested

$$\frac{ds}{dt} \sim - P_{02}^{1/4}\ P_{H20}^{1/2}\ T^{-1/2} \exp\ (-19000/T)$$

Hiroyasu and Kadota (1976) used

$$\frac{ds}{dt} \sim - \frac{6s}{\rho_s d_s} P_{02} \exp\ (-20000/T)$$

and, Lee et al (1962) proposed

$$\frac{ds}{dt} \sim d_s^2 \, P_{O2} \, T^{-1/2} \exp(-20000/T)$$

It is seen that there are wide differences between the various models proposed to date. This is perhaps not too surprising, as the formation and burn up mechanisms overlap and thus are difficult to reliably separate, and this is probably responsible for the difficulties encountered by researchers in this field, as evidenced by the differences in the empirical models developed to date. Furthermore, much of the data on which these models are based were obtained in laboratory burner flames rather than in diesel engines.

Since none of these models have been validated for diesel engines, there was no clear choice for a model to adopt. It was, therefore, decided to develop a new model, whose form would be guided by previously proposed models, engine parameters known to affect soot levels, and available diesel engine data.

An important part of the model formulation is its linkage to the combustion model. The soot model can incorporate only the available variables that the combustion model actually calculates, and the dependence on temperatures, equivalence ratio, partial pressures of certain species, etc., is strongly influenced by the details of the combustion model which in itself is an inexact representation. As a result, the final expressions employed in the present work are in many ways empirical correlations rather than first principle models.

In the model, the time development of soot mass is described as a process taking place in two regions: 1) an actively burning region, and 2) a fully burned region. The amount of fuel burned in any finite time increment is assumed to produce soot, which immediately begins to burn up. Since the mass from the actively burning zone is continuously being entrained into the fully burned zone, the soot formed in the actively burning zone is entrained as well. The actively burning zone is assumed

to be a very thin layer separating the burned and unburned zones and as such does not require a separate thermodynamic zone.

The amount of soot entering the burned zone is described in the model by a net formation term

$$ds/dt = A_1 \dot{m}_d \exp(-A_2/T_f) / (1 + 4.76\ YO_2)^3 \qquad (1\text{-}7)$$

representing the processes taking place in the actively burning zone. The variable YO_2 is the mole fraction of available oxygen in the actively burning zone, and $\dot{m}_d$ is the rate of fuel burned in the diffusion burning mode. The fuel burned in premixed mode produces no soot, in accordance with experimental evidence presented by Flynn et al (1974), Bryzik and Smith (1977) and others. The values of the constants, obtained by optimization and comparison to literature data, are $A_1 = 0.38$ and $A_2 = 5000$.

The subsequent burn up in the burned zone is described by

$$ds/dt = - B_1 s/(\rho_s d_s) \exp(-B_2/T_f) \times PO_2^{1/2} \qquad (1\text{-}8)$$

where ρ_s is soot density, d_s diameter of an elementary soot particle (a single soot particle consists of strings of many such elementary particles) and PO2 is the partial pressure of oxygen in the burned zone. The reason for using the elementary soot particle diameter is that is much more representative of the soot surface area than the total soot particle diameter. The optimum values of the constants are $B_1 = 0.015$ and $B_2 = 5000$. The soot density is taken to be $\rho_s = 900$ kg/m^3, which is the mean of values quoted in the literature (400-1500 kg/m^3). The diameter of elementary soot particles entering the burned zone is taken to be $d_s = 0.040\ \phi_{total}$ (μm). In the range of interest, $\phi = 0.3$-0.8, this gives values of $d_s = 0.012$-0.032 μm, which is in agreement with values quoted in the literature (see eg. Siegla and Smith, 1981).

Extensive study of available literature on soot levels occurring during combustion and on tailpipe levels provided guidelines for adjusting the constants of the model.

With these constants the model was exercised over a range of engine speeds and loads for a turbocharged heavy duty engine and for a naturally aspirated engine. The results will be presented in a later section.

Spatial Distribution of Radiation Heat Flux. The next element to be tackled was the method of calculation of the spatial distribution of the radiation heat flux. The complete solution of this problem requires solution of the radiation transfer equation, which includes wall emission, gas emission and absorption, and scattering. The scattering term, representing scattering from fuel droplets, can be neglected, as shown in the Phase I report of this program. This reduces the transfer equation to a form which lends itself to zonal approximation, a procedure developed by Hottel and Sarofim to solve the equation of radiant transfer in enclosures containing a radiating medium. Its principle is the discretization of the radiating medium into sub-volumes and of the enveloping surface into subsurfaces, each of which has uniform temperature and uniform absorption coefficient or emissivity, respectively. These smaller elements are referred to as zones. The equation of transfer is then integrated over each individual surface zone over all directions from which it can receive radiation. Since the conditions are uniform over the other N-1 zones from which the radiation arrives, the double integrals can be split into N-1 parts, which can be written as a product of two factors: one is the emissive power of the zone and the other is a function of the geometrical configuration of the two zones that face each other and of the absorption coefficient in the medium separating the two zones.

The zonal method is very powerful and it includes the representation of all key heat radiation mechanisms indicated in Figure 1-2 i.e.:

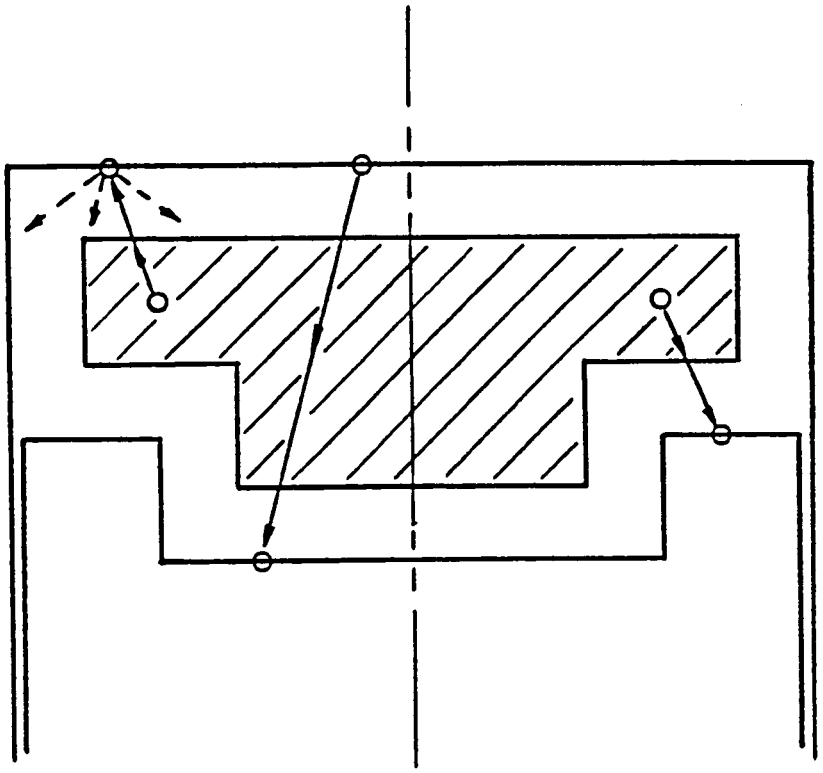

Figure 1-2 Representation of heat radiation processes, including radiation from gas to wall, reflection from one wall onto another and back into the gas, and radiation from one wall to another with absorption in the sooting gas.

1. soot radiation to walls,
2. surface radiation from one wall to other walls, including absorption in the gaseous medium,
3. reflection of incident radiation from one surface to other surfaces.

Following the derivations of Siegel and Howell (1981, p. 646) one starts with heat flux at surface k which may be written as the difference between the incoming and outgoing heat fluxes

$$q_k = q_{i,k} - q_{o,k} \tag{1-9}$$

where the outgoing flux for a gray diffuse surface may be expressed as

$$q_{o,k} = \varepsilon_k \sigma T_k^4 + (1 - \varepsilon_k) q_{i,k} \tag{1-10}$$

that is as the sum of radiation emitted by that surface and reflected portion of incoming radiation. The incoming flux may be expressed as

$$A_k q_{i,k} = \Sigma \overline{s_j s_k} q_{o,j} + \Sigma \overline{g_n s_k} \sigma T_n^4 \tag{1-11}$$

It may be noted that the above summations contain terms which are the products of emissive power and of geometrical/absorption factors $\overline{s_j s_k}$ and $\overline{g_n s_k}$, as discussed above. These geometrical/absorption factors have the dimension of area and are called direct viewing areas (DVA).

Substituting from equations (1-10) and (1-11) into (1-9), and after some manipulation, one obtains

$$q_k[A_k - \overline{s_k s_k}(1-\varepsilon_k)] = \tag{1-12}$$
$$= \varepsilon_k [\Sigma \overline{s_j s_k} ((1-\varepsilon_j)/\varepsilon_j q_j + \sigma T_j^4) + \Sigma \overline{g_n s_k} \sigma T_n^4 - A_k T_k^4]$$

This equation describes heat absorbed by a surface (lhs of equation (1-12)) in terms of incoming radiation from reflections from other surfaces, heat radiated by other surfaces, heat radiated by the gas, less the heat loss by outgoing radiation from the surface itself. In mathematical terms, this is a set of coupled algebraic equations, one for each subsurface of the combustion chamber. As seen in Figure 1-1, in the present work we discretize the combustion chamber into six subsurfaces (seven if piston has re-entrant bowl shape). In the present formulation there is only one gas zone, i.e., n = 1.

Equation (1-12) requires the determination of the DVA's - 49 surface-to-surface DVA's and 7 gas-to-surface DVA's. Due to symmetry of $\overline{s_j s_k}$ and due to the presence of a number of zero terms, much smaller numbers need to be determined. Also, it may be shown that $\overline{s_j s_k}$ and $\overline{g_n s_k}$ are related, and this further reduces the computational effort.

The DVA's can be calculated from

$$\overline{s_j s_k} = 1/\pi \iint \tau(s) \cos \theta_k \, d\omega_k \, dA_k \qquad (1\text{-}13)$$

$$\overline{g_n s_k} = 1/\pi \iint \alpha(s) \cos \theta_k \, d\omega_k \, dA_k \qquad (1\text{-}14)$$

i.e., they are the result of double integration over the surface area A_k, and over a unit hemisphere contructed above an infinitesimal part of A_k, of the incoming radiation from an area A_j passing through an absorbing medium with absorption coefficient a. Along each radiation ray extending from surface A_j to surface A_k one can calculate the integrated values of absorptance

$$\alpha(s) = 1 - \exp(-\int a ds)$$

and of transmittance

$$\tau(s) = \exp(-\int a ds) = 1 - \alpha(s)$$

needed for integration on equations (1-13) and (1-14).

It should be noted that the method treats the burned zone as transparent when the absorption coefficient is small, and it automatically progresses to an opaque (surface) model as the absorption coefficient increases. Even when a is very large, rays grazing the burned volume are only partially absorbed, however, rather than fully absorbed as they would be in a surface model such as that of Chapman et al (1983).

In calculating the DVA's one can use the tabulated results available for simpler geometries, such as axisymmetric ones, in numerous textbooks and handbooks dealing with radiation heat transfer.

Another method of calculation of the requisite DVA's is through the solution of the differential approximation to the equation of transfer for the whole combustion chamber. There is a whole series of such n-order methods, the simplest of them being the P_1 approximation (Siegel and Howell, 1981), the derivation of which is presented in the Appendix.

PREDICTION OF HEAT RADIATION IN A CONVENTIONAL COOLED DIESEL ENGINE

Turbocharged Engine at Rated Conditions

Baseline case. The model was first applied to a turbocharged Cummins NH series engine operating at rated conditions (2100 RPM, 350 BHP, intake pressure 2.26 bar, intake temperature 371K, trapped air fuel ratio 30.1, injection timing 21°BTDC). Emissivity of all surfaces was assumed to equal 0.85. The burn rate predicted using a combustion correlation for a two-zone combustion model that is part of the IRIS code is shown in Figure 1-3. The dotted line shows the apparent burn rate that would be deduced by a single zone model.

The combustion model provides essential inputs into the soot model, such as the burned zone temperature and composition. The burned zone temperature (Figure 1-4) rises to over 2800°K, and then decreases during

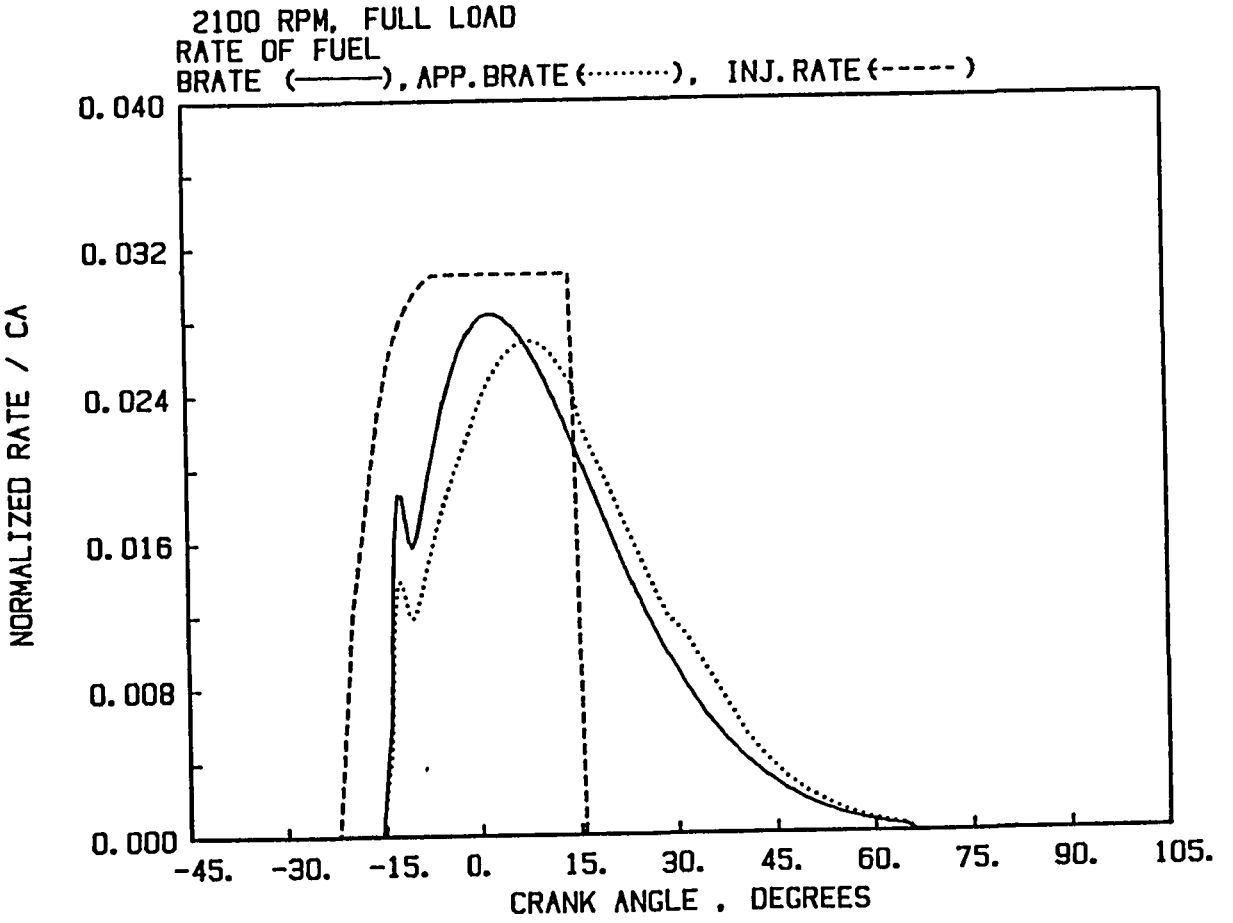

Figure 1-3 Rate of fuel burned at rated conditions; —— actual rate of fuel burned, ····· apparent burn rate deduced from a single zone model, --- fuel injection rate.

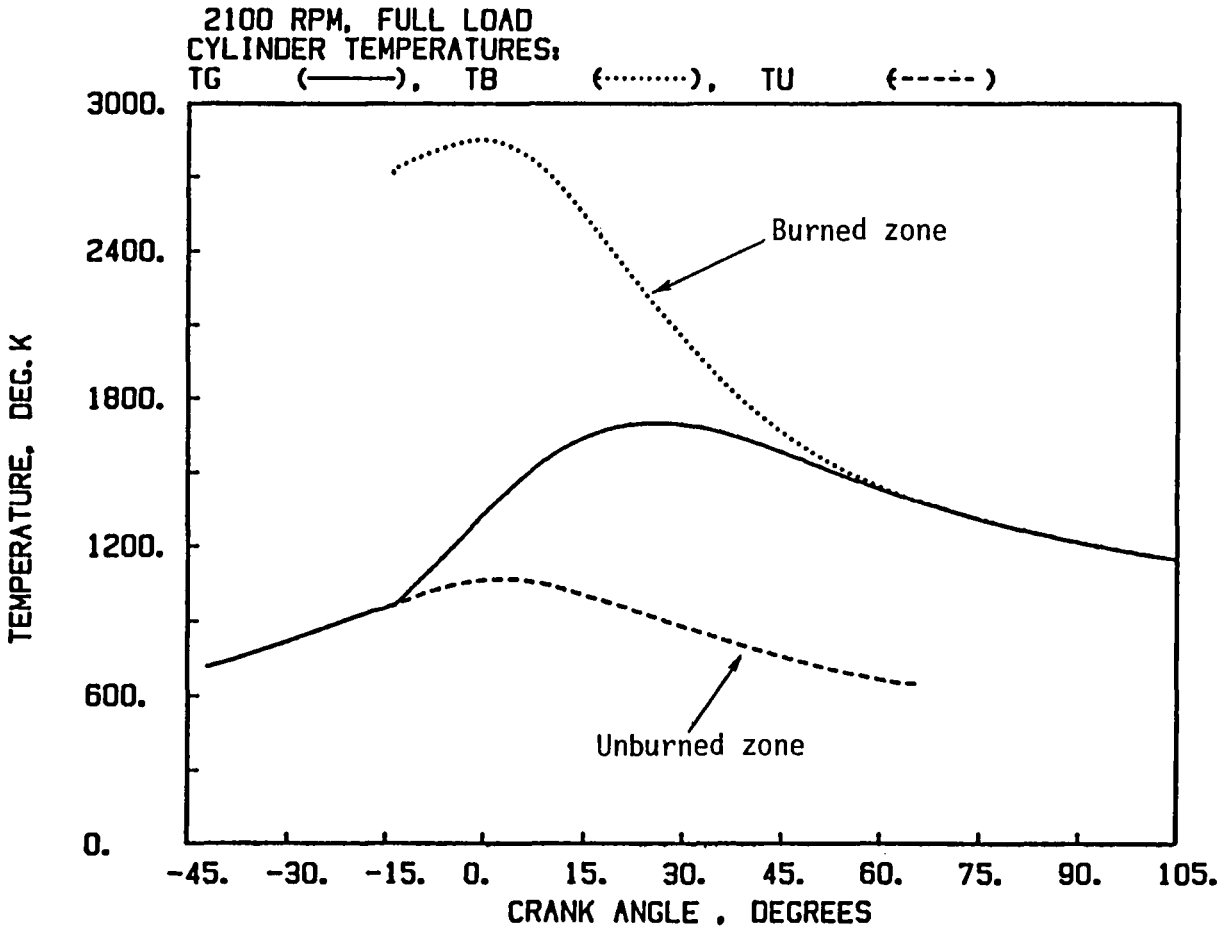

Figure 1-4 Gas temperatures during the combustion period; —— mass-averaged temperature.

the later stages of combustion. This temperature is important to the kinetics of both formation and burn up. Cylinder pressure reaches a peak of almost 130 bar and then rapidly decreases during the expansion. The soot burnup process is sensitive to the instantaneous values of the partial pressure of O_2, i.e., the product of pressure and molar fraction of O_2. The latter quantity rises during the latter portions of the combustion process, as the burned zone entrains air from the unburned zone. The product of the two reflects these two trends, as shown in Figure 1-5. The variation of the soot kinetic rates with crank angle is shown in Figure 1-6. Both curves of formation and of burn up have similar shapes. The formation leads the burn up and is responsible for the initial growth of the soot mass. Where the two curves cross is the point where the soot mass reaches the maximum. The burnup mechanism then takes over and it governs the level to which the soot is reduced by the end of combustion. This level is strongly linked to the exhaust levels, since only a relatively small amount of burnup takes place after the end of combustion.

The resulting soot instantaneous concentration level (Figure 1-7) reflects the trends discussed above. It rises sharply in the early stages of combustion, reaches a maximum and then decays to a low value. The maximum concentration level reaches 0.48 g/m^3 based on total cylinder mass (expanded to ambient conditions), while when based on burned zone mass it reaches a value of 3.1 g/m^3. This latter magnitude is in a good agreement with the data deduced by Matsuoka (1981). The shape of the instantaneous soot mass curve also agrees well with the experimental results of Matsuoka.

The soot concentration has a direct effect on the absorption coefficient of the burned zone. The emissivity of the burned zone depends on the product of the absorption coefficient and of the optical depth of the burned zone. Representing the optical depth by a mean beam length (L_m) calculated from the volume of the burned zone, one can calculate the product aL_m shown in Figure 1-8, which is indicative of the average zone conditions. The average emissivity is an exponential function of aL_m i.e.

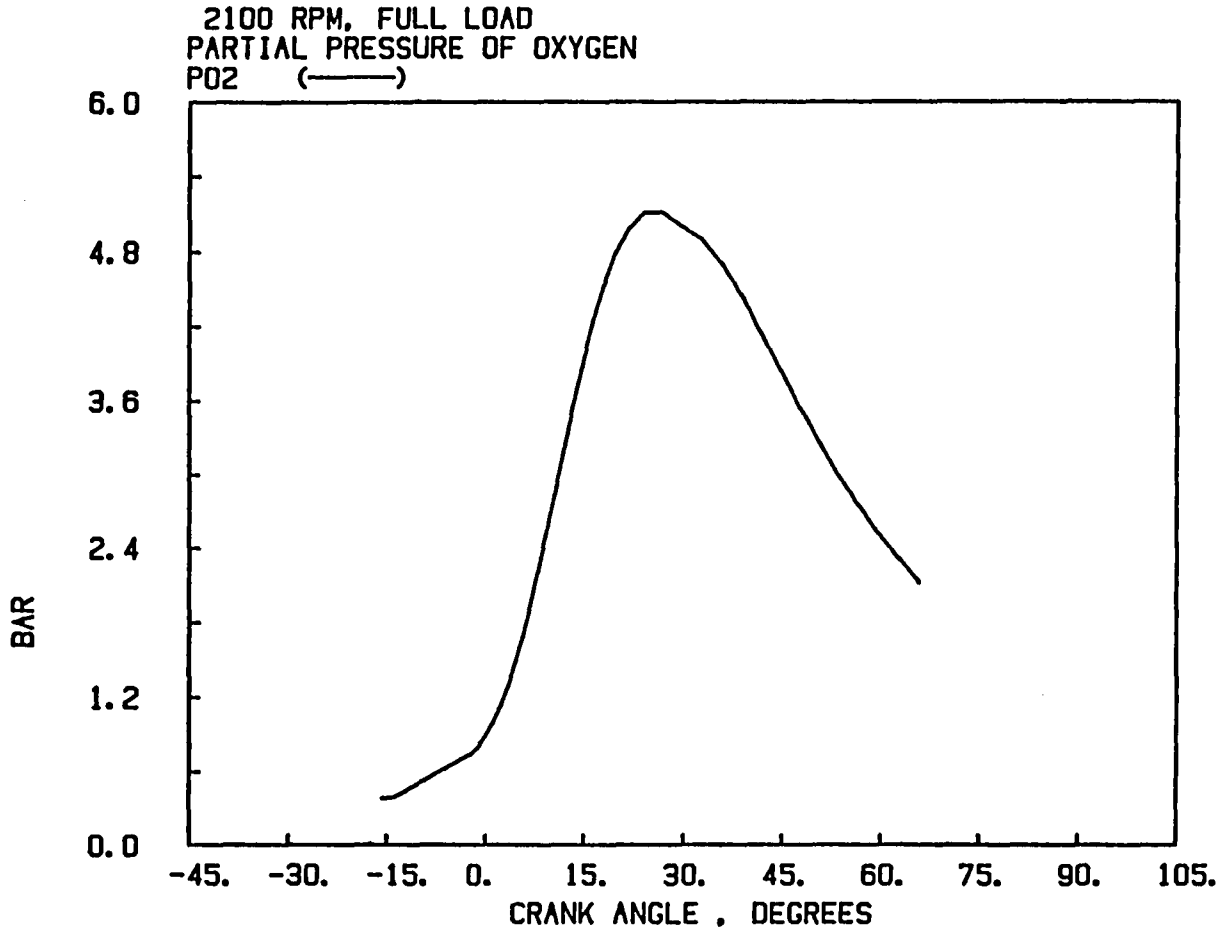

Figure 1-5 Partial pressure of oxygen in the burned zone, at rated conditions.

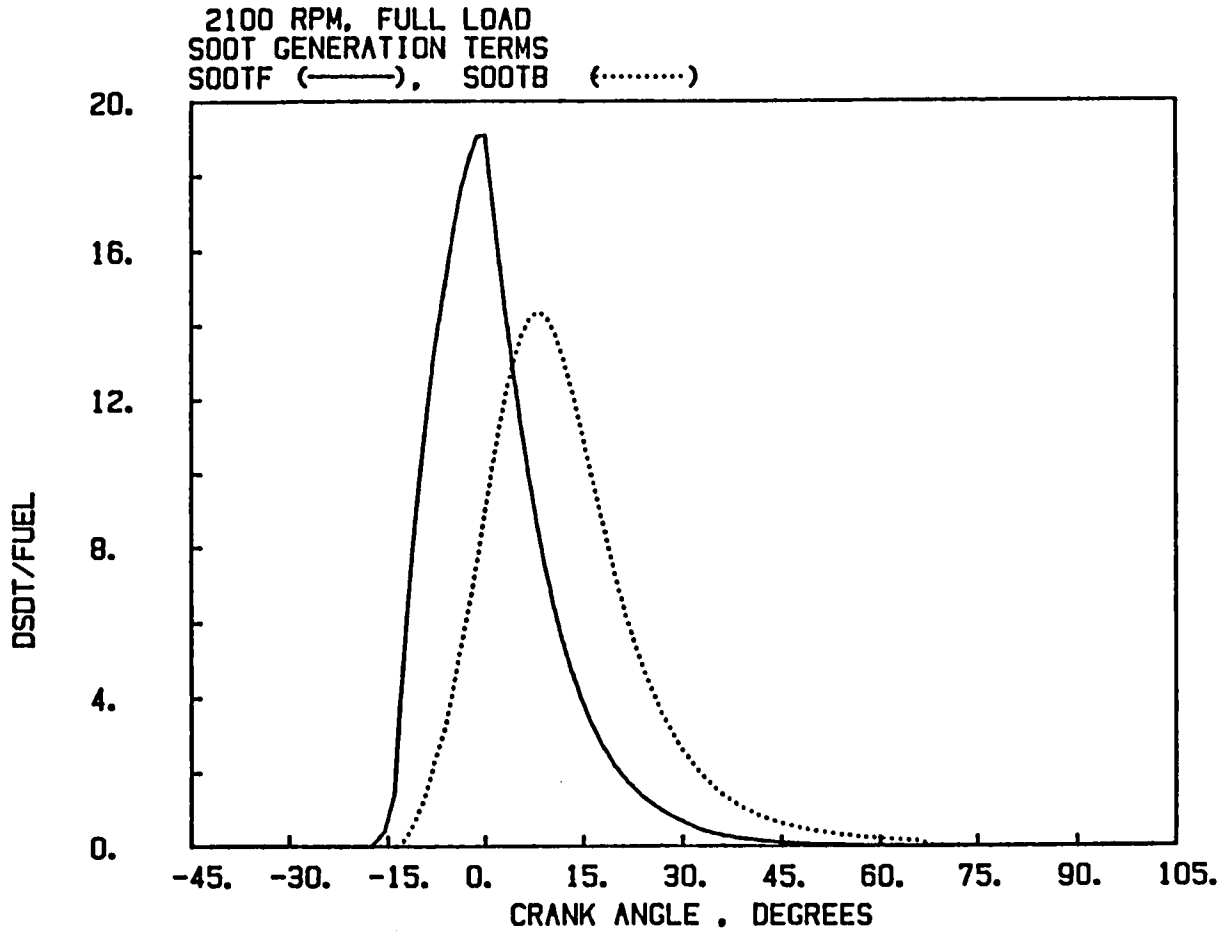

Figure 1-6 Soot generation and burn up rates normalized by fuel injected per cycle; ——— soot generation, ····· soot burn up.

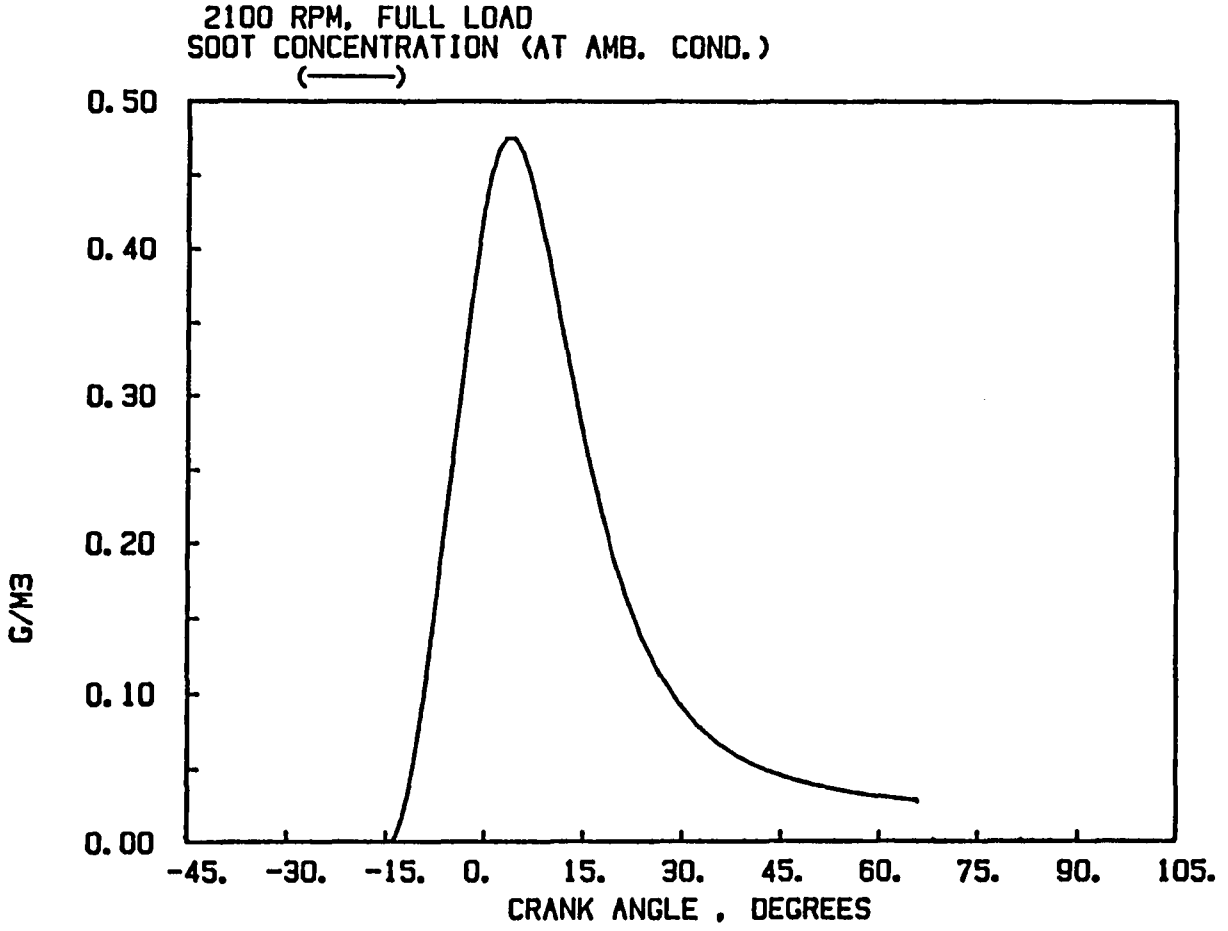

Figure 1-7 Soot concentration in the burned zone per total cylinder mass volume at ambient conditions.

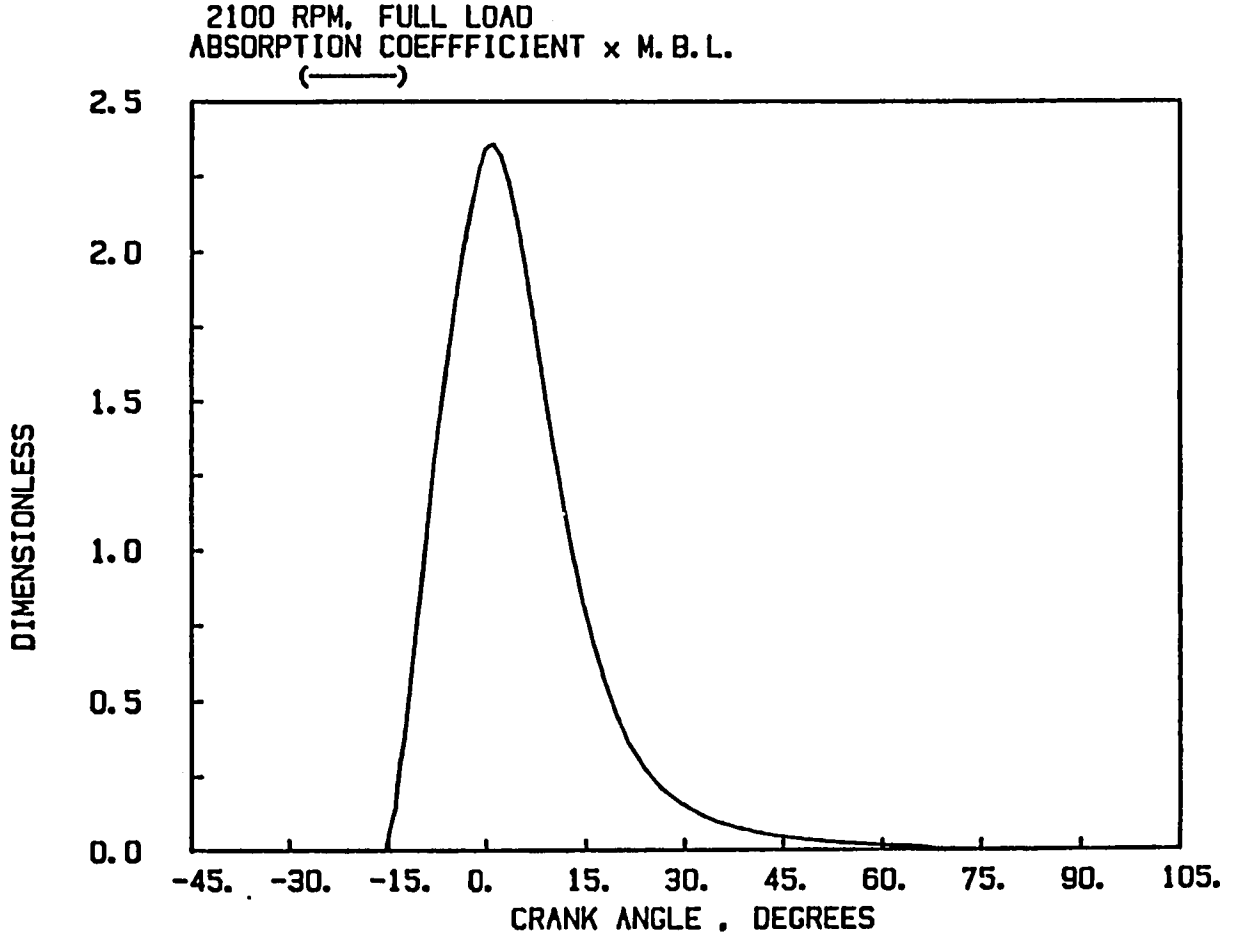

Figure 1-8 Burned zone absorption coefficient times mean beam length of the burned zone volume.

$$\varepsilon = 1-\exp(-aL_m)$$

and it follows that near TDC the burned zone is optically quite thick and almost opaque, getting less thick as soot burns up during the expansion stroke.

The resultant radiation fluxes per unit area are shown in Figures 1-9a and 1-9b. They display a wide variation from surface to surface according to the effective view factors between the burned gas zone and the surfaces on one hand, and between the various surfaces on the other hand. The peak flux values reach 1.4 MW/m^2, which agrees with the findings of Flynn et al (1972). These high rates pertain to the surfaces closest to the flame near TDC, i.e. the cup surfaces and the head surface above it. The squish zone surfaces and the liner have substantially lower radiation fluxes per unit area, especially early on, when all of the burned zone is still contained inside the cup. Towards the end of combustion all surfaces tend to receive similar levels of heat flux. The abrupt increase in flux visible in the curves of Figure 1-9 is due to the beginning of burned zone expansion from the cup into the squish zone.

The breakdown of total radiation heat transfer rate between piston, head and liner is shown in Figure 1-10, displaying a much lower heat transfer into the liner due to the piston shielding action. The split between the convection and radiation heat transfer is given in Figure 1-11, indicating that radiation accounts for only a little over ten percent of the total heat transfer at this operating condition.

Effects of Wall Emissivity. The radiation that reaches the surfaces of the combustion chamber is partly reflected back into the chamber. There it travels towards the other surfaces and is attenuated as it passes through the burned gases which absorb part of the radiation. Upon reaching a solid surface, the radiation is again partly absorbed and partly reflected, and so there is an infinite sequence of reflections with rapidly decreasing intensity.

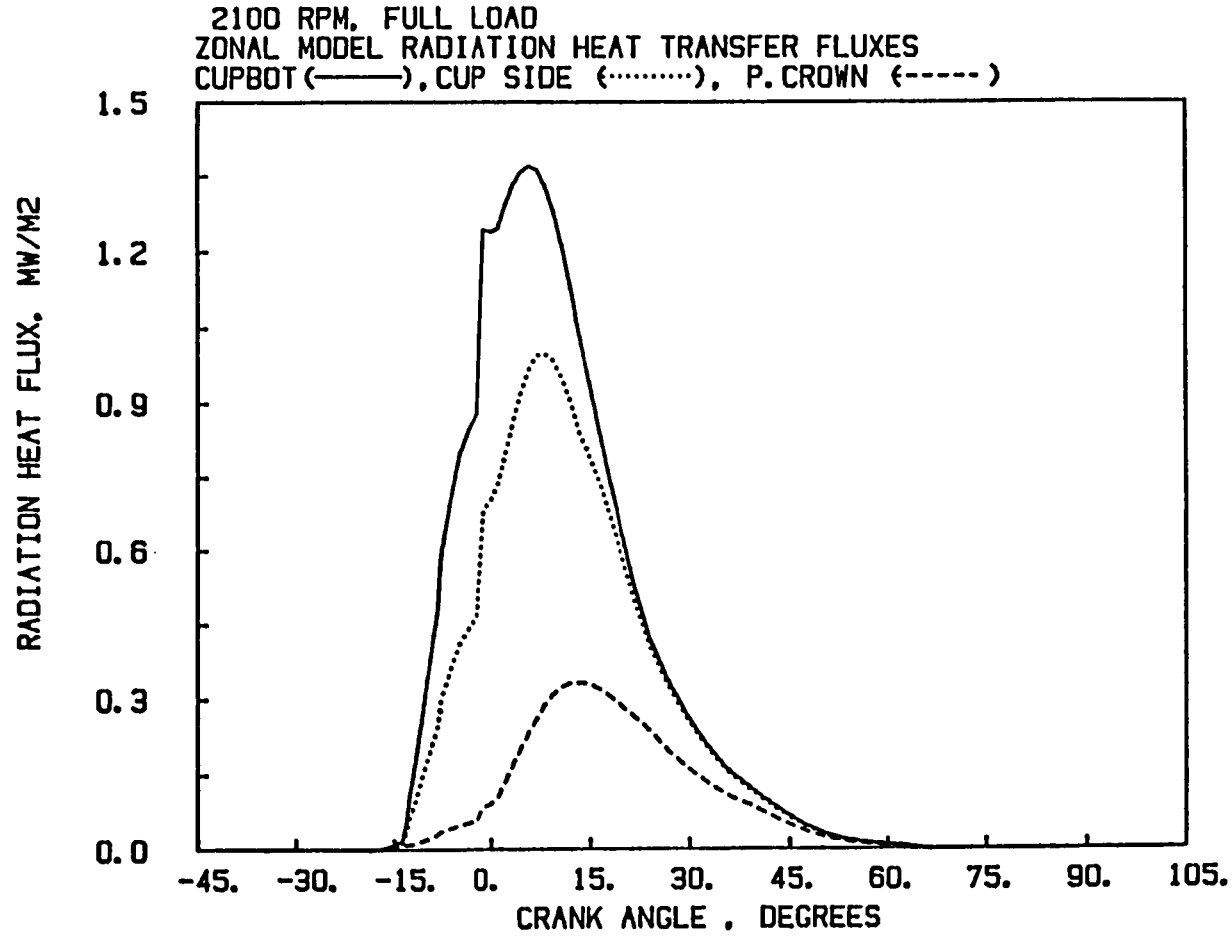

Figure 1-9a Heat radiation flux per unit area; —— cup bottom, ----- cup side, --- piston crown.

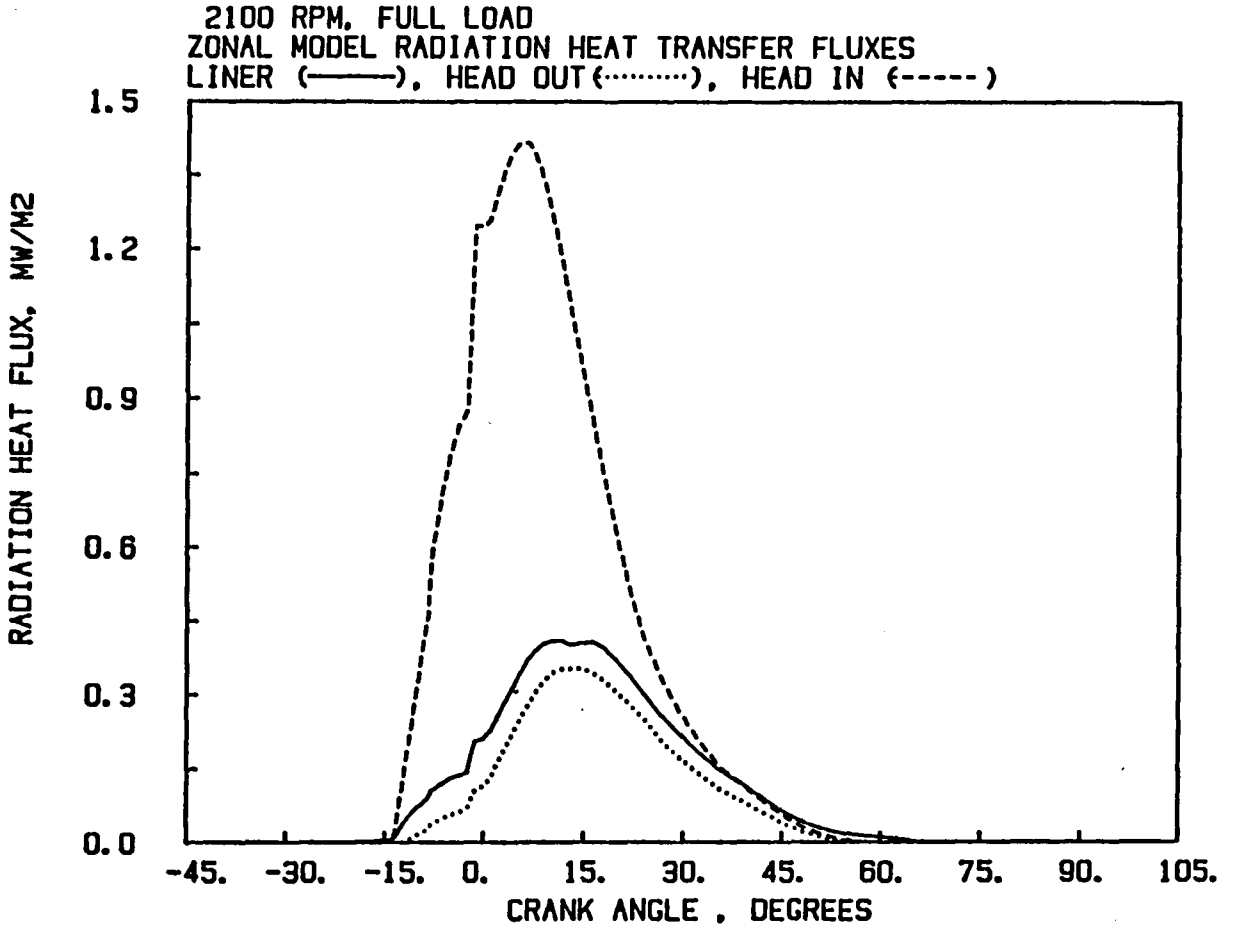

Figure 1-9b Heat radiation flux per unit area; ——liner, ···· head above piston crown, --- head above cup.

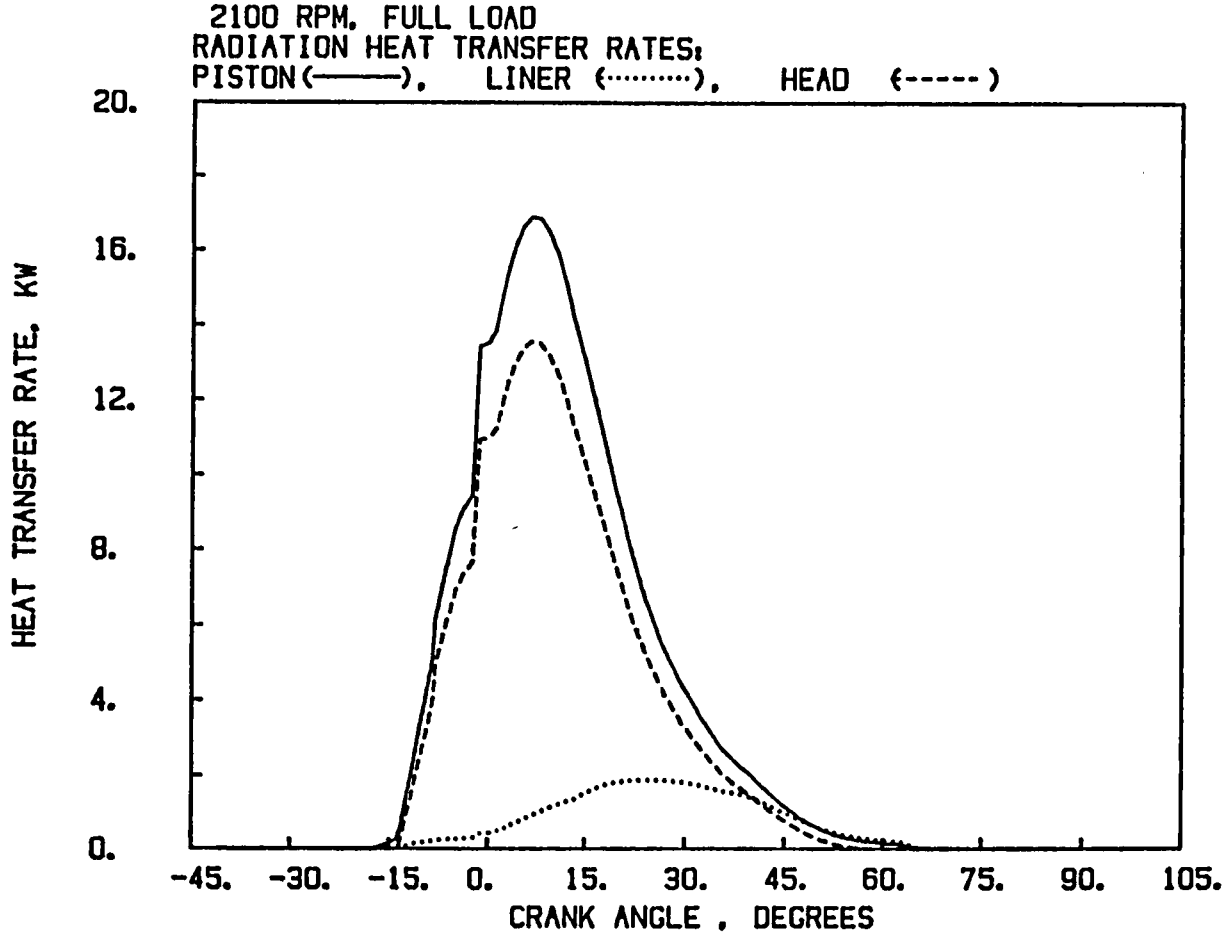

Figure 1-10 Breakdown of radiation heat transfer; —— piston, ...liner, --- head.

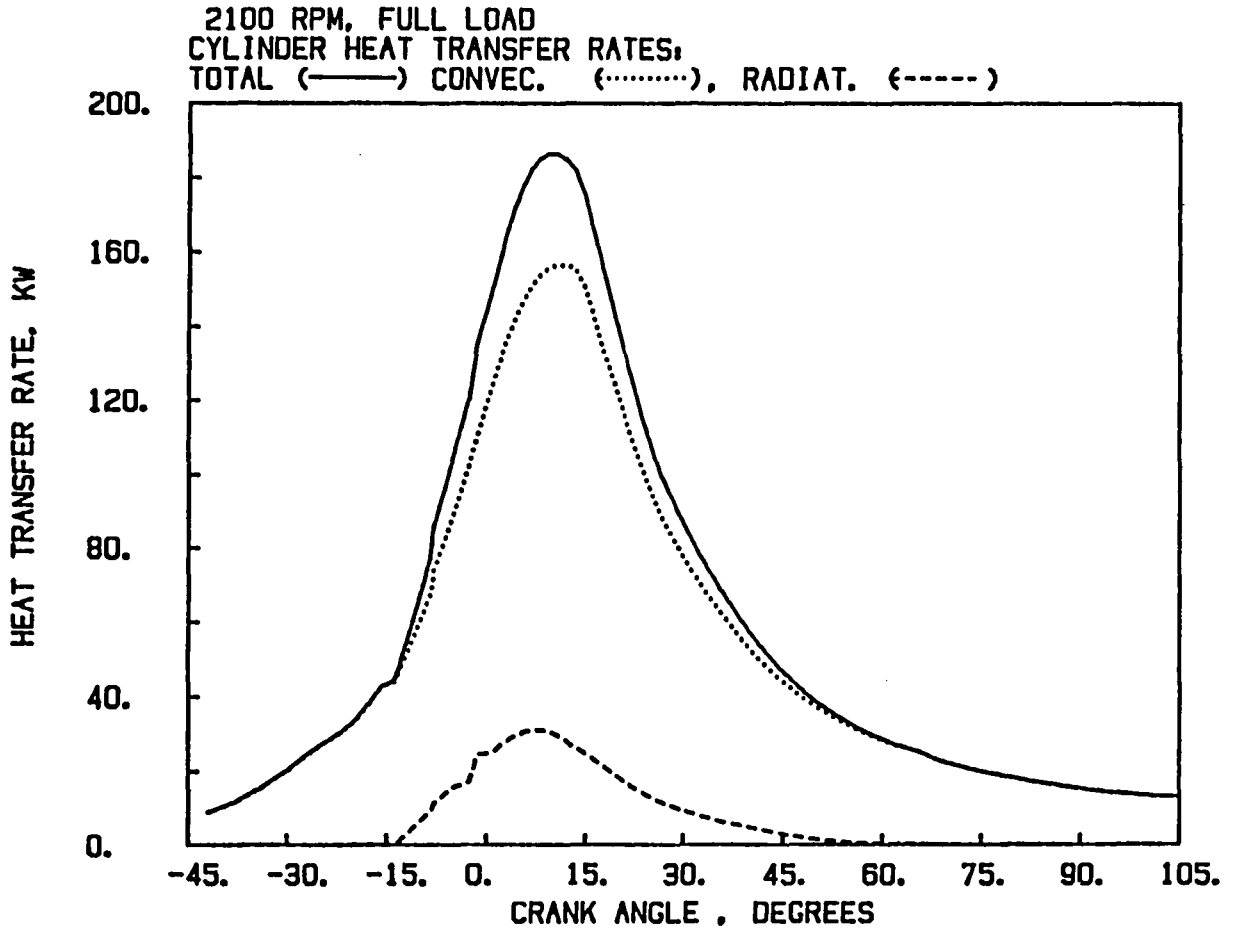

Figure 1-11 Total-cylinder heat transfer; ·····convection, --- radiation, —— total.

The case where the bottom of the cup is replaced by a highly polished surface with essentially zero emissivity is shown in Figure 1-12. Comparing these results with Figure 1-9 one observes that the bottom of the cup now receives no radiation (all is reflected), while other surfaces absorb increased radiation fluxes. The main beneficiaries are seen to be the cup side and the central portion of the head, followed by the outside portion of the head. The liner and the piston crown, which do not have a direct view of the piston cup bottom during the active radiation period, show only a very small increase coming from secondary reflections off the other surfaces.

Another example is shown in Figure 1-13 which pertains to a case where all walls are highly reflective with ε=0.01. The most noticeable result is the uniformity of flux over all the surfaces due to multiple reflections. The overall level of heat flux is seen to be very low, and this is due to the fact that the reflected radiation passes after each reflection through the absorbing medium which absorbs a large part of the reflected energy. This is mostly so during the latter part of combustion when the burned zone extends over most of the volume. Early on there is less absorption of the multiply-reflected radiation by the gas and this accounts for the skew of the flux profiles towards the beginning of combustion.

Effect of Cup Geometry. One of the capabilities of the method is the representation of gas zone and in-cylinder geometry and of their effects on heat flux per unit area absorbed by separate portions of the combustion chamber surfaces. The importance of such resolution may be seen in Figure 1-14, which describes the results obtained with a different piston cup shape: a deeper cup with d/bore=0.43 and depth/bore=0.40, as compared to the baseline cup with d/bore=0.73 and depth/bore=0.09. It may be observed that for this geometry the flux into surfaces surrounding the squish zone is significantly reduced (Figures 1-14a and 1-14b), while the surfaces adjacent to the cup retain the high flux levels seen in Figure 1-9. Area integrated heat transfer rates show even more pronounced differences, with head and liner being

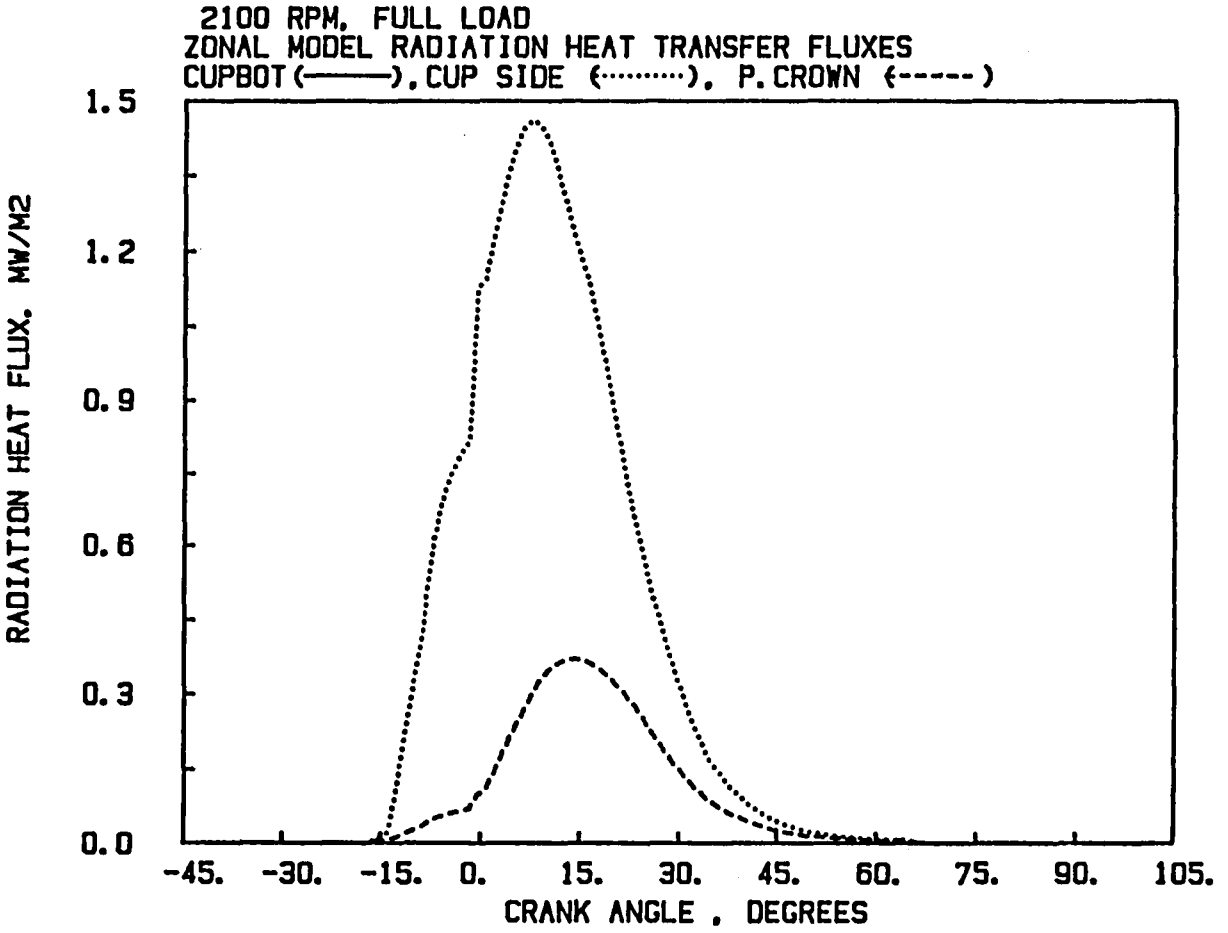

Figure 1-12a Effect of wall emissivity: highly reflective cup bottom; —— cup bottom, ····· cup side, --- piston crown.

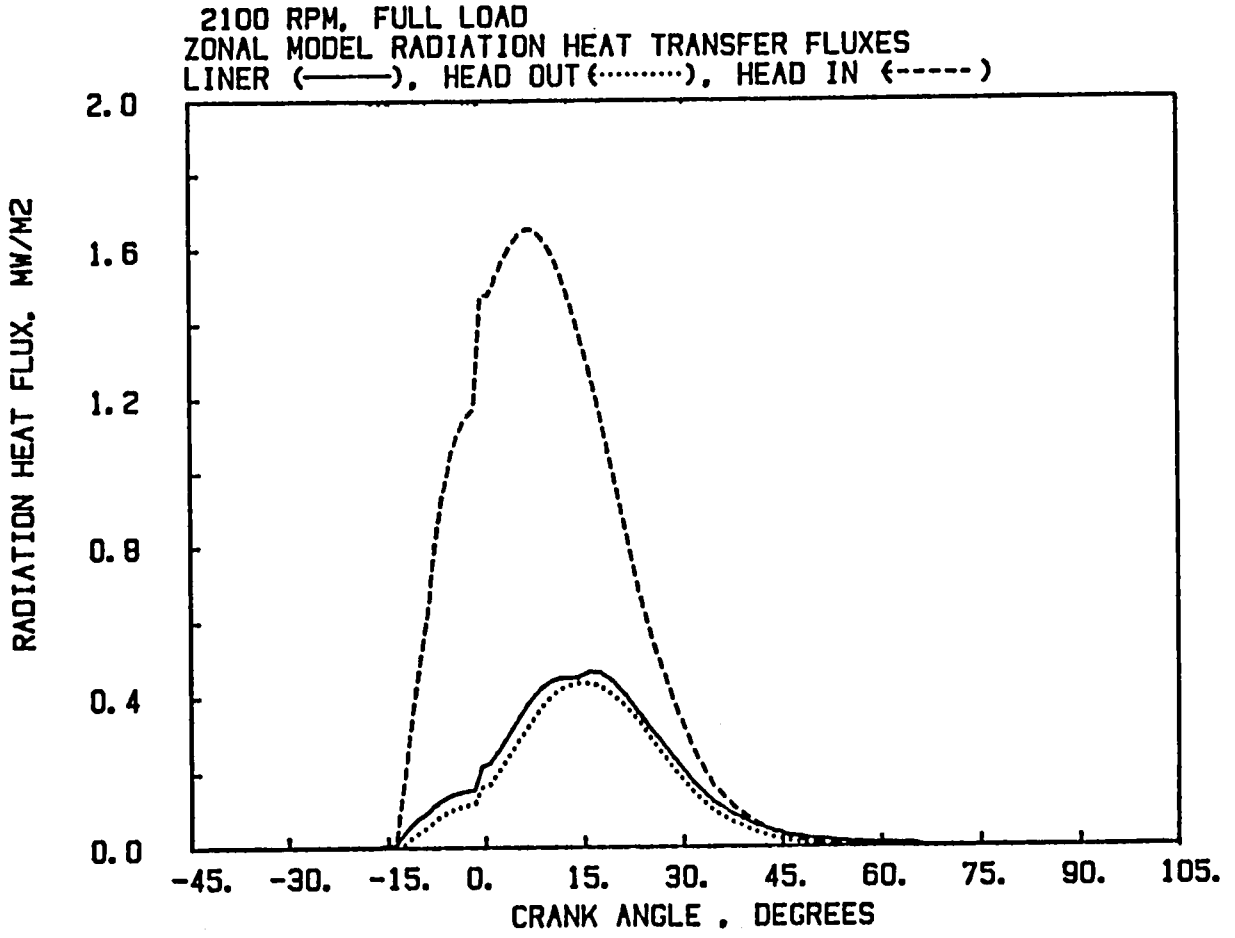

Figure 1-12b Effect of wall emissivity: highly reflective cup bottom; —— liner, ····· head above piston crown, --- head above cup.

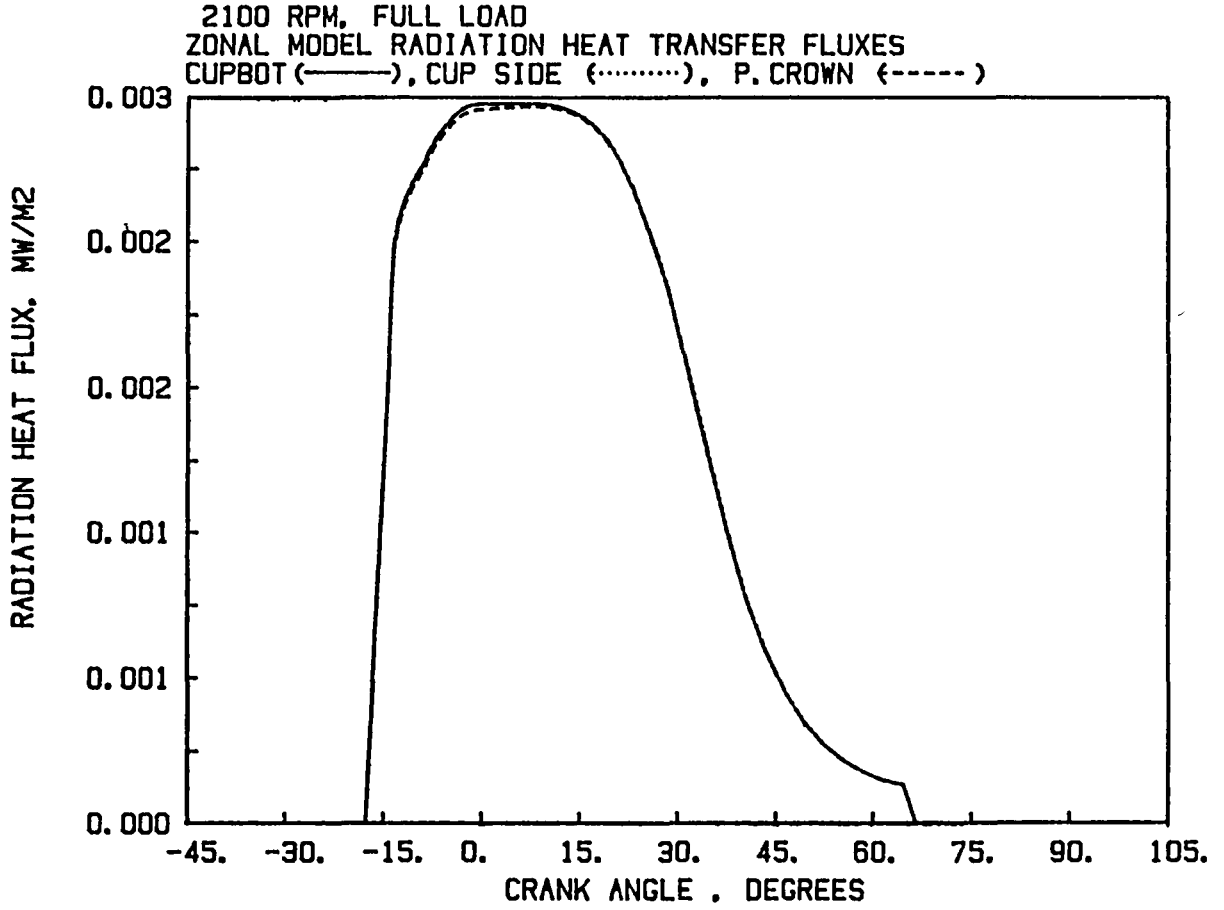

Figure 1-13 Effect of wall emissivity: all surfaces highly polished; —— cup bottom; ----- cup side, --- piston crown.

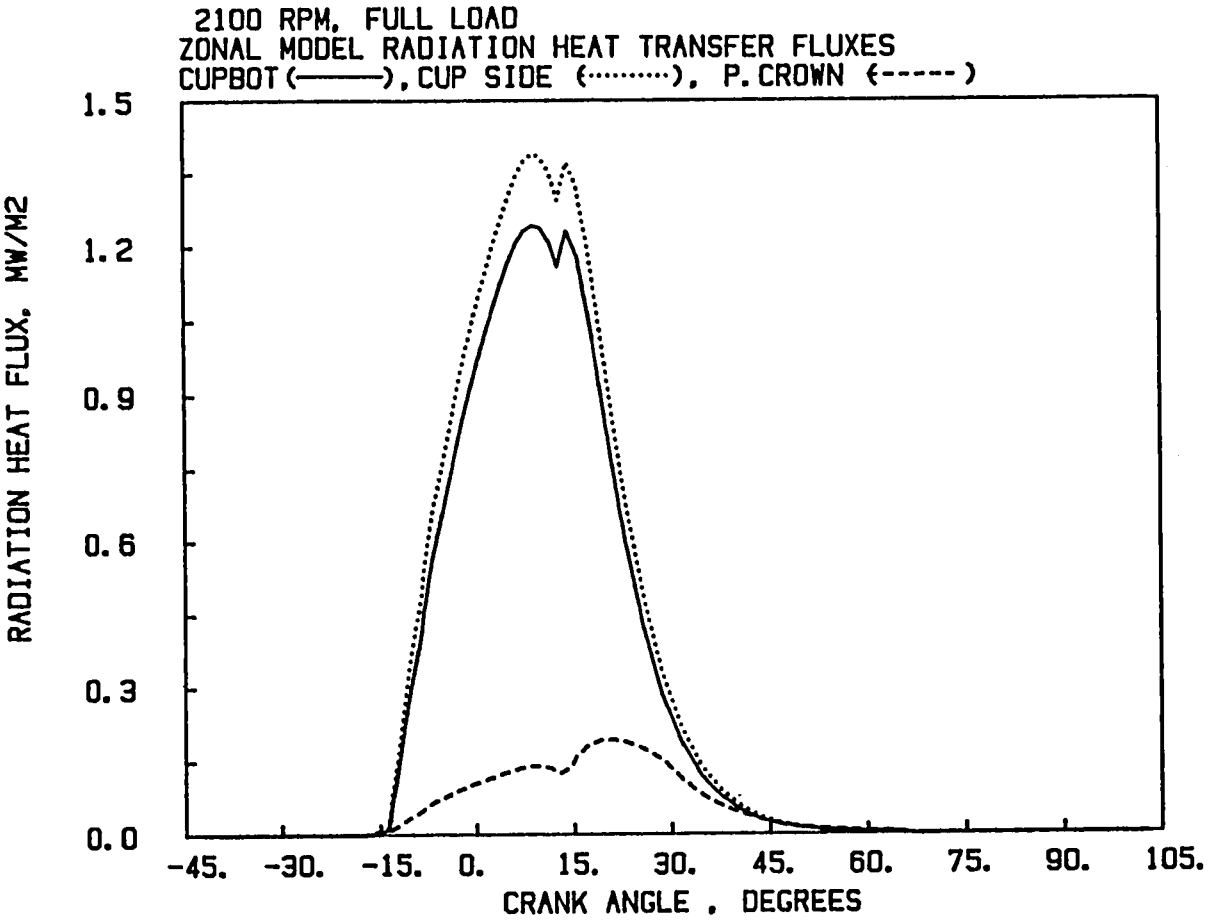

Figure 1-14a Effect of cup geometry: deep cup; —— cup bottom, ... cup side, --- piston crown.

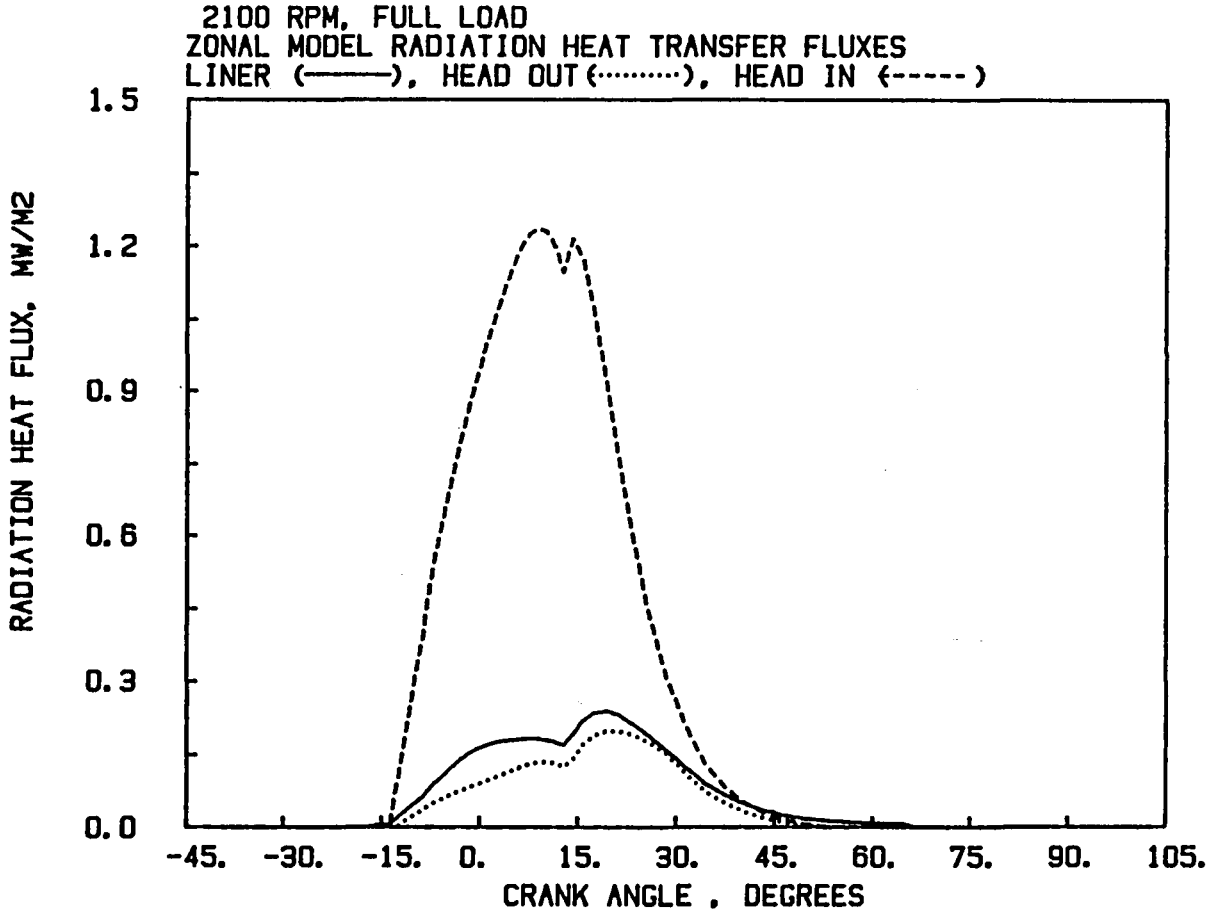

Figure 1-14b Effect of cup geometry: deep cup; —— liner, ...head above piston crown, --- head above piston cup.

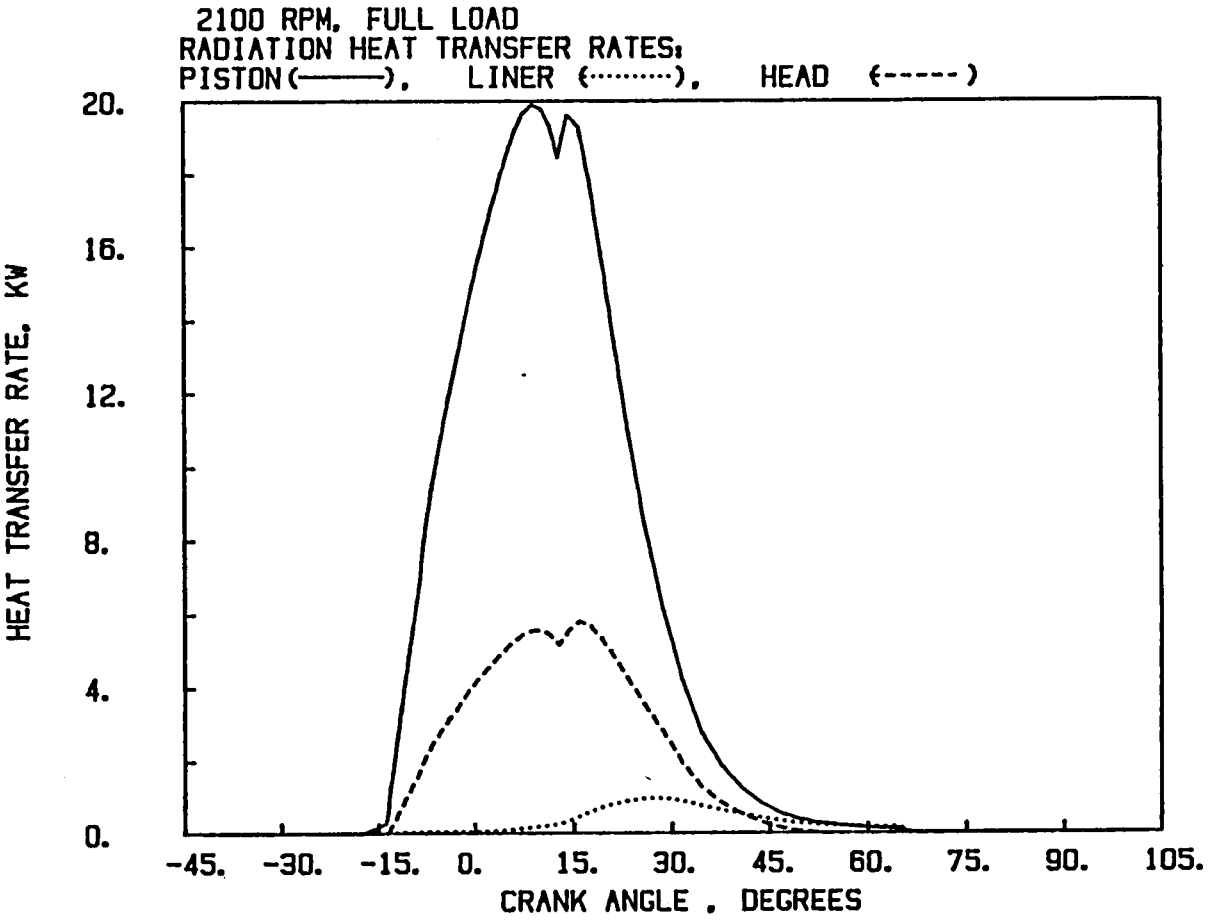

Figure 1-14c Effect of cup geometry: deep cup; breakdown of radiation into —— piston, ····· liner, --- head.

much lower due to shielding produced by the deep piston cup (Figure 1-14c).

Load and Speed Dependence

To analyze the model performance over a range of conditions, calculations were made for a range of speeds and loads for a simulated turbocharged NTC-305 Cummins engine. The starting point for this set of calculations was a set of performance data for a multicylinder engine obtained from Cummins and used in the Phase I Report. These data pertain to peak load conditions at speeds from 2100 RPM down to 800 RPM. Using Cummins' - supplied turbocharger maps a very good agreement was obtained between IRIS calculations and the data (see Morel et al, 1985). In this present work we varied the engine fueling rate and ran the full turbocharged engine simulation using the same maps to obtain the proper intake and exhaust plenum conditions at lower loads (100, 75, 50, 35 and 25 percent of full load fueling rate) at 2100, 1300 and 1000 RPM. The calculations included heat conduction through the structure, and as a result the wall temperatures were decreasing with decreasing engine load. This decrease has an important effect on the calculated convective heat transfer, but only a very minor effect on the heat radiation.

The results are shown in Table I, which includes several variables related to the soot model, i.e. the maximum value of instantaneous soot mass divided by mass of fuel burned up to that time, maximum burned zone soot concentration, soot concentration at end of combustion, and maximum partial pressure of oxygen in the burned zone. It further includes radiative, convective and total cycle-integrated heat transfer expressed as percent of fuel energy, and ratio of radiation to total heat transfer.

The first of these quantities shows the maximum fraction of the fuel mass burned up to that time that is converted into soot particles. This maximum occurs early in the combustion process (at fifteen to twenty percent point of combustion duration) and its magnitude varies moder-

	ϕ	(s/fuel)* max	conc$_{max}$**	P02 max (bar)	conc$_{final}$***	%fuel energy rad	%fuel energy conv	%fuel energy total	% rad/total
2100 RPM, full load	0.47	0.039	3.08	0.029	5.1	1.2	10.4	11.6	10.5
75%	0.41	0.034	2.63	0.038	3.7	1.2	10.5	11.7	10.2
50%	0.36	0.030	2.23	0.042	2.9	1.1	11.7	12.8	8.8
35%	0.29	0.022	1.62	0.031	2.4	0.9	13.1	14.0	6.4
25%	0.22	0.017	1.22	0.020	2.0	0.7	16.6	17.3	4.2
1300 RPM, full load	0.68	0.042	3.87	0.041	3.3	2.6	13.7	16.3	16.0
75%	0.61	0.040	3.47	0.041	3.1	2.4	14.1	16.5	14.6
50%	0.50	0.035	2.80	0.032	2.9	2.0	14.8	16.8	11.7
35%	0.40	0.029	2.21	0.022	2.8	1.4	16.2	17.6	8.1
25%	0.30	0.023	1.68	0.013	2.7	1.0	18.4	19.4	5.1
1000 RPM, full load	0.77	0.043	4.24	0.084	2.0	3.8	15.0	18.8	20.5
70%	0.68	0.041	3.71	0.047	2.3	3.5	16.8	20.3	17.2
50%	0.55	0.036	3.01	0.024	2.7	2.6	17.9	20.5	12.5
37%	0.44	0.031	2.40	0.013	2.9	1.8	19.4	21.2	8.3
25%	0.31	0.025	1.80	0.007	3.0	1.0	21.3	22.4	4.7

*Maximum value of instantaneous soot mass as a fraction of cumulative mass of fuel burned.
**Maximum concentration based on the volume of the burned zone mass at that instant evaluated at ambient pressure and temperature, g/m^3.
***Concentration at end of combustion based on total cylinder mass at ambient pressure and temperature, g/m^3.

Table I. Parametric Study of Soot Levels and Radiant Heat Transfer Over a Range of Speeds and Loads

ately with load, reaching over four percent at higher loads. It varies over a relatively narrow range from 2.0 to 5.1 bar. The second quantity is the maximum concentration of soot based on the volume of the burned zone mass at that instant, evaluated at ambient pressure and temperature. The maximum of this quantity occurs at about the same point in the process as the first one, and its magnitude reaches levels over 4g/m3, which, as already pointed out, agrees with the data of Matsuoka (1981). The third quantity is the maximum value of the partial pressure of oxygen, which is the product of the molar fraction of oxygen YO2 and cylinder pressure. Increasing the load raises pressure and decreases YO2, and the final value thus depends on the balance of these two trends.

The last of these quantities is the soot concentration at the end of combustion based on the volume of the total cylinder mass, evaluated at ambient pressure and temperature. This quantity displays a large variation with load and speed. The sensitivity of this parameter is not surprising, since the end-of-combustion value is the difference between two large numbers, cumulative soot production and soot burn up, which amplifies the effects due to temperature and oxygen concentration (load) and time available for soot oxidation (speed). It is also quite well correlated with PO2. The resultant values given in Table I and in Figure 1-15 reflect all of these dependencies. In general, they show an increase in the final levels of soot concentrations with increasing overall equivalence ratio ϕ, which is mainly due to the reduction in the partial pressure of oxygen.

The results for 2100 RPM show a somewhat surprising trend, where the final soot concentration is maximum at $\phi = 0.36$ and decreases towards the rated load. At 1300 RPM there is an indication that a maximum soot concentration is reached at the maximum point. At the lowest speed, where PO2 decreases with increasing ϕ, the soot concentration increases monotonically. This is due to a combination of higher burned zone temperature and higher PO2 which produces high rates of soot burnup. A review of broad range of literature data dealing with exhaust soot levels shows that the calculated values are of the right magnitude.

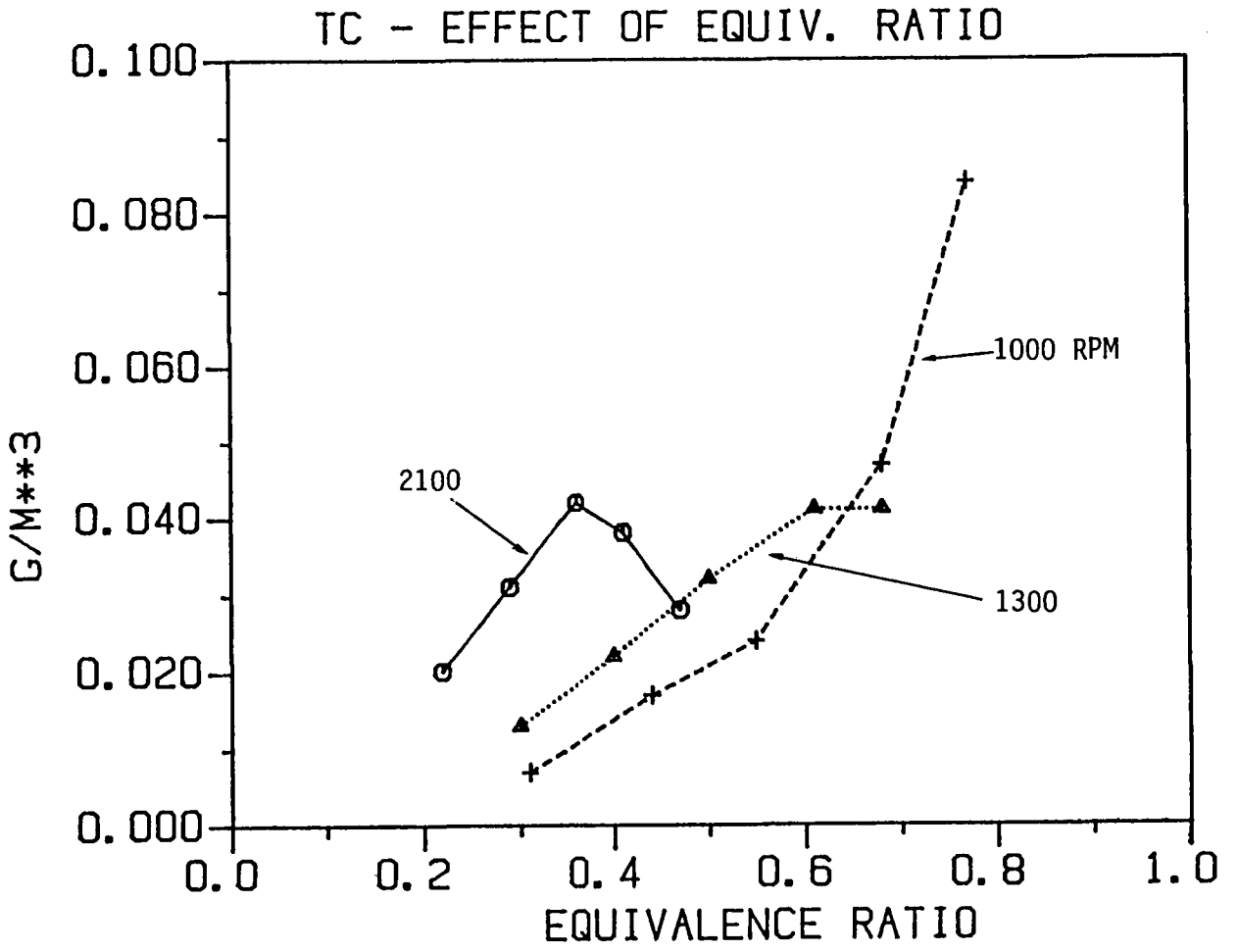

Figure 1-15 Soot concentration at the end of combustion.

Table I also contains the results of the associated heat transfer calculations. They show the ratio of the radiant, convective and total in-cylinder heat transfer to the fuel energy, and the ratio of the radiant to the total heat transfer. The radiant heat transfer is seen to vary from 0.7 to 3.8 percent of fuel energy (Figure 1-16). It is higher at lower speeds due to higher soot concentrations and also longer period (in seconds) over which it acts. The convective heat transfer varies less strongly, from 10.4 to 21.3 percent of fuel energy. The total heat transfer varies from 11.6 to 22.4 percent of fuel energy over the range investigated. Finally, the fraction of the radiant heat transfer as a part of the total in-cylinder heat transfer, varies from 4.2 to 20.5 percent; as seen in Figure 1-17, this ratio correlates well with the equivalence ratio independent of engine speed, but it should be realized that this plot also includes the effects of the variations in the boost pressure, and so this finding is not necessarily universal.

Injection Timing

One of the engine parameters influencing the radiation is injection timing. It affects the peak temperatures and pressures, and also the proportion of fuel burned in the premixed mode, which does not generate soot. To test the model predictions, a timing sweep was made at two engine conditions: rated and peak torque (1300 RPM). In these calculations the inlet and exhaust plenum conditions were held at the values calculated at the nominal timing for each case. The results showed that due to lowered rates of burnup the exhaust soot concentration increased sharply with retarded injection (Figure 1-18), and radiation heat transfer rate increased as a consequence (Figure 1-19). For this supercharged case, the amount of fuel burned in the premixed mode (which does not produce soot) varied from a maximum of 9.8% of total injected fuel at -31^{o} timing, down to a minimum of 0.4% as -1^{o} timing in the rated case, and in a similar manner in the peak torque case. These amounts were small enough to have only a secondary effect on the trends seen in Figure 1-19. Comparing the radiation rate to the trends obtained by Flynn et al (1972), one finds that the experiments

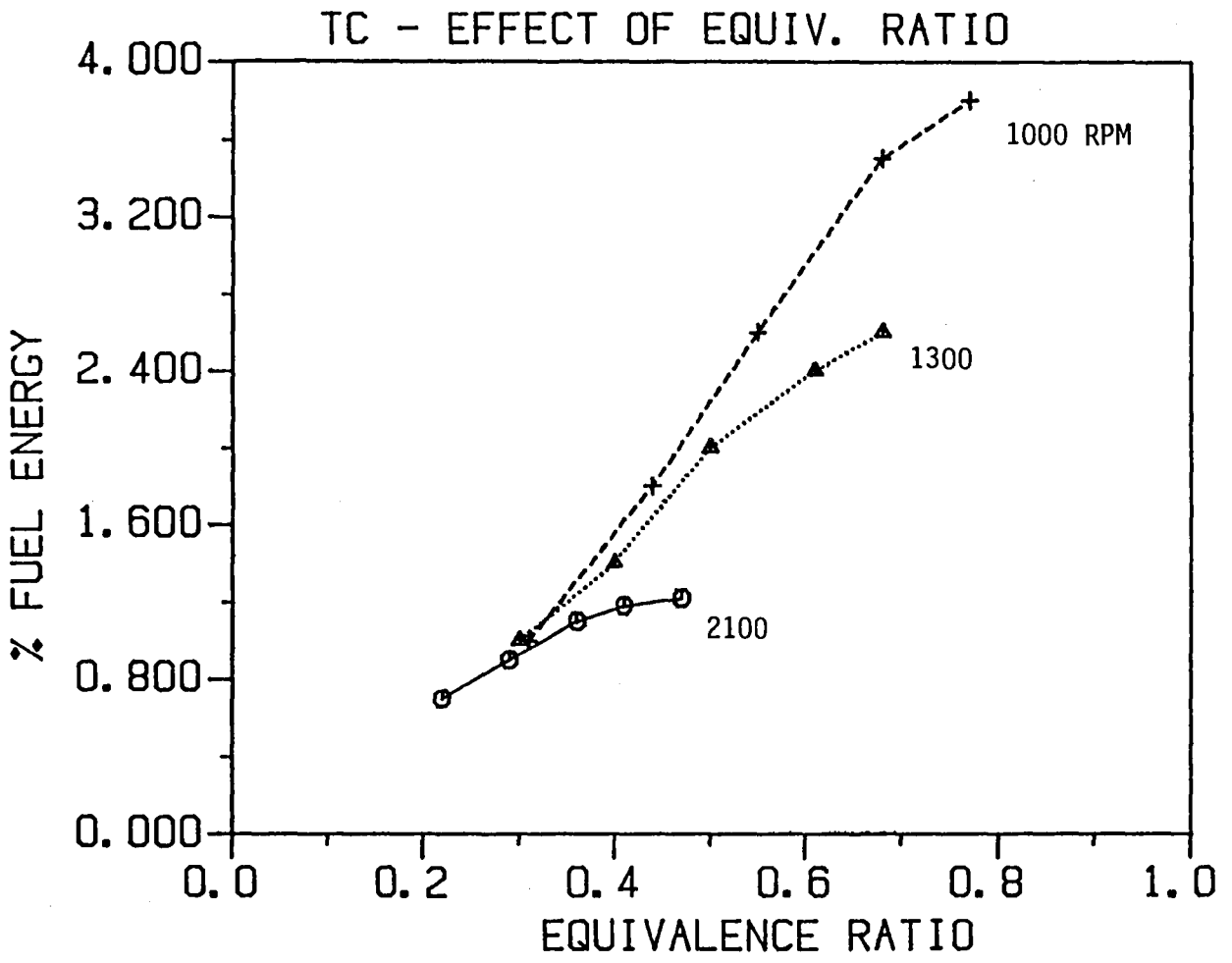

Figure 1-16 Radiation heat transfer expressed in percent of fuel energy.

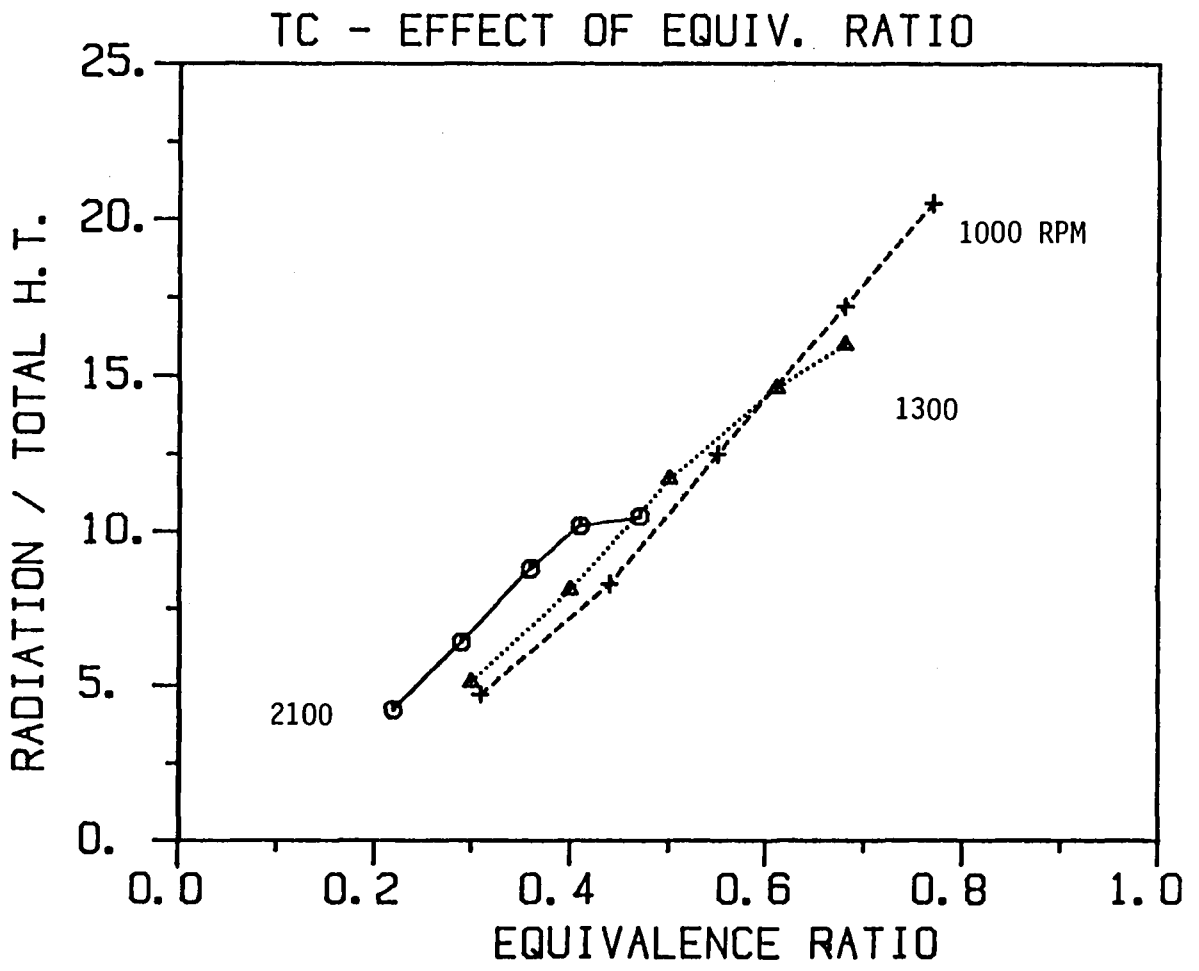

Figure 1-17 Radiation heat transfer expressed in percent of total heat transfer.

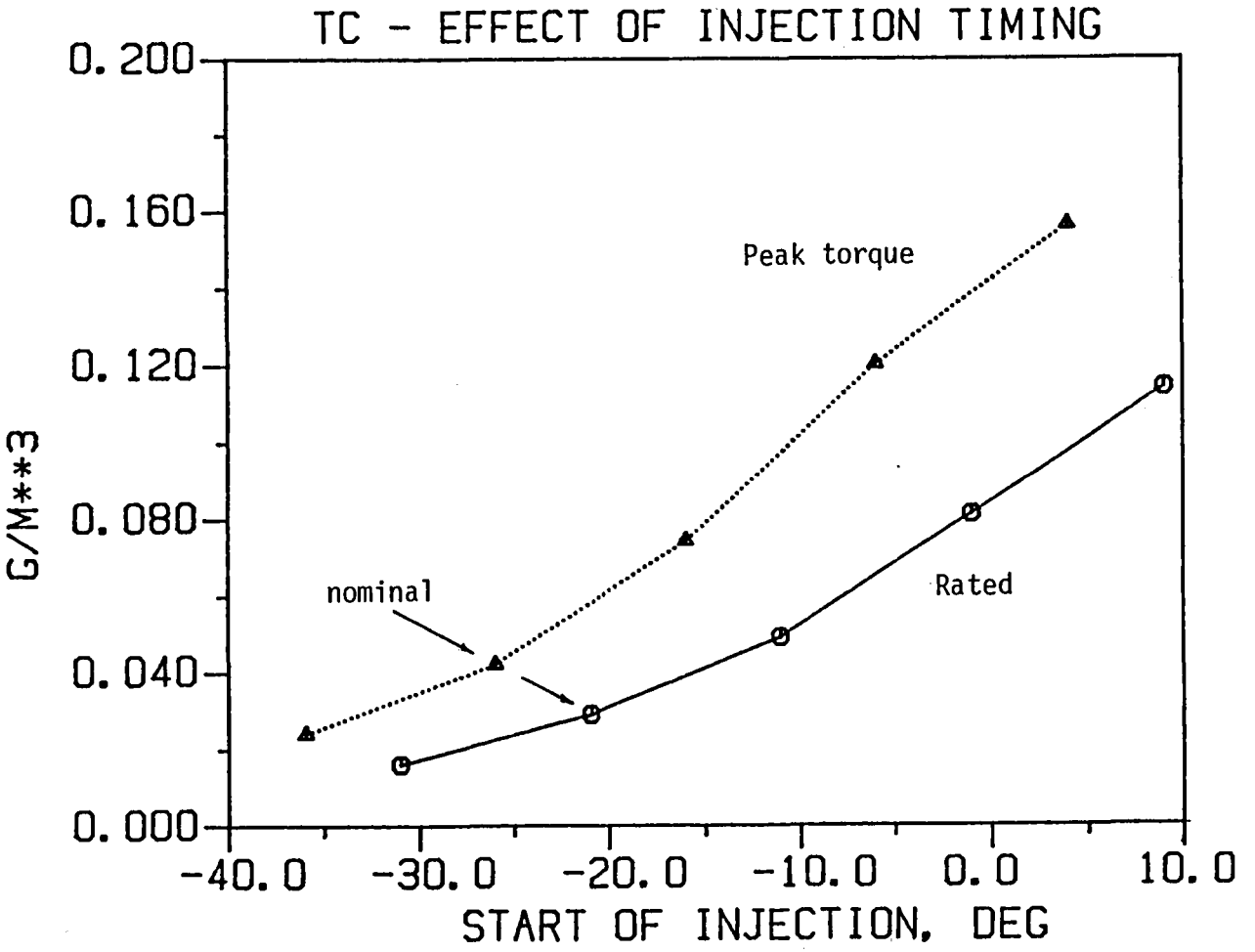

Figure 1-18 Effect of injection timing on soot concentration at end of combustion.

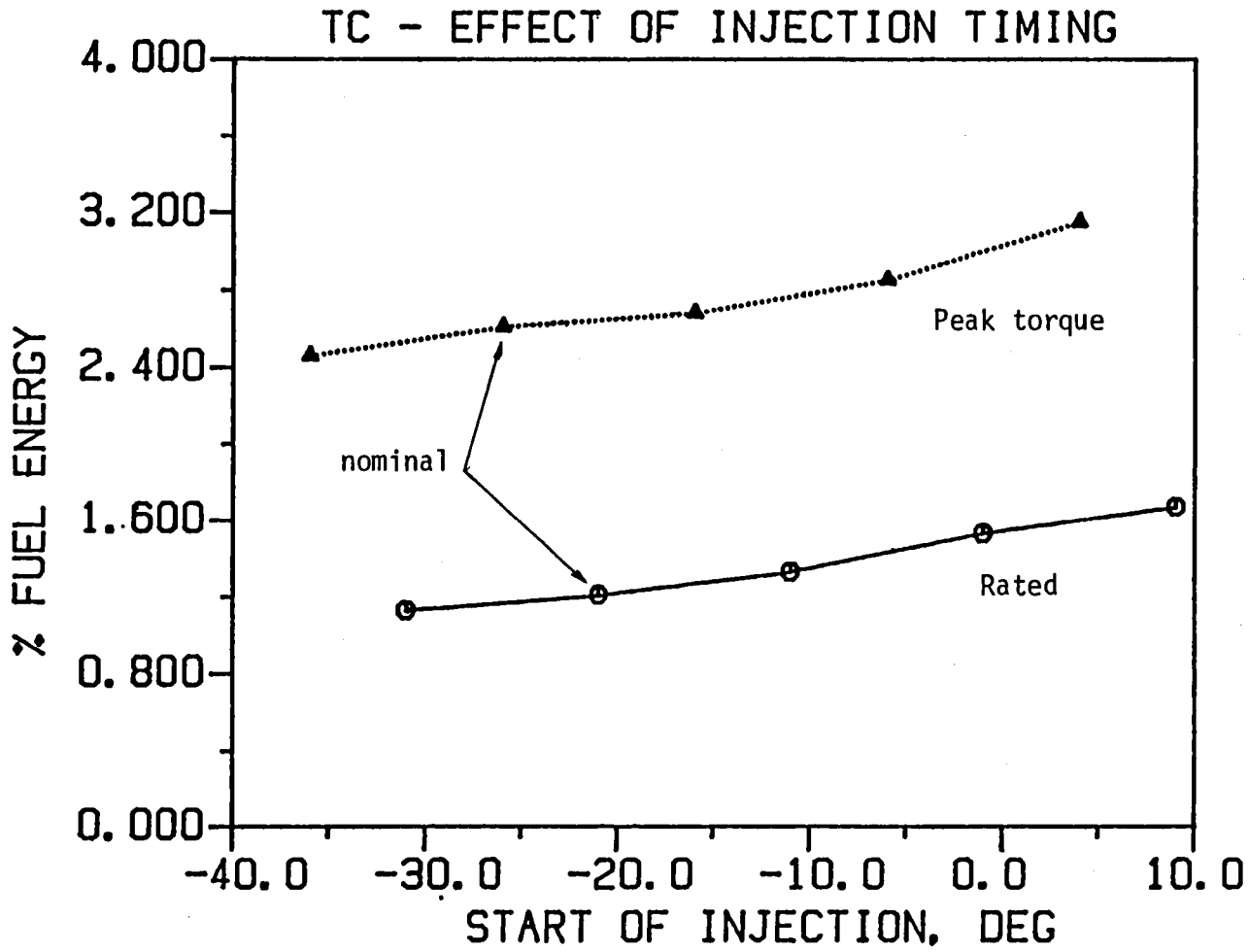

Figure 1-19 Effect of injection timing on radiation heat transfer expressed in percent of fuel energy.

had the same trends with timing, except that the slope of radiation heat transfer rate with timing was larger.

Intake Temperature

The next parameter investigated was the effect of intake temperature. A parametric study was made, in which the intake and exhaust pressures were kept constant and the IVC chamber temperature was varied from 310 to 510° K. The fueling rate was also varied to keep the overall equivalence ratio fixed at the rated value of 0.47. Over this range, the premixed burn fraction showed only a minor variation from 6% down to 2%, and it had almost no effect on the observed results. The increased temperature produced larger peak soot concentrations and lower exhaust soot levels, which agrees with the trends observed by Kadota and Henein (1981). The total radiation heat transfer was almost unaffected by the variation of the inlet temperature, despite the fact that the peak burned zone temperature increased by almost 180°K over this range of inlet temperatures. The likely reason for this may be the changing ignition delay, which decreased from 10°CA to 5.2°CA. As was seen in Figure 1-19, ignition advance produces a decrease in heat radiation, and this decrease may have offset any increase that would have been generated by the higher burned zone temperature. By contrast, the increasing intake temperatures increased the convective heat transfer substantially from 5.9% for the 310°K case (this IVC temperature is equivalent to about 250°K intake temperature) which was highly fueled to maintain constant ϕ, to 15.2% for the 510°K case which was fueled at a correspondingly lower rate.

Intake Pressure

Another important variable is intake pressure. It's effect was studied by varying the pressure at IVC while keeping ϕ constant through adjustments of the fueling rate, and keeping IVC temperature constant as well. As the intake pressure is changed, a number of key variables vary as well. These include ignition delay, premixed burn fraction, burned zone

temperature and partial pressure of oxygen. The last two of these parameters had a strong effect on the soot burnup and their effect is quite clearly seen in Figure 1-20, showing a decrease in end of combustion soot levels with increasing pressure. The premixed burn fraction decreased with increasing boost from 19.4% at p=0.95 bar down to 0.2% at p=3.0 bar, increasing the rate of soot formation and thus partially offsetting the effects of increased burnup. Nevertheless, the radiation heat transfer expressed in percent of fuel energy decreased by about 0.8 percentage points (Figure 1-21). The convective heat transfer decreased over the same range by about 2.6 percentage points of fuel energy. Calculating the time-average heat radiation rate from a formula correlating the data of Flynn et al (1972, et.al) one finds that increasing the intake pressure from 1 bar to 2 bar decreases the radiation heat transfer (in terms of fuel energy) by 19% and increasing it to 3 bar decreases it by a total of 35%. This compares quite well with the reductions seen in Figure 1-21, of 23 and 41 percent, respectively.

Naturally Aspirated Engine

To explore the predictions of heat radiation for naturally aspirated engines, a simulation was carried out for an engine based on the Cummins NH. The only difference was in the compression ratio which was increased from 14.5 to 15.5 by reducing the TDC clearance. The engine was simulated at 2100 RPM as the rated point, it was fueled at a rate producing ϕ = 0.52 and injection timing was set at - 18° to control the peak rate of pressure rise. The rate of combustion calculated from a combustion correlation is shown in Figure 1-22, and it shows a pronounced ignition delay of 14.1°CA producing a sizable premixed burn peak. The predicted soot concentration levels (Figure 1-23) were somewhat higher at the peak than those calculated for the turbocharged engine (Figure 1-7), and much higher than the TC engine at the end of combustion.

The calculated radiation heat flux per unit area (Figure 1-24) was lower in magnitude in the cup area than for the TC engine, but about the same

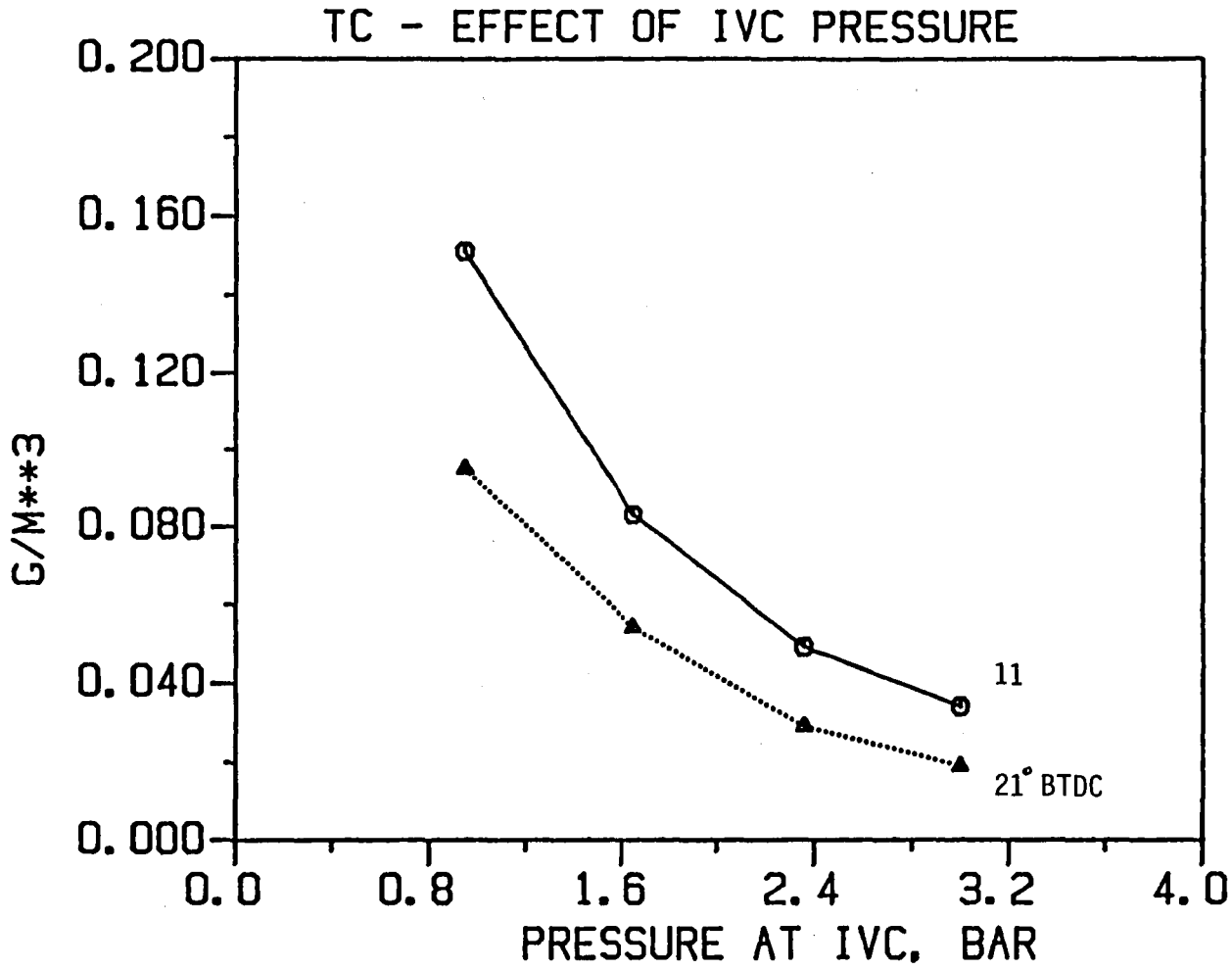

Figure 1-20 Effect of IVC pressure on soot concentration at the end of combustion.

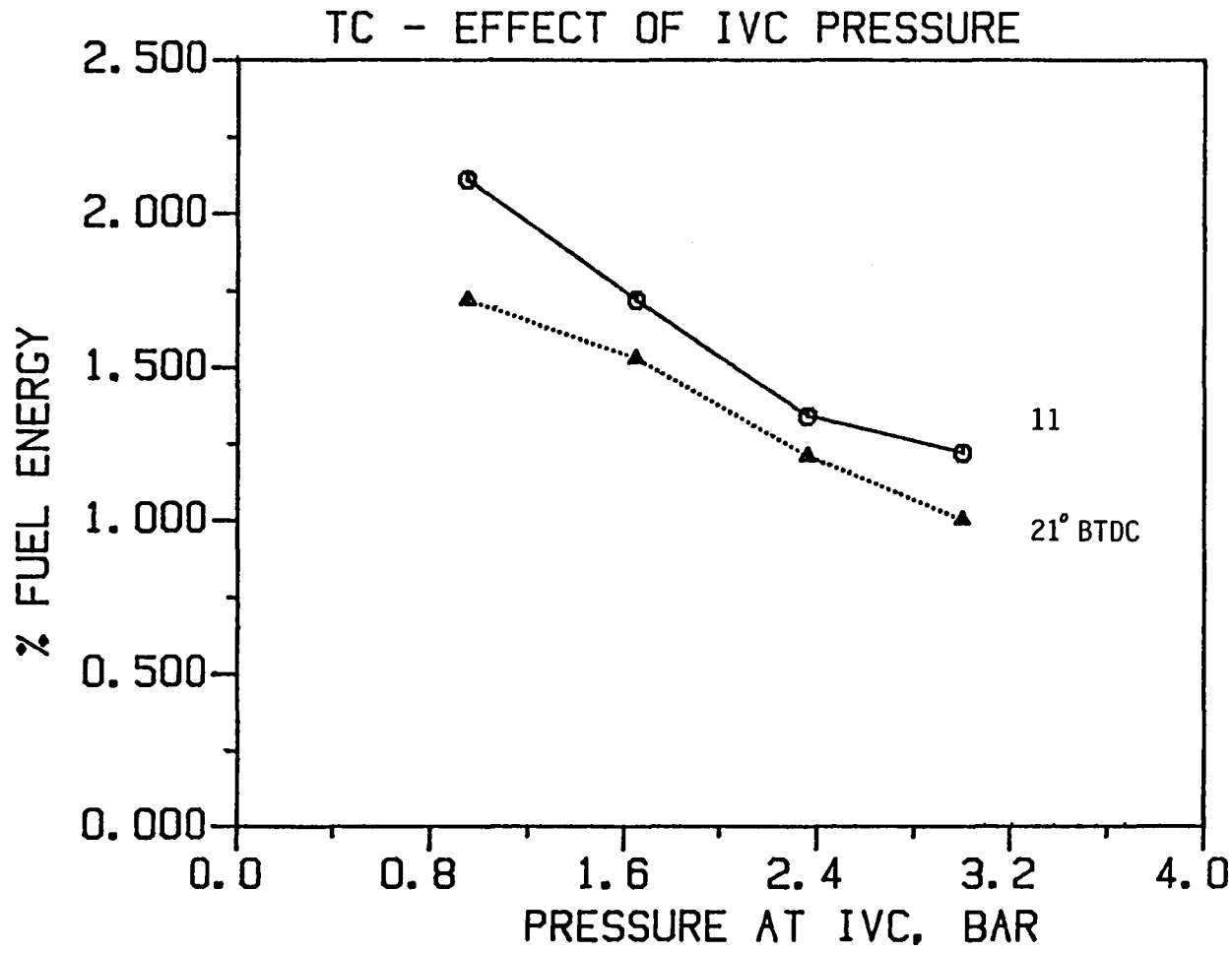

Figure 1-21 Effect of IVC pressure on radiation heat transfer expressed in percent of fuel energy.

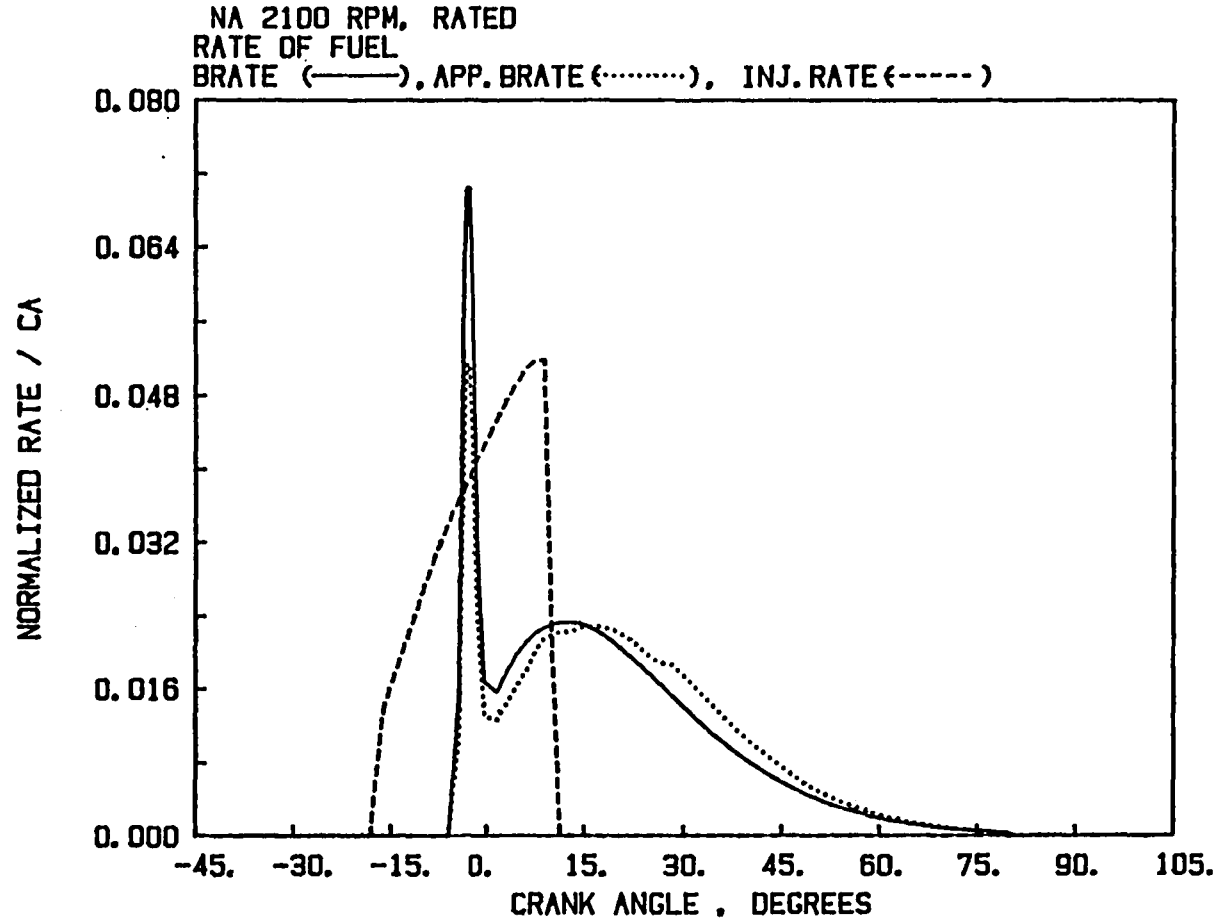

Figure 1-22 Rate of fuel burned -- naturally aspirated engine; —— actual rate of fuel burned, ... apparent burn rate deduced for a single zone model, --- fuel injection rate.

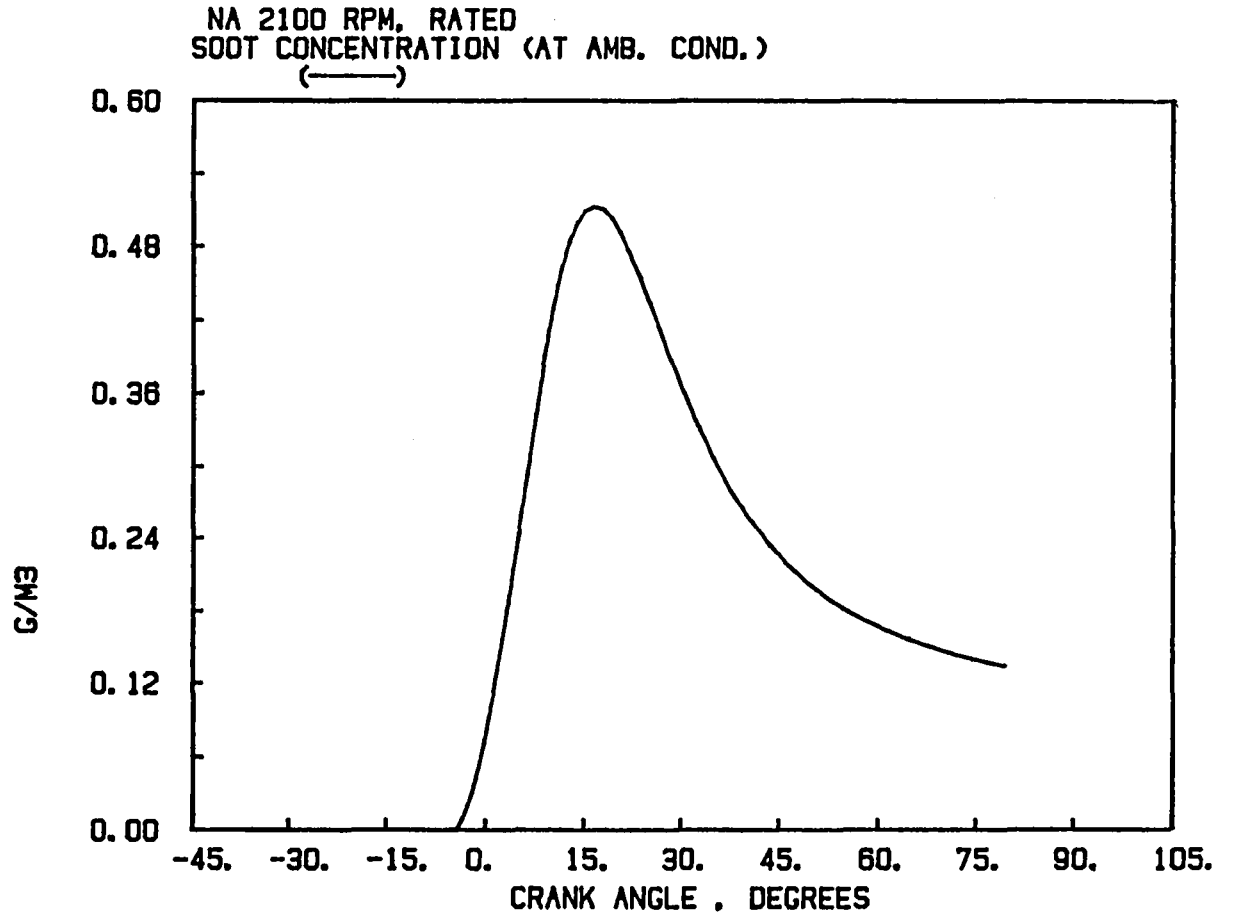

Figure 1-23 Soot concentration in the burned zone per total cylinder mass volume, naturally aspirated engine.

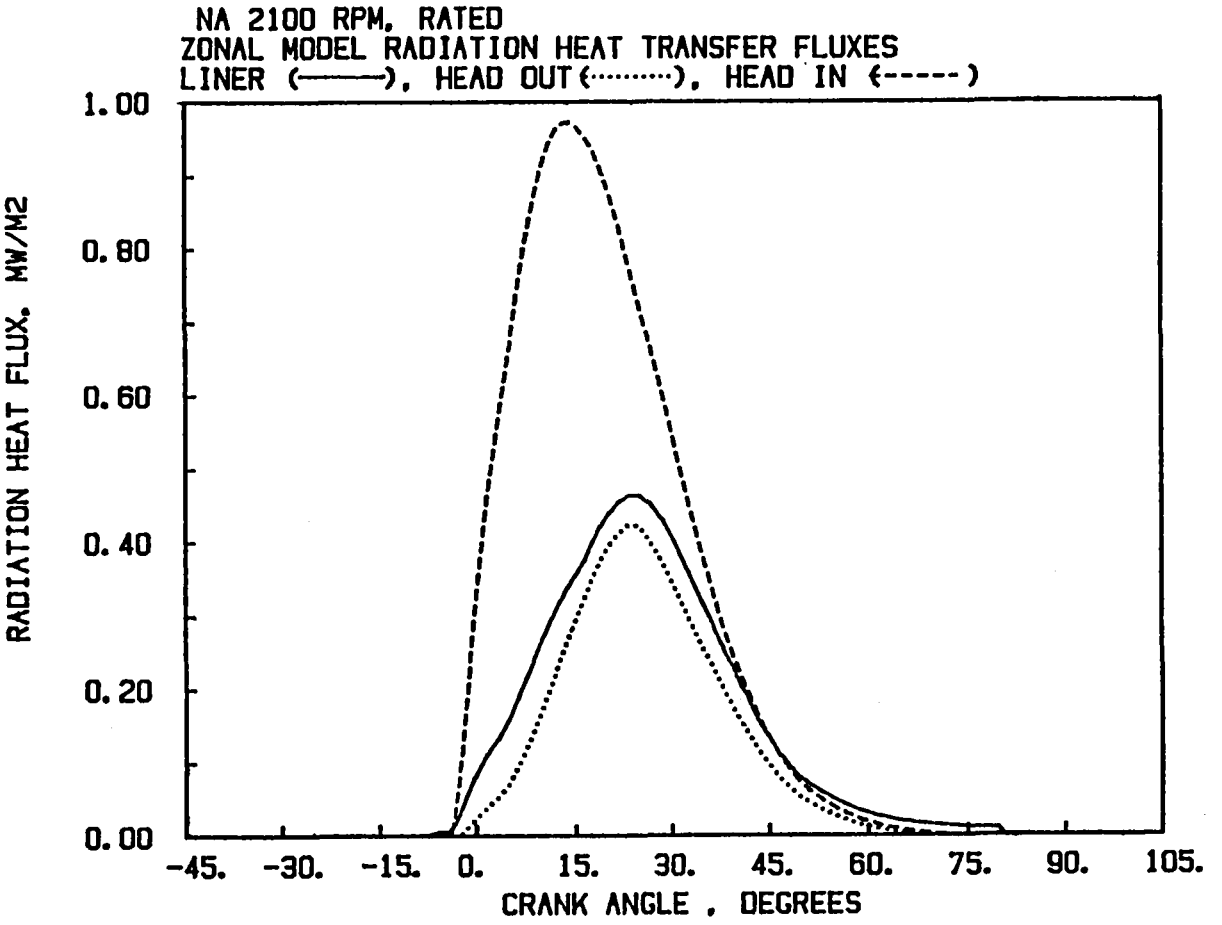

Figure 1-24 Heat radiation per unit area in a naturally aspirated engine; —— liner, ····· head above piston crown, --- head above cup.

in the squish zone. The area-integrated radiation heat transfer rates (Figure 1-25) were lower for the piston and the head, but larger on the liner due to the combustion and radiation shift (produced by the long ignition delay) towards higher crank angles where the piston is in a lower position. Integrated over all surfaces, the radiation heat transfer accounted for about 18 percent of the total heat transfer (Figure 1-26).

A timing sweep was carried out to investigate the sensitivity to this parameter for naturally aspirated engines. This sweep showed a rapid rise in calculated soot levels of the end of combustion (Figure 1-27a). To this rise corresponded a rise in the radiation heat transfer, reaching a peak of over two percent of the fuel energy (Figure 1-27b), near injection timing of -7°, beyond which radiation began to decrease due to lower radiation temperatures. The radiation share of the total heat transfer rose with retarded timing to over 20 percent (Figure 1-27c). The premixed fraction varied considerably with timing, having a value of 43% at -28°, 28% at -23°, 18% at -18° and a minimum of 10% at -8°. Since no soot is formed in the model from the fuel burned in the premixed mode, this variation contributed significantly to the observed sharp initial rise in radiation heat transfer seen in Figure 1-27b.

EFFECT OF INSULATION ON HEAT RADIATION

A significant question involved in the design and optimization of insulated (low heat rejection) diesels concerns the importance of heat radiation under insulated conditions. The main effect of wall insulation is to raise wall temperatures and thus reduce the temperature difference between the gas and the walls, which drives the heat transfer. Since effective gas temperatures for convective heat transfer (cycle-averaged and weighted by the heat transfer coefficient) are on the order of 800-1200°K depending on speed and load, it is necessary to raise the wall temperatures to those levels in order to completely eliminate convective heat transfer. Since heat radiation is driven by the soot temperatures, which are on the order of 2000-2500°K, and its

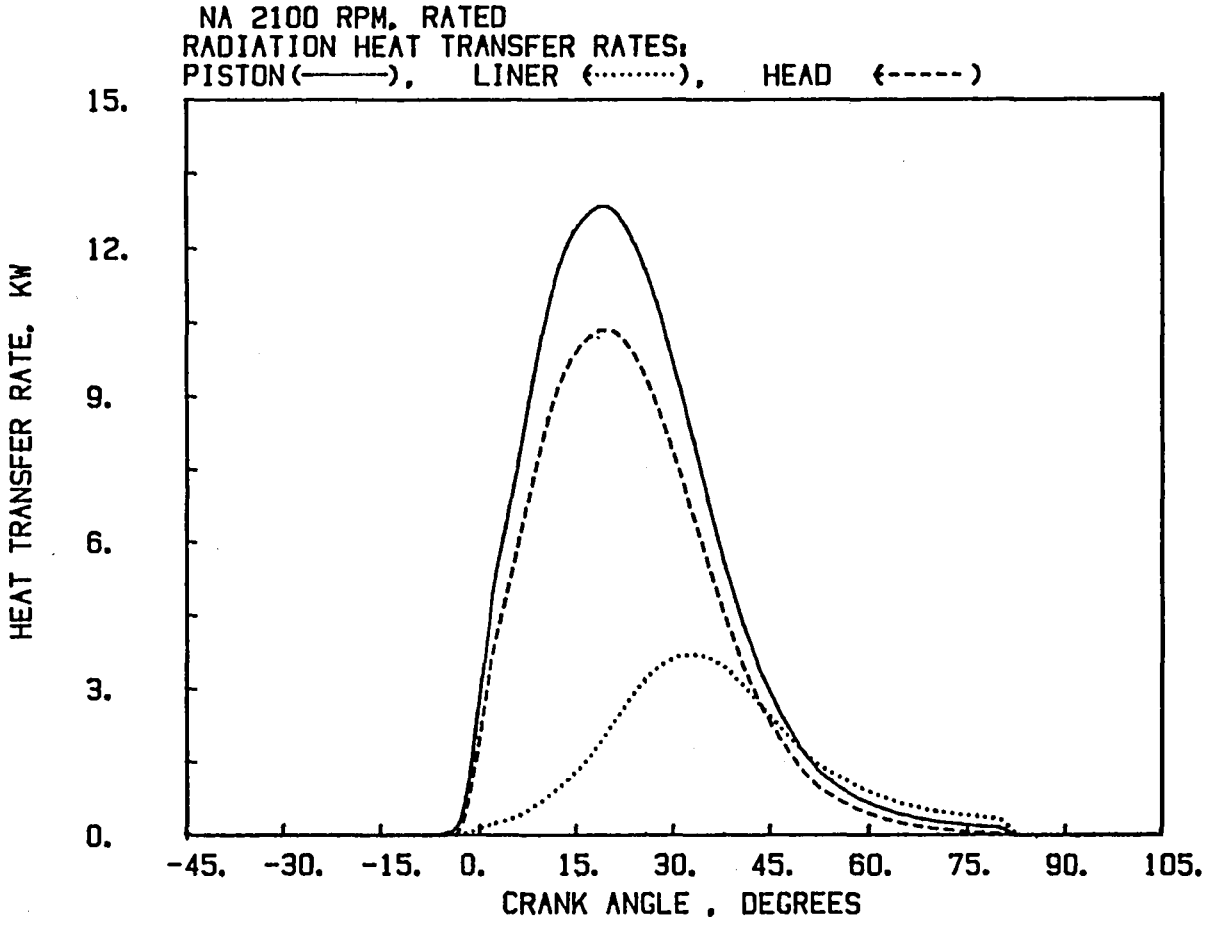

Figure 1-25 Breakdown of radiation heat transfer in a naturally aspirated engine; ——— piston, ... liner, --- head.

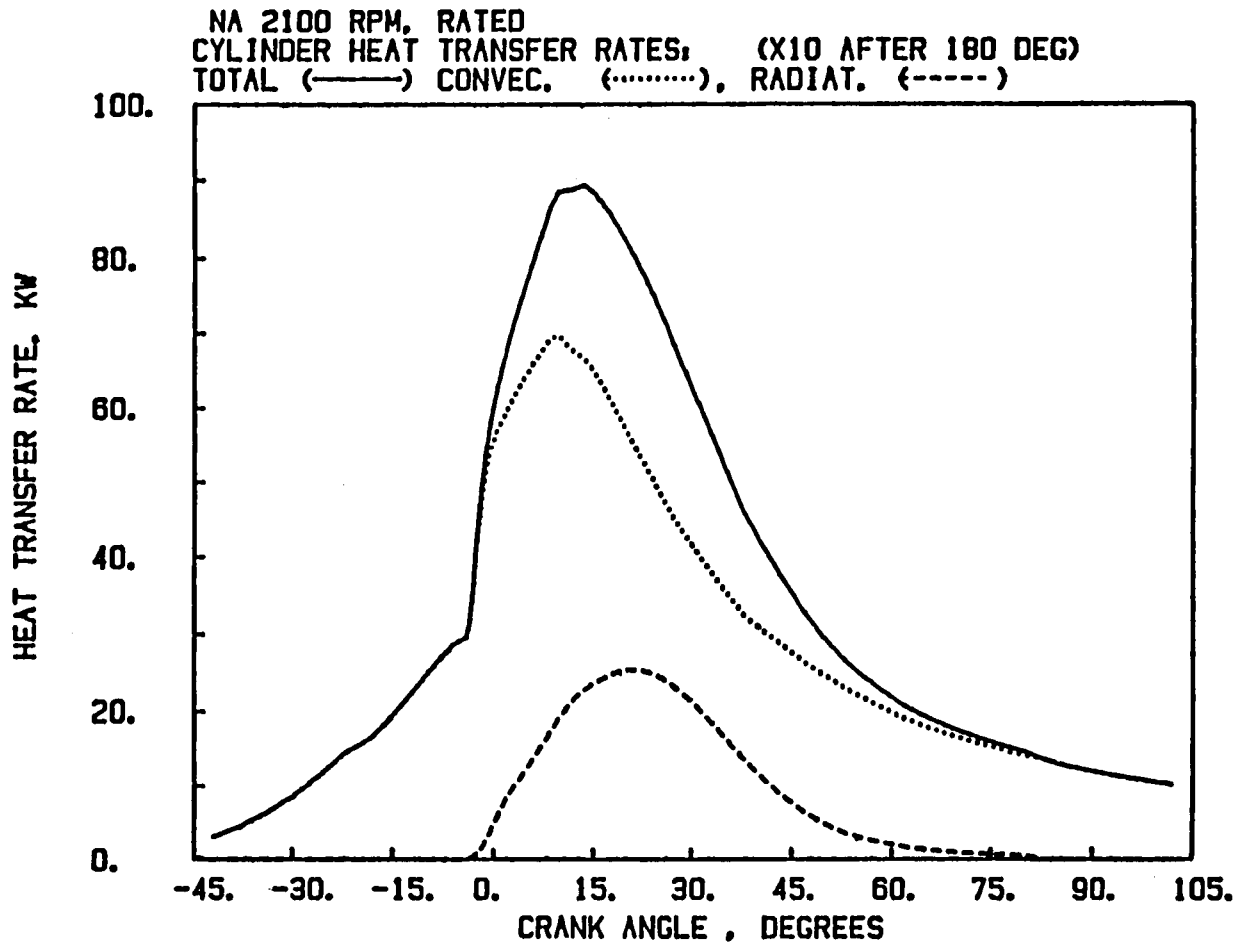

Figure 1-26 Total-cylinder heat transfer of a naturally aspirated engine; ····· convection, --- radiation, ——— total.

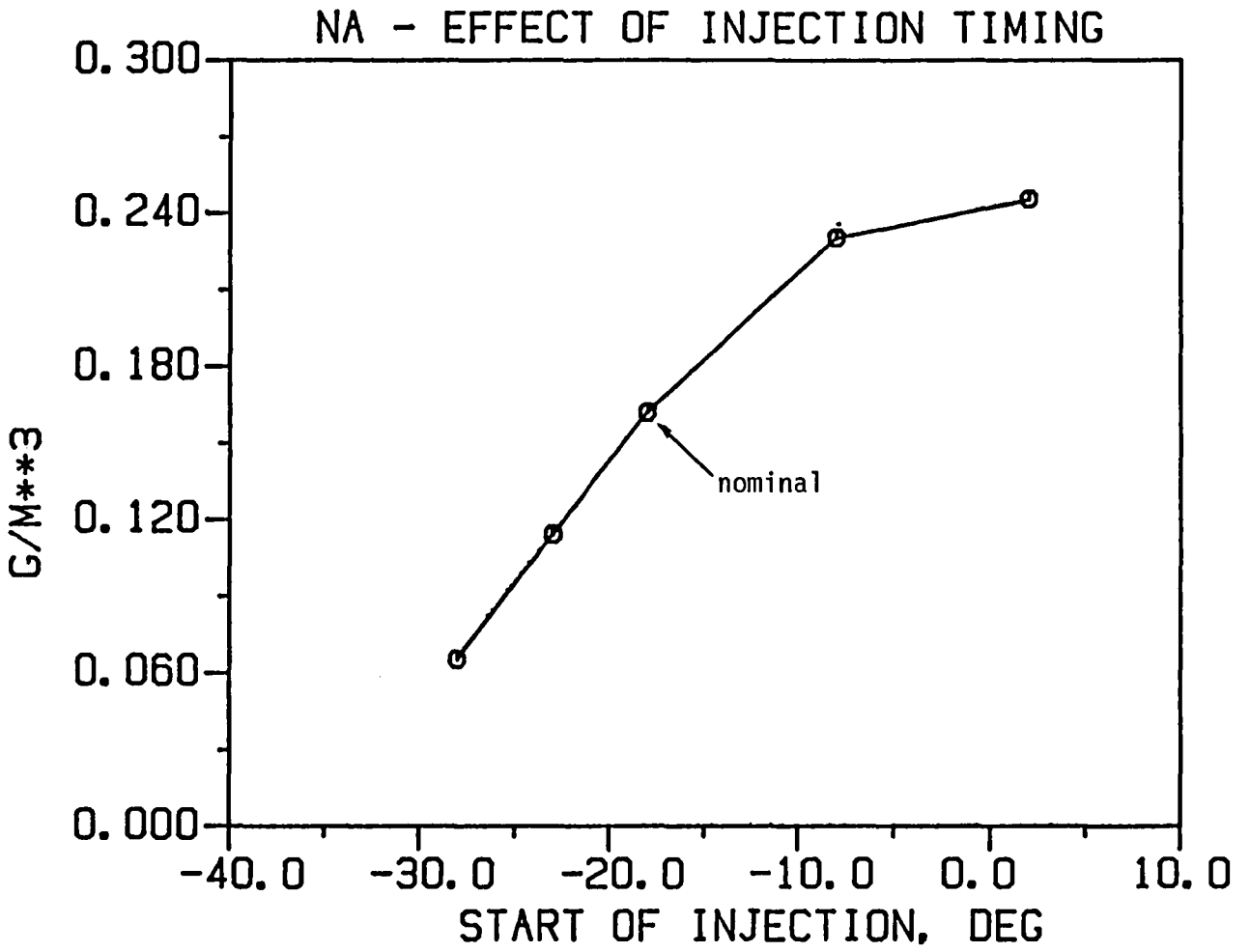

Figure 1-27a Effect of injection timing on soot concentration at end of combustion, naturally aspirated engine.

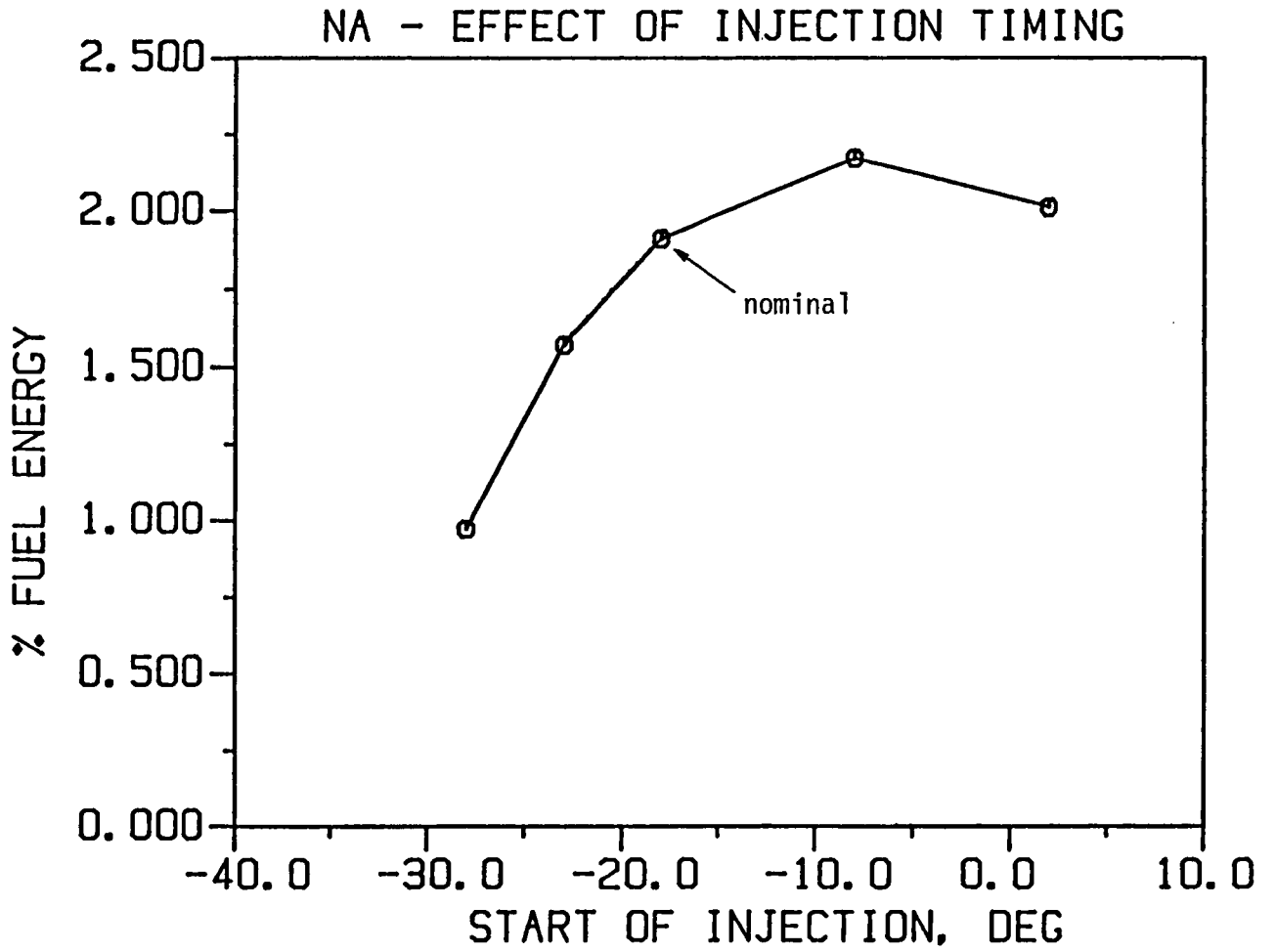

Figure 1-27b Effect of injection timing on radiation heat transfer expressed in percent of fuel energy, naturally aspirated engine.

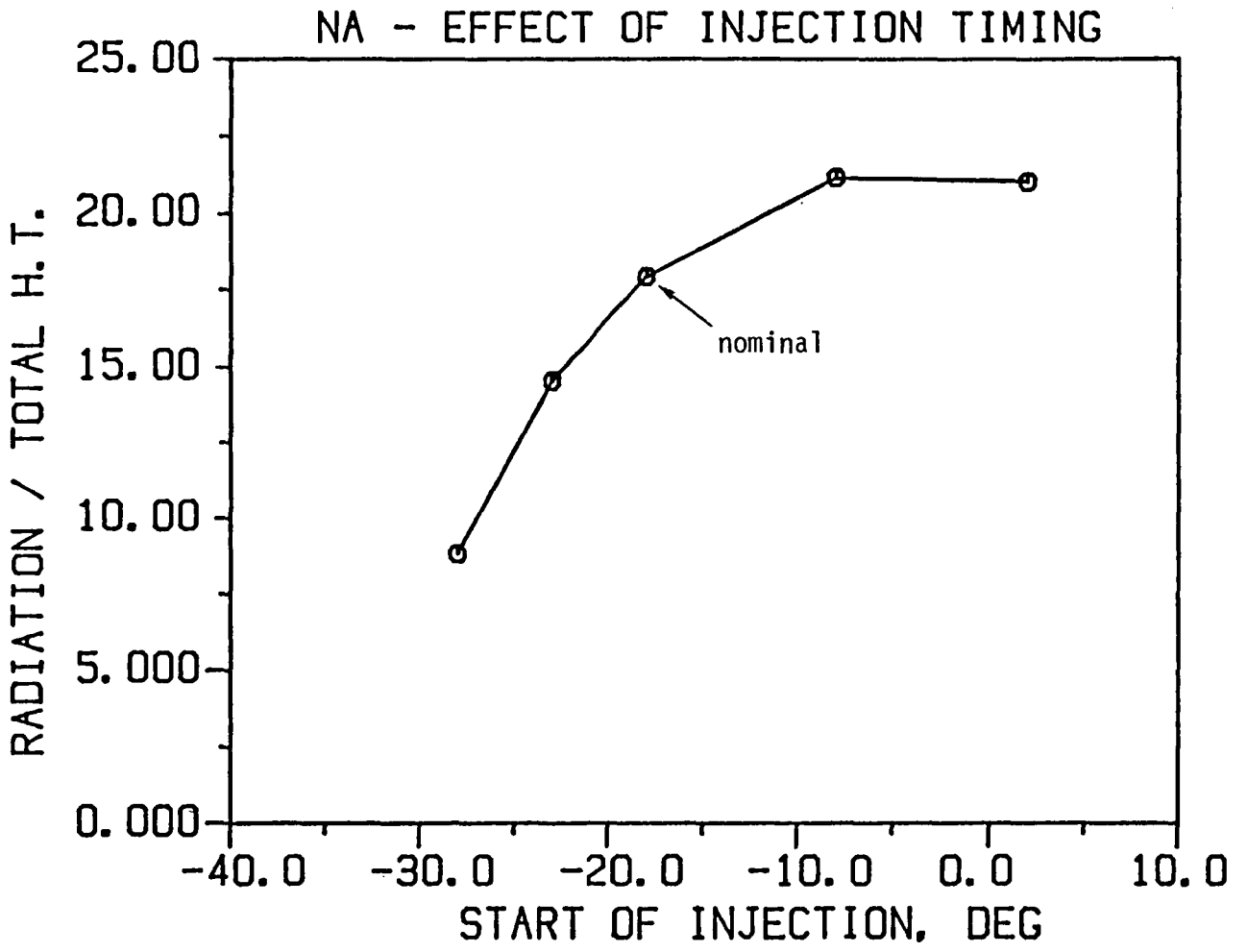

Figure 1-27c Effect of injection timing on radiation heat transfer as percentage of total heat transfer, naturally aspirated engine.

dependence on temperature is high order (fourth power), raising wall temperatures even to 1200°K which will reduce heat radiation by a much smaller amount than it does the convective heat transfer. As a result, the radiation heat transfer may be expected to become a much more significant gas-phase heat transfer mechanism under highly insulated conditions, and thus needs to be analyzed and assessed in a detailed form.

When extrapolating the radiation heat transfer levels from conventionally cooled to insulated engines, one needs to account for two effects produced by the insulation:

(1) higher gas temperatures due to lower gas-to-wall heat transfer which affect:
   - soot production and burnup
   - soot absorption coefficient
   - soot radiation temperature and emissive power; and

(2) higher wall temperatures that begin to influence the overall radiation level and wall-to-wall radiative heat transfer.

All of these effects, some of which increase and some decrease radiation heat transfer, are included in the present model, which thus can be used to make predictions of the final balance, i.e., the net effect.

The engine insulation chosen for this part of the study, and used in most of the surfaces, was an advanced zirconia plasma-sprayed coating whose conductivity was 0.6 W/mK and heat capacity ρc = 1.1 MJ/m^{3}K. The coating thickness was 1.5 mm on piston, head and upper part of the liner, and 1 mm on valve heads. The liner below the top ring reversal point was made of 5 mm thick partially stabilized zirconia with conductivity of 2.0 W/mK and heat capacity of 2.5 MJ/m^{3}K. The ports were lined with alumina titanate. The same engine was used as in the cooled engine calculations, but the turbocharger turbine was resized from the cooled engine baseline to take the full advantage of the high exhaust temperatures (at rated conditions). The fueling rate was slightly reduced to maintain the same overall equivalence ratio and peak pressure

as in the baseline cooled engine. Two engine conditions were analyzed -- rated speed and load, and the 1000 RPM/peak-load condition at which the highest heat radiation was found in the cooled baseline.

Rated speed and load. The insulation package used raised the head and piston temperatures to about 950 K and reduced the total in-cylinder heat transfer from 10.5 percent of fuel energy to 4.6 percent. The reduced heat transfer raised the maximum mass-averaged chamber temperature by 120 K and maximum burned zone temperature by 50 K. The higher temperature increased the rates of soot formation and burnup (compare Figure 1-28a to Figure 1-6). The resultant maximum soot concentration levels were slightly higher, with the peak shifted to lower crank angles, and the end-of-combustion level was 25 percent lower. The curves of radiation fluxes had very similar shapes with respect to crank angle as in the cooled case, being several percent higher at the peak. They tended to exceed the cooled engine values during the early part of combustion and were somewhat lower during the latter part, in agreement with the soot concentration trends. The distribution of heat transfer rates between piston, head and liner was also quite the same as in the cooled case, except for the increased heat radiation to liner at higher crank angles (Figure 1-28b; compare it to Figure 1-10). This radiation is due to hot combustion surface chamber walls radiating to the cool lower portion of the liner. In terms of fuel energy, the radiation remained at the same level as in the cooled case: 1.2 percent of the fuel energy. However, the radiation contribution to the total heat transfer increased from 10.5 to 26.1 percent (Figure 1-28c).

1000 RPM, Maximum Load. At the lower engine speed, the engine operates at a substantially higher equivalence ratio, $\phi = 0.77$ versus $\phi = 0.47$ for the rated conditions. The results were quite similar to those obtained at the rated conditions. At this condition, insulating the combustion chamber raised the wall temperatures on piston and head to about 1150 K, and reduced the total in-cylinder heat transfer from 18.8 to 10.1 percent of fuel energy. The maximum mass-averaged chamber

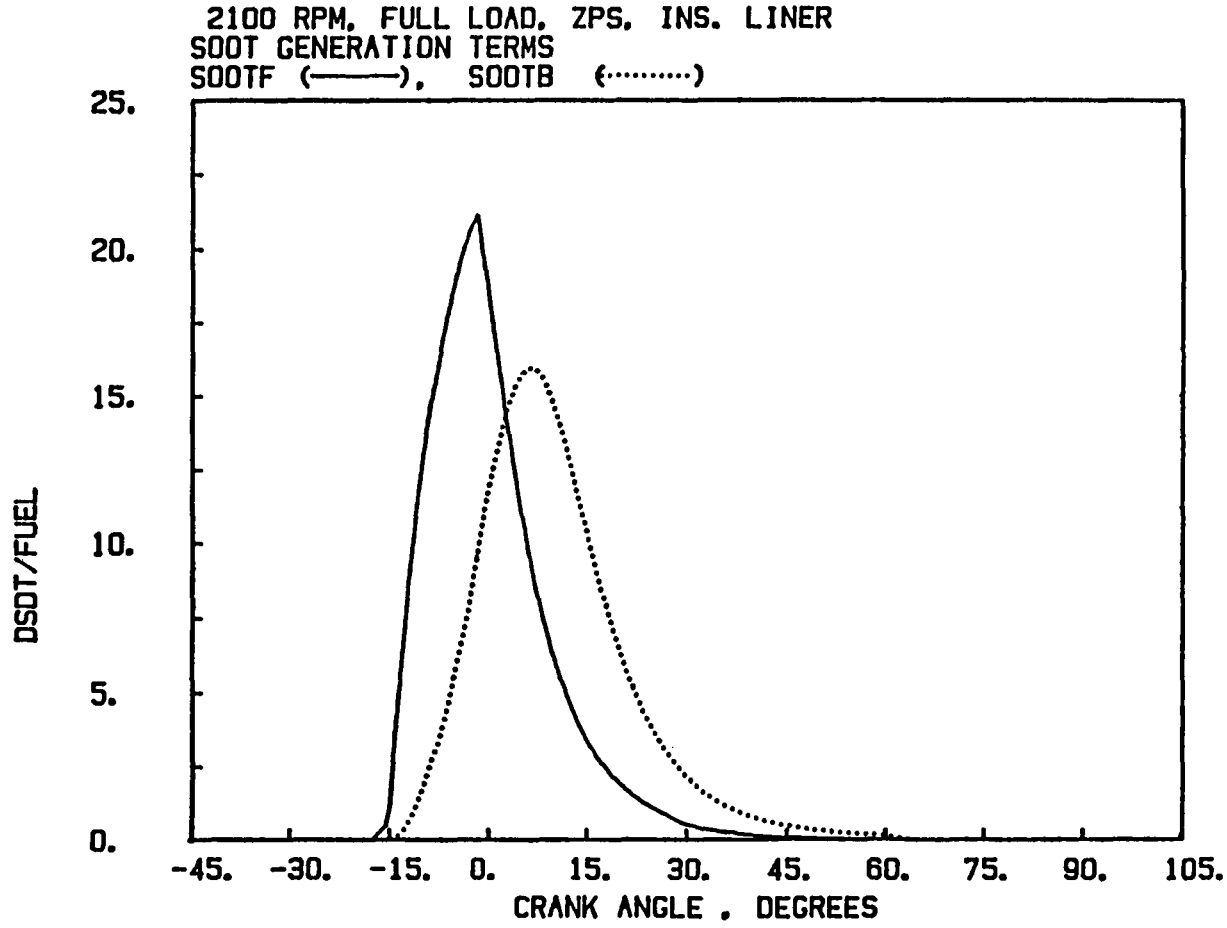

Figure 1-28a Effect of insulation of turbocharged engine: soot generation (——) and burn up (.....) rates.

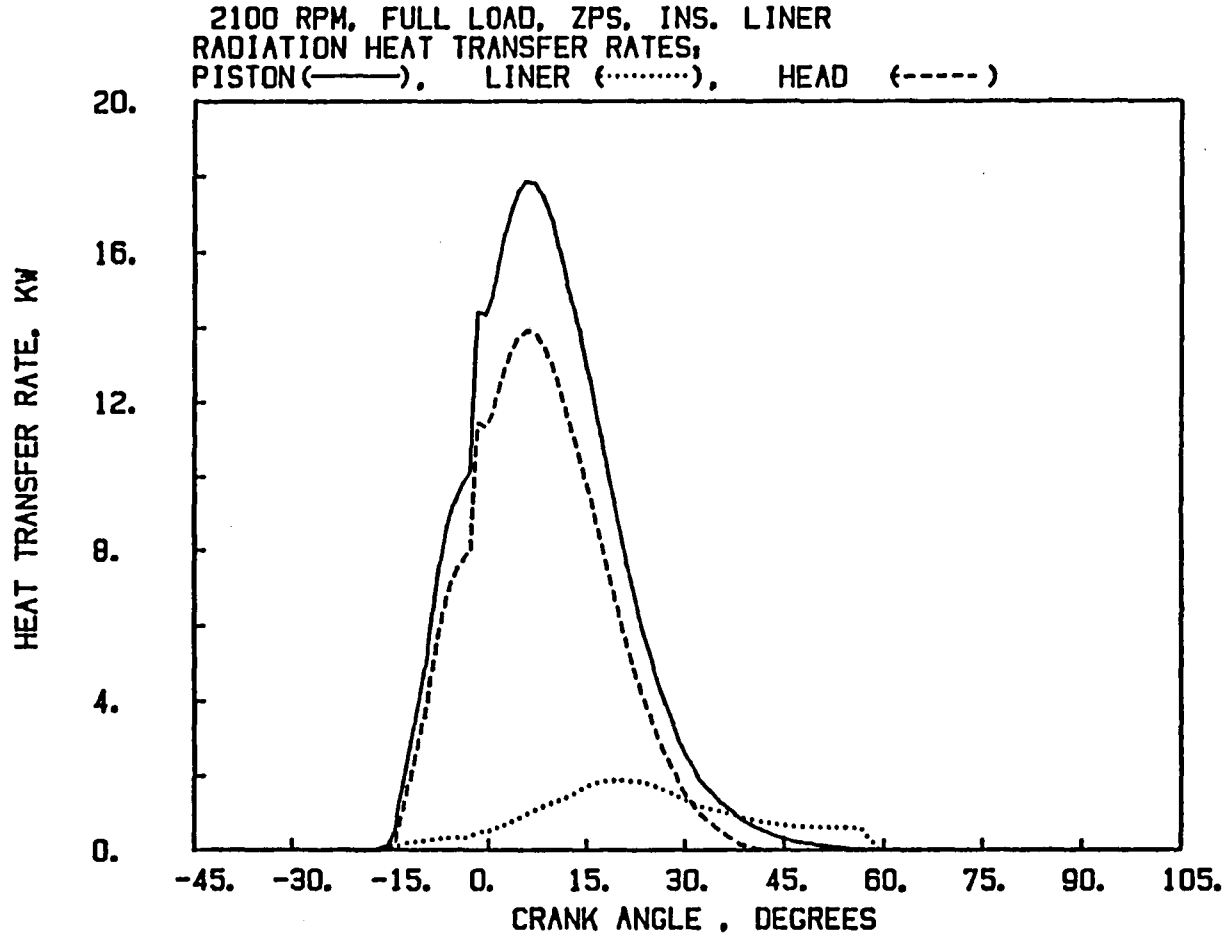

Figure 1-28b Effect of insulation of turbocharged engine: breakdown of radiation into —— piston, ... liner, --- head.

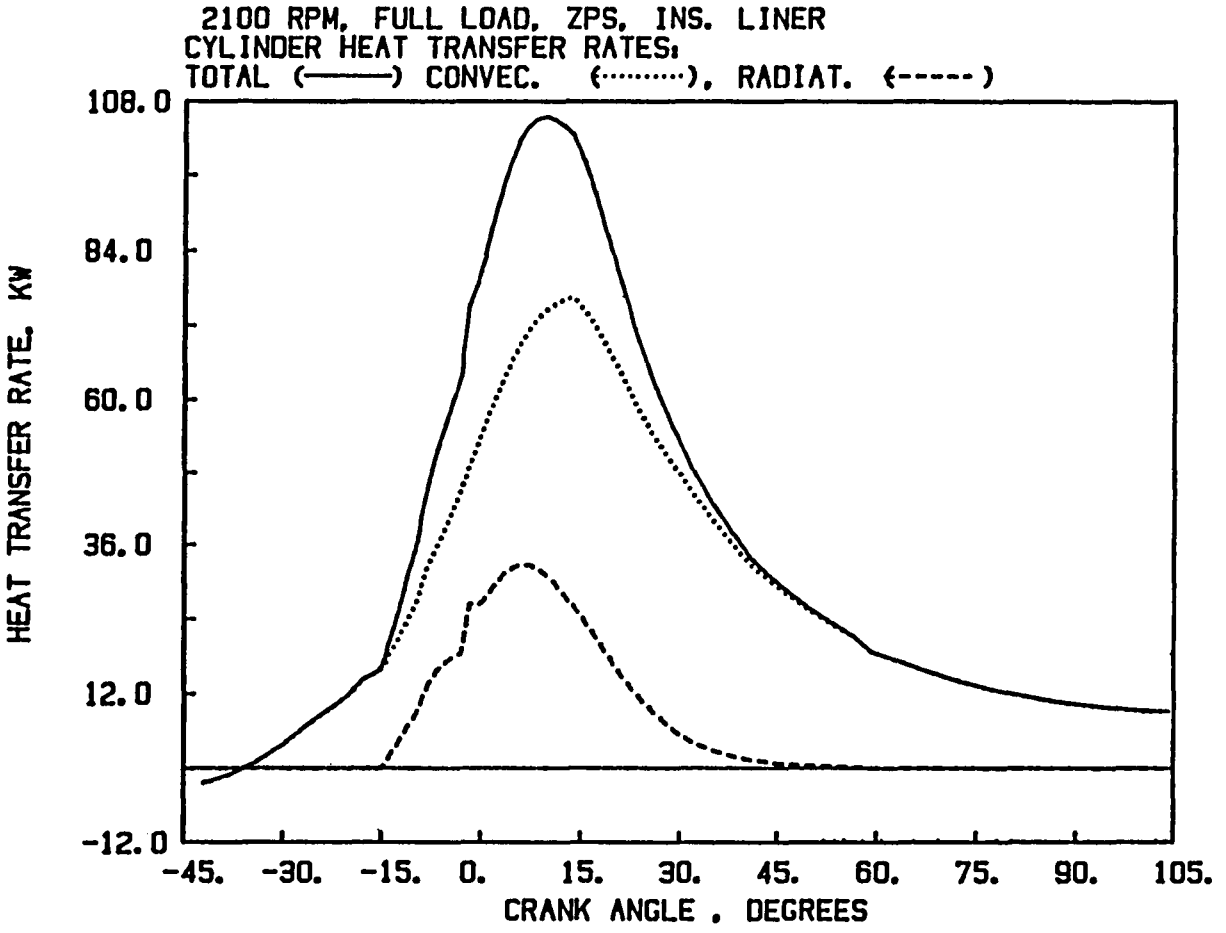

Figure 1-28c Effect of insulation of turbocharged engine: —— total heat transfer, ····· convection, --- radiation.

temperature rose by 220 K and maximum burned zone temperature rose by 120 K. The peak soot concentration level again increased slightly, compared to the cooled case, and the final value decreased by 30 percent. The radiation fluxes per unit area increased by about 15 percent. Expressed in terms of fuel energy, the radiation heat transfer increased from 3.8 to 4.3 percent. At the same time, the radiation fraction of the total heat transfer increased from 20.5 to 43.0 percent.

Summary. The wall insulation increased the wall temperatures to 950 and 1150 K, respectively, producing burned zone temperatures increases of 50 and 120 K, respectively. The increased gas temperature raised the levels of soot production and burnup, which led to an increase in peak soot concentration values and reductions in end-of-combustion levels. This higher soot radiation temperature also increased the radiation fluxes, while the higher wall temperatures gave rise to a measurable wall-to-wall radiation, especially to the cool lower portion of the liner. The contribution of radiation to the total in-cylinder heat transfer increased by factor of more than two, to 43 percent in the lower speed case. These results confirm the increased importance of heat radiation in insulated engines.

CONCLUSIONS

1. A comprehensive model has been developed that represents the key phenomena and processes which affect radiation heat transfer in diesel engines, including:
    a) two-zone combustion representation with realistic burned gas temperatures,
    b) absorption and emission of heat by soot, and
    c) geometrical representation of burned zone and combustion chamber geometry and pertinent view factors.

2. The absorption and emission by soot is treated by a model which relies on experimental data linking soot absorption coefficient to

soot concentration, and which also calculates the soot level through a kinetic model of soot formation and burnup.

3. The geometrical problem is approached by a zonal model which calculates spatial distribution of radiation heat flux including soot radiation to walls, wall-to-wall radiation, absorption of radiation in soot, and multiple reflections of incident radiation from one surface to the others.

4. The calculated radiation fluxes per unit area agree with magnitudes observed in previous experimental studies.

5. Predictions of heat radiation for a turbocharged heavy duty diesel indicate that heat radiation, cycle averaged, varies from 0.7 to 3.8 percent of fuel energy, depending on speed and load. Expressed in terms of the total heat transfer, radiation heat transfer represents from 4.2 to 20.5 of the total.

6. When the engine is insulated for low heat rejection, the higher gas temperatures affect both the soot mechanisms and radiation fluxes. The contribution of radiation to the total heat transfer increases very significantly, mainly due to a decrease in the convection heat transfer, and to a lesser degree due to an increase in radiation.

REFERENCES

Annand, W.J.D. (1963), "Heat Transfer in the Cylinders of Reciprocating Internal Combustion Engines", Proc. IMech E, 1963, vol. 177, p 973.

Bryzik, W. and Smith, C. O. (1977), "Relationships Between Exhaust Smoke Emissions and Operating Variables in Diesel Engines", SAE Pages 770718.

Chang, S.L. and Rhee, K.T. (1983), "Computation of Radiation Heat Transfer in Diesel Combustion," SAE Paper 831332.

Chapman, M., Friedman, M.C., and Aghan A. (1983), "A Time-Dependent Spatial Model for Radiant Heat Transfer in Diesel Engines," SAE Paper 831725.

Dent, J.C. and Suliaman, S.J. (1977), "Convective and Radiation Heat Transfer in a High Swirl DI Diesel Engine", SAE Paper 770407.

Ebersole, G.D., Myers, P.S. and Uyehara, O.A. (1963) "The Radiant and Convective Components of Diesel Engine Heat Transfer", SAE Paper 701 C, 1963.

Flynn, P., Mizukawa, M., Uyehara, O.A. and Myers, P.S (1972), "An Experimental Determination of the Instantaneous Potential Radiant Heat Transfer Within an Operating Diesel Engine", SAE Paper 720022.

Gray, W. A. and Mueller, R. (1974), Engineering Calculations in Heat Transfer, Pergamon Press.

Hiroyasu, H. and Kadota, T. (1976), "Models for Combustion and Formation of Nitric Oxide and Soot in DI Diesel Engines", SAE Paper 760129.

Hottel, H. C. (1954), "Radiant-Heat Transmission," in Heat Transmission, Ed. W.M. McAdams, McGraw-Hill, Chapter 4, 1954.

Kadota T. and Henein, N.A. (1981), "Time Resolved Soot Particulates In Diesel Spray Combustion" in Particulate Carbon - Formation During Combustion, Plenum Press, 1981, pp 391-422.

Kamimoto, T., Matsuoka, S., Matsui, T. and Aoyagi, T. (1975), "The Measurement of Flame Temperature and the Thermodynamic Analysis of Combustion Processes in a Direct Injection Diesel Engine", IMechE, C96/75.

Khan, I.M., Greeves, G., and Wang, C.H.T., (1973), "Factors Affecting Smoke and Gaseous Emissions From Direct Injection Engines and a Method of Calculation", SAE Paper 730169.

Kunitomo, T., Matsuoka, K. and Oguri, T. (1975), "Prediction of Radiative Heat Flux in a Diesel Engine", SAE Paper 750786.

Lee, K.B., Thring, M.W. and Beer, J.M. (1962), "On the Rate of Combustion of Soot in a Laminar Flame", Combustion and Flame, vol. 6, p. 137.

Matsuoka, S. (1981), Discussion presented at a Symposium on Particulate Carbon - Formation During Combustion, Plenum Press, 1981, pp. 418-421.

Menguc, M.P. and Viskanta, R. (1984), "Radiative Transfer in Axisymmetric, Finite Cylindrical Enclosures," Submitted for ASME Annual Meeting, New Orleans, Louisiana.

T. Morel and R. Keribar, "A Model for Predicting Spatially and Time Resolved Convective Heat Transfer in Bowl-in-Piston Combustion Chambers," SAE Paper 850204, SAE Congress, Detroit, 1985.

T. Morel, E. F. Fort, and P. N. Blumberg, "Effect of Insulation Strategy and Design Paremeters on Diesel Engine Heat Rejection and Performance," SAE Paper 850506, SAE Congress, Detroit, 1985.

Oguri, T. and Inaba, S. (1972), "Radiant Heat Transfer in Diesel Engines," SAE Paper 720023.

Siegel, R. and Howell, J. R. (1981), Thermal Radiation Heat Transfer, 2nd Edition, McGraw-Hill Book Company, New York.

Siegla, D.C. and Smith, G.W. (1981), Editors, Particulate Carbon-Formation During Combustion, Plenum Press, 1981.

Sitkei, G. and Ramanaiah, G.V. (1972), "A Rational Approach for Calculation of Heat Transfer in Diesel Engines", SAE Paper 720027.

Sitkei, G. (1974), "Flame Radiation in High Speed Diesel Engines", in Heat Transfer in Flames, Ed. N.H. Afgan and J.M. Beer, Hemisphere Publishing, 1974, Chapter 26.

Whitehouse, N.D. and Shahad, H.A.K. (1984), "Radiative Heat Transfer Calculations From Soot Clouds for a Quiescent Combustion Chamber Diesel Engine", ASME Symposium FED-20 on Flows in I.C. Engines, Ed. T. Uzkan, Dec 1984, p. 89.

Yuen, W.W. and Tien, C.L. (1977), "A Simple Calculation Scheme for the Luminous-Flame Emissivity," Sixteenth Int. Symp. Combustion, The Combustion Institute, pp. 1481-1487.

APPENDIX - P_1 Approximation Method

The radiation heat fluxes within the combustion chamber may be calculated by one of multi-dimensional methods which employ the differential approximation to the equation of transfer for the whole combustion chamber. There is a whole series of such n-order methods, the simplest of them being the P_1 approximation (Siegel and Howell, 1981).

The multi-dimensional equation of transfer can be written as

$$\sum_{j=1}^{3} l_j \frac{\partial i(r,s)}{\partial x_j} = a[i_b(r) - i(r,s)] \qquad \text{(A-1)}$$

where the l_j's are the direction cosines, and r and s are position vector and unit vector in S direction, respectively.

The moments of i are generated by multiplying l_j and integrating over all solid angles ω. Some new notation is introduced to designate the moments:

$$i^{(0)}(r) = \int_{\omega=4\pi} i(r,s)\,d\omega$$
$$i_j^{(1)}(r) = \int_{\omega=4\pi} l_j\, i(r,s)\,d\omega$$
$$i_{kj}^{(2)}(r) = \int_{\omega=4\pi} l_k l_j\, i(r,s)\,d\omega$$

The zeroth-order moment $i^{(0)}$ represents the incident radiation G(r). The first moment $i_j^{(1)}$ is the radiative energy flux q(r) in the j-direction. The second moment $i_{kj}^{(2)}$ is the radiative pressure. The zeroth-order moment equation is the integral of Eqn. (A-1) itself over solid angles. Applying the definition of $i^{(o)}$ and $i^{(1)}$ one writes

$$\sum_{j=1}^{3} \frac{\partial i_j^{(1)}(r)}{\partial x_j} = a[4\pi i_b(r) - i^{(0)}(r)]$$

The first moment equation is obtained by multiplying Eqn. (A-1) by l_j and integrating over all solid angles.

$$\sum_{j=1}^{3} \frac{\partial i_{kj}^{(2)}(r)}{\partial x_j} = -a i_k^{(1)}(r) \qquad \text{(A-2)}$$

By continuing the process, an infinite set of moment equation can be generated.

The next step is to approximate the infinite set of moment equation by a finite set. When such a truncation is carried out, there will in general be n equations and n+1 unknowns. The additional equation needed to relate the moments and provide a determinate set is obtained by representing the unknown angular distribution of i as a series of spherical harmonics and then truncating this series after a finite number of terms. The series expression used to represent i is

$$i(r,s) = \sum_{l=0}^{\infty} \sum_{m=-l}^{+l} A_l^m(r) Y_l^m(\omega)$$

where $A_l^{m(r)}$ are coefficients to be determined, and the Y_l^m are the normalized spherical harmonics. For the P-1 approximation the series retain only the 0,1 terms. This gives an equation for i(r,s) that is satisfied into the first three moment equations to give

$$i^{(0)}(r) = 2\pi^{0.5} A_0^0(r) \qquad \text{(A-3)}$$

$$i_{kj}^{(2)}(r) = \frac{2}{3}\pi^{0.5} A_0^0(r) \delta_{kj} \qquad \text{(A-4)}$$

where δ_{kj} is the Kronecker delta. Eliminating $A_0^0(r)$ by combining Eqns. (A-3) and (A-4) gives

$$\delta_{kj} i^{(0)}(r) = 3i_{kj}^{(2)}(r) \tag{A-5}$$

Substituting Eqn. (A-5) into Eqn. (A-2) gives

$$\sum_{j=1}^{3} \frac{\partial}{\partial x_j}\left(\frac{1}{3} i^{(0)}(r)\right) = -a i_j^{(1)}(r) \tag{A-6}$$

Combining Eqns. (A-5) and (A-6) and eliminating $i^{(1)}(r)$ gives P_1 approximation to the equation of transfer

$$\sum_{j=1}^{3} \frac{\partial}{\partial x_j}\left(\frac{1}{a}\frac{\partial G(r)}{\partial x_j}\right) = 3a[G(r) - 4\pi i_b] \tag{A-7}$$

where G(r) is replaced by $i^{(0)}$. Using Eqn. (A-7) P_1 approximation in a two-dimensional axisymmetric cylinder can be written as

$$\frac{\partial}{\partial z}\left(\frac{1}{a}\frac{\partial G}{\partial z}\right) + \frac{1}{r}\frac{\partial}{\partial r}\left(\frac{r}{a}\frac{\partial G}{\partial r}\right) = 3a[G - 4\pi i_b] \tag{A-8}$$

The first term at the left-hand side of Eqn. (A-8) can be written in a finite-difference form as

$$\frac{\partial}{\partial z}\left(d\frac{\partial G}{\partial z}\right) = \left[\left(d\frac{\partial G}{\partial z}\right)_{i+1} - \left(d\frac{\partial G}{\partial z}\right)_{i}\right]/\Delta z$$

$$= \left[\, d_{i+1}\left(\frac{G_{i+1}-G_{i}}{\Delta z}\right) - d_{i}\left(\frac{G_{i} - G_{i-1}}{\Delta z}\right)\right]/\nabla z \qquad \text{(A-9)}$$

$$= \left[\left(d_{i+1}G_{i+1} - (d_{i+1}+d_{i})G_{i}+d_{i}G_{i-1}\right)\right]/(\Delta z)^{2}$$

where d replaced 1/a. The second term at the left-hand side of Eqn. (A-8) is expressed as a finite-difference form

$$\frac{1}{r}\frac{\partial}{\partial r}\left(dr\frac{\partial G}{\partial r}\right) = \frac{1}{r_{j}}\left[d_{j+1}r_{j+1}\left(\frac{\partial G}{\partial r}\right)_{j+1} - d_{j}r_{j}\left(\frac{\partial G}{\partial r}\right)_{j}\right]/\Delta r \qquad \text{(A-10)}$$

$$= \frac{1}{r_{j}}\left[d_{j+1}r_{j+1}G_{j+1} - \left[d_{j+1}r_{j+1}+d_{j}r_{j}\right]G_{j}+d_{j}r_{j}G_{j-1}\right]/\Delta r^{2}$$

Substituting Eqns. (A-9) and (A-10) to (A-8) gives a finite difference equation

$$G_{i,j}\left[d_{i+1,j}+d_{i,j}+\frac{1}{r_{j}}\left(\frac{\Delta z}{\Delta r}\right)^{2}\left(d_{i,j+1}r_{j+1}+d_{i,j}r_{j}\right)+3\Delta z^{2}a_{i,j}\right]$$

$$= d_{i+1,j}G_{i+1,j}+d_{i,j}G_{i-1,j} + 12a_{i,j}\sigma T_{i,j}^{4}(\Delta z)^{2}$$

$$+ \left(\frac{1}{r_{j}}\right)\left(\frac{\Delta z}{\Delta r}\right)^{2}\left[d_{i,j+1}r_{j+1}G_{i,j+1}+d_{i,j}r_{j}G_{i,j-1}\right]$$

Using Marshak boundary condition, the wall boundary condition is prescribed by

$$\varepsilon G_w - \frac{2}{3}(2-\varepsilon)\frac{1}{a}\left(\frac{\partial G}{\partial n}\right)_w = 4\varepsilon n^2 \sigma T_w^4 \qquad \text{(A-11)}$$

Eqn. (A-11) can be expressed in a finite difference form as

$$G_w = \frac{4\varepsilon n^2 \sigma T_w^4 + \frac{2}{3}(2-\varepsilon)\frac{G_{w+1}}{a\Delta n}}{\varepsilon + \frac{2}{3}(2-\varepsilon)\frac{1}{a\Delta n}}$$

The P_1-approximation results for a finite cylinder containing an absorbing and emitting medium are compared with the exact numerical results and P_3-approximation (Menguc and Viskanta, 1984) in Figure A-1. The normalized heat fluxes obtained from the P_1 approximation at the wall are generally in good agreement with those based on exact analysis. For a thin medium (i.e. $\tau = aR = 0.1$), the P_1-approximation is almost the same as the P_3-approximation; however, for larger τ, it tends to overpredict the heat flux.

II. INTEGRATED MODELING OF STRUCTURAL HEAT CONDUCTION IN THE CONTEXT OF ENGINE CYCLE SIMULATION

INTRODUCTION

PRIOR METHODS OF MODELING HEAT CONDUCTION IN CYCLE SIMULATION

CURRENT MODELING NEEDS

STEADY STATE CONDUCTION: METHODOLOGY

- Engine cycle simulation
- Finite element modeling of engine heat conduction

STEADY-STATE CONDUCTION: APPLICATION

- Network conduction model
- Finite element model of Cummins NH engine components
- Contact resistances and coolant boundary conditions
- Network results
- Finite element results
- Liner surface heat transfer

CYCLIC COMBUSTION CHAMBER WALL TEMPERATURE TRANSIENTS

- Incorporation of transient 1-D model for cyclic transients into cycle simulation
- Treatment of piston-liner thermal interaction and wall temperature transients
- Cyclic transient temperature and piston-liner heat transfer results

SUMMARY

II. INTEGRATED MODELING OF STRUCTURAL HEAT CONDUCTION IN THE CONTEXT OF ENGINE CYCLE SIMULATION

INTRODUCTION

The heat deposited on the surfaces of engine components by gas convection and radiation, and heat generated by friction between engine components, is transmitted by conduction heat transfer through the structural components to coolant, oil and the environment.

The problem of calculation of heat conduction in the engine structure involves the following elements: a) calculation of surface thermal loads, due to gas convection and radiation, coolant convection, and frictional heat; b) specification of structure thermal properties; c) representation of engine structure geometry; d) derivation of a tractable approximation of the heat conduction equation as it applies to the particular geometry (e.g., by the finite element or equivalent technique); and e) solution of derived equations for temperature distributions. The first two items above depend on structural temperatures, which make the problem non-linear, and couple the solution of the conductive equations to the solution of the appropriate convective/radiant heat transfer and frictional heat generation problems.

In the context of engine thermodynamic cycle simulation an additional coupling derives from the fact that combustion gas pressures and temperatures, which affect the convective, radiant and frictional thermal loads on the structure, are themselves functions of the instantaneous energy balance that includes heat transfer to the structure, which in turn depends on structure temperatures. To the extent that heat conduction controls overall heat transfer, a model for it ought to be integrated into the simulation.

This chapter describes approaches for integration of steady-state and cyclic (surface) conduction heat transfer computation to cycle simula-

tion procedures. First, prior work related to heat conduction computations in cycle simulation is briefly covered and today's modeling needs are reviewed. Then, a methodology is described for application of the finite element method for modeling of heat conduction within the engine structure in the context of engine cycle simulation. The techniques described are general and can be utilized with all cycle simulation procedures to an extent that depends on the degree of the spatial resolution they comprise.

Following the outline of the methodology, a description is given of two structural models, namely a network model of steady-state heat conduction in diesel geometries and a detailed FEM model of a Cummins engine. Results obtained by cycle simulation runs with both network and FEM methodologies are presented. Effects of speed, load and progressive insulation on zonal temperatures and heat transfer rates have been investigated. In the presentation of the FEM results, emphasis has been placed on temperature distributions, peak temperatures, details of liner surface heat transfer and comparison to network predictions. The results document sensitivities to various parameters, and they demonstrate the capabilities of the methodology.

The last section of this chapter concerns the modeling of cyclic surface thermal transients. The model used for this purpose is described in the Phase I report. This section focuses on the incorporation of the model in a cycle simulation code and describes an extension of the technique for coupling steady-state and transient computations, which allows rigorous treatment of the piston-liner interface and accurate prediction of liner temperature excursions. Results showing effects of progressive insulation on this aspect of heat conduction, are also documented.

PRIOR METHODS OF MODELING HEAT CONDUCTION IN CYCLE SIMULATION

Since the convective and radiative heat transfer from combustion gases to combustion chamber walls provides the bulk of the heat load on the structure of I.C. engines and directly affects performance and fuel

efficiency, heat transfer modeling efforts for the purposes of cycle simulation have tended to focus on the gas phase heat transfer. In addition, in conventionally cooled engines the range of wall temperatures is relatively narrow. Consequently, steady-state conduction heat transfer has been represented in cycle simulations by very simple models:

1) Prescribed values, based on estimated or measured wall temperatures were input into the simulation.

2) Lumped characterization of the engine structure by a single thermal resistance between combustion chamber surfaces and coolant surface, where a coolant temperature and heat transfer coefficient are prescribed, i.e.:

$$Q_{rad} + h_{gas} A_{gas} (T_{gas} - T_{wg}) = (T_{wg} - T_{wc})/R_{struc} = h_{cool} A_{cool} (T_{wc} - T_{cool}) \quad (1)$$

where h_{gas} and T_{gas} are the effective mean gas heat transfer coefficient and temperature, Q_{rad} is the mean radiant heat transfer rate, T_{wg} and T_{wc} are mean gas-side and coolant side wall temperatures and A_{gas} and A_{cool} are surface areas on the gas and coolant sides, respectively. Thus, gas and coolant side surface temperatures T_{wg} and T_{wc} representing the entire surfaces are solved for, but there is no accompanying spatial resolution. In addition, there is the obvious difficulty posed by the need to estimate the equivalent structure resistance, R_{struc}.

3) Thermal resistance network concept which uses several different temperatures T_{wg} to characterize different combustion chamber (and coolant/oil side) surfaces of the structure. The surfaces are joined by a network of thermal resistances forming an analog electrical circuit (Figure 2-1a,b). A set of algebraic linear equations is solved to determine temperatures at all surfaces and nodes

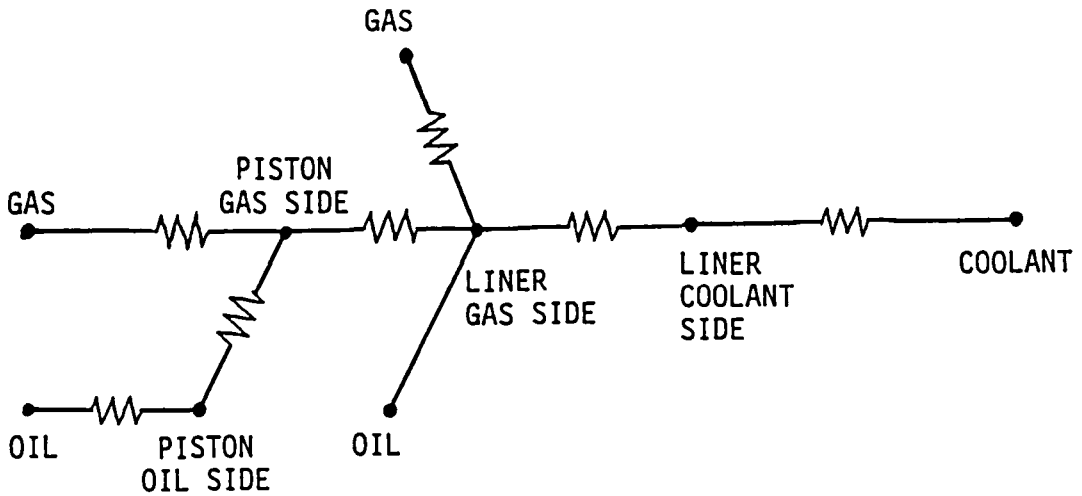

(a)

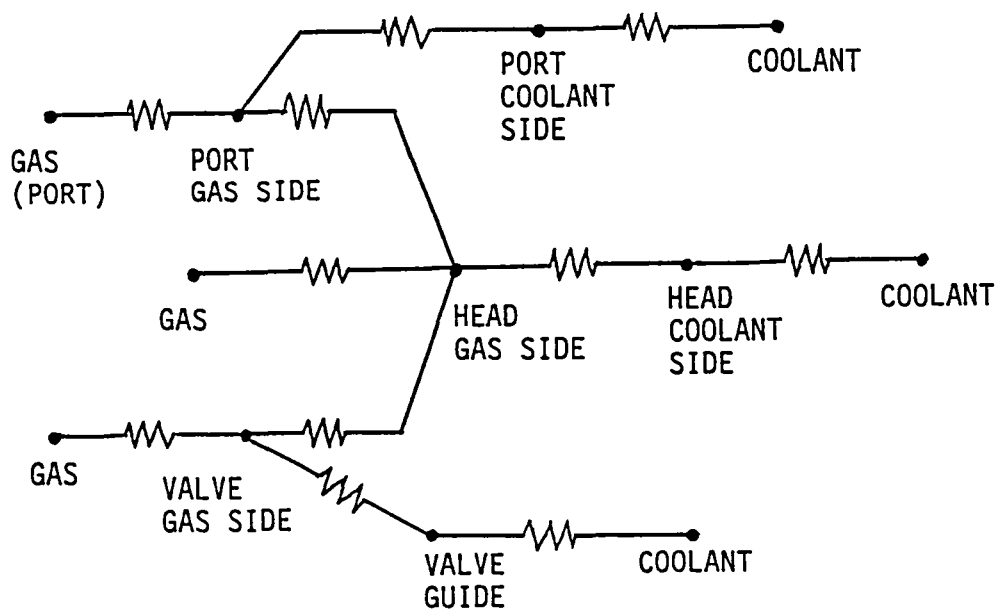

(b)

Figure 2-1 Examples of simple thermal resistance networks for a) piston-liner heat transfer; and b) heat transfer in a diesel engine head.

of the network. A good example of such a network, including separate piston, liner and head and port surface nodes is given by Borman (1964). Using such models, effects of individual component dimensions and mean thermal properties on heat transfer and thus engine performance can be estimated. The technique also lends itself to further generalization, in that increasingly complex networks can be constructed to characterize more geometrical detail and/or materials differentiation.

In the last two decades, advances in speed of computation have allowed detailed investigations of heat conduction in engine components via extended or geometrical networks and the mathematically more formal finite difference and finite element methods. The latter has allowed the modeling of structure geometry and thermal properties at a level of great detail (e.g., Li, 1982, Holtman et al., 1984, McDonald, 1985). A need to couple solutions of combustion gas thermodynamics and component temperatures has also occasionally been recognized: Woschni (1980), has suggested the alternating application of cycle simulation and some form of heat conduction solution for the engine structure. Kao and Wallace (1981) have proposed a technique in which piston temperature results obtained from a finite element solution could be condensed into a one-dimensional form so as to compute an equivalent conductance which can be utilized in conjunction with a global cycle simulation model. However, no examples of detailed conduction models, completely integrated into cycle simulation procedures in order to account for all of the couplings, have been reported in the literature .

Effects of combustion chamber wall cyclic temperature excursions on heat transfer and engine performance have also been acknowledged but ignored in cycle simulation procedures. This practice is acceptable for conventional metal engines due to the small magnitudes of these transients, but introduces measurable inaccuracies for insulated engines.

CURRENT MODELING NEEDS

Some of the more recent developments in engine design and research, as well as in modeling techniques, are providing the impetus for total integration of more sophisticated structural heat conduction models into cycle simulation methodologies:

1) The trend toward development of low heat rejection (insulated) engines by the use of low conductivity ceramics, has provided an entirely new structural environment. The wall temperatures rise significantly and their level can be calculated only by a detailed combined convection/radiation/conduction solution. In addition, there is interest in predicting the steady state and transient temperature distributions in engine components so that thermal stresses in insulating (ceramic) parts may be calculated.

2) Due to the increasing firing pressures and thermal loads that accompany high BMEP engines, material temperatures are approaching allowable limits, and there is increasing interest in accurate prediction of local component temperatures.

3) The general level of sophistication of gas-to-surface (convection, radiation) heat transfer models for diesel geometries has increased to the extent that they make possible the prediction of gas-to-surface heat transfer in a spatially and time-resolved manner (Phase I Report, NASA CR-174783; also Chapter I of present report). These physically-based quasi-dimensional zonal models predict the thermal load levels combustion chamber surfaces in a spatially resolved manner. Thus, they can provide the requisite boundary conditions needed by detailed heat conduction models.

When current engine design analysis needs, and especially those related to insulated engines, are carefully reviewed, there emerge two separate appropriate levels for the proposed coupling of heat conduction methodologies to cycle simulation procedures:

- o Heat resistance network models generic to an entire series or class of engines, which can be utilized at the concept analysis stage of development, for parametric studies of effect of geometry, materials or insulation strategies on engine performance. While resolving gross features of geometry, such models would not incorporate fine geometrical details and would be used in the period prior to establishment of a final design.

- o Multi-dimensional models, accurately characterizing geometry and materials for a specific engine, meant for studies of effect of engine operating conditions on detailed component temperature and stress distributions.

At either level it is desirable to have the capabilities to model not only the steady-state conduction, but also to represent and study the cyclic transients in surface layers, and transient conduction due to engine load and speed changes (thermal shock).

Cyclic transients (discussed in detail in Morel et al, 1985) affect combustion chamber thermodynamics and also impact the computation of steady-state conduction in the rest of the engine structure. Since their magnitudes can reach several hundred degrees Kelvin for insulating materials, they might be linked to fatigue and the failure of surface layers in ceramics that has been observed in engine tests. The load and speed transients are much slower than the cyclic transients, and they affect the whole structure. Consequently, there is a need to evaluate the thermostructural behavior of insulation materials under engine conditions such as sudden load changes, cold start etc.

STEADY-STATE CONDUCTION

Engine Cycle Simulation

To carry out the simulations in a realistic manner, the conduction representation must be coupled to a thermodynamic cycle simulation

providing the boundary conditions for the conduction calculations. In this work we used the IRIS engine simulation code, which incorporates highly detailed global or zonal descriptions of key engine processes and predicts a variety of engine parameters (see Appendix of Phase I Report). Convection and radiation submodels resolve gas temperatures, heat transfer coefficients and radiation heat fluxes on a number of surfaces representative of diesel geometries (i.e, piston, liner, head, with further resolution on each surface). A physically based friction model, which tracks boundary and hydrodynamic friction separately at ring-liner and piston-liner contacts, computes frictional heat deposited at a prescribed number of piston, ring and liner surfaces. Convective heat transfer from piston crevice to the appropriate piston and liner surfaces is also computed. In the ports, thermodynamic simulation of port gases accounts for heat transfer, which is computed at a number of port surfaces including port walls, valve backs and stems. In total, the simulation distinguishes between 19 surfaces in contact with combustion (or intake exhaust) gases, 9 additional friction (piston/liner) surfaces and 21 surfaces in contact with coolant or oil. These surfaces form the link used to interface heat conduction methodologies to the thermodynamic cycle simulation.

Finite Element Modeling of Heat Conduction

In order to accommodate the need for detailed multi-dimensional analysis for specific design studies, an interface procedure was developed for coupling finite element conduction computations to an engine cycle simulation code. The procedure utilizes external finite element structure models for heat conduction modeling. The interface was constructed in a way that makes it generic, i.e., independent of details of the finite element model: the level of resolution of geometrical detail and materials differentiation is left to the FEM analyst, to be chosen according to the ultimate purpose of the analysis, e.g., peak materials temperature determination, or thermal stress analysis. A complete engine model (an assembly of engine component geometry models including piston, rings, liner, head, valves, etc. and the descriptions of thermal interactions among components) must be used to describe all

of the heat paths, but the level of resolution need not be uniform. Only components where local temperatures are of interest need to be modeled in full detail, while coarser mesh can be used for the rest.

In the context of a distributed computational model (network, finite differences or FEM) and for the general, transient problem, the heat conduction equation is expressed as

$$[C]\ \dot{T} + [K]\ T = \text{Thermal load vector} \qquad (2\text{-}2)$$

where [C] and [K] are thermal capacitance and resistance matrices, respectively, and T is the vector of nodal temperatures.

The thermal load vector (Q) acts on the surface nodes, and it can be expressed in general as

$$\begin{aligned} Q_j = Z_{ij}\, X_{gjk} & \left[Q_{rad,k} + h_{geff,k}\, A_k\, (T_{geff,k} - T_i - C'_g)\right] \\ & + Z_{ij} X_{cjk} \left[h_{ck}\, A_{ck}\, (T_{ck} - T_i)\right] \\ & + Z_{ij} X_{fjk} \left[Q_{fric,k}\right] \end{aligned} \qquad (2\text{-}3)$$

where

j	= boundary element nodes ($j = 1, n_i$; $n_i = 1\text{-}4$)
i	= boundary elements number ($i = 1, m$)
T_j	= temperature at node j
k^J	= thermal load surface number for cycle simulation
A_k	= thermal load surface area for surface k

Z_{ij} is a shape function (determined from boundary element geometry) which distributes load on boundary element i to each of its nodes j. The network approach is a special case of the above procedures, where a boundary element has a single node ($n_i = 1$) and $Z_{ij}=1$.

X_{sik}, X_{cik}, X_{fik} are weights that map boundary finite elements i onto areas k on cycle code gas/coolant side and friction surfaces. The weights account for the area fraction needed in case more than one boundary node maps onto a surface, and also for the fraction of time the surface is exposed to the thermal load, e.g,

$$X_{gik} = \frac{A_i}{A_k} \frac{\int A_{gk}}{A_k} \qquad (2\text{-}4)$$

where the integral indicates a cycle average of instantaneous area (e.g a liner surface) exposed to gas. The variables $Q_{rad,k}$, $h_{g,eff,k}$, and $T_{g,eff,k}$ in equation (2-3) are mean radiation heat transfer rate, effective gas heat transfer coefficient and effective temperature for surface k ($h_{g,eff} = \int h_g A_g / \int A_g$, $T_{g,eff} = \int h_g T_g A_g / \int h_g A_g$), and $h_{c,k}$ and $T_{c,k}$ are coolant or oil surface heat transfer coefficients and temperatures. The term C'_g is a surface temperature correction related to surface cyclic transients on surfaces exposed to combustion gases, and will be described in a later section.

The FEM heat conduction interface requires as an input the global finite element heat conductance [C] and capacitance [K] matrices, and a directory of all boundary elements of the finite element model mapping them onto one or more cycle simulation heat transfer surfaces. Also required in the directory are areas and nodal connectivities of the boundary elements.

The global conductance and capacitance matrices describe the linear equations to be solved. They are computed by formal finite element matrix assembly procedures. The global conductance matrix for a structure is assembled from conductance matrices characterizing each element. The conductance matrix of each finite element describes the linear (or higher order) relationships between element nodal temperatures that a) establish the heat balance and b) best approximate the heat conduction equation within the spatial domain of the element. For the models and results discussed here, COSMIC/NASTRAN was used to construct geometry representations and compute global matrices, although any other multi-purpose finite element code could be utilized. Data on the boundary (surface) elements of the FEM model is passed to the cycle code in the form of a directory, which associates each boundary element with one or more heat transfer areas. Also provided for each boundary element in the directory, are the element area (A_i in eq. 2-4), a weight

that allows partial mapping onto more than one heat transfer area, and the ID's and coordinates for nodes connected to the element. The latter are used to generate the "shape functions" which distribute the element thermal load to the connected nodes.

The interaction of NASTRAN and cycle simulation code, including the FEM interface and the coupling of between steady-state conduction and thermodynamic cycle simulation, is shown schematically in Figure 2-2. With the above information acquired by the cycle code through its FEM interface, the steady-state heat conduction computations are carried out, as in the network approach, at the end of each engine cycle. The thermal load for each element is computed based on mean thermal load quantities on the cycle code heat transfer surfaces onto which the element has been mapped. This load is in turn distributed to the appropriate individual nodal equation right hand sides. Following that the equations are solved simultaneously for all nodal temperatures. The resulting surface temperatures feed back into the gas heat transfer calculations and the process is repeated until convergence of heat transfer computations. Structural temperatures are then output and postprocessed for contour plotting of component temperature profiles.

The average time for execution of one cycle of IRIS simulation, with FEM computations for a 1860 node model, is 3 CPU minutes on the DEC VAX 11/750. Larger and more detailed engine FEM models involving several thousand nodes would have larger CPU time requirements.

STEADY-STATE CONDUCTION: APPLICATION

Network Conduction Model

A heat conduction model representative of most DI diesel geometries was constructed using a thermal resistance network approach, developed separately by ITI, and was interfaced to the engine simulation code. The representative simplified diesel geometry and the thermal resistance network are shown in Figures 2-3 and 2-4 respectively. The network consists of 159 nodes linked by 252 resistances; its surface nodes map

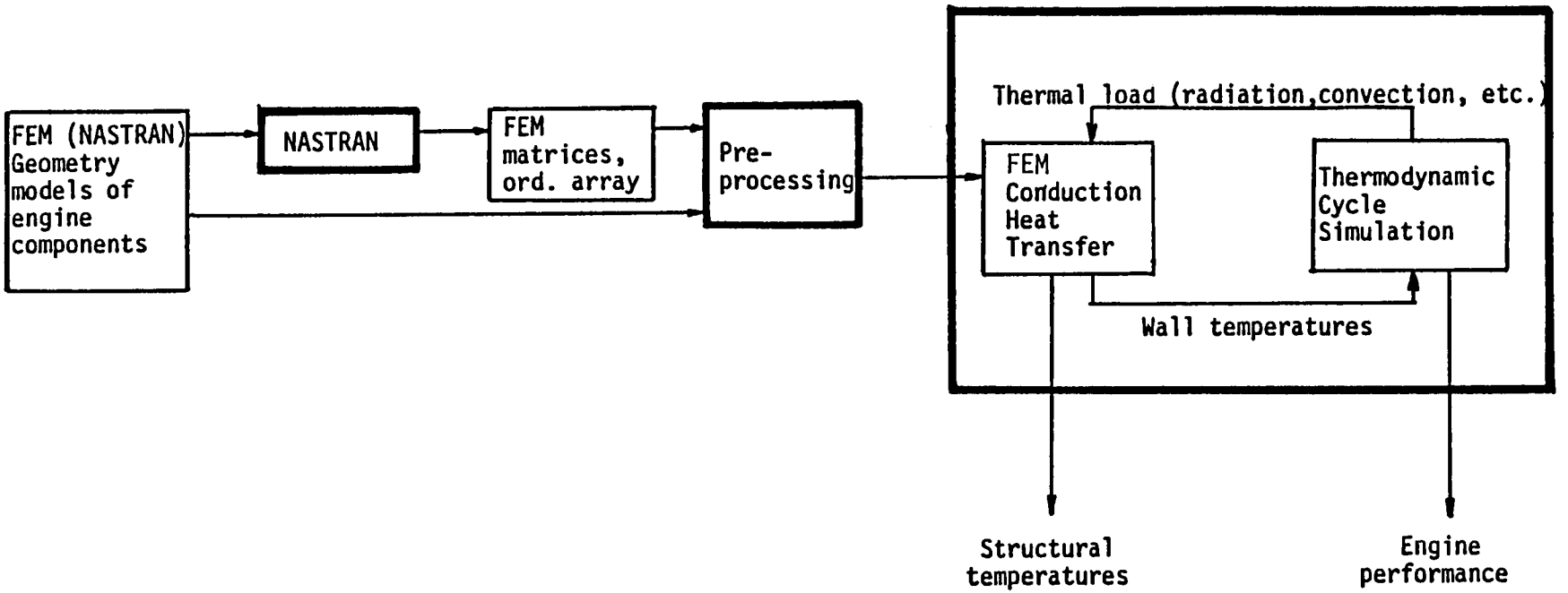

Figure 2-2 Schematic of the interaction between NASTRAN and cycle simulation.

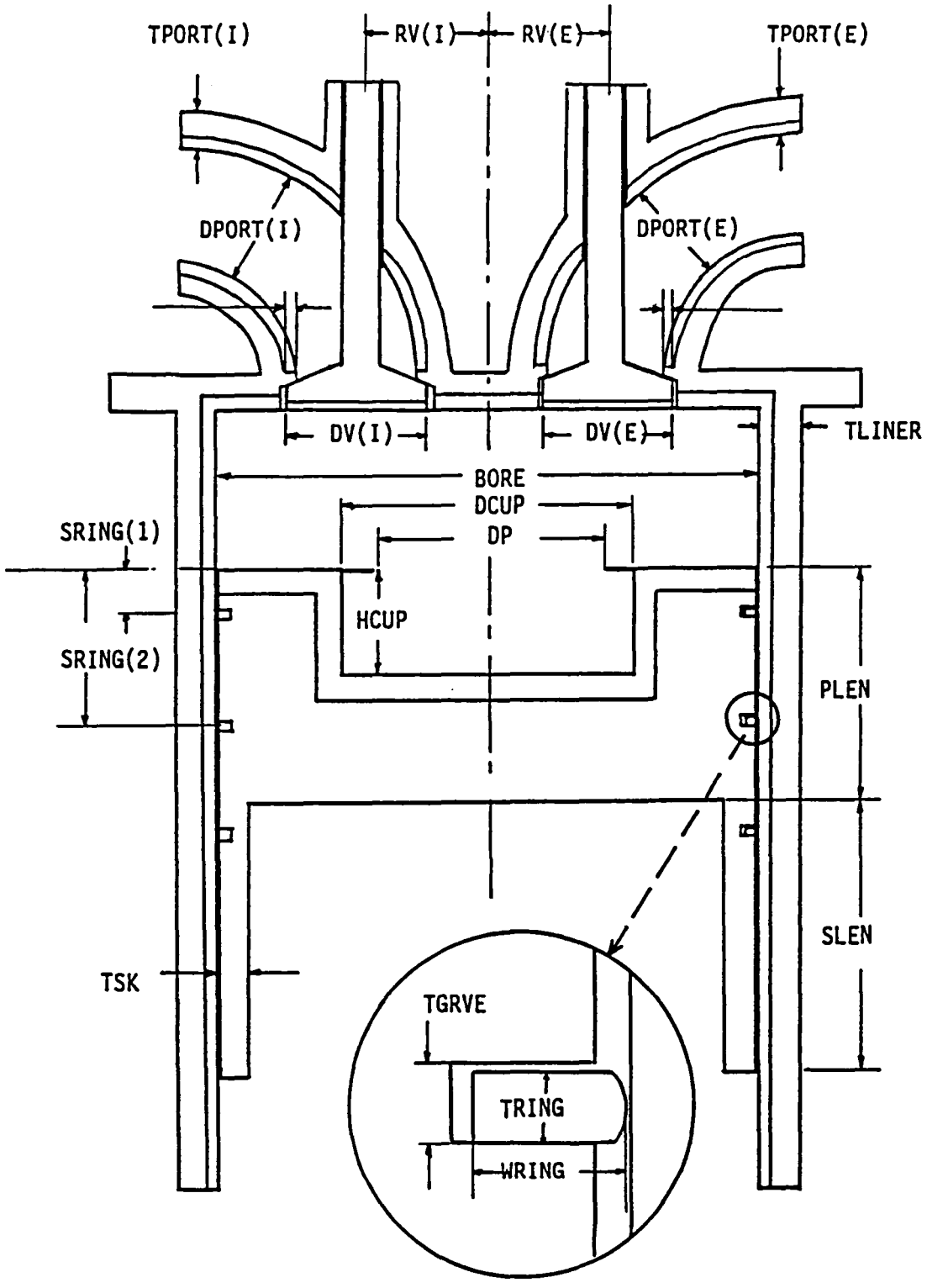

Figure 2-3 Schematic of the representative diesel engine geometry used for the network model of heat conduction in IRIS. Labeled dimensions are those used as input to the calculations.

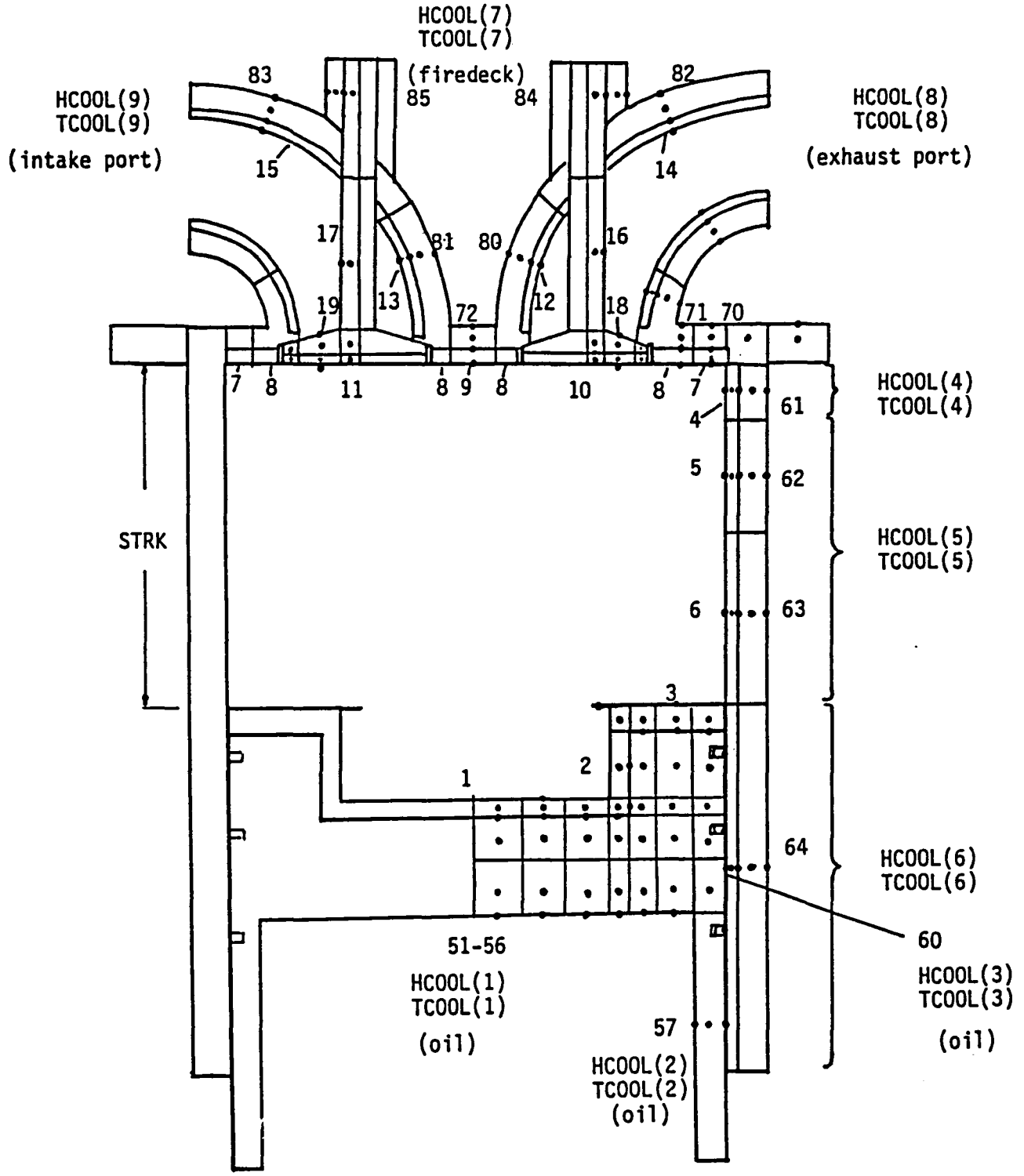

Figure 2-4 Schematic of representative geometry showing locations of network nodes, IRIS gas and coolant side surface ID's and surfaces used for differential oil and coolant cooling.

exactly onto the 49 heat transfer (thermal load) surfaces recognized by the parent code.

As shown in Figure 2-4, all combustion chamber and port surfaces have surface layer nodes and associated cells for which individual thicknesses and thermal properties can be prescribed. In addition to the structural resistances, resistances between surfaces in contact and relative motion (such as piston-liner, ring-liner and valve-seat surfaces) are computed based on prescribed contact heat transfer coefficients and the fraction of time surfaces of a pair are in contact with each other. Single or multiple (exhaust or intake) valve or ports can be handled. The resistances are calculated using exact geometrical relationships for simple axisymmetric geometries, except for complex geometries such as the head, where approximations are made using equivalent mean lengths and areas. Thus for a representative piston with a cylindrical cup and a cylindrical-shell liner, the constructed equations are equivalent to the finite difference approximation to the heat conduction equation.

Finite Element Model of Cummins NH Engine Components

A Cummins NH series engine was selected for construction of a finite element engine structure model. The total number of nodes in the model was 1860, which could be considered an intermediate number for a heat conduction model of complex structure. This level is adequate for representing an important part of the geometrical detail without excessively burdening the simulation with excessive CPU time requirements, because the simulation is often executed in parametric studies involving multiple runs with numerous cycles in each run.

The finite element model was constructed using NASTRAN 2-D axisymmetric, 3-D and scalar elements. The piston geometry, which is mostly axisymmetric except for the wristpin area, was modeled by 2-D axisymmetric elements. A 3-dimensional representation would not be a significant improvement in this particular case, since it would affect only the crankcase side of the piston where convective boundary conditions are

prescribed only in the average sense, with no spatial resolution. The FEM models of piston, liner and rings (which are axisymmetric and were modeled as such) are shown in Figure 2-5(a). Not shown in the figure are a large number of scalar elements that link piston liner and rings with each other. The thermal resistances for these elements were computed from the contact resistance and the fraction of time areas associated with nodes in a pair are in contact. Figure 2-5(b) shows an axisymmetric valve geometry model. The valve guide above the port was also included in this representation. The valves were linked by scalar elements to the head structure model at the seats as well as at the valve guides. Scalar elements at the valve-seat contacts account for contact resistance and contact time fraction.

The engine head geometry is truly 3-dimensional and complex, as may be seen from a simplified sketch in Figure 2-6. A 3-D model of the head is necessary to model all heat paths. A heavy-duty diesel engine head, with all its ports, manifolds, coolant, oil and fuel passages and bolt holes, valve and injector guides, presents the FEM analyst with a formidable 3-D modeling task. The task and model size was kept manageable by the following modeling decisions:

a) of primary importance are direct gas-metal-coolant heat paths such as those through the firedeck and through port or manifold walls. Other heat paths such as those between coolant passages, and from coolant to the exterior through metal were not precisely and geometrically modeled, although the correct extent of structure connecting interior surfaces to exterior, was maintained; and

b) to keep resolution within acceptable bounds, finer details of the geometry, expecially on the coolant side, where boundary conditions are only known in the average sense, were omitted.

Thus the important details of the head that were emphasized included the area directly above the cylinder (firedeck), firedeck topography on the coolant side, details of exhaust and intake ports, and the shapes and thicknesses of ports. Since the NH head is constructed to span two

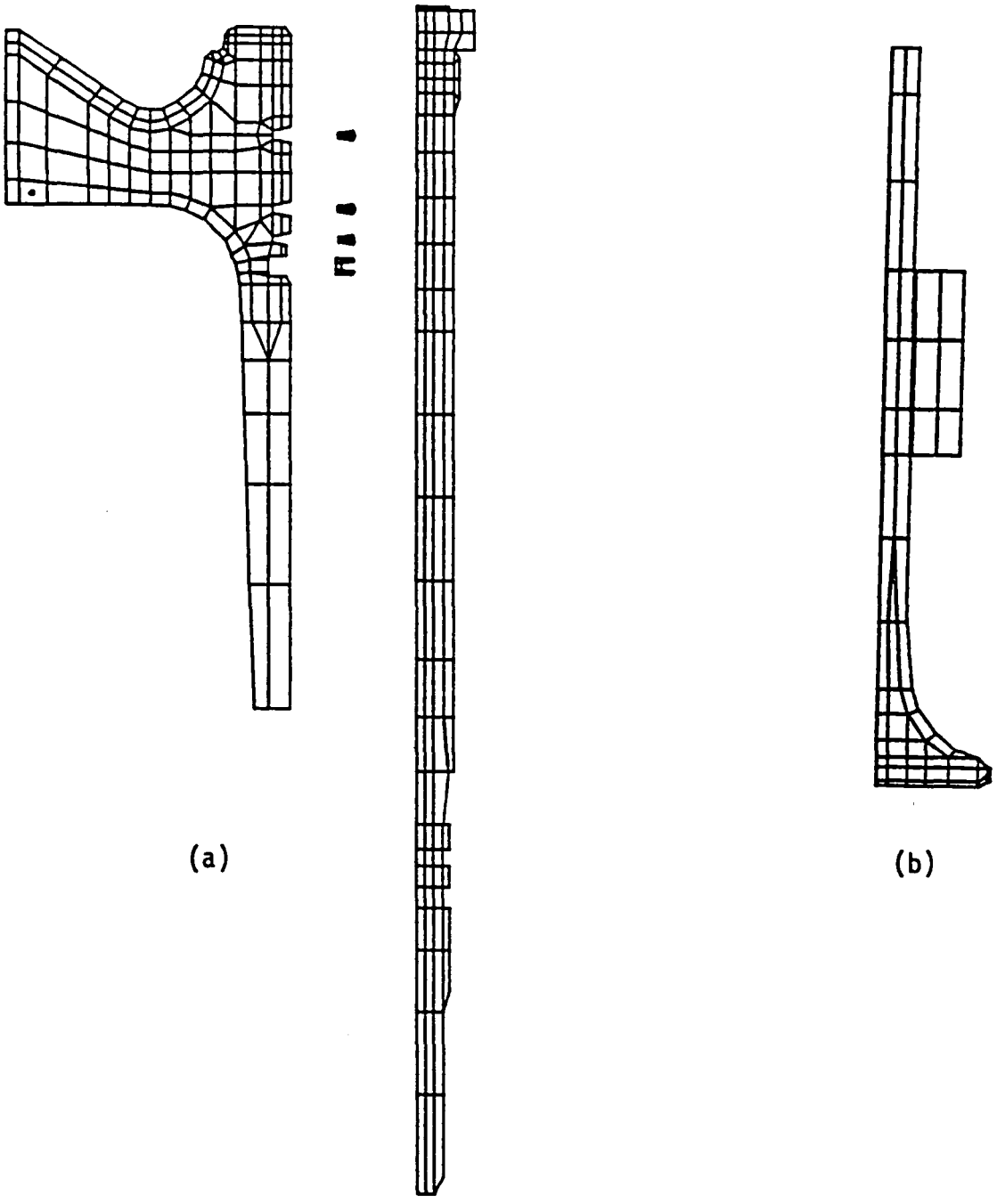

Figure 2-5 a) 2-D Axisymmetric FEM model of Cummins engine piston-liner ring assembly. Piston-liner relative axial positions as at TDC. b) 2-D axisymmetric model of valve geometry including valve guide. Intake and exhaust valves identical.

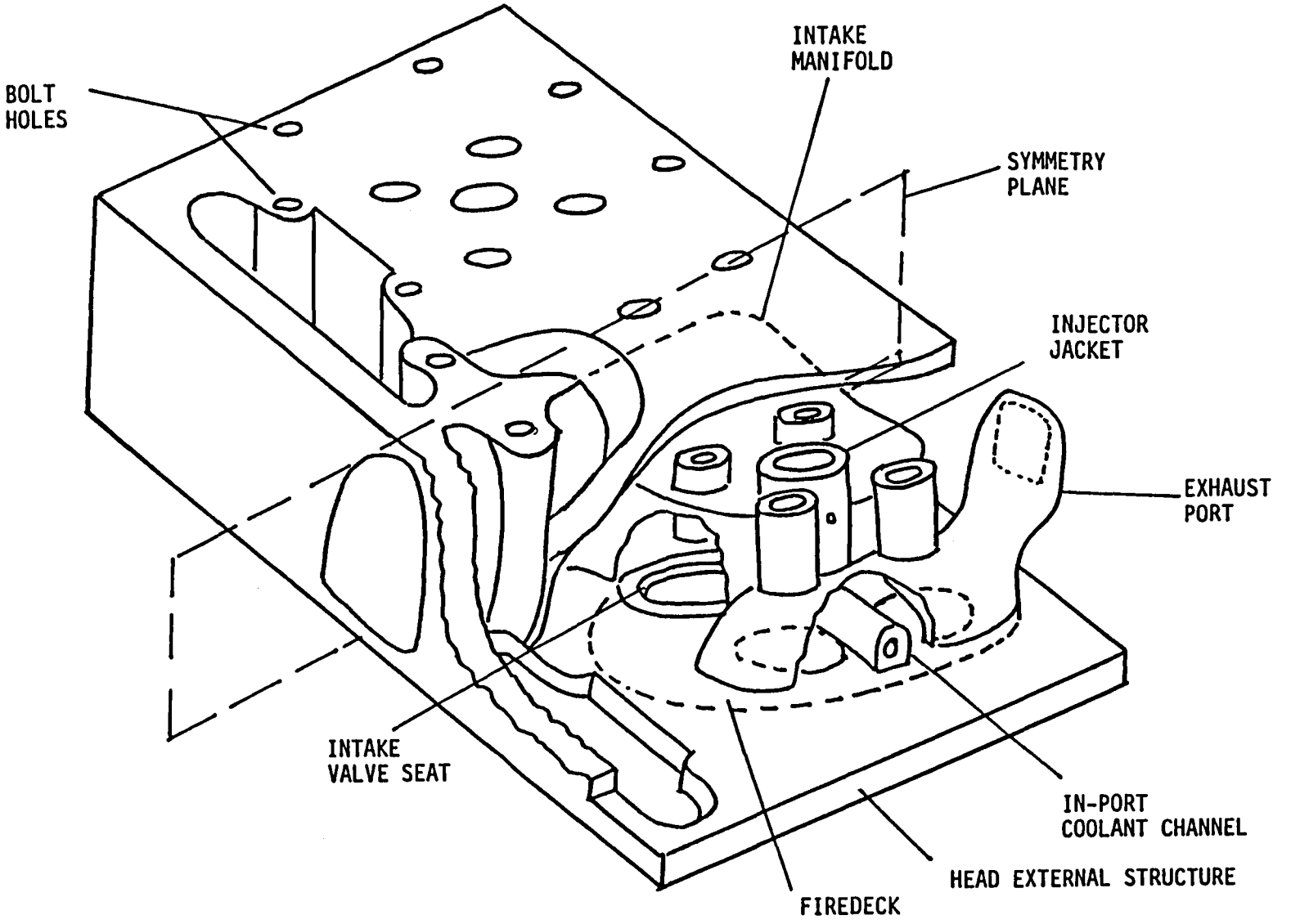

Figure 2-6 Schematic diagram of Cummins engine head. A cutout view of the symmetric one-half of the structure shows major internal elements above one cylinder.

cylinders and has near-symmetry between its sides on each cylinder, only one half of the structure was modeled. The structure was divided into three major elements: firedeck, intake manifold and exhaust port. Models for geometries of these three components were supplemented by additional representations of heat paths between them and other surfaces of the head, such as the injector jacket and the outer surfaces. Scalar elements with appropriately computed thermal resistances were used to link structures as well as to establish heat paths to valves and liner. The firedeck, intake manifold and exhaust port models are shown in Figures 2-7, and 2-8(a)-(b). The symmetry plane in the head runs through the center of the intake manifold, which is common to two cylinders. Thus only the symmetric one-half of the intake manifold was modeled.

Contact Resistances and Coolant Heat Transfer Coefficients

In IC engines, contact thermal resistances exist between parts of assembled or composite components, at the interfaces between stationary components, and between components in relative motion. Of these three types, the last one is usually the most important. Contact heat transfer coefficients are a function of the contact pressure, the thermal properties of the interfacial medium, the surface finish and hardness of surfaces in contact. Where motion between components is along the interface, the contact resistance is typically higher due to the provided clearance and existence of a lubricant film.

Determination of the correct values of the contact resistances is difficult, but since they are often not too large, their precise value is not critical. However, when their magnitudes are large compared to thermal resistances on either side of the contact, or if they lie on an important heat path, careful attention must be paid to them. Five such contacts, namely ring-liner, piston-ring, piston-liner, valve-seat and valve stem-guide, were included in both the network and FEM representations. For each of these contacts a contact heat transfer coefficient h_i is defined to relate the heat flux to the temperature drop across the

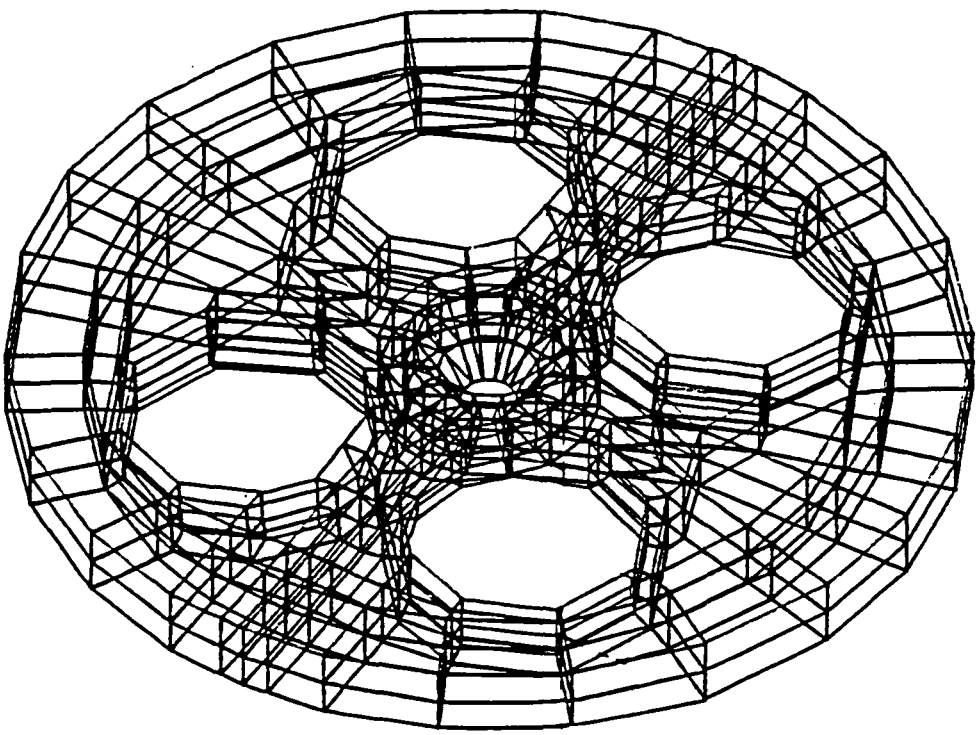

Figure 2-7 3-D finite element model of firedeck: orthographic view.

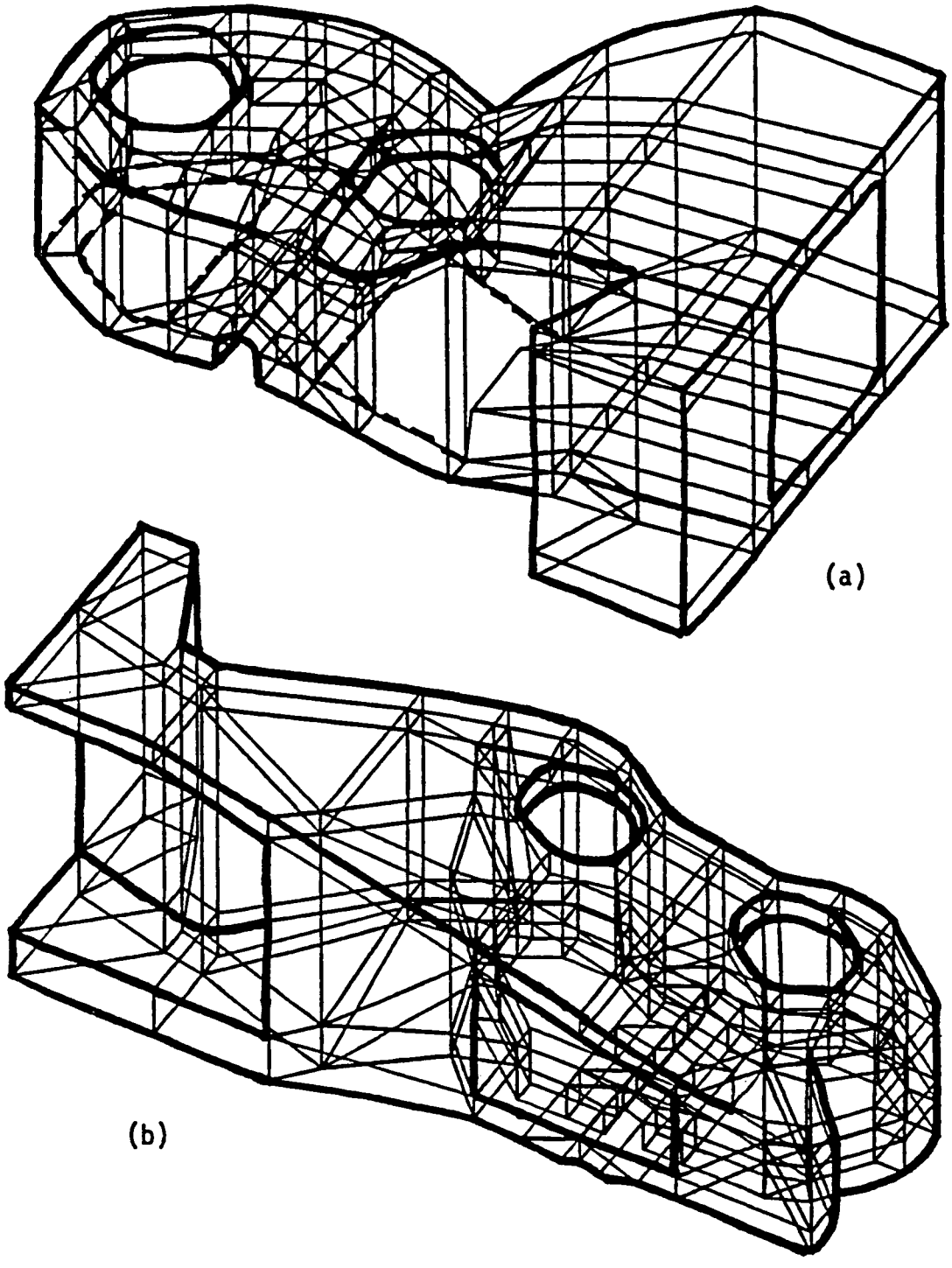

Figure 2-8 Orthographic views of 3-D FEM models of a) exhaust port; b) symmetric one-half of intake manifold.

interface, i.e., $Q/A = h_i(T_1-T_2)$. In reality h_i varies spatially and temporally (with crank angle) for each of the contacts. Since this only affects surface transients (which are not large on liner, rings, valve seals or stems), an average coefficient is appropriate for use in the methodology. The average itself may vary with engine parameters such as speed, load, valve spring compression, etc. In the present methodology, nominal heat transfer coefficients for the contacts identified for a particular design are prescribed as input data to be specified by the user. Cycle averages are computed from these nominal values based on contact times between various surfaces or subsurfaces.

Coolant or oil heat transfer coefficients are sensitive to coolant and oil velocities and thermal properties, the mechanisms of heat transfer (forced convection, impinging jet, splashing, nucleate boiling, etc.) and the details of the geometry and fluid flow. Magnitudes of coolant/oil heat transfer coefficients cited in the literature vary greatly. Reported correlations are generally specific to engine geometry or mode of cooling and cannot be universally applied. For results presented in present study coolant/oil and contact heat transfer coefficients were arrived at by running sensitivity studies aimed at matching measured temperatures.

Network Results

A sample output of network nodal temperatures (Cummins NH engine, rated speed/load) arranged into a schematic of diesel combustion chamber geometry (not to scale), is shown in Figure 2-9, where G refers to gas-side surfaces and C to coolant-side surfaces. In addition to temperatures, heat transfer rates on individual cycle code heat transfer surfaces are recovered from the calculations. At the network level of resolution, predicted steady-state temperatures and heat transfer rates are spatial averages computed for each surface or volume. Local variations, which can be significant - as will be seen in FEM results - are not resolved. However, there is enough detail in the description of the heat paths to produce accurate global heat transfer results. Most of

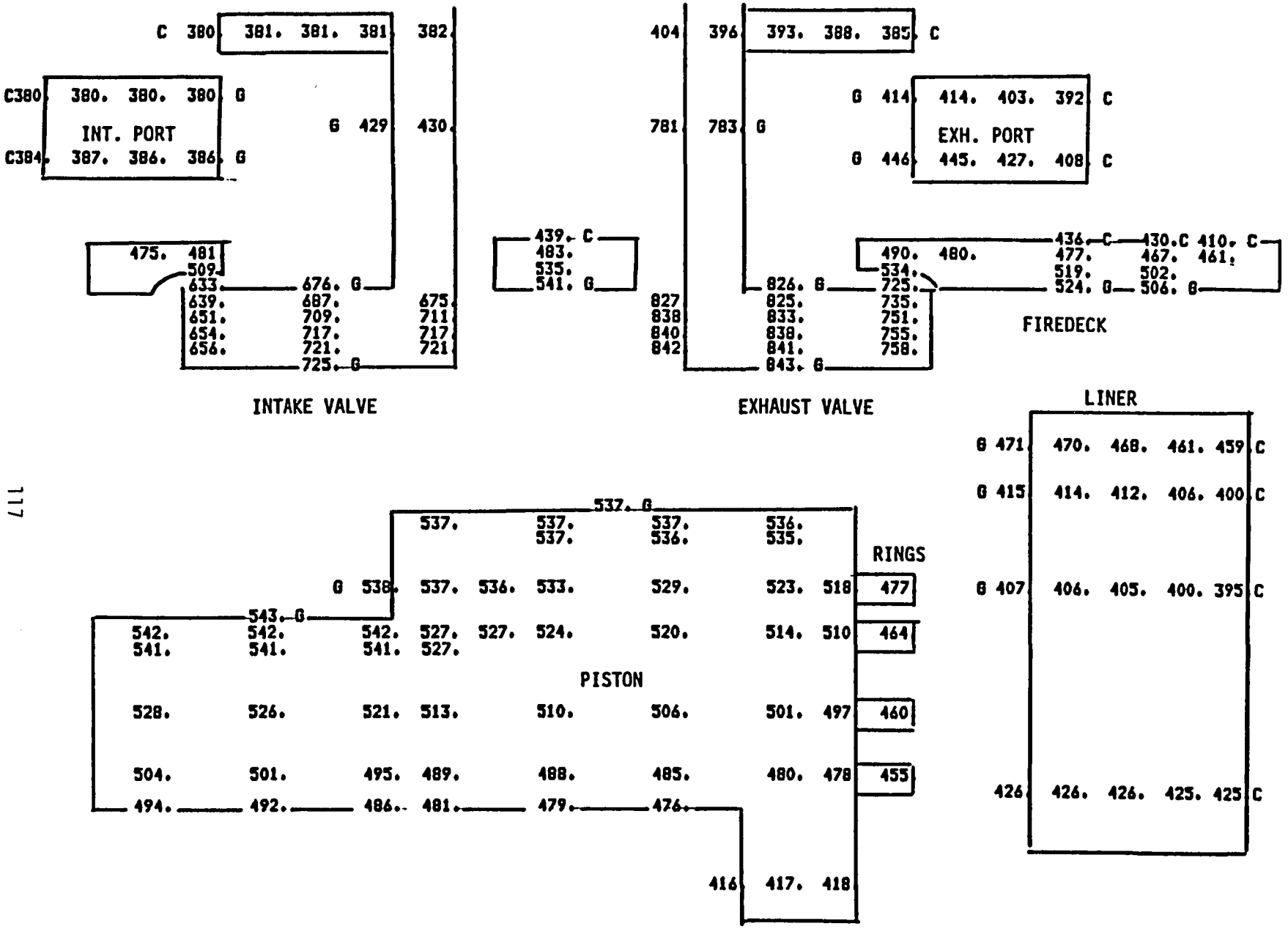

Figure 2-9 Sample IRIS output of network nodal temperatures (deg-K) arranged into an (unscaled) schematic of combustion chamber geometry.

the documented effects of speed and load, as well as progressive insulation at varying load, discussed below, cannot be explained in the context of the heat conduction methodology alone. They are the product of the complex interactions with all the cycle code submodels with thermal implications, including cylinder and port thermodynamics, flow and convection, radiation, friction and soot kinetics in this completely coupled methodology.

Speed and load effects. Variation with speed and load of the fraction of fuel energy rejected as combustion chamber heat transfer, is shown in Figure 2-10. The plotted points correspond to 100, 70, 50, 35 and 25% of full load fuel rate at each of the three speeds. The variation of this quantity is the result of combined effects of changes in gas heat transfer coefficients, effective gas temperature, radiation flux and cooling rate with speed and load. Exhaust port heat transfer (as a fraction of fuel energy) also decreases with speed, but has a peak at a lower load (Figure 2-11). Effects on heat rejection to oil are shown in Figure 2-12. The increase in heat rejected to oil (as a fraction of cylinder heat transfer) with speed is partly due to increasing frictional heat generation, but also indicates that the relative importance of the main heat paths changes with speed and load. The fraction of in-cylinder heat transfer rejected to oil increases with speed, the effect being more pronounced between 1300 and 2100 rpm. Variation with load is small and exhibits opposite trends at lower and higher speeds, respectively. Effects on average temperatures of various component surfaces exposed to combustion chamber gases are documented in Figure 2-13. Wall temperatures increase with load but decrease with speed (at a constant fuel rate), as would be expected from results shown in Figure 2-10. Detailed analysis of the code outputs showed that this is caused by decreases with speed in radiation heat transfer and mean effective gas temperature, and increase in coolant heat transfer coefficients, which more than compensate for the effect of increasing gas heat transfer coefficients.

Effects of Insulation. A study of effects of progressive insulation of the Cummins NH engine components at rated speed and varying load levels was conducted using the capability of the IRIS thermal resistance net-

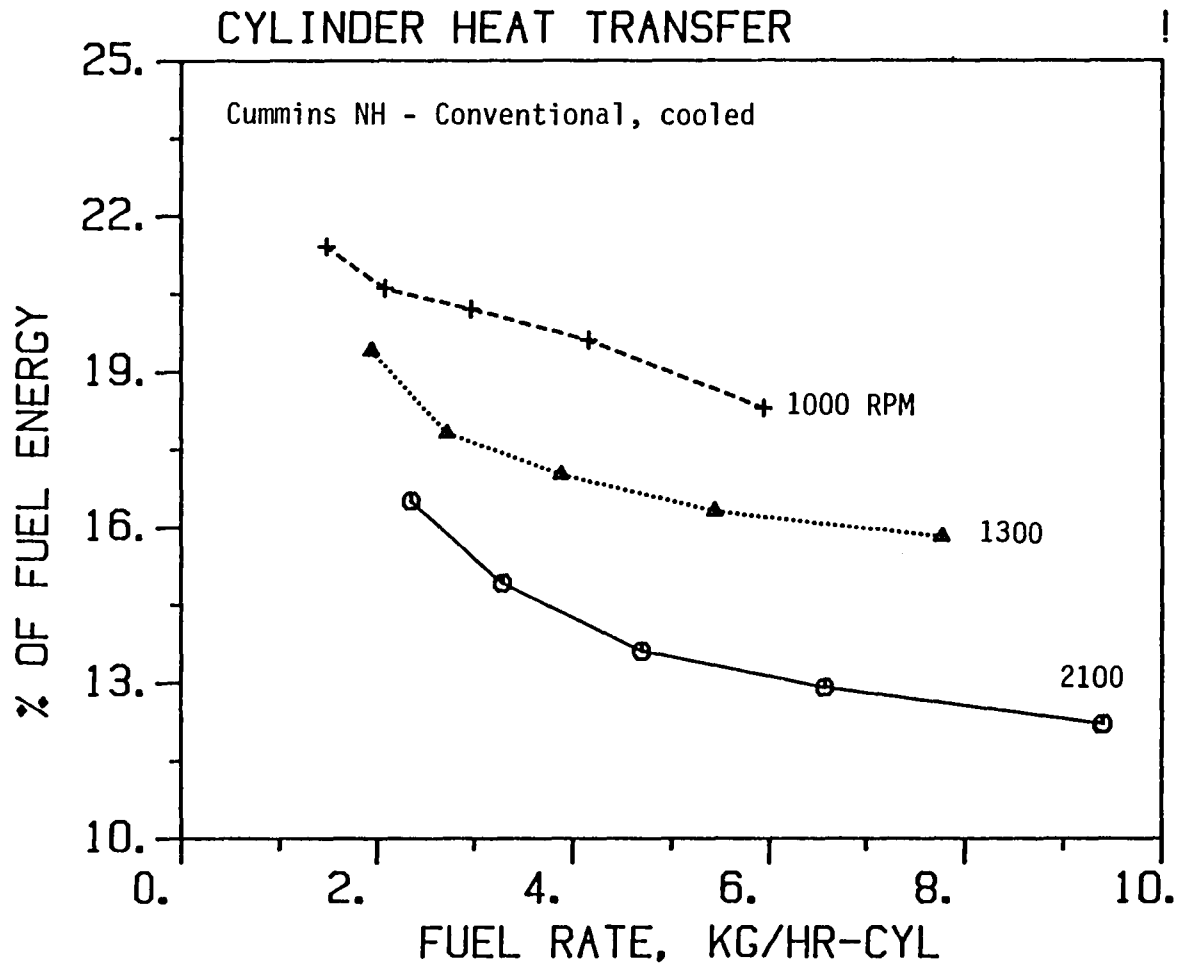

Figure 2-10 Variation with speed and load of cylinder heat transfer as a fraction of fuel energy (network results).

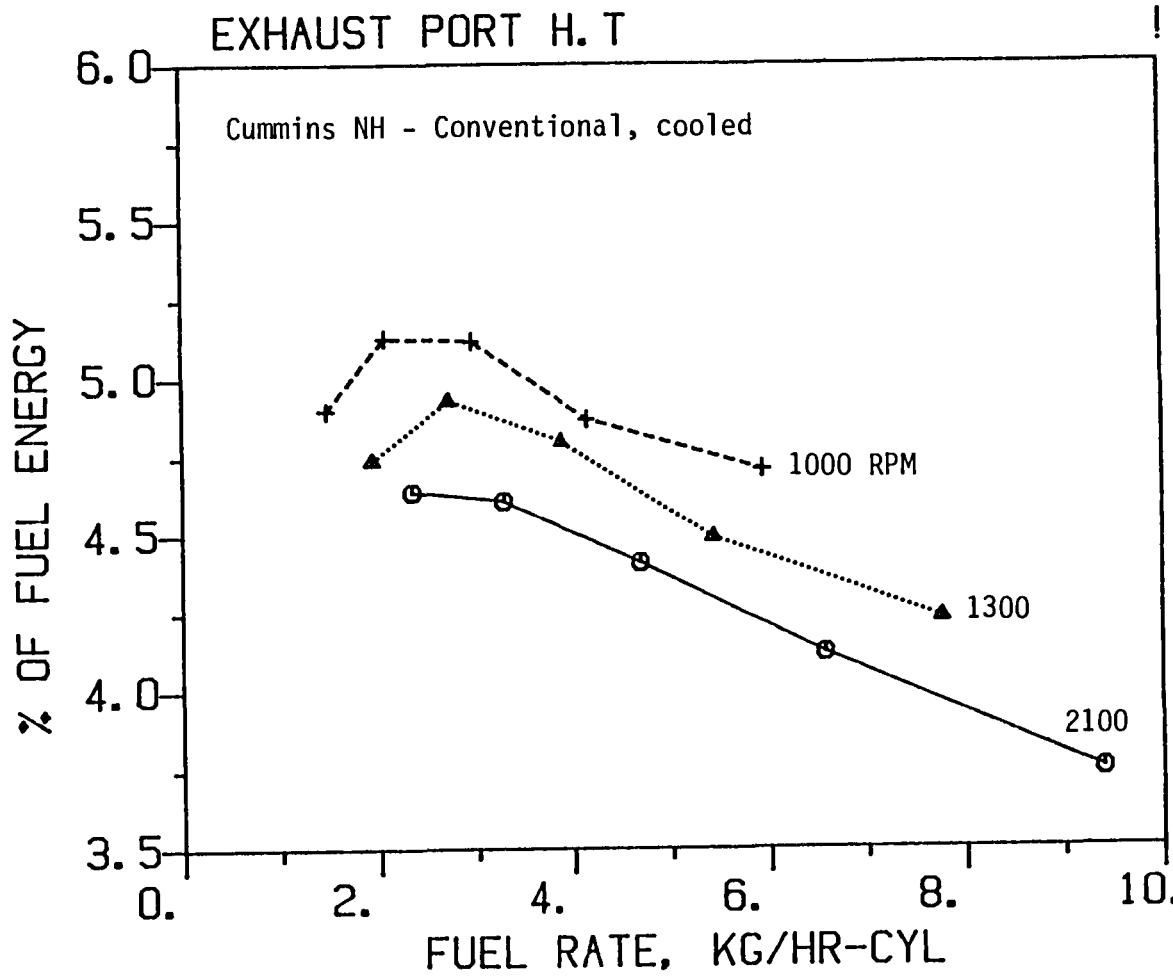

Figure 2-11 Variation with speed and load of exhaust port heat transfer as a fraction of fuel energy (network results).

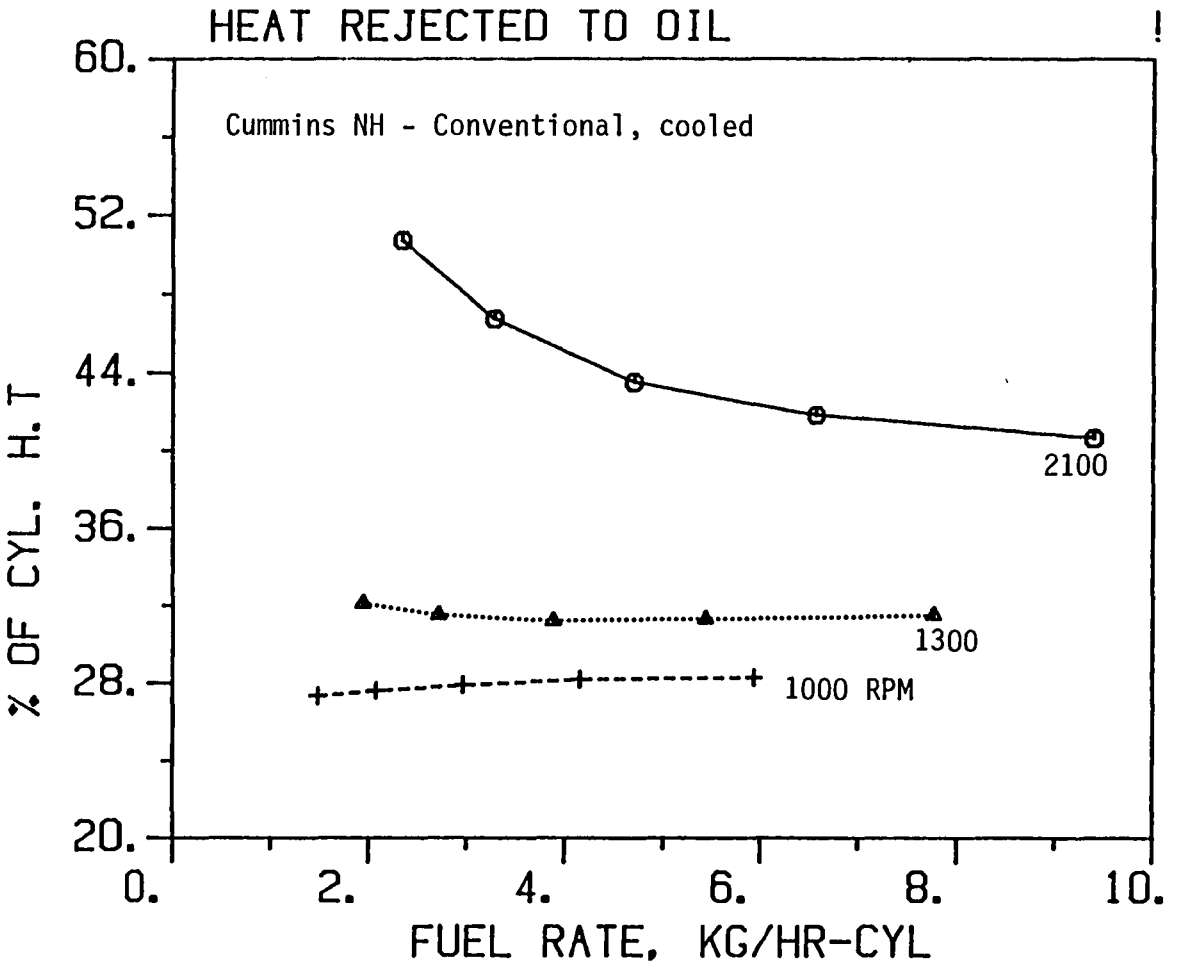

Figure 2-12 Variation with speed and load of the fraction of in-cylinder heat transfer rejected to oil (network results).

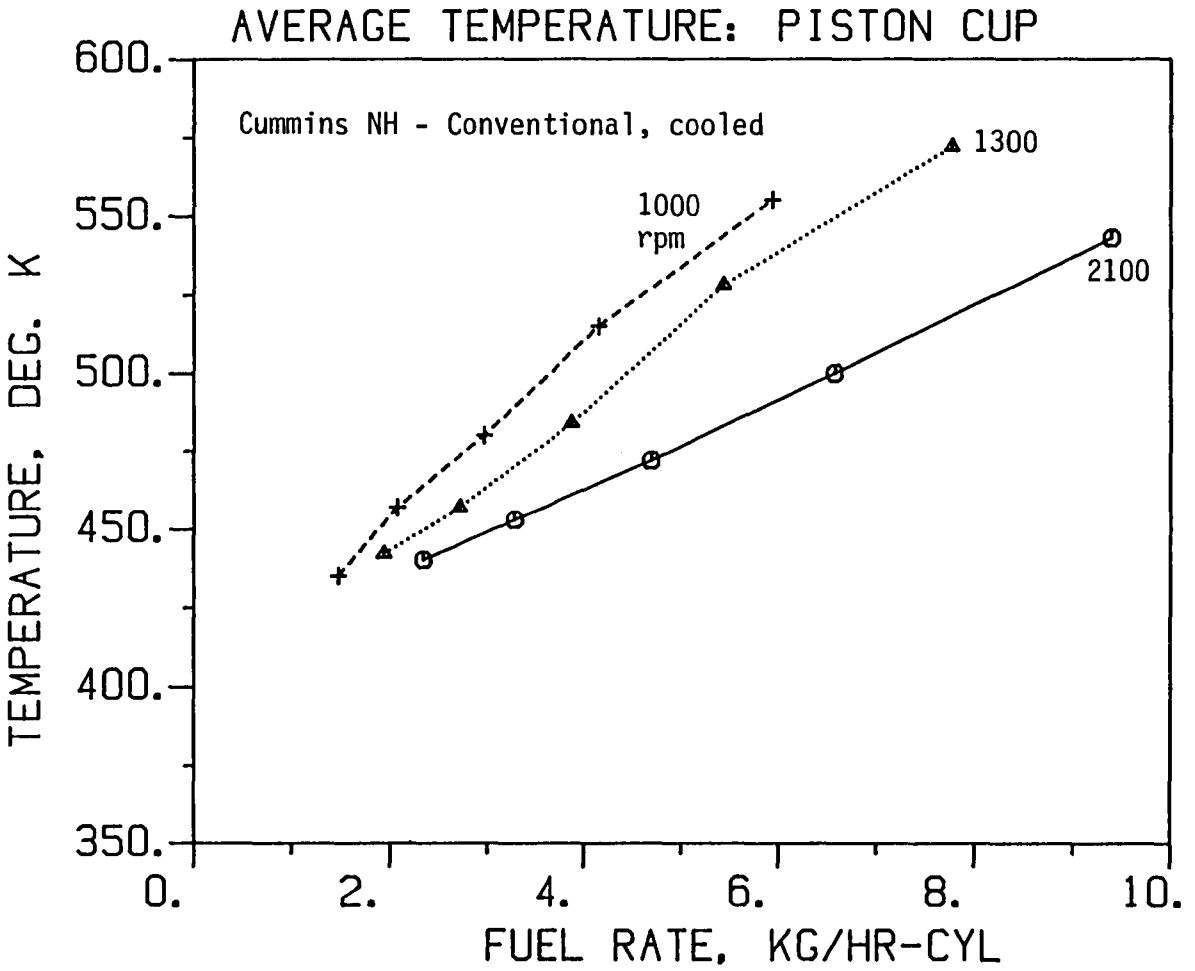

Figure 2-13a Variation with speed and load of network-predicted average temperatures for piston cup bottom, (network results).

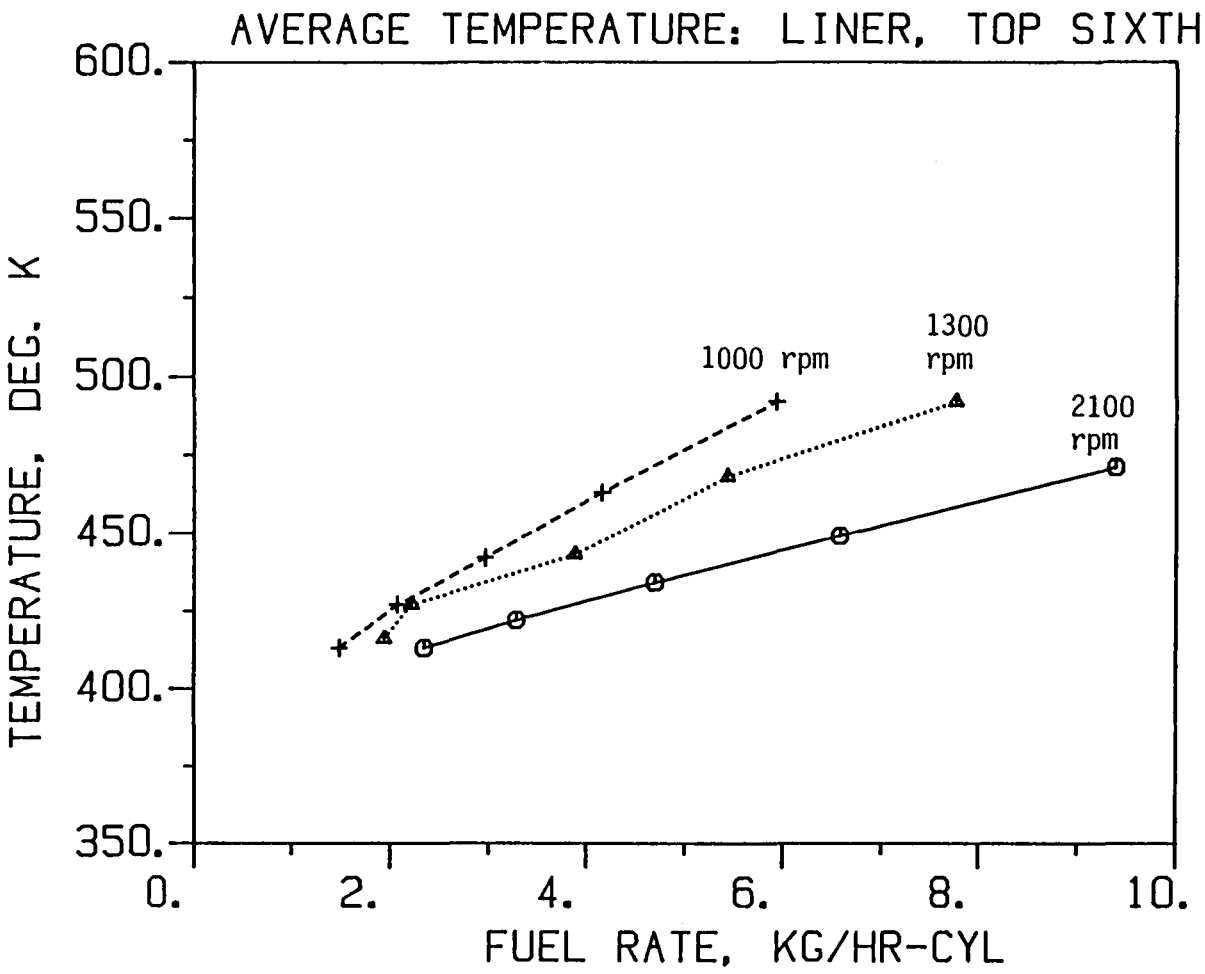

Figure 2-13b Variation with speed and load of network-predicted average temperatures for top sixth of exposed portion of liner.

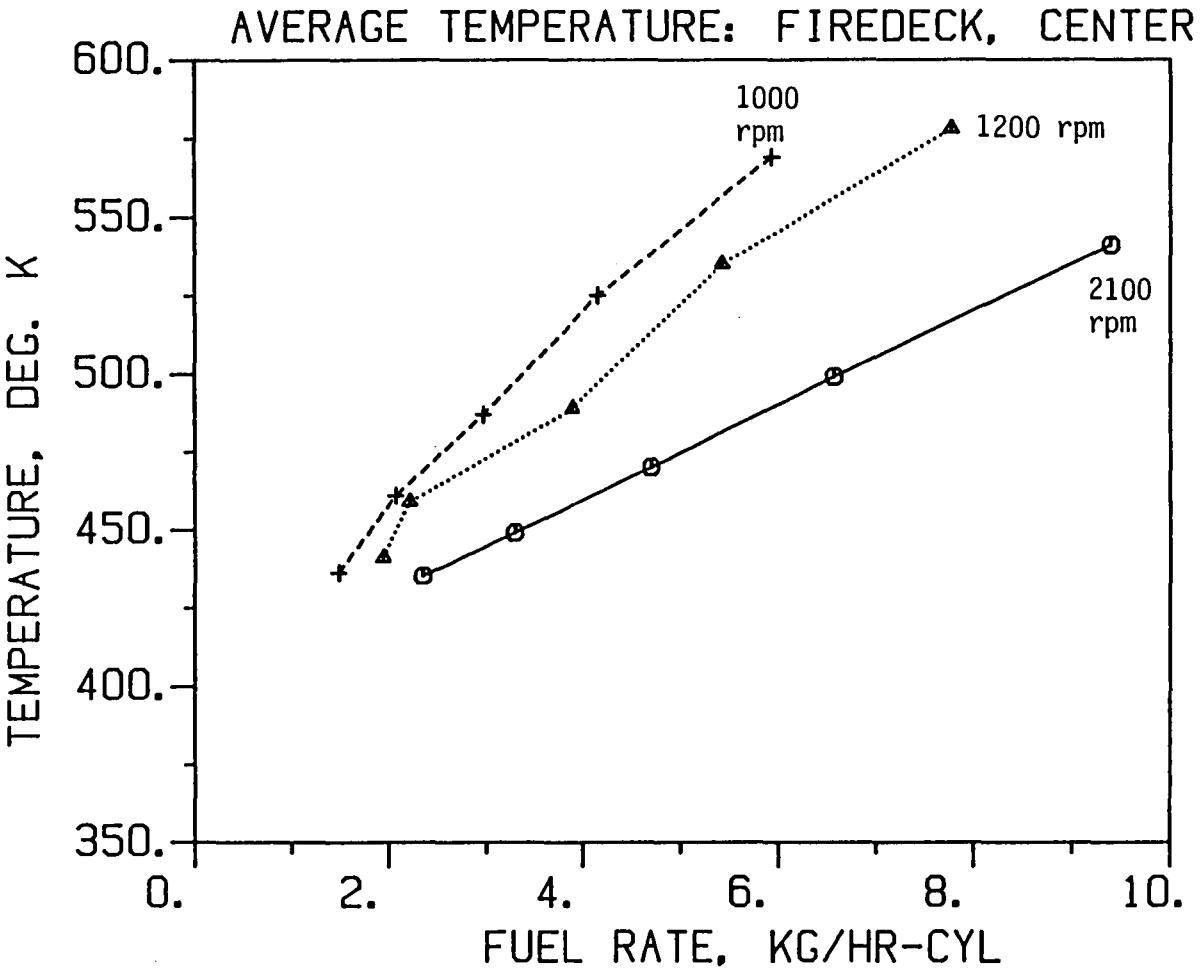

Figure 2-13c Variation with speed and load of network-predicted average temperatures for the firedeck central area.

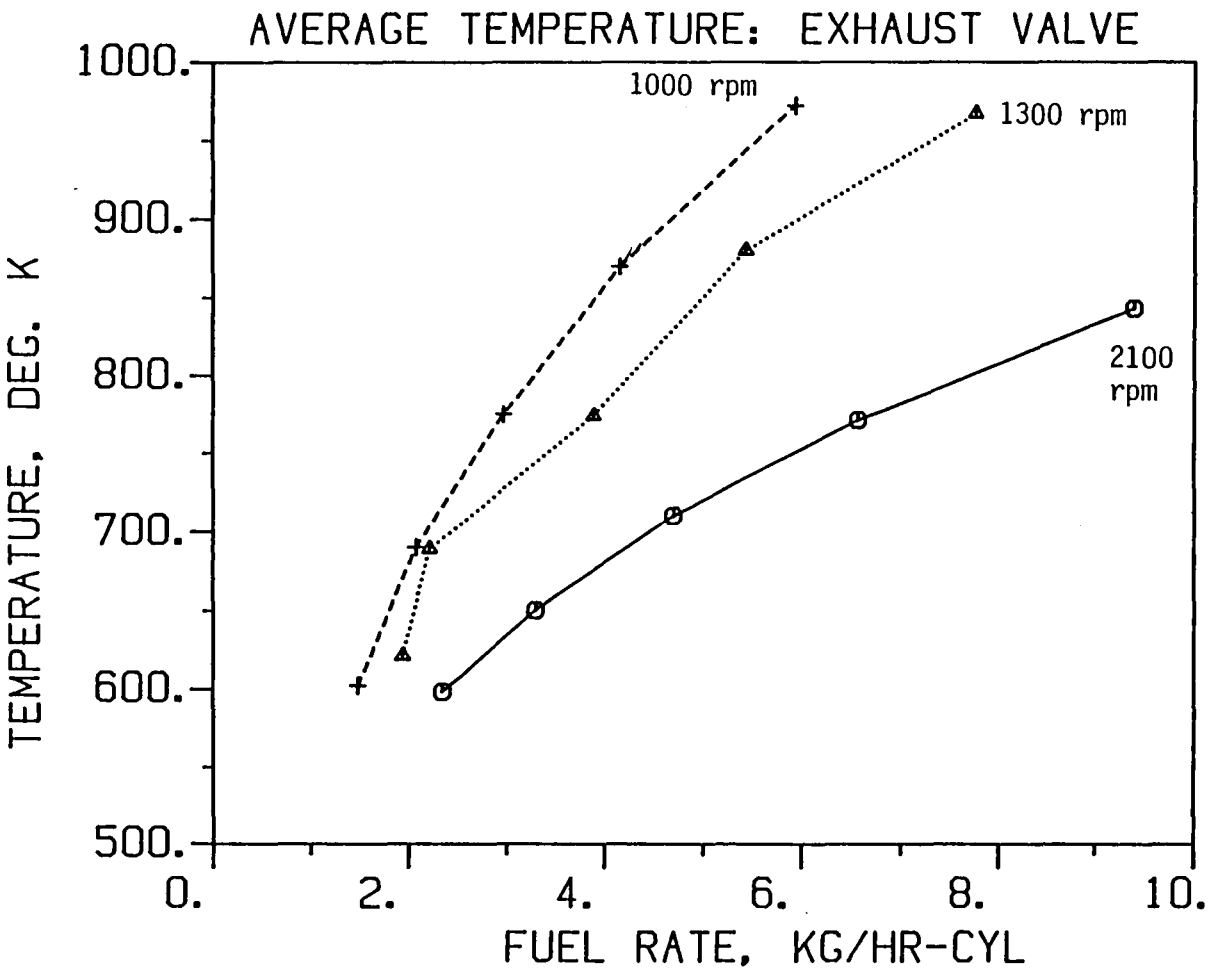

Figure 2-13d Variation with speed and load of network-predicted average temperatures for the exhaust valves.

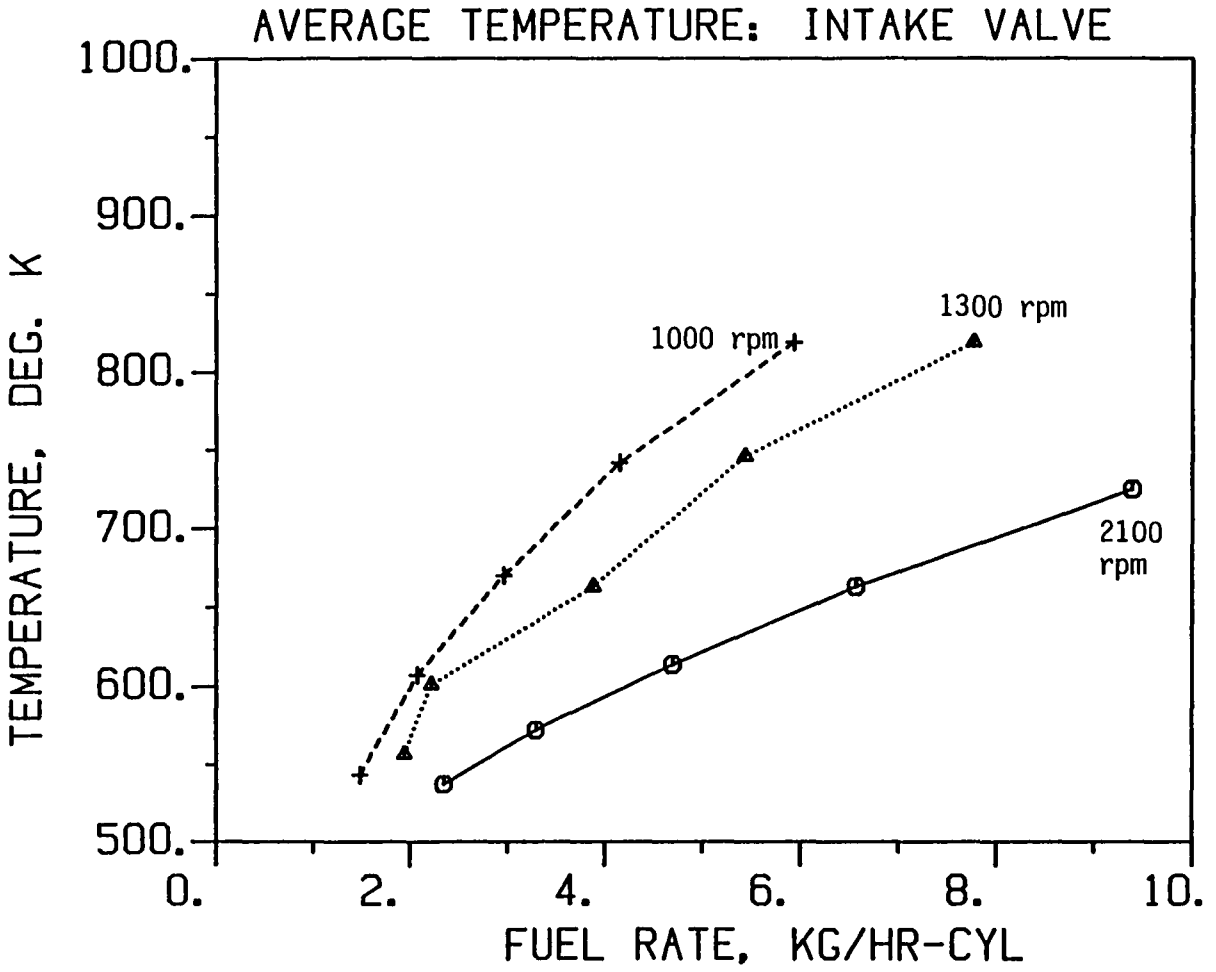

Figure 2-13e Variation with speed and load of network-predicted average temperatures for the intake valves.

work to represent thermal barrier layers on combustion chamber surfaces. Effects on surface temperatures as well as on heat transfer rates and on heat balance were investigated. The three levels of progressive thermal insulation were: a) conventional metallic engine (aluminum piston); b) insulated engine with components, including liner, insulated with 1.5 mm of zirconia plasma sprayed (ZPS) with k = 0.6 W/mK; c) superinsulated engine with all components including liner made of a hypothetical, very low conductivity material with k = 0.01 W/mK. The cooling of the structure was reduced for the insulated and superinsulated configurations by decreasing heat transfer coefficients on the coolant side of the structure. Oil heat transfer coefficients were kept constant.

Variation of various component temperatures with load at the three levels of thermal insulation is shown in Figure 2-14(a)-(e). ZPS insulation raises component surface temperatures by 100-500^{o}K depending on load and the particular component, with head (firedeck) and piston temperatures being affected the most. Effects on valve and liner temperatures are somewhat lower. For the liner this is due to lower effectiveness of ZPS as a thermal barrier on the liner, caused by the heat flow path to the oil coolant through the reciprocating piston which exists in both the metallic and ZPS cases. This is seen in Figure 2-15 where the effect of ZPS on heat transfer reduction at various load levels is documented separately for individual components. The effectiveness of the liner insulation is less than that of the piston and firedeck at intermediate and high loads. This lower insulation effectiveness, combined with adverse effects of high liner temperatures on volumetric efficiency and the lubrication of the piston liner interface, make liner insulation a questionable strategy. This issue is further discussed in Chapter III. Figure 2-16 shows effects of liner insulation on top compression ring face temperature, for the insulated and superinsulated configurations above. It can be seen that liner insulation increases very significantly the ring face temperature compared to the baseline. By contrast the configuraton with insulated piston and cooled liner actually have lower ring temperatures than the baseline due to the reduced heat flux into the piston.

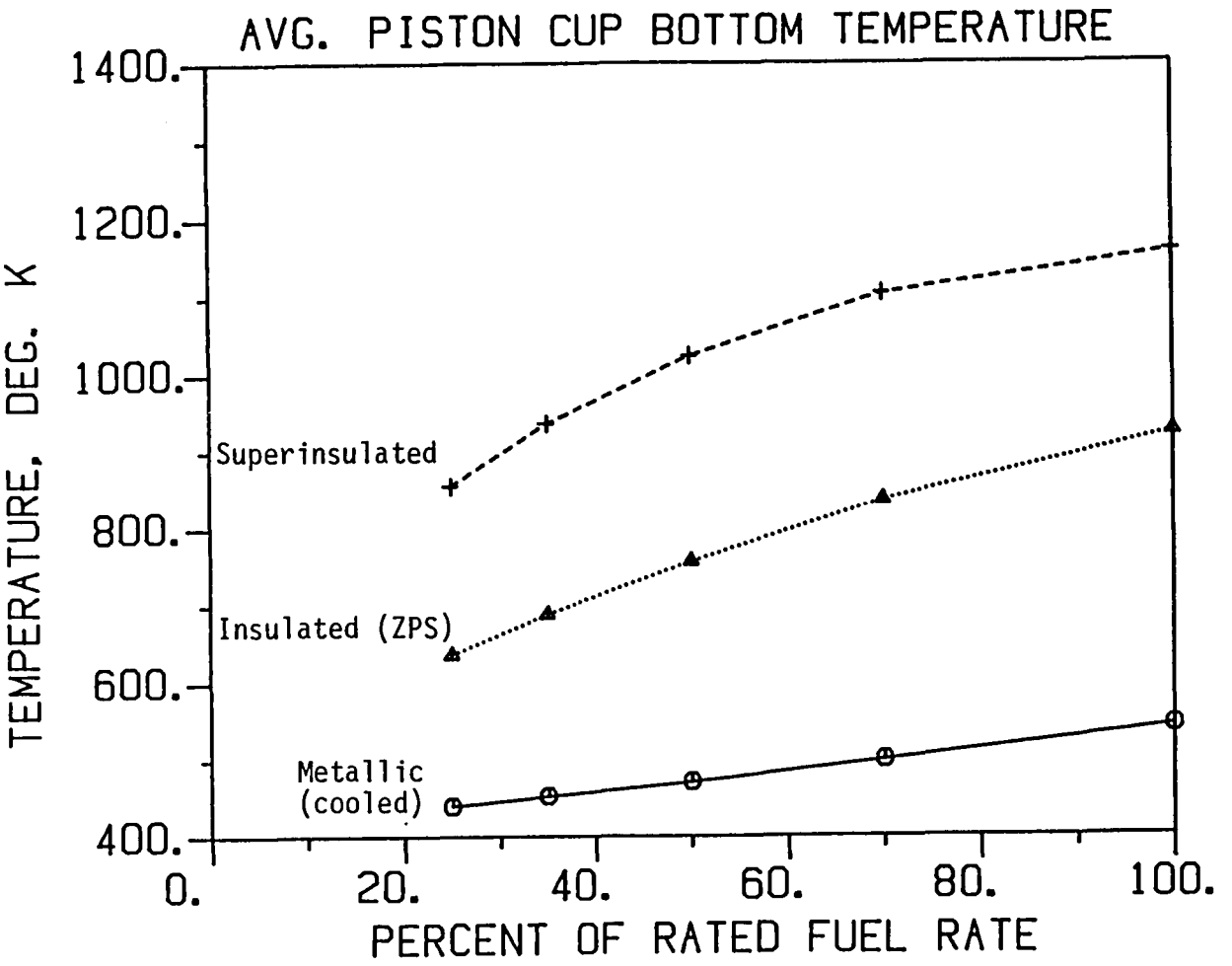

Figure 2-14a Effects of load and insulation on average piston cup floor temperature, 2100 rpm.

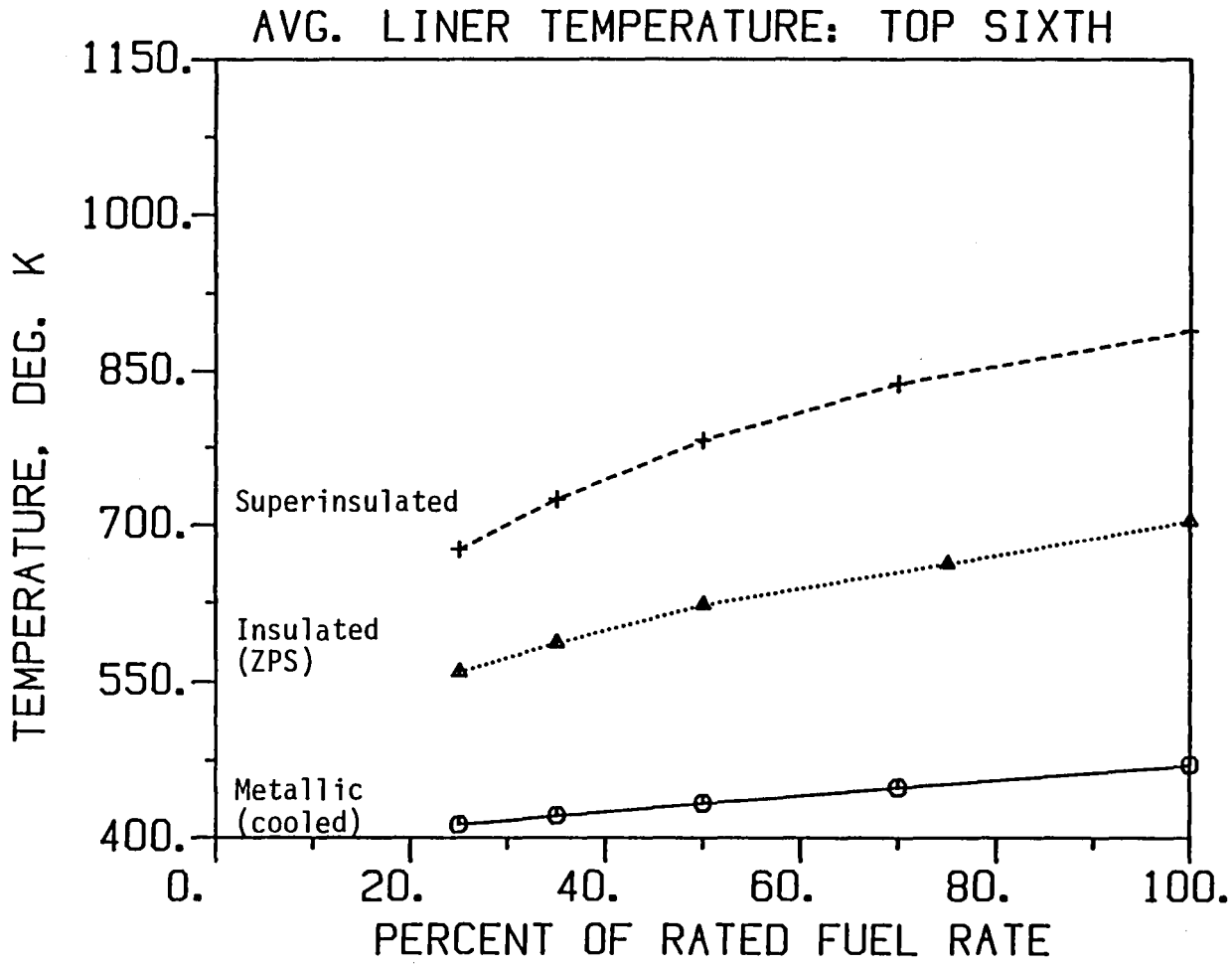

Figure 2-14b Effect of load and insulation on average temperature of top sixth of liner, 2100 rpm.

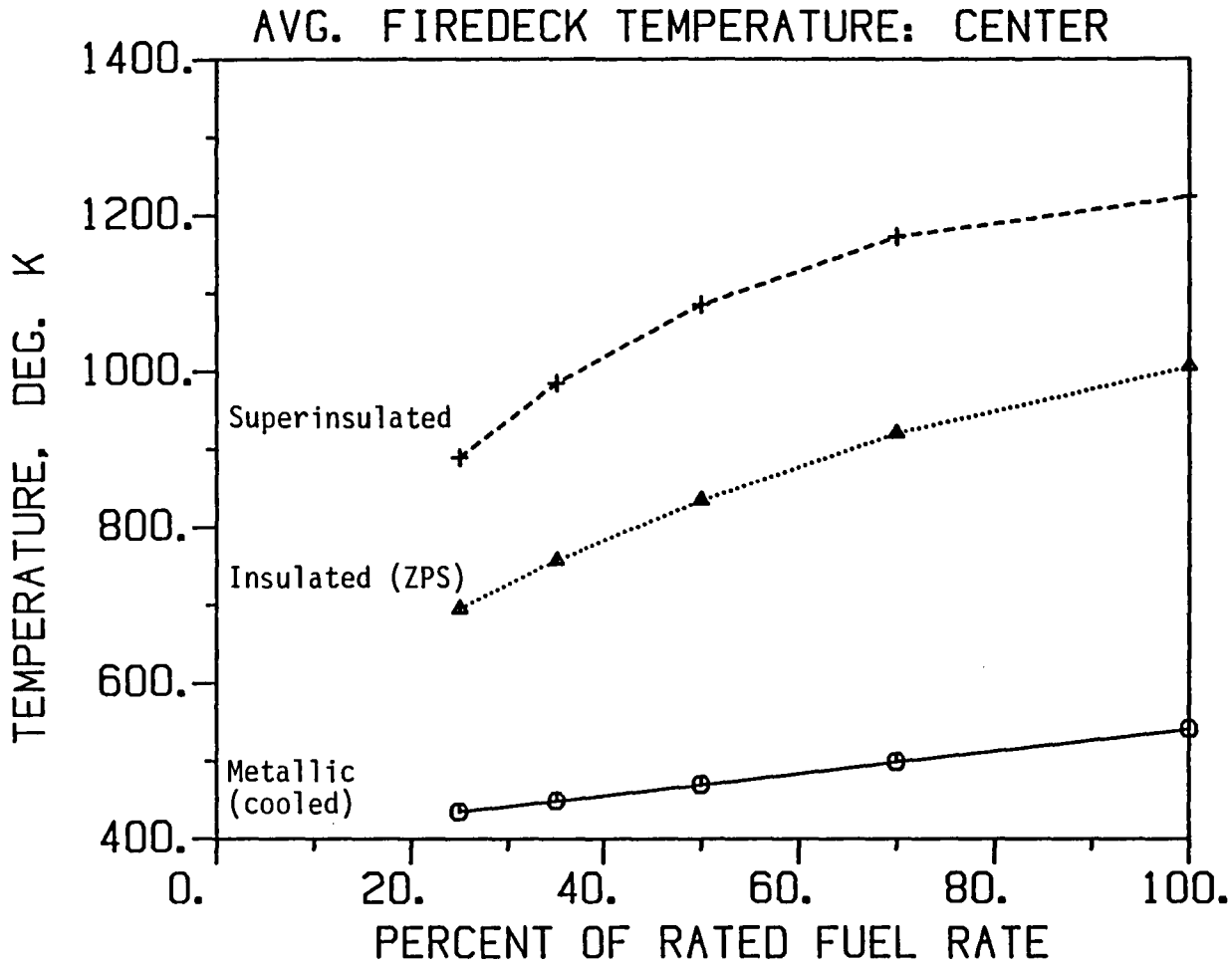

Figure 2-14c Effect of load and insulation on firedeck center temperature, 2100 rpm.

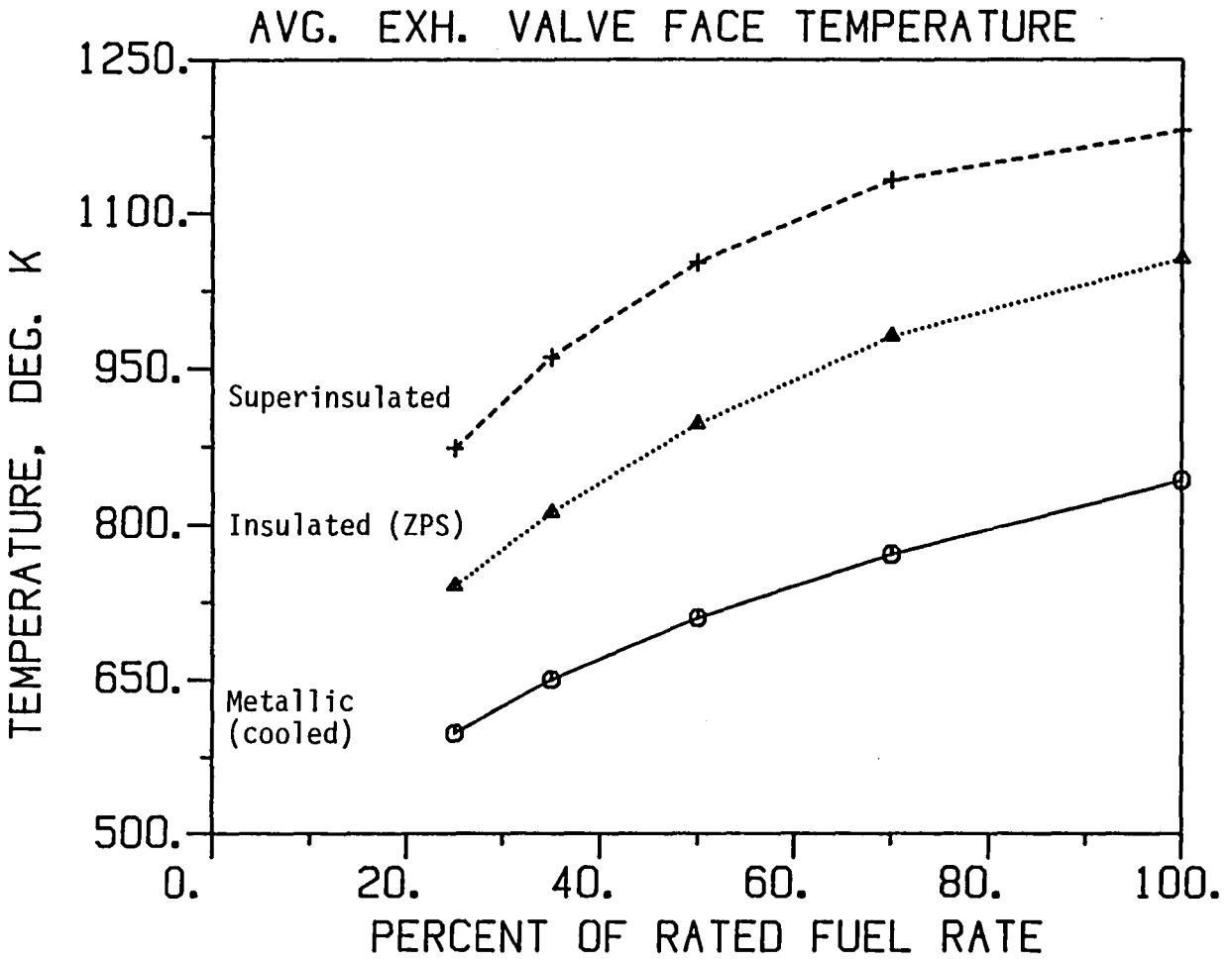

Figure 2-14d Effect of load and insulation on exhaust valve temperature, 2100 rpm.

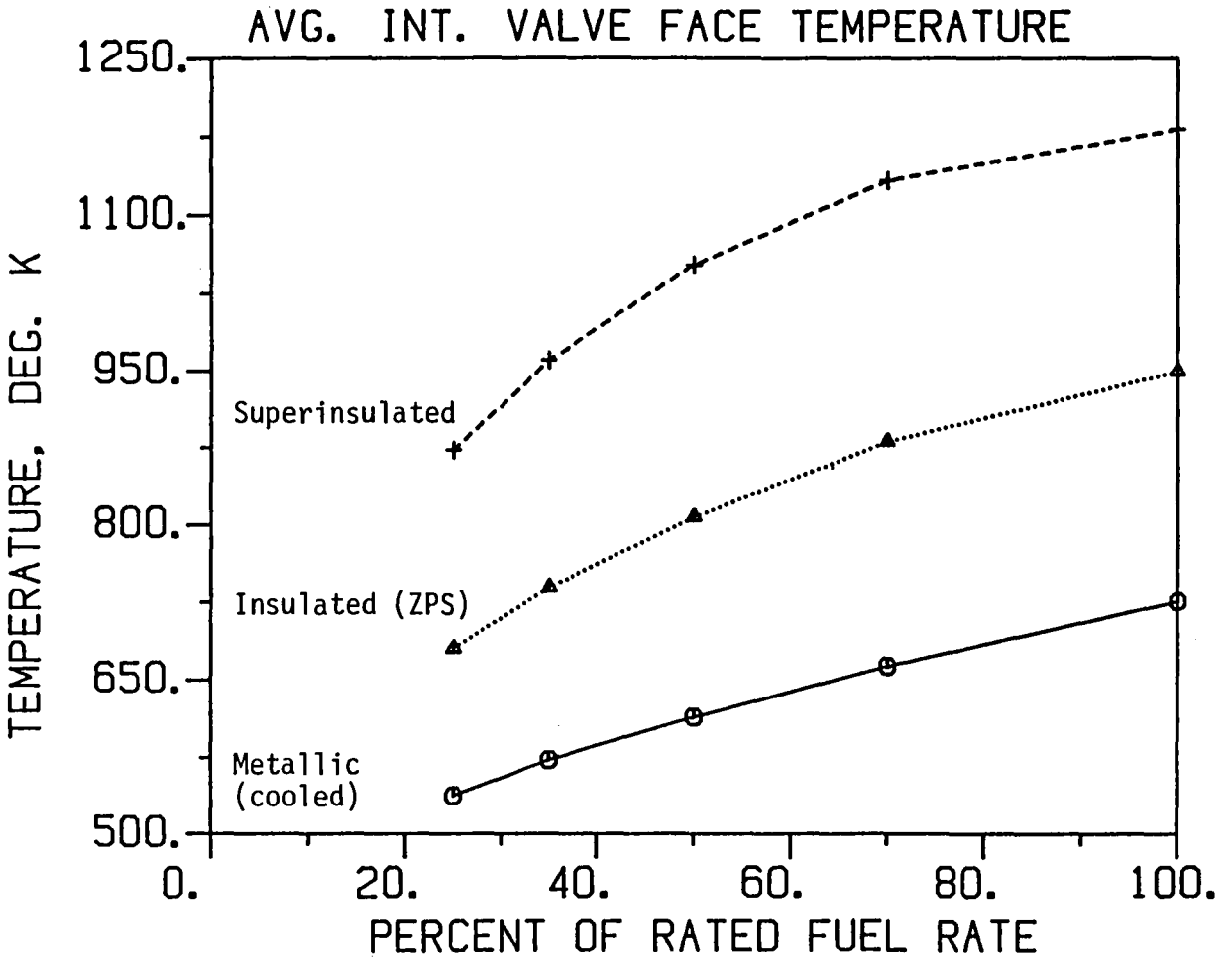

Figure 2-14e Effect of load and insulation on intake valve temperature, 2100 rpm.

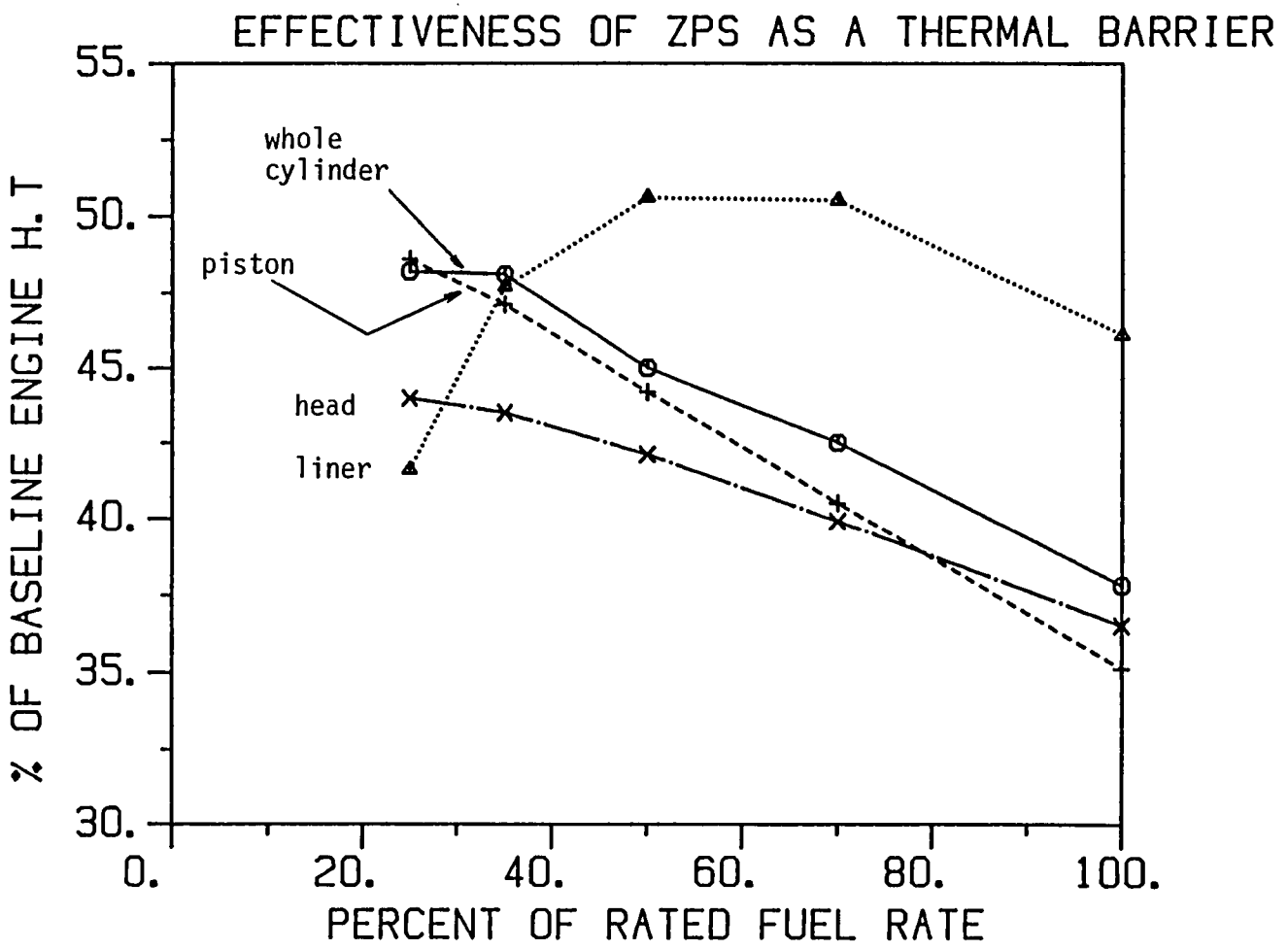

Figure 2-15 Heat transfer reduction due to ZPS insulation (1.5 mm coating) on various combustion chamber surfaces: effect of load.

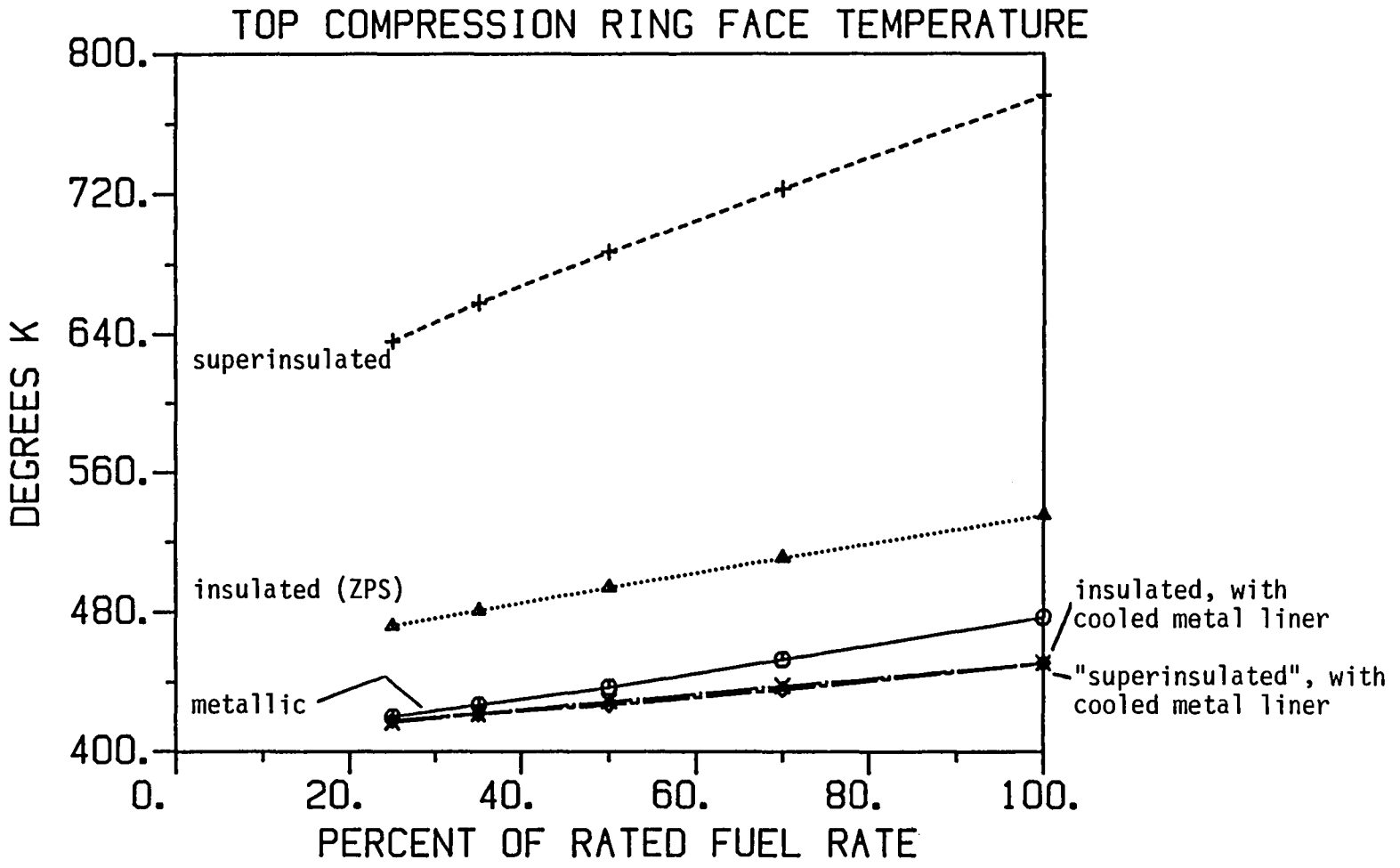

Figure 2-16 Top compression ring face temperature: effect of insulation and load.

The effect of insulation on in-cylinder and on exhaust and intake port heat transfer rates is given in Figure 2-17 and 2-18. For the metallic and insulated configurations, gas-wall heat exchange - as a fraction of fuel energy - increases with decreasing load for the cylinder as well as intake and exhaust ports. Heat exchange also decreases with progressive insulation. The increase in intake port heat transfer with ZPS insulation is the exception and is caused by reduced cooling and higher intake port wall temperatures. Heat transfer is near-zero on all the surfaces of the superinsulated configuration except the liner, where the balance of the deposited (positive) radiant and (negative) convective heat transfer rate result in a small negative overall cylinder net heat transfer rate, implying the transfer of frictional heat to the combustion chamber gases.

An important effect of insulation is on the main heat paths. This is seen in Figure 2-19, displaying the effect of load and insulation on heat rejected to oil. ZPS insulation increases heat rejection to oil due to the shifting of part of the liner thermal load, including friction heat, to the oil, through the path in the piston structure. For the superinsulated configuration this path is removed due to a non-conducting piston; a new higher-resistance path through the piston-liner moving interface is established and heat rejection to oil decreases to levels close to those in the cooled case.

Finite Element Results

Using the finite element model of the NH engine component geometries and the FEM heat transfer methodology described above, a study of effect of load (at rated RPM) on component temperatures, was conducted for the baseline metallic engine. Of interest in this study were peak temperatures as well as temperature and heat flux distributions. Figure 2-20 shows variation with load of peak temperatures on gas side surfaces of various components exposed to combustion gases. The variation for each component reflects the resistance of the gas-coolant heat path through the component, as well as the geometry. As expected, peak surface temperatures are higher for components not directly cooled, such

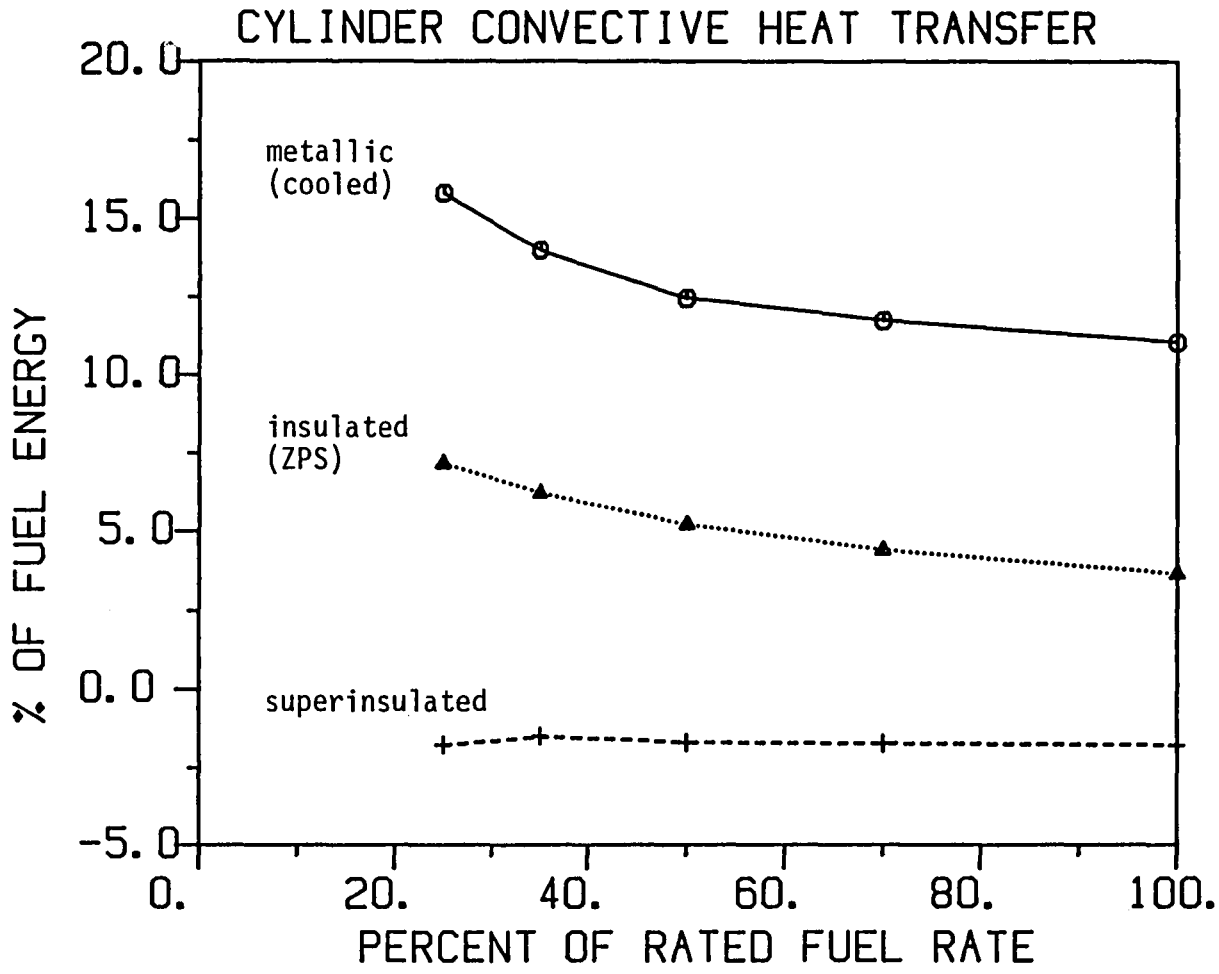

Figure 2-17a Effect of load and insulation on cylinder convective heat transfer as a fraction of fuel energy.

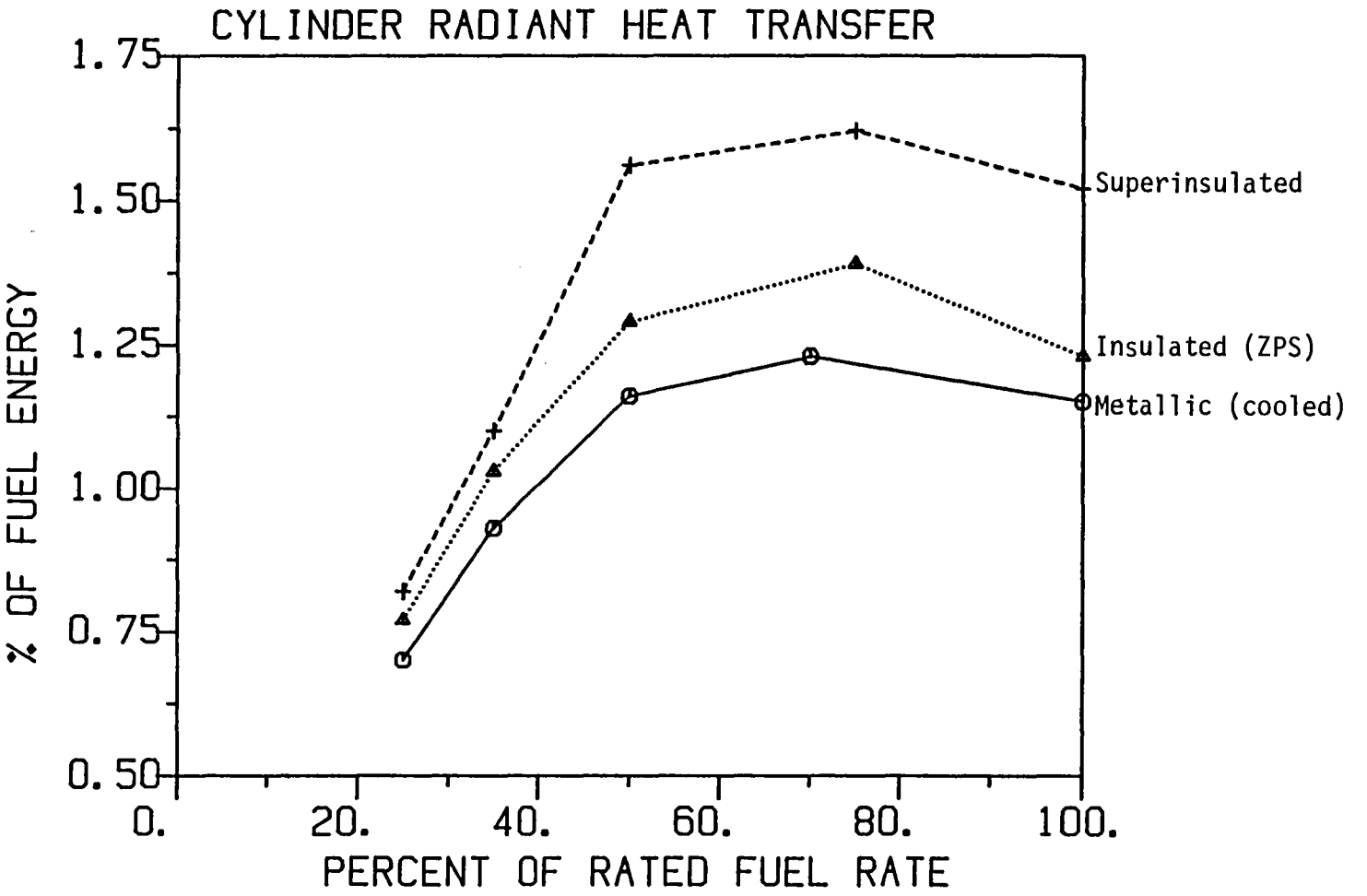

Figure 2-17b Effect of load and insulation on cylinder radiation heat transfer as a fraction of fuel energy.

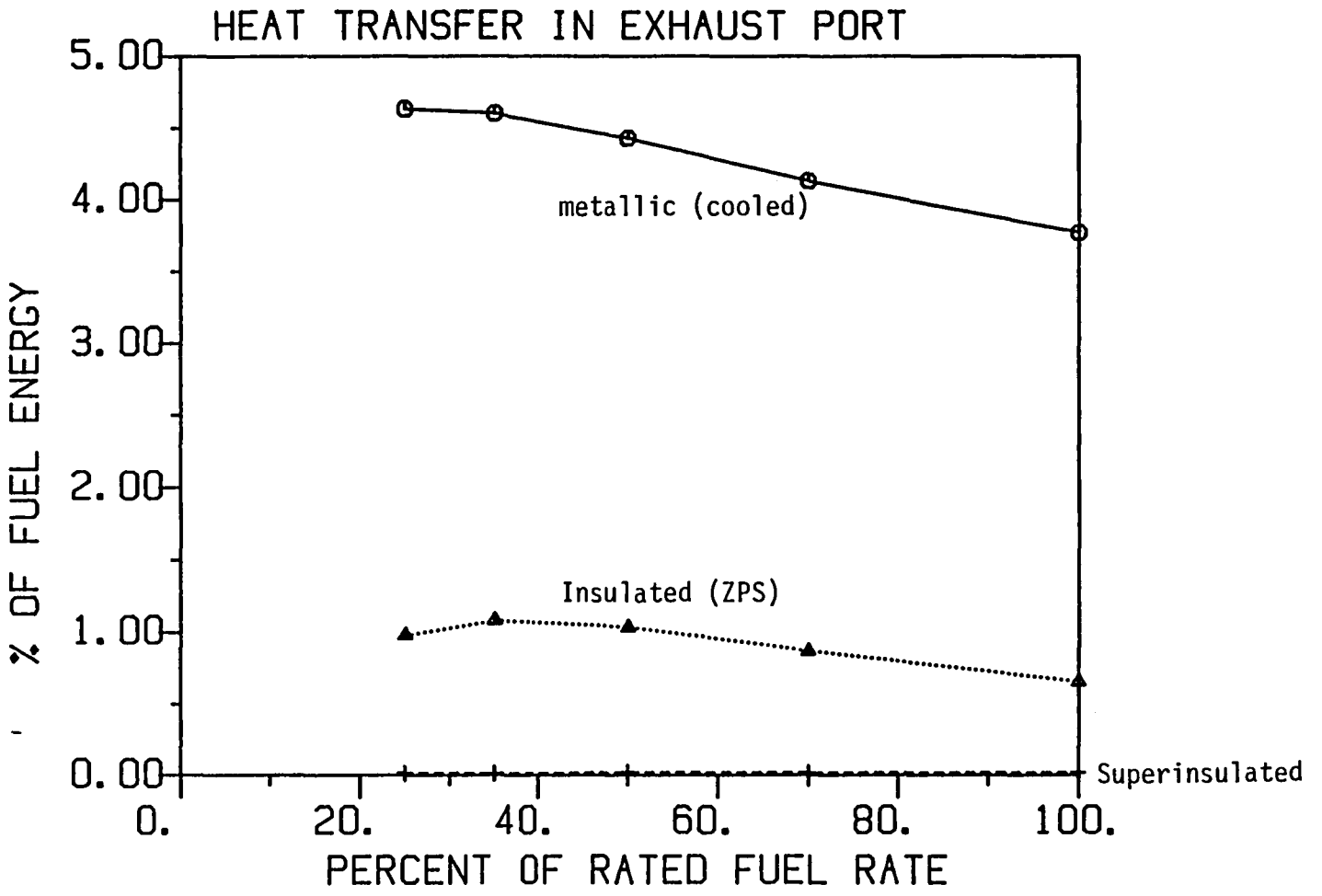

Figure 2-18a Effect of load and insulation on heat transfer in the exhaust as a fraction of fuel energy.

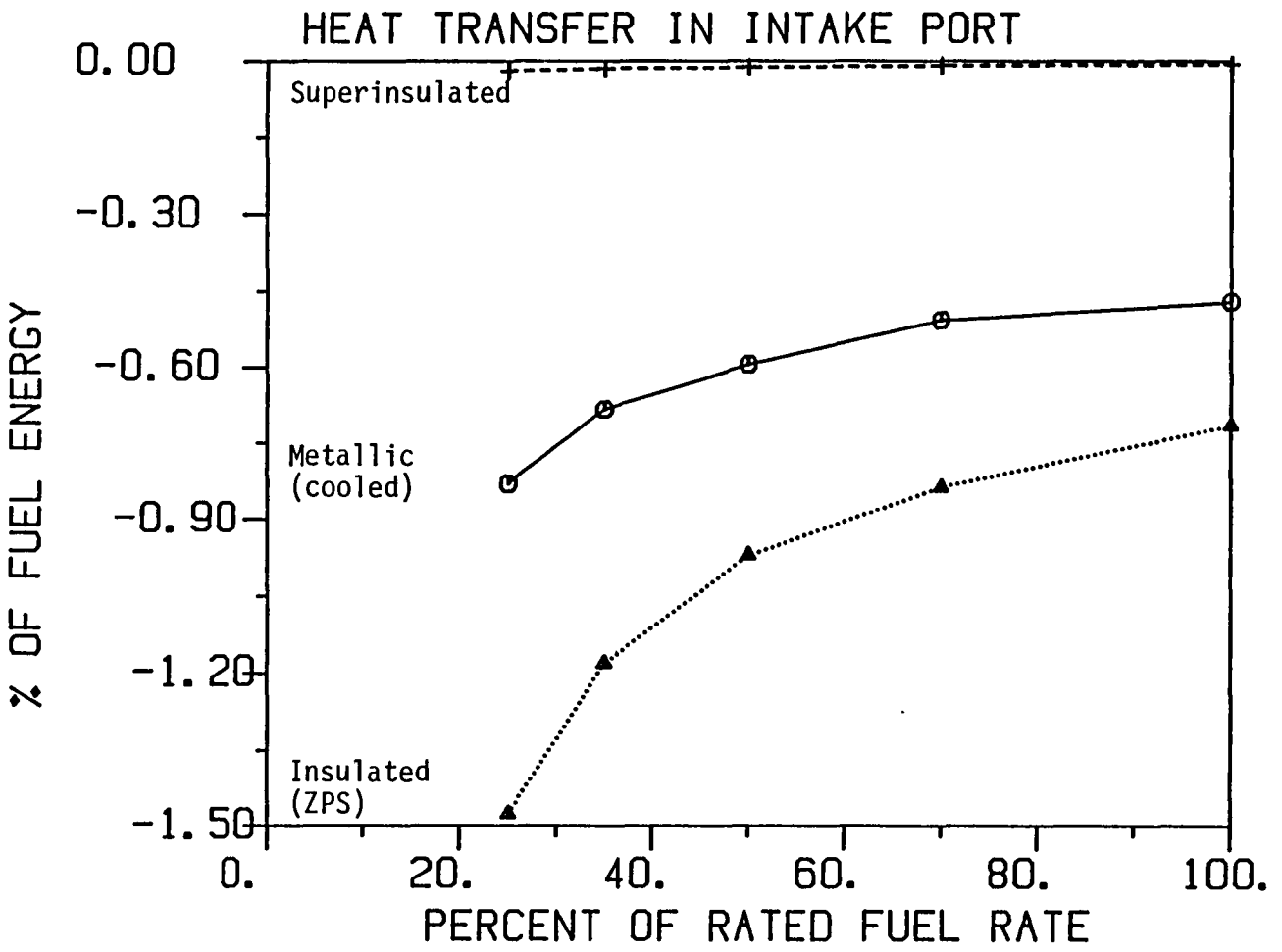

Figure 2-18b Effect of load and insulation on heat transfer in the intake port as a fraction of fuel energy.

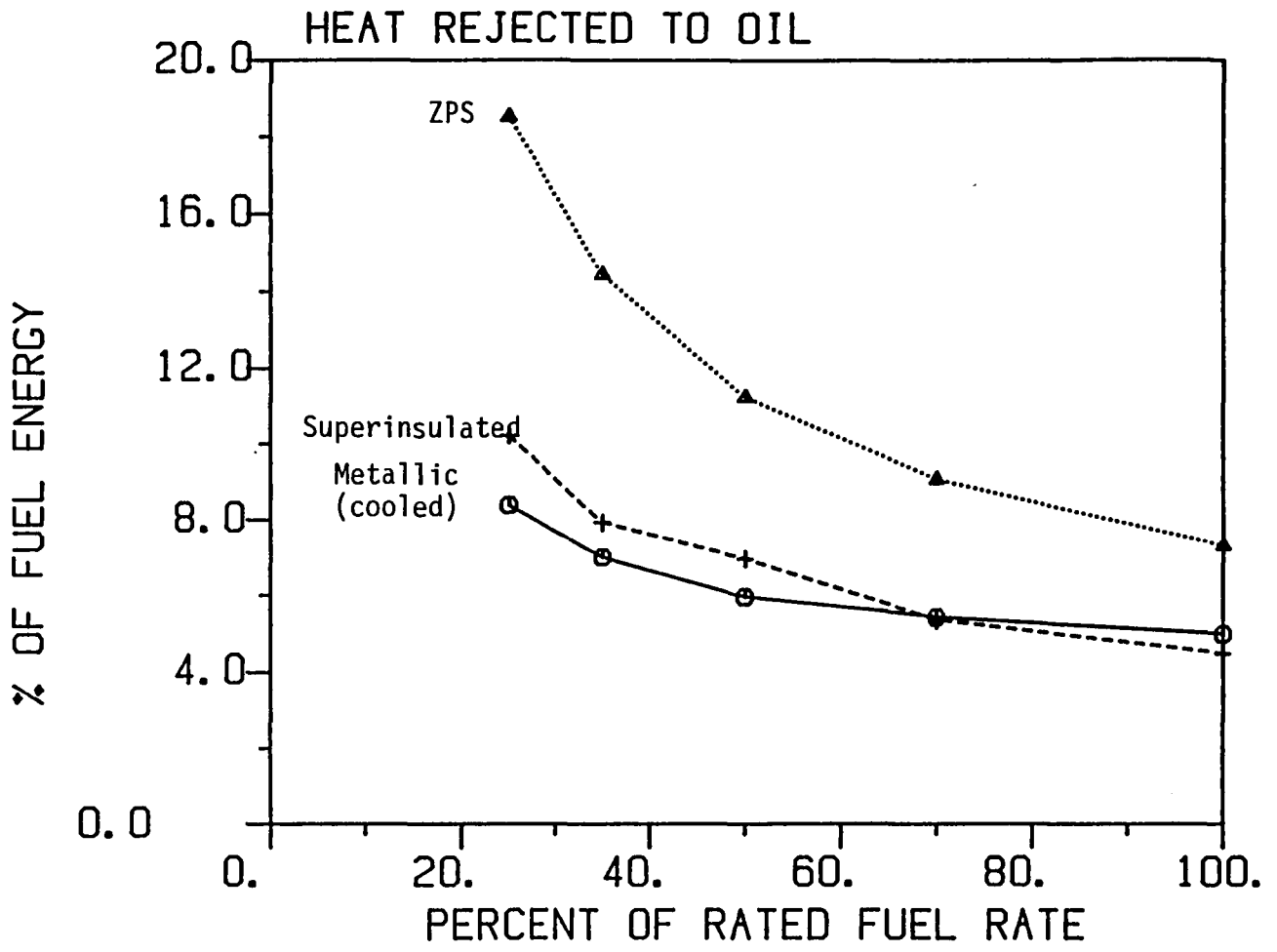

Figure 2-19 Effect of load and insulation of heat rejected to oil as a fraction of fuel energy.

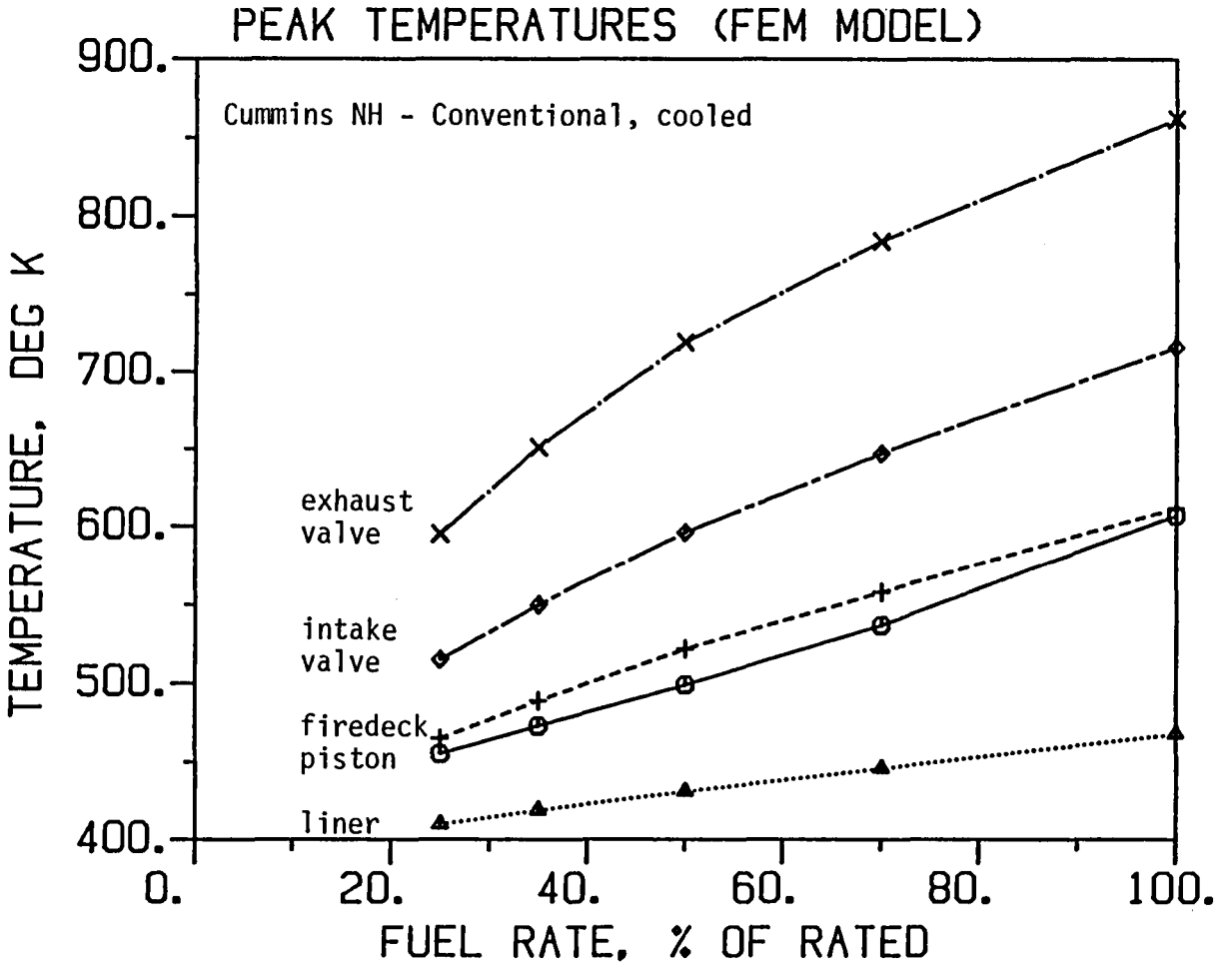

Figure 2-20 Variation of peak (FEM) component temperatures with load, 2100 rpm.

as valves and lowest for the liner, which has a large cooled area. The sensitivity to load (slopes of the curves) decreases with increasing load for most of the components, except the piston.

Differences between temperatures averaged from FEM distributions and the single network temperatures for various regions are given in Figure 2-21, which shows that they tend to increase with load. These differences are not large, indicating that the network representation gives a good estimate of the average conditions. The FEM of course provides more detail, including the temperature distribution in each region. Taking a difference between the peak steady-state temperature in a given region from the FEM solution and the single network temperature which is in effect the region average, one obtains an idea of the temperature distribution resolution that is lost in the network approach, as documented by Figure 2-22. Large differences on the piston are due to high temperatures on the conical protrusion in the cup. On the firedeck, large mean-to-peak temperature differences reflect local contacts with valves and variations of cooling rate on the coolant side.

Variation of piston temperature profiles with load is shown in Figure 2-23. The same contour levels (spread $10^{o}K$ apart) have been used for all load levels so as to maintain a basis for comparison of gradients. The temperature at the tip of the central conical protrusion in the cup is shown to increase much faster with load than average piston crown temperature. While it is only about $10^{o}K$ higher than the latter for 25% load, it is as much as $60^{o}K$ higher for full load. The direction of heat flow (indicated by the angle of the normals to contour lines) also varies with load, so as to become more radial with increasing load. This is supported by integrated heat transfer rates from the same study, which indicate that the fraction of heat deposited on the piston that is rejected to oil (largely at the underside of the piston) decreases by 20% with increasing load within the load range studied. This is due to an increase with load in the temperature difference at the piston-liner interface, caused by the relative insensitivity of liner temperatures to load; the larger this difference the greater the heat flux from the piston to the liner.

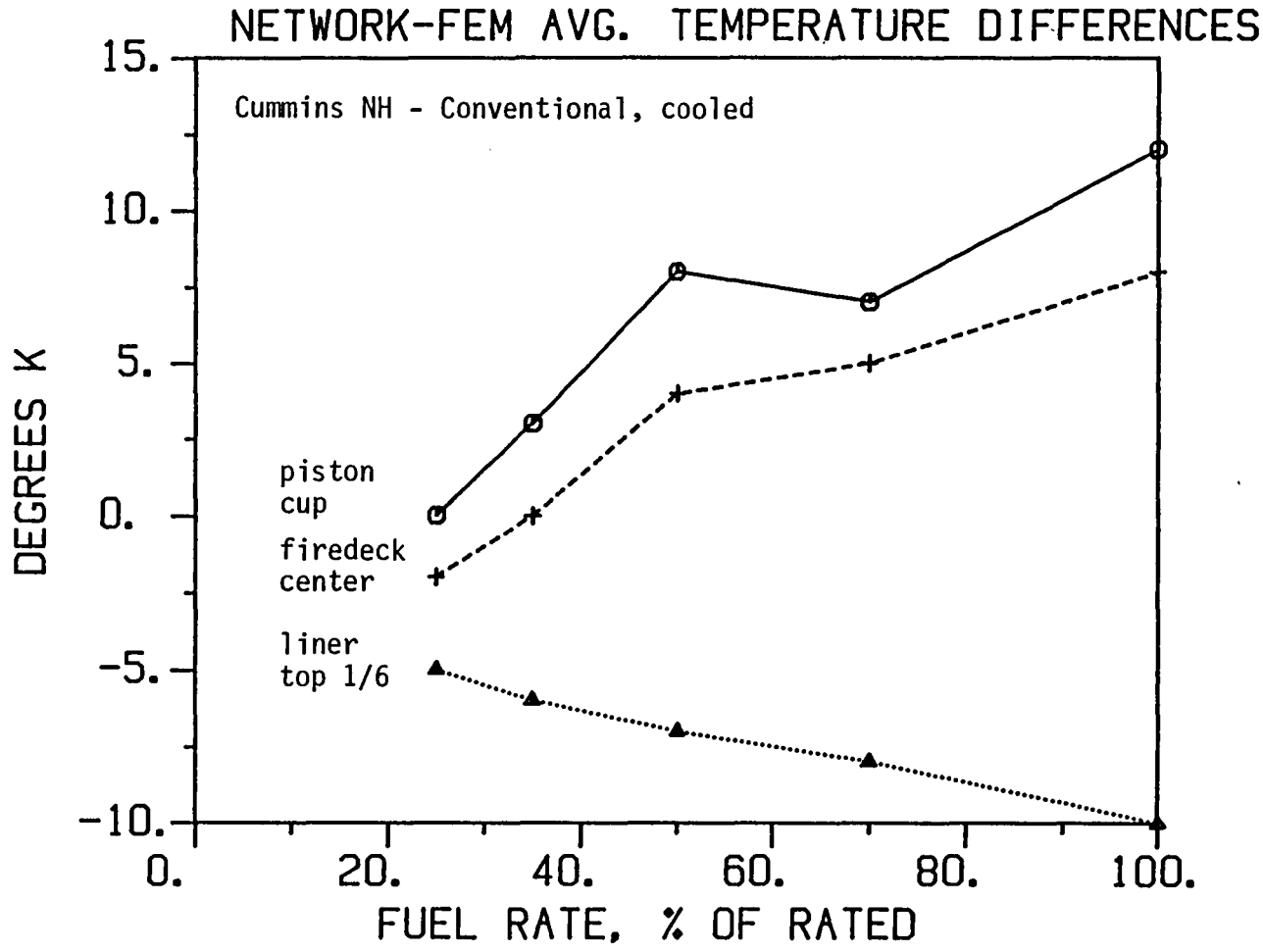

Figure 2-21 Effect of load on difference between FEM and network-predicted average temperatures for selected in-cylinder combustion chamber surfaces.

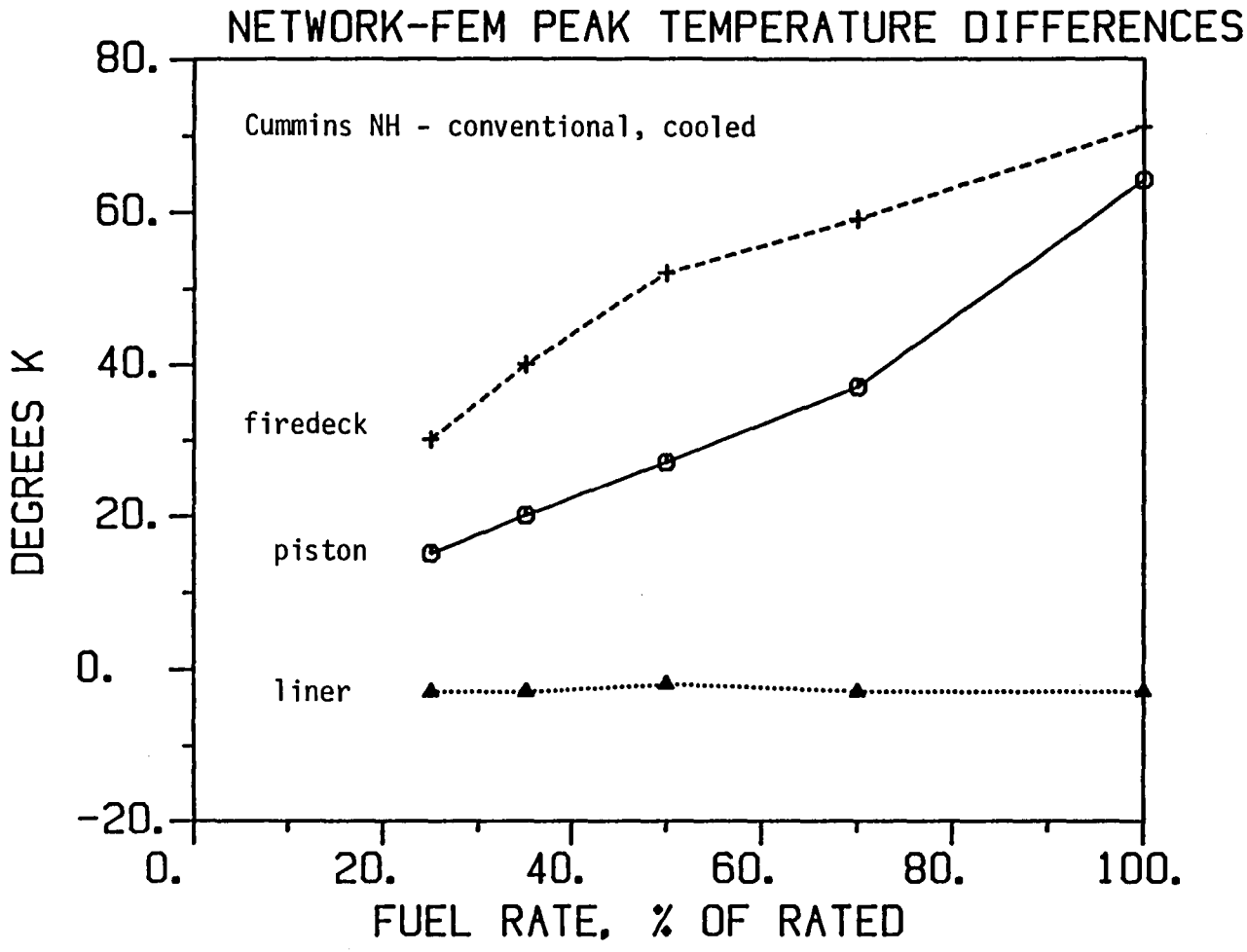

Figure 2-22 Effect of load on differences between peak FEM- and network-predicted temperatures for selected components.

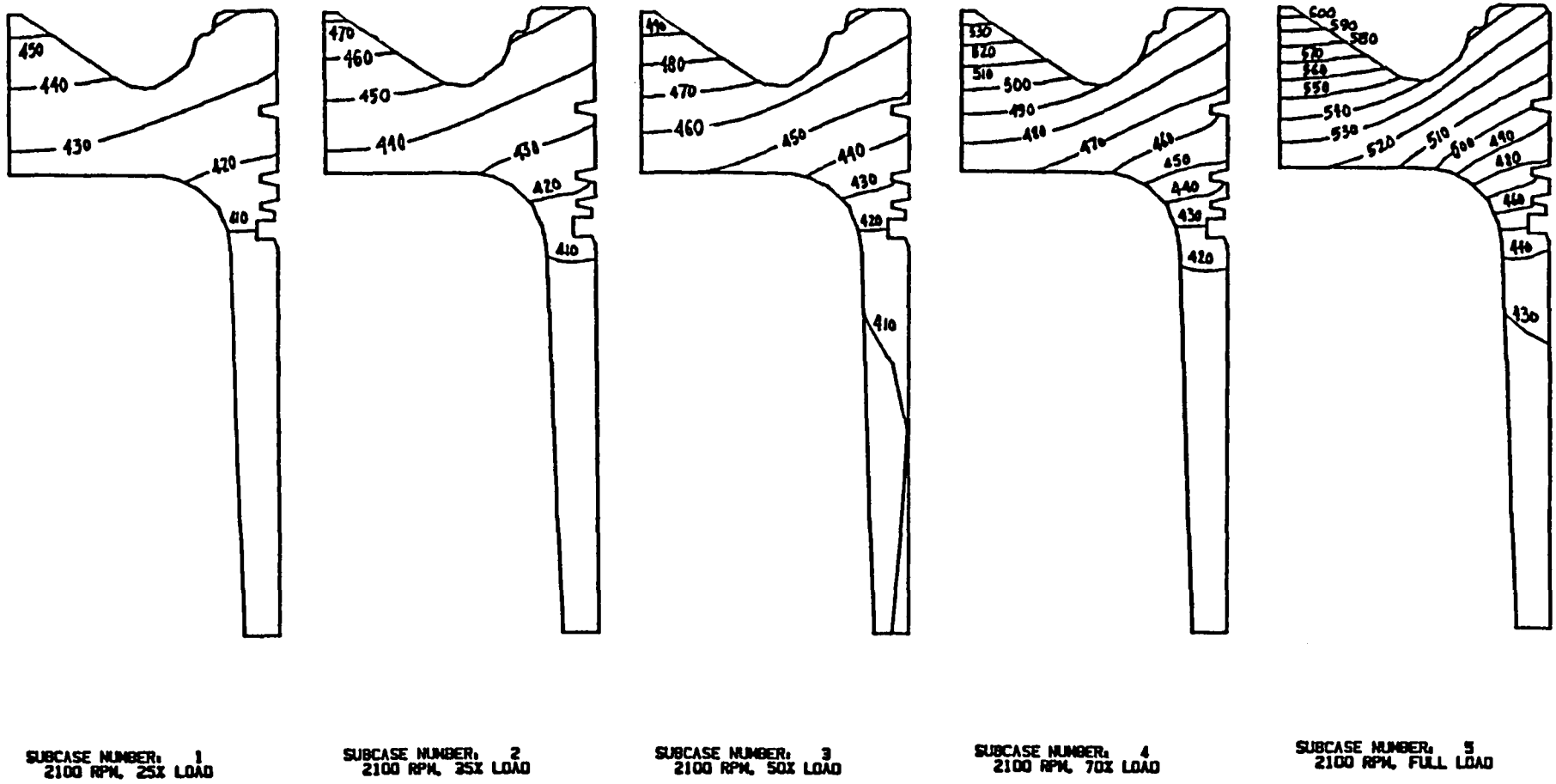

Figure 2-23 Temperature contours (degrees K) for FEM-predicted piston temperature distribution at 25, 35, 50, 70 and 100 percent of full load fuel rate at rated speed (Cummins NH engine; conventional, cooled)

Liner temperature distribution and its variation with load is shown in Figure 2-24. Liner temperature profiles are characterized by a peak temperature just below the portion of the liner permanently exposed to combustion gases, caused by the high thermal load as well as absence of direct cooling in the region. The heat in this region flows down toward the lower (cooled) portion of the liner, sideways to the engine block, and up to the firedeck.

Figure 2-25 shows temperature contours for the gas side surface of the firedeck at the five load levels studied. The difference between the levels of temperature in the intake and exhaust sides is evident in all load cases, with the peak steady-state temperatures always between two valves and typically on the valve seats. Near-peak temperatures also prevail at the center of the firedeck, where presence of the injector jacket prevents direct contact with coolant. Largest gradients are between intake and exhaust sides and also near the liner on the exhaust side. Temperatures, as well as temperature gradients, are lower in a plane 7 mm beneath the exposed surface of the firedeck (Figure 2-26) where effects of local surface load differences and hot valves contacting the seats are attenuated by thermal diffusion.

Variation of temperature distributions in intake and exhaust valves with load is shown in Figures 2-27 and 2-28, respectively. Differences between local temperatures at identical locations on (each of the pair of) intake or exhaust valves were within 5°K. The intake valve is cooled at the seat contact by intake air and also by conduction through the stem and guide. Its temperature is highest at the center of its face exposed to cylinder gas and decreases roughly linearly with distance from the face. The peak temperature is 50-100K higher than peak firedeck temperature, but 70-150K lower than the highest exhaust valve temperature. The latter occurs at the center of the exhaust valve face. Temperature distribution in the exhaust valve is also significantly different from that in the intake valve. The exhaust valve is cooled at the seat contact and by conduction through the stem, but it is heated on its back face by the hot exhaust gases. The result is a large region of near-uniform high temperature at the valve neck, and high

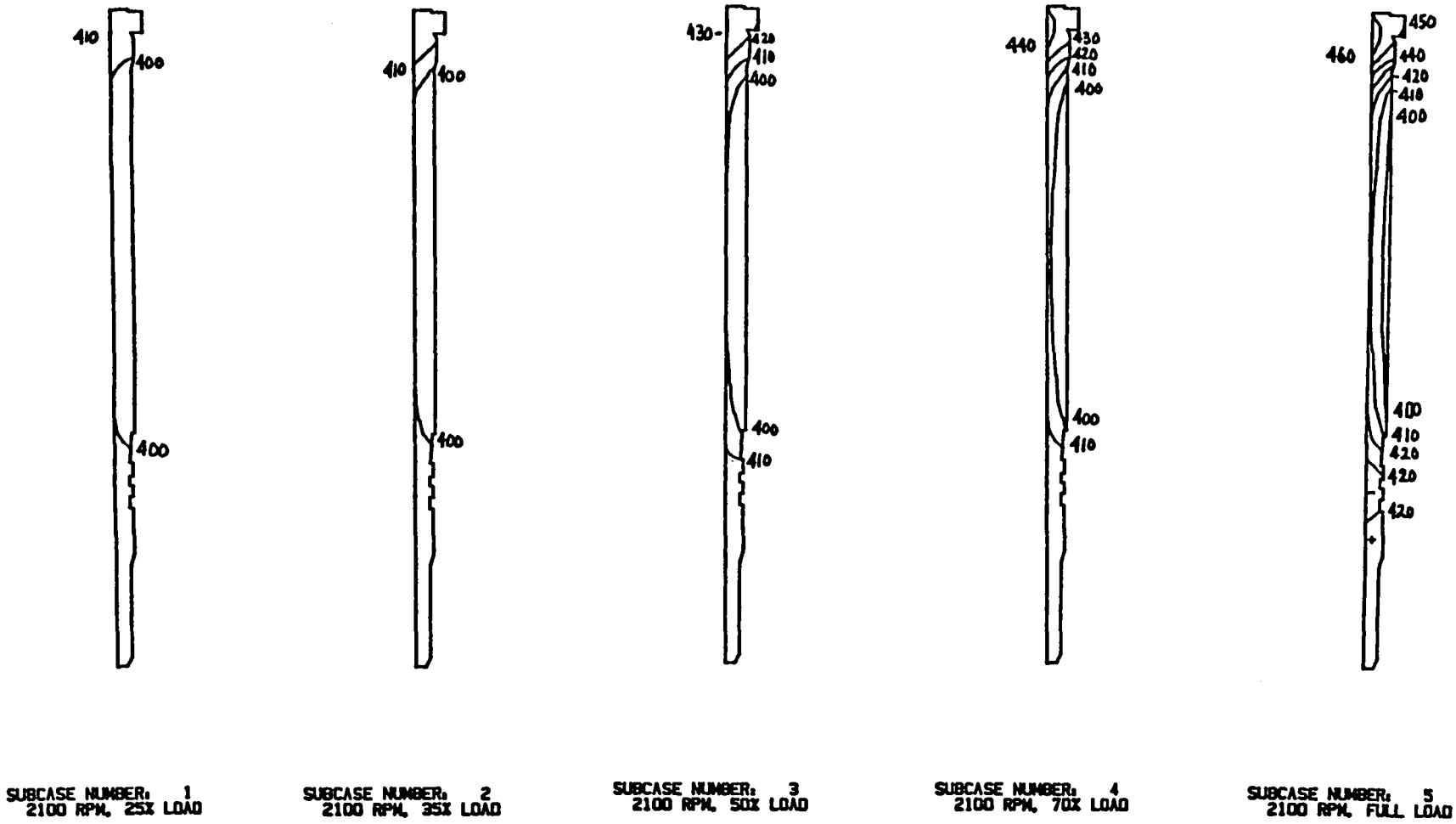

Figure 2-24 Finite element results for liner temperature distribution (contour levels in degrees K) at rated speed and varying fuel rate. (Cummins NH engine; conventional, cooled).

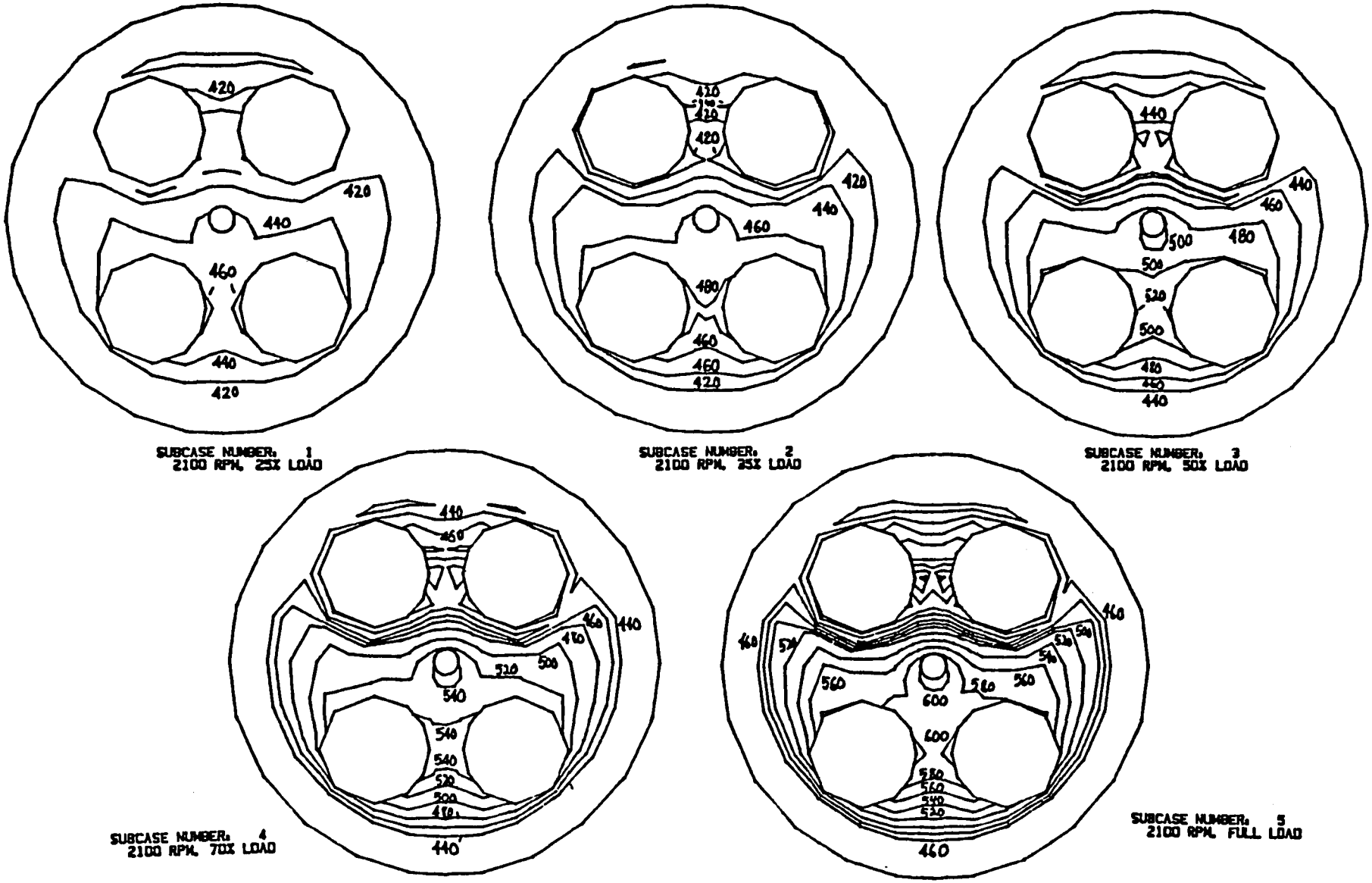

Figure 2-25 Finite element results for temperature distribution on the gas side of firedeck (contour levels in degrees K) at rated speed and varying fuel rate. (Cummins NH engine, conventional, cooled)

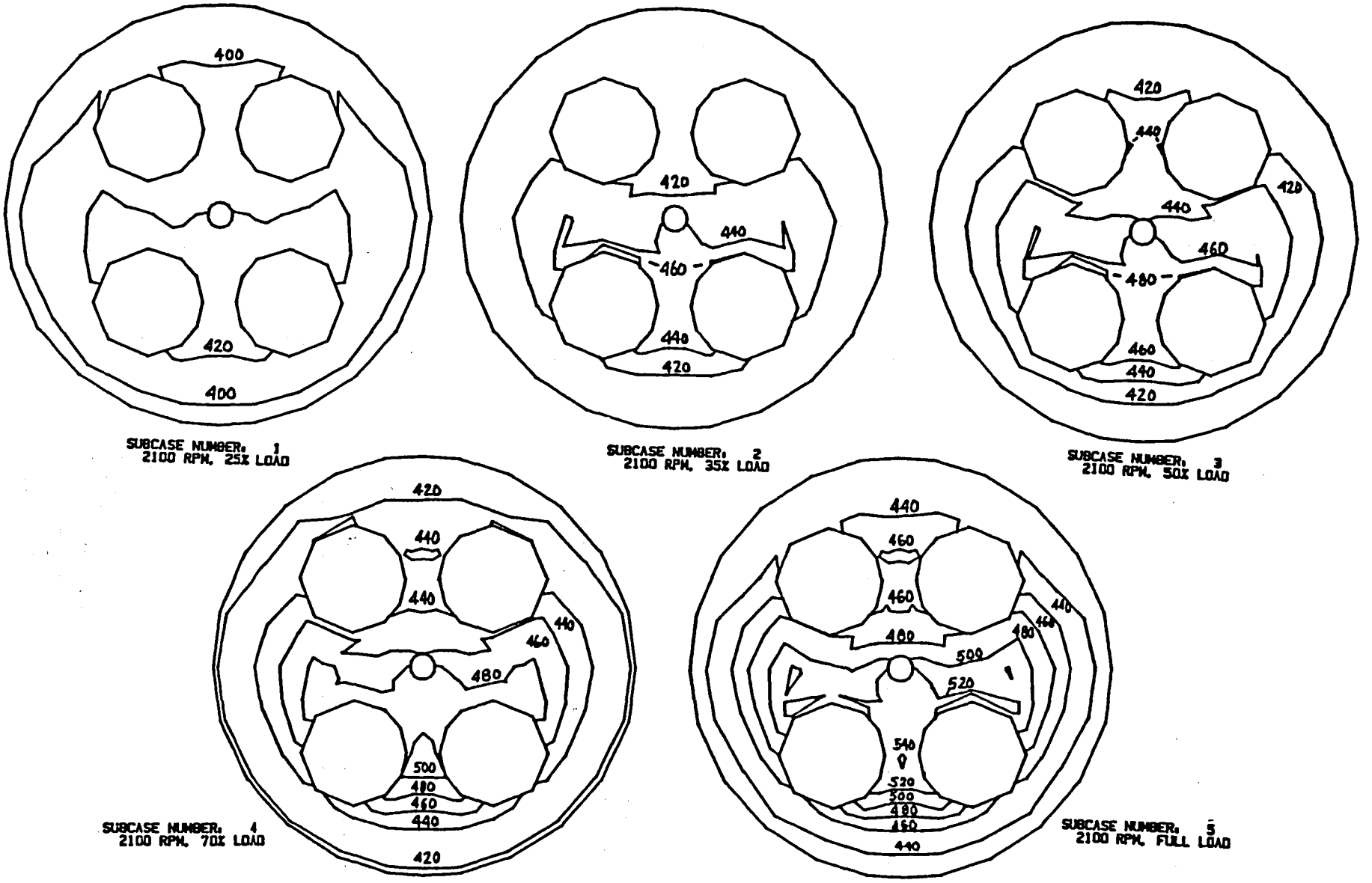

Figure 2-26 Firedeck temperature distribution in a plane 7 mm behind gas side surface at rated speed and varying load. (Contour levels in degrees K; Cummins NH engine; conventional, cooled).

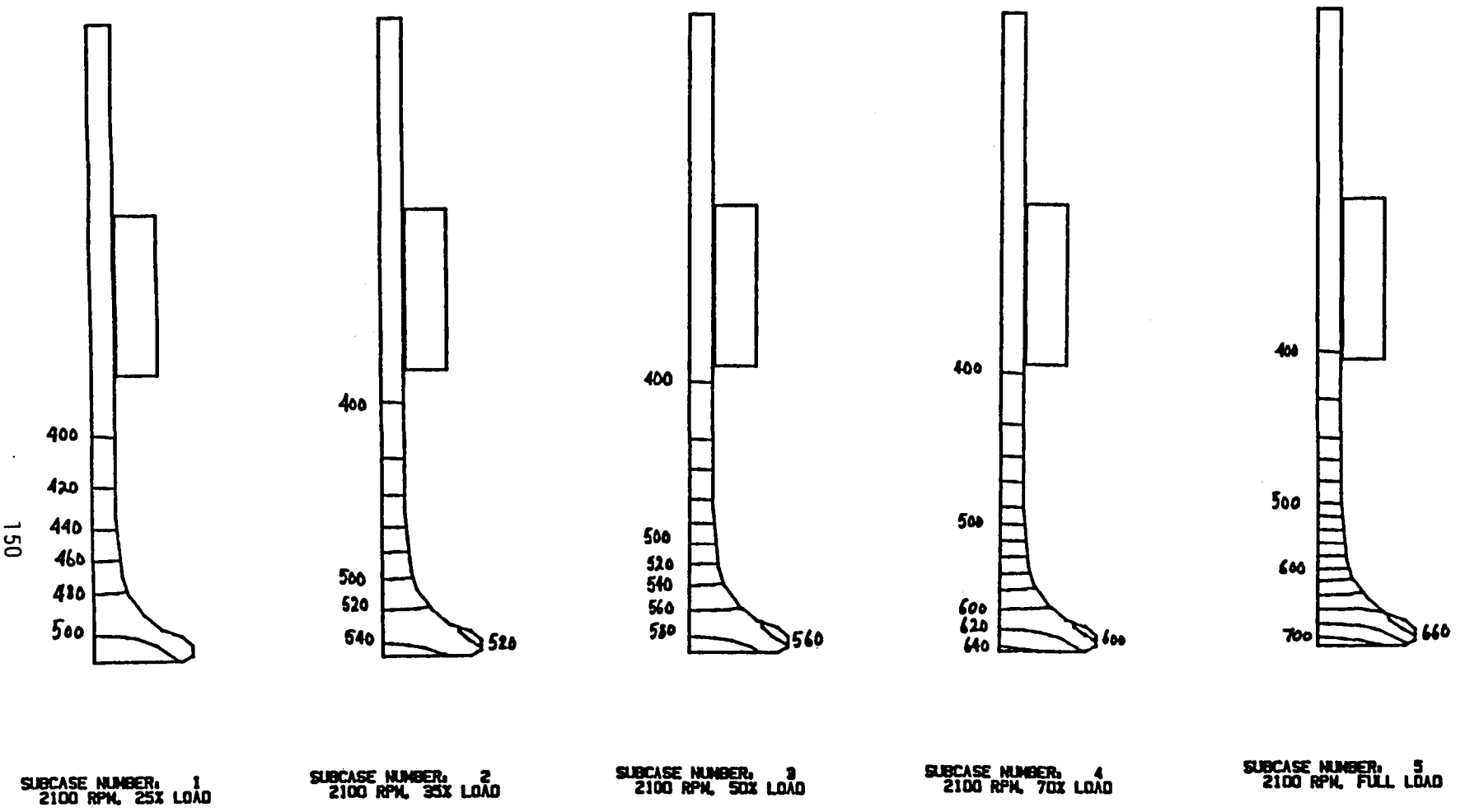

Figure 2-27 FEM-predicted intake valve temperature profiles (contour levels in degrees K) at rated speed and varying fuel rate. (Cummins NH engine; conventional, cooled).

temperature gradients where the stem emerges from the guide. Due to the highly specific nature of exhaust port and intake manifold geometries, temperature distributions on their surfaces may not be of general significance. Temperatures on these surfaces are the highest where the exhaust port and intake manifold join the firedeck, and rapidly decrease with distance from the junctions due to effective cooling of port walls. A plot of printed (full load) nodal temperatures superimposed on an orthographic view of the exhaust port is shown in Figure 2-29.

Liner Surface Heat Transfer

One of the unique features of the current methodology is the detailed analysis of liner heat transfer that resolves thermal loads on the liner spatially and in time while rigorously accounting for piston motion and piston-liner thermal interactions. The correct representation of this aspect of heat transfer in reciprocating engines allows the detailed resolution of heat paths and temperatures on the liner surface. The detail built into the methodology allows investigation of sensitivity to geometry and properties of surfaces at the interface (including rings) individual conduct resistances as well as gross geometry and global simulation variables. This information is valuable in the evaluation of liner insulation strategies and characterization of the thermal environment for tribological phenomena on the piston-liner interface. Mean (steady-state FEM) results are discussed here, while the transient aspects of these calculations will be presented in a later section.

Variation of liner surface temperature with distance from head and with load is shown in Figure 2-30. The peak temperature near the top of the liner rapidly decreases with distance from head. The center of the liner is kept cool by coolant flow behind it; the lower, uncooled portion is hotter due to heat flow from piston and frictional heat. Careful observation also reveals shallow "humps" at the beginning and end of the cooled region where there is prolonged contact with the hotter piston as it slows down around each TDC and BDC. The above pattern repeats itself at all load levels, although load has an amplifying effect on the range of local temperature variations.

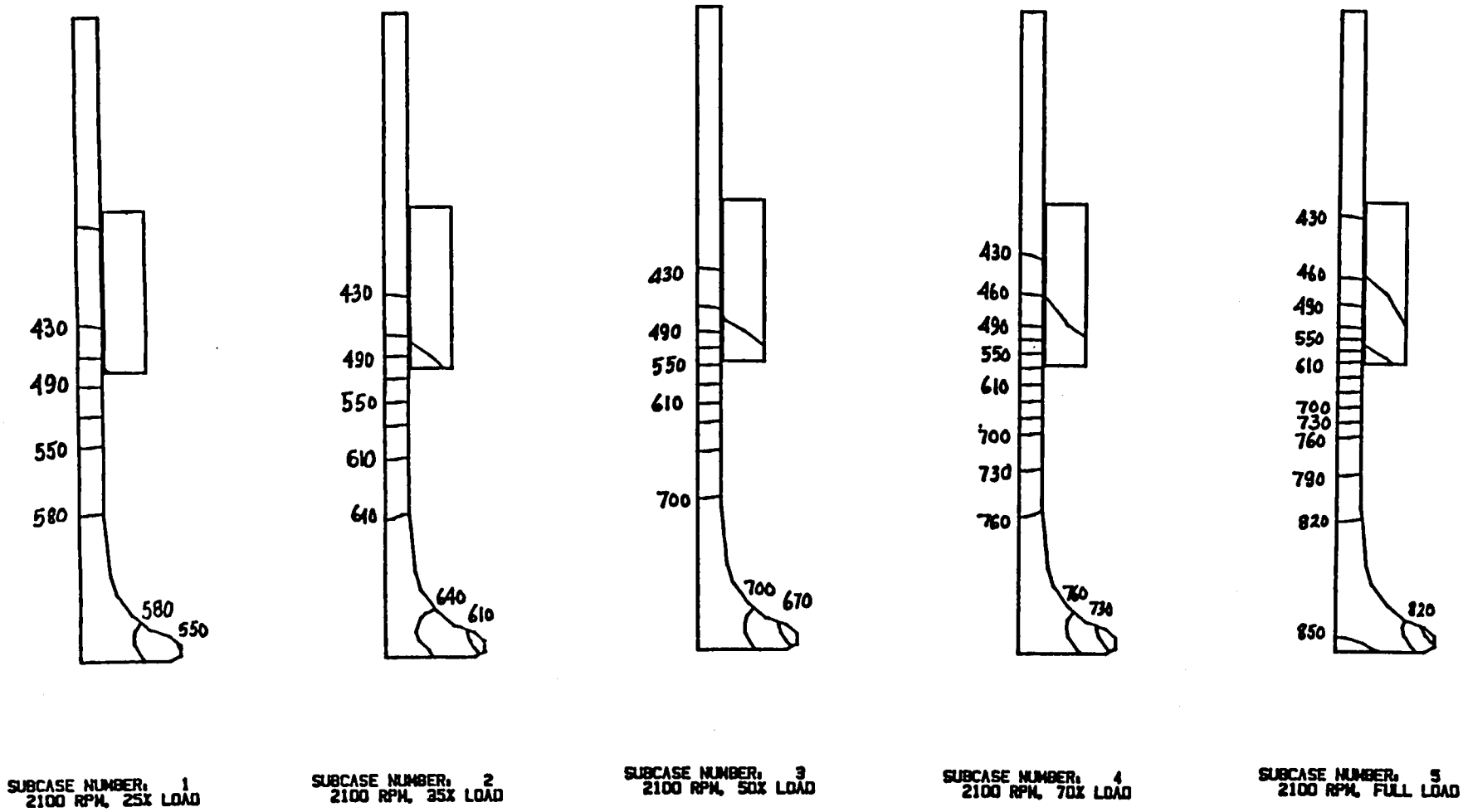

Figure 2-28 FEM-predicted exhaust valve temperature profiles (contour levels in degrees K) at rated speed and varying fuel rate. (Cummins NH engine; conventional, cooled).

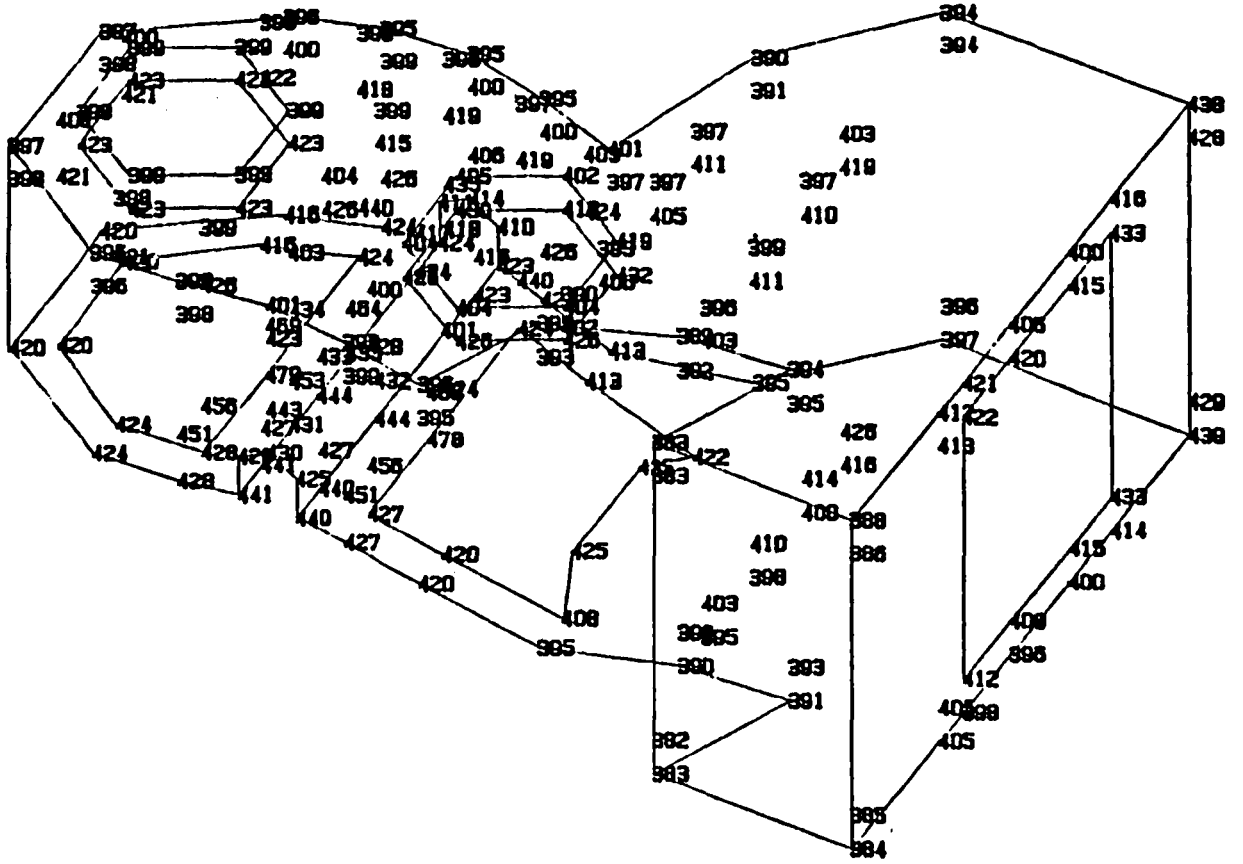

Figure 2-29 Plot of local exhaust port temperature results, superimposed on outline of exhaust port: 2100 rpm, full load. (Cummins NH engine; conventional, cooled).

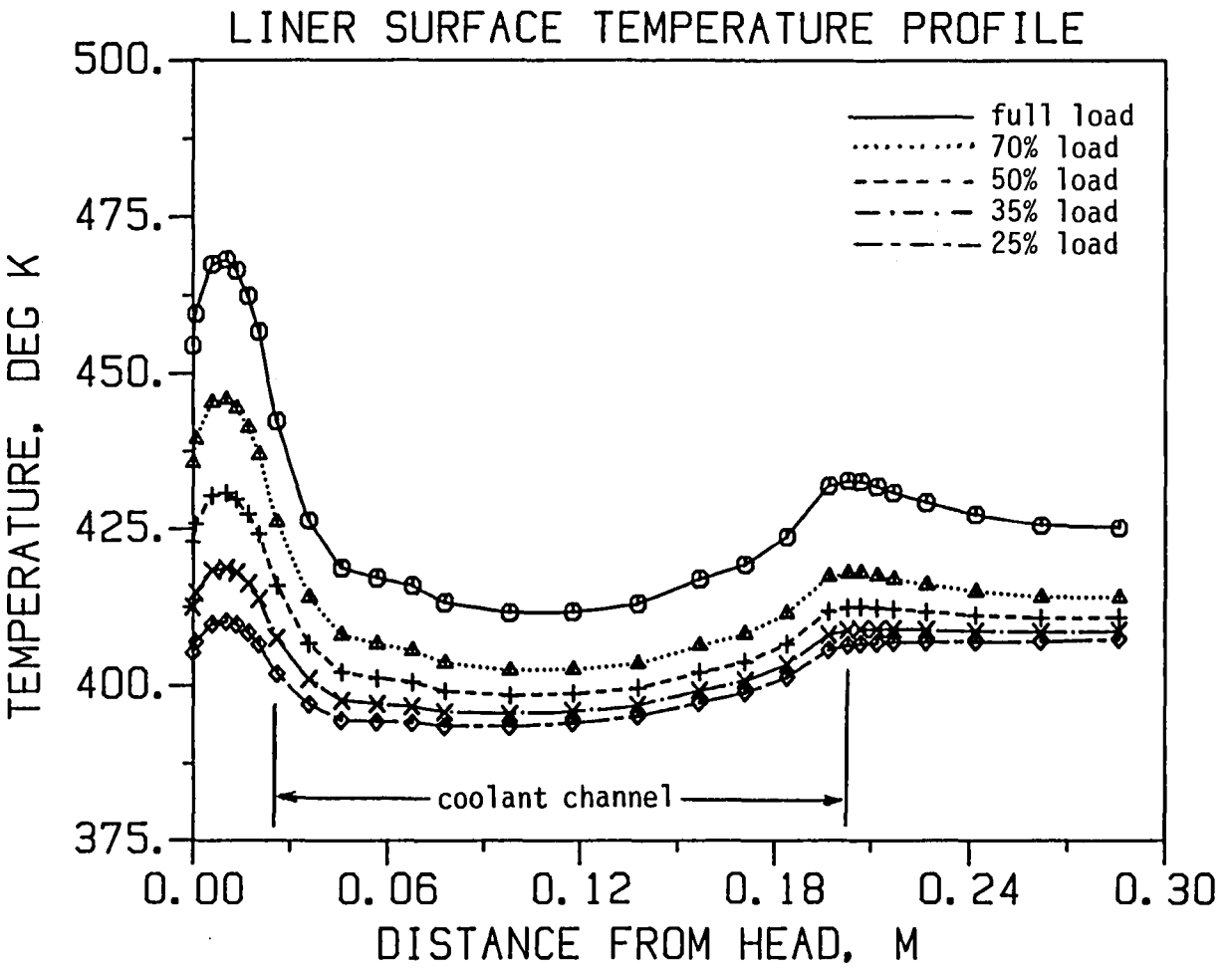

Figure 2-30 Axial temperature distribution along the gas side of liner at rated speed and varying fuel rate. (Finite element results; Cummins NH engine, conventional, cooled).

Distribution of total mean local heat flux on the liner is shown in Figure 2-31. It is characterized by a high flux region at the top (always exposed to gas), followed by a relatively flat high heat flux zone (coinciding with the coolant channel length) and a third region where net heat flux is slightly negative due to heat rejected to crankcase oil. There is a minimum around the 0.03m location. This area is in contact with the piston only shortly and does not receive the full effect of piston-liner heat flux. At the same time gas temperatures and heat transfer coefficients are reduced by the time it is exposed to gas. Spatial and load variations of the individual components of this total heat flux, i.e., gas-liner, piston-liner, oil-liner and friction heat fluxes, are shown in Figures 2-32, 2-33, 2-34 and 2-35, respectively. These plots augment Figure 2-31 by documenting the contribution of each heat flux component to the variations in the total. Gas-liner and piston-liner heat fluxes were further broken down and they are discussed below. The oil-liner heat flux (Fig. 2-34) is negative indicating heat loss to crankcase oil. It exists for the portion of the liner exposed to crankcase oil as piston rises from BDC to TDC. Frictional heat flux (Fig. 2-35) peaks at both ring reversal locations due to boundary piston-liner and ring-liner boundary friction. The general rise toward the BDC reversal is due to increased effect of hydrodynamic piston skirt friction, which exists only below the ring pack.

Figures 2-36(a) and (b) show distribution of the convective and radiative components of the gas heat flux on the liner. Radiative heat flux is present only for the region near the head; this is the only part of the liner exposed to gases during the relatively short period in the expansion stroke, when a radiant sooting flame is present in the combustion chamber. The spatial and load variation components of total piston-to-liner heat flux that are due to piston-liner and ring-liner thermal interaction are shown in Figures 2-37 and 2-38, respectively. The split between piston-liner and ring-liner heat flux appears to be roughly equal. Piston-liner heat flux slowly increases with distance from head and peaks at the BDC liner-piston crown contact, where the highest temperature difference between piston and liner is reached. Due to groove-ring resistances, successive ring temperatures vary less than

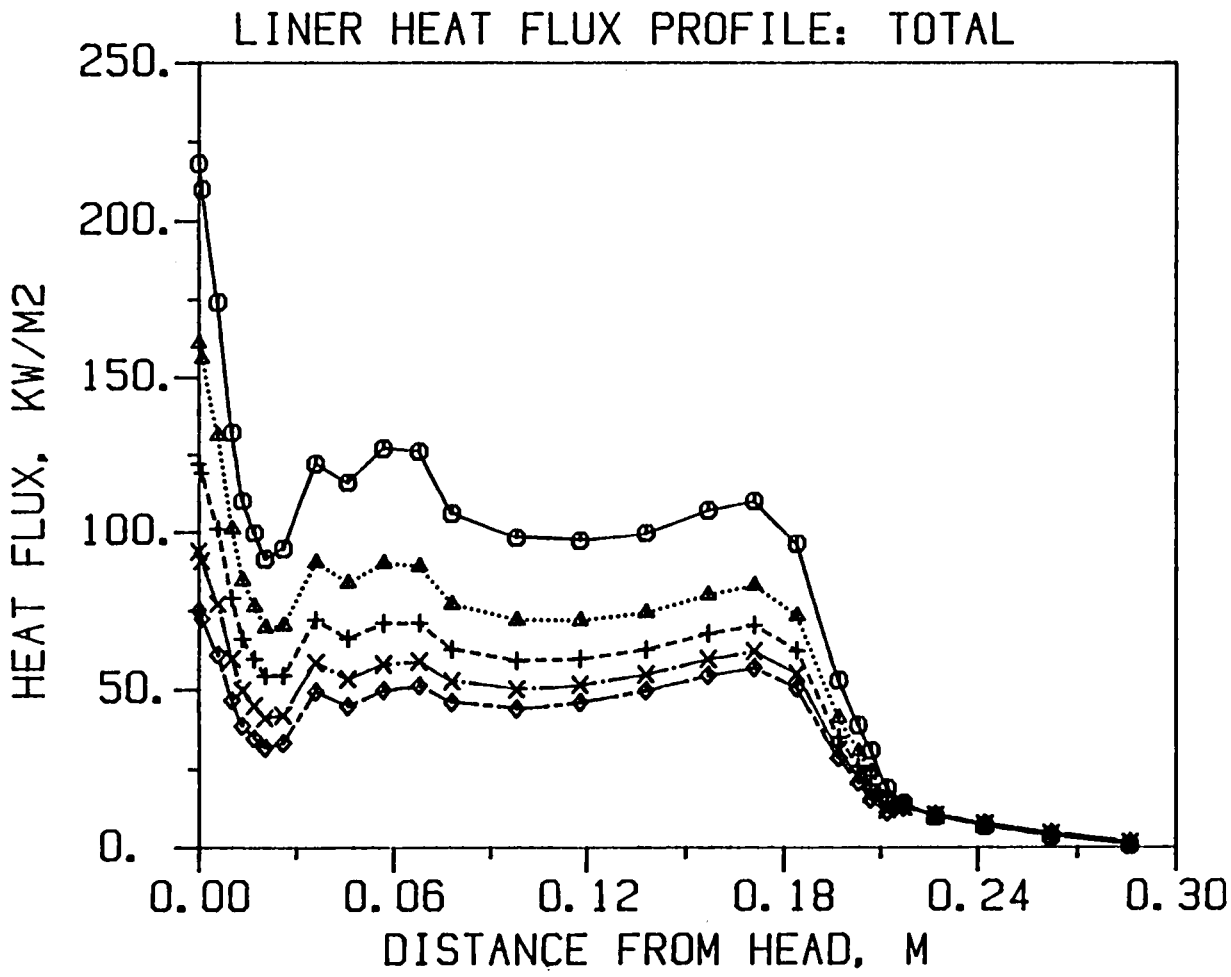

Figure 2-31 Distribution of total heat flux along the gas side of liner at rated speed and varying fuel rate (FEM results; Cummins NH engine; conventional, cooled; symbols as in Figure 2-30).

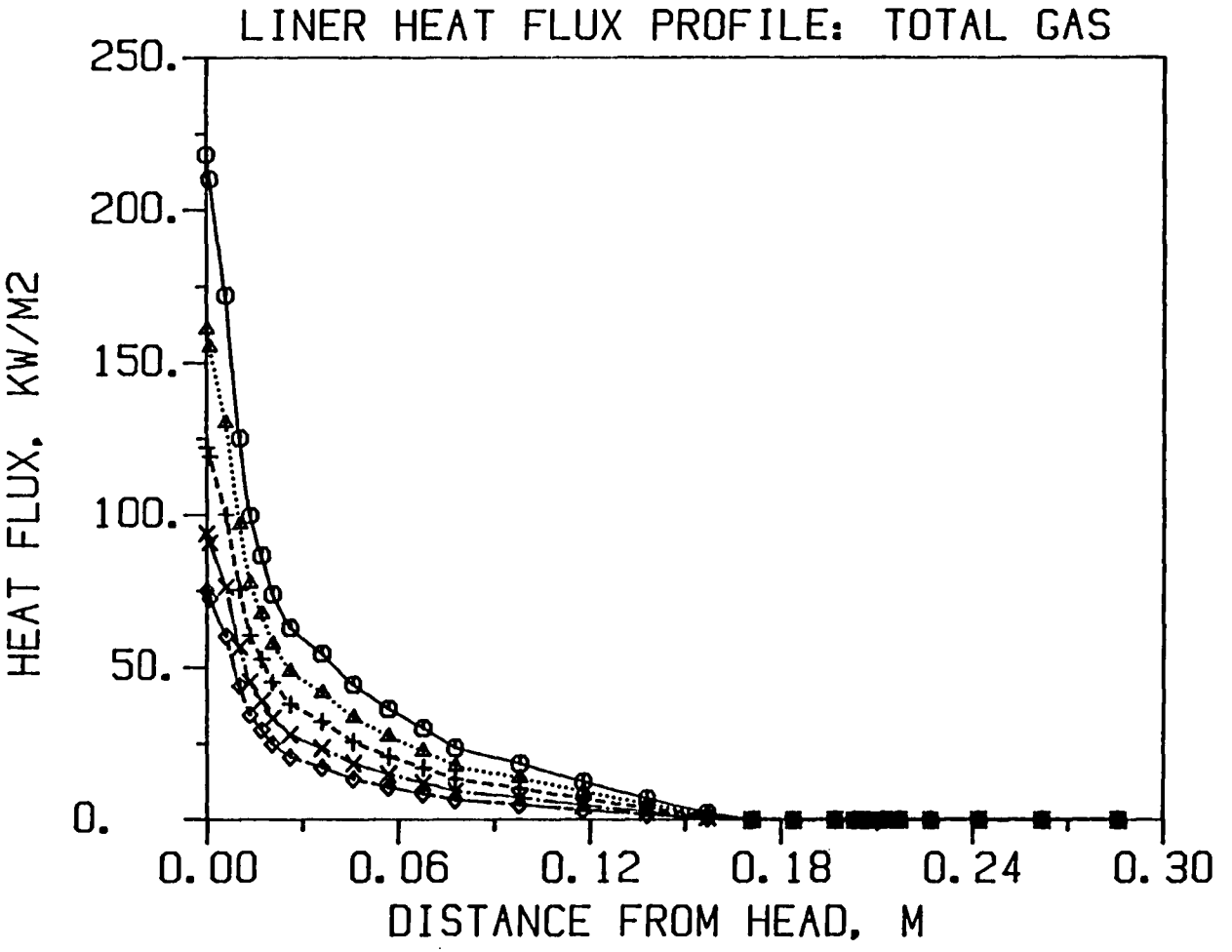

Figure 2-32 Distribution of gas-liner heat flux along the gas side of the liner at rated speed and varying fuel rate. (FEM results; Cummins NH engine; conventional, cooled; symbols as in Figure 2-30).

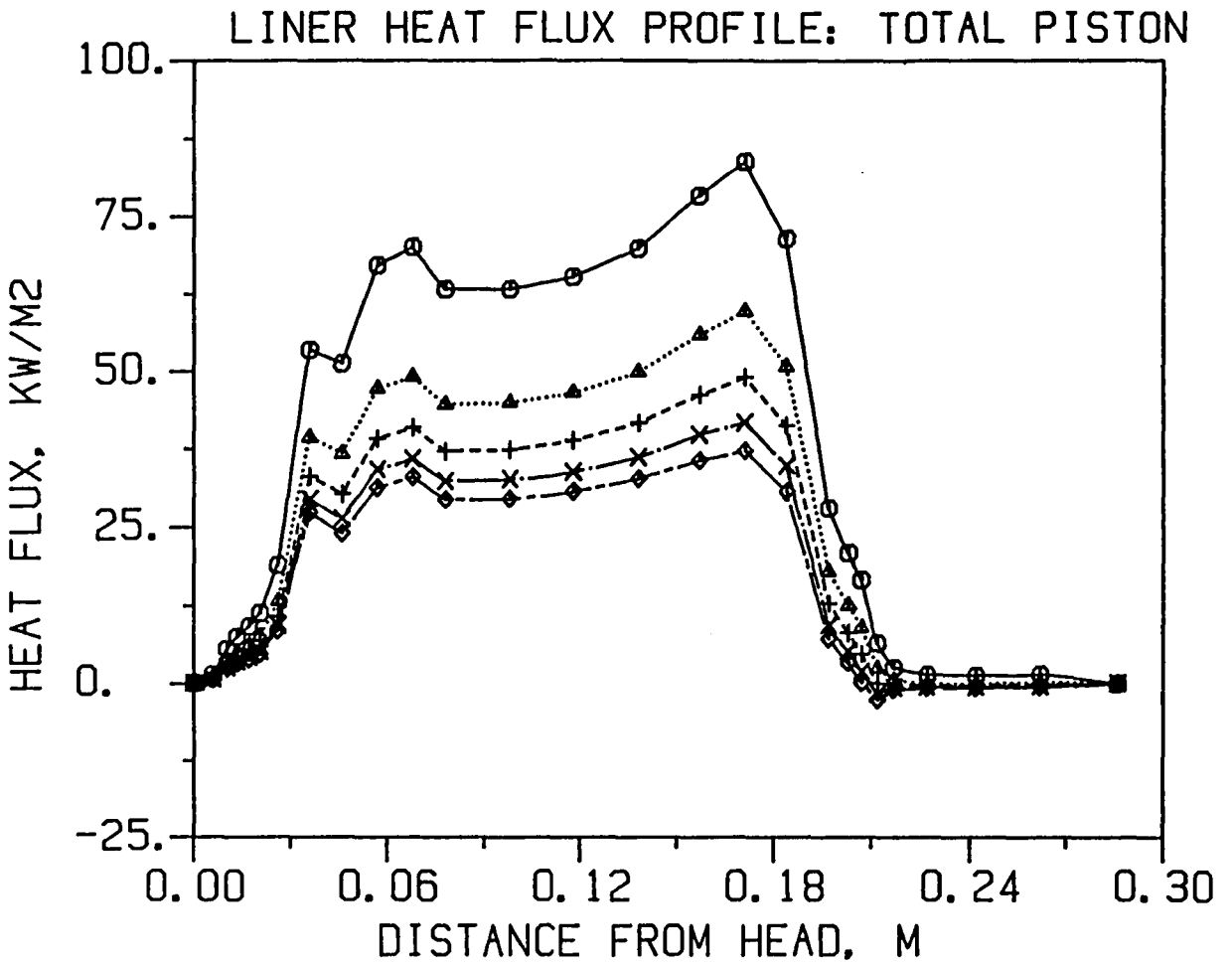

Figure 2-33 Distribution of piston-liner heat flux along the gas side of the liner at rated speed and varying fuel rate. (FEM results; Cummins NH engine; conventional, cooled; symbols as in Figure 2-30).

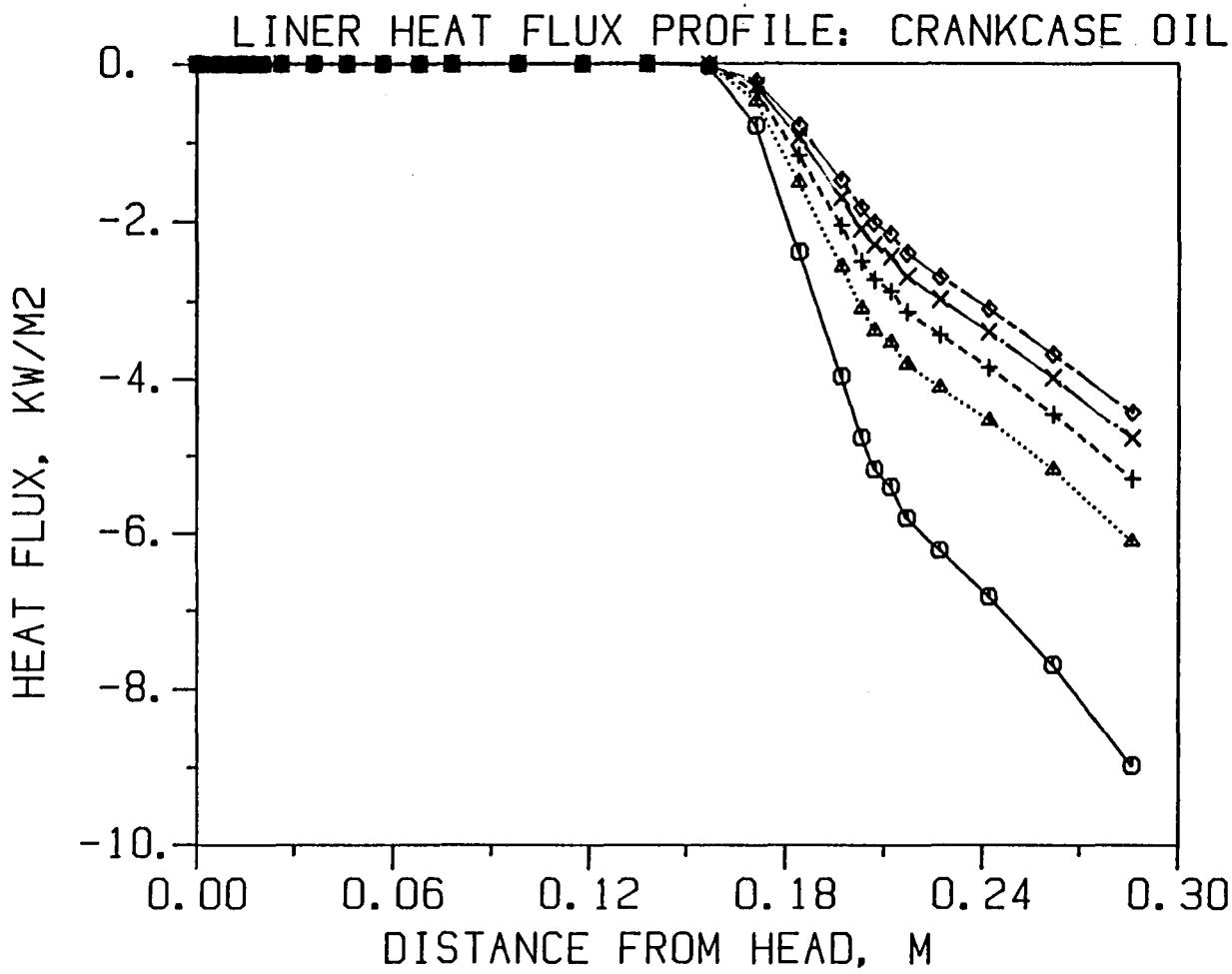

Figure 2-34 Distribution of heat flux associated with heat rejection in crankcase oil, on the gas side of liner at rated speed and varying fuel rates. (FEM results; Cummins NH engine; conventional, cooled; symbols as in Figure 2-30).

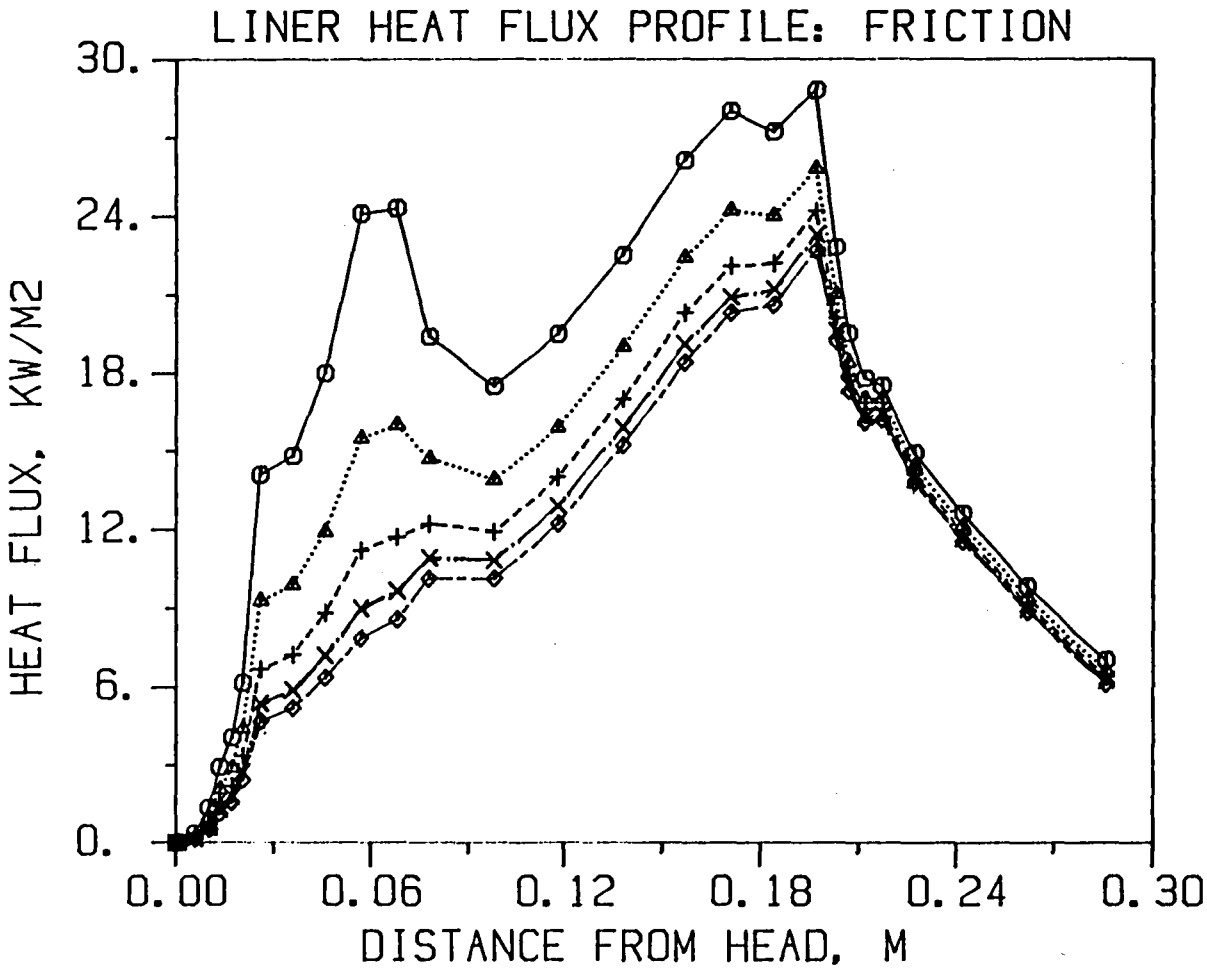

Figure 2-35 Distribution of frictional heat flux along the liner: effects of load at rated speed. (FEM results; Cummins NH engine; conventional, cooled; symbols as in Figure 2-30).

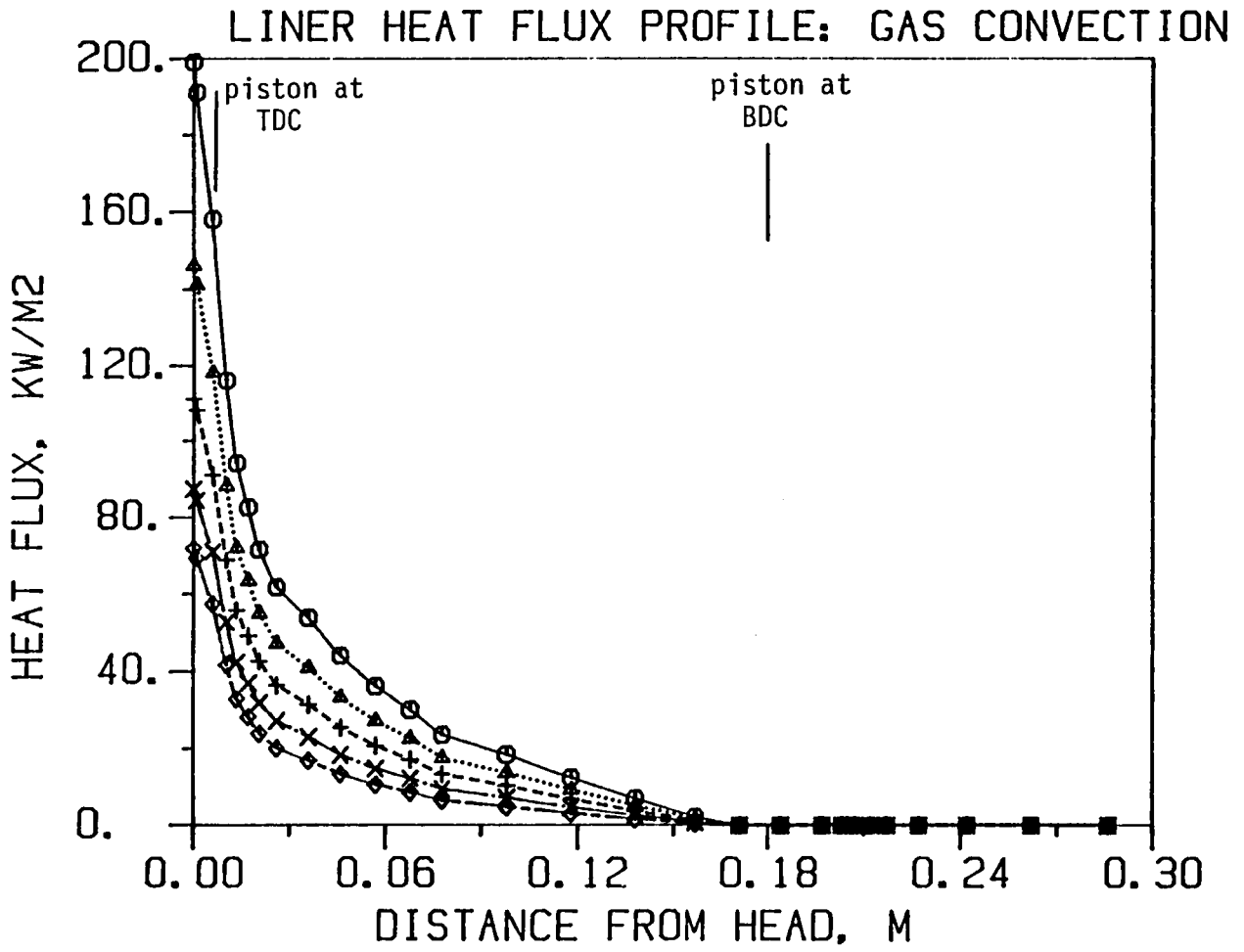

Figure 2-36a Distribution of convective components of gas-liner heat flux along liner surface; effects of varying fuel rate at rated speed (FEM results; Cummins NH engine; conventionally cooled; symbols as in Figure 2-30).

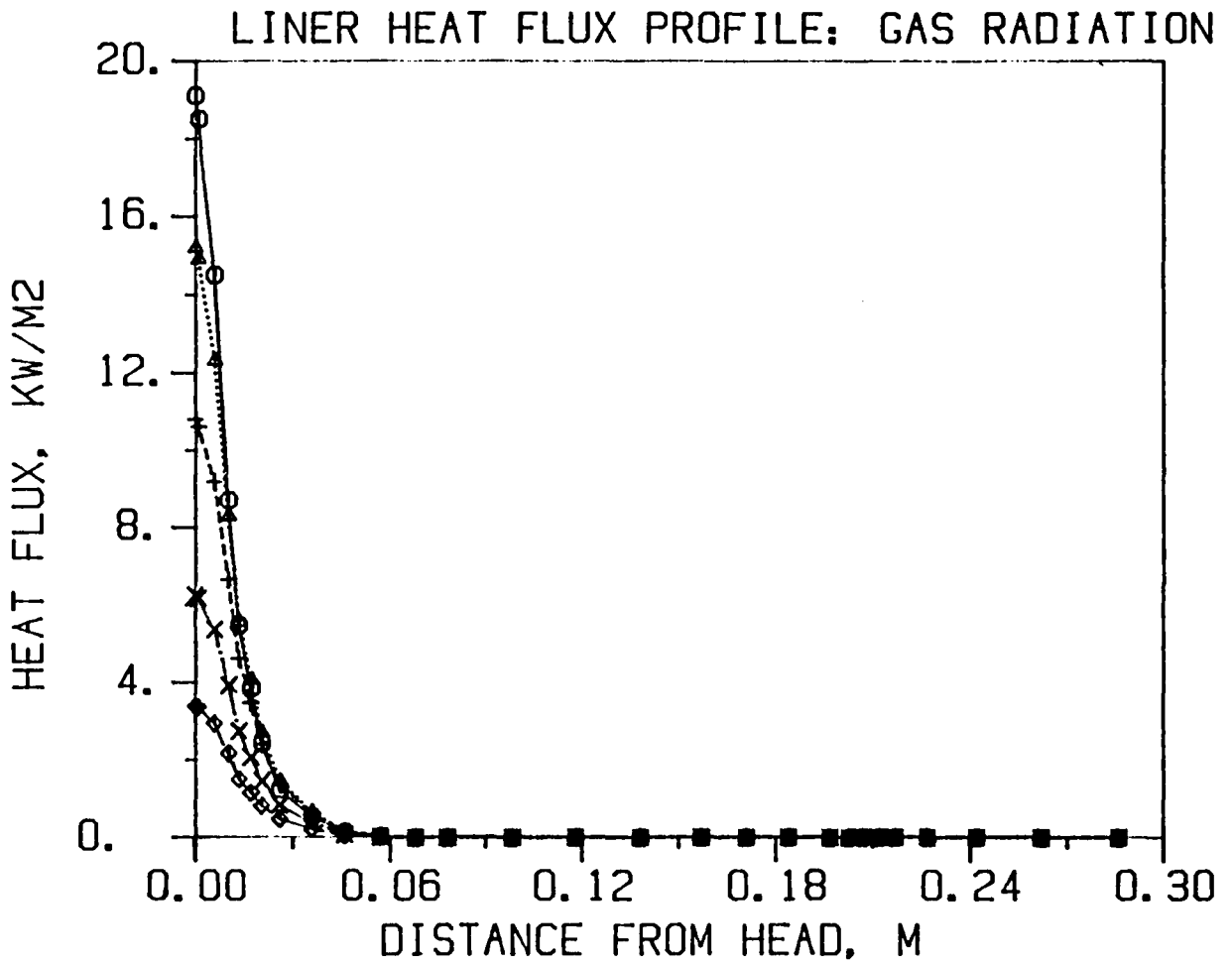

Figure 2-36b Distribution of radiant component of gas-liner heat flux along liner surface: effect of varying fuel rate at rated speed (FEM results; Cummins NH engine; conventionally cooled; symbols as in Figure 2-30).

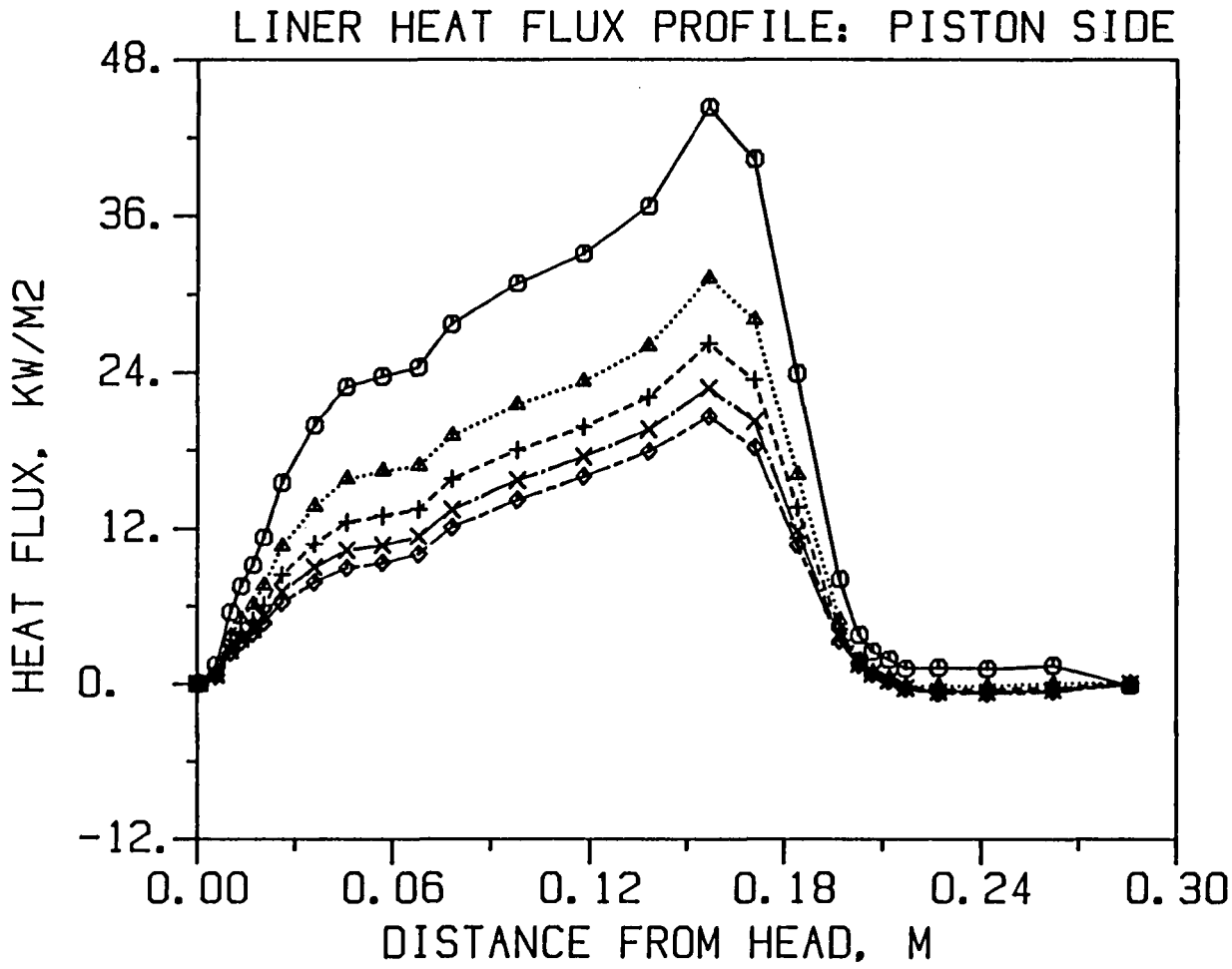

Figure 2-37 Distribution of portion of piston-liner heat flux associated with contact between piston side and liner, along liner surface. Effects of varying fuel rate at rated speed. (FEM results; Cummins NH engine; conventional, cooled; symbols as in Figure 2-30).

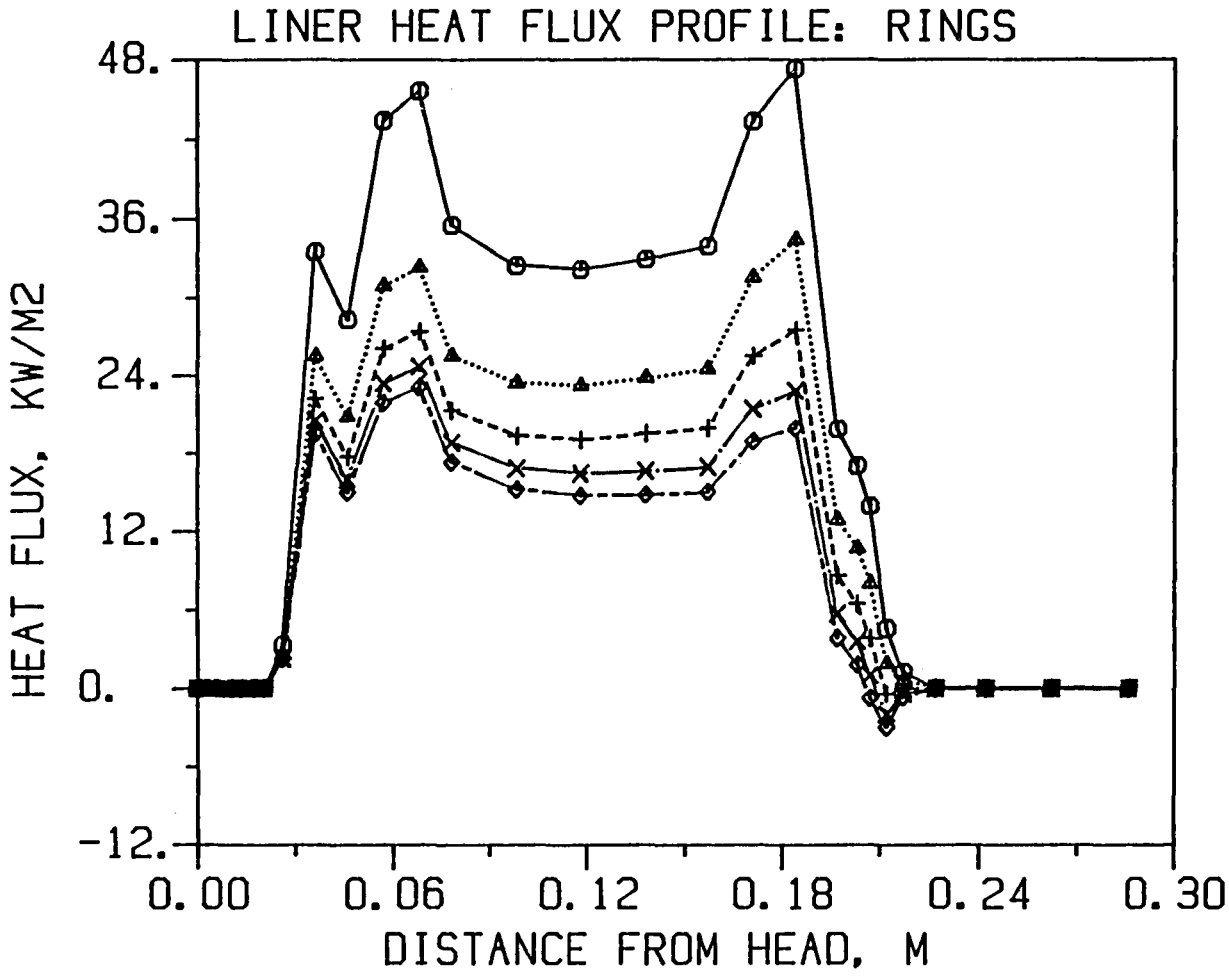

Figure 2-38 Distribution of part of the piston-liner heat flux associated with contact between rings and liner, along liner surface: effects of varying fuel rate at rated speed. (FEM results; Cummins NH engine; conventional, cooled; symbols as in Figure 2-30).

temperature on the side of the piston. Thus, distribution of ring-to-liner heat flux is mostly determined by the instantaneous piston speed, and it peaks at both the TDC and BDC top-compression-ring-liner contacts. Piston-liner heat flux and its components have a weaker dependence on load than both gas convection and radiation fluxes on the liner.

CYCLIC COMBUSTION CHAMBER WALL TEMPERATURE TRANSIENTS

One of the complex features of engine conduction heat transfer is the existence of temperature excursions (swings) produced in surfaces exposed to combustion gases by the cyclical and highly peaked nature of gas-to-wall heat transfer. The magnitudes of these swings are low for conventional metallic engines (<30° K) but may reach 200° - 250° K for ceramic materials currently proposed for insulated engines. The study of cyclic transients is important due to their implications regarding materials fatigue and thermal stress and also because of their effects on insulated engine performance. During Phase I, a one-dimensional transient heat conduction model was developed for computing cyclic transients on engine surfaces exposed to combustion gases. This model and its application are discussed in detail in the Phase I report and also in Morel et al, (1985).

Incorporation of 1-D transient heat conduction model into cycle simulation

The 1-D transient heat conduction model can be used in conjunction with the finite element or network steady-state conduction methodologies described previously. It can be applied to each of the individual in-cylinder heat transfer surfaces recognized by the cycle simulation. There are eleven separate in-cylinder surfaces which include three piston surfaces, three liner surfaces (top sixth, middle third and bottom half) three concentric head surfaces, and exhaust and intake valves. To perform these calculations within the computational time constraints of the coupled approach, both the time step and the mesh size within the penetration depth have been optimized (Phase I Report). Since it is sufficient to integrate the transient heat equation at

three-degree crankangle increments for adequate accuracy, the 1-D transient heat transfer computations need not be done synchronously with the cycle simulation but are performed at the end of each cycle using stored information. In addition, the convergence of the computation is assisted every cycle by adjusting the profile within the penetration depth for the mean heat flow predicted by the steady-state conduction model. Thus it suffices to iterate only a few times per cycle and for most cases only once, before a true cyclic solution is attained. The mean cyclic heat flux on a surface i of area A_i exposed to gas is expressed as

$$\bar{q}_i = \int h_{gi} A_i (T_{gi} - T_{wi}) = \int h_{gi} A_i (T_{gi} - \bar{T}_{wi} - T'_{wi})$$

$$= A_i \int h_{gi} \frac{\int h_{gi} \bar{T}_{gi}}{\int h_{gi}} - T_{wi} - \frac{\int h_g T'_{wi}}{\int h_{gi}} \qquad (2\text{-}5)$$

where subscript g refers to gas and w refers to wall.

The wall temperature deviation from mean, T'_{wi} ($= T_{wi} - T_{wi}$) predicted by the 1-D transient heat transfer model is used to calculate the third term inside the parentheses in the above expression, which defines C'_{gi} in eq. (2-3), which is the second order correction on time average surface temperature. These corrections are fed back to the steady-state conduction model for use in the convective boundary conditions as indicated in equation (2-3). At the same time, the instantaneous wall temperature is used in the computation of the heat transfer component of the gas energy balance. Thus, a three-way coupling between cycle thermodynamics, steady-state and transient heat transfer is established.

Treatment of piston/liner thermal interaction and wall temperature transients

In addition to surfaces permanently exposed to gas, the coupled 1-D transient model was implemented for liner surfaces and for piston ring faces in sliding contact with the liner. The relative motion of the

piston with respect to the liner has been accounted for in the steady-state conduction model described above, by prescribing time averaged resistances based on clearances, heat transfer coefficients and contact times between piston ring and liner surface nodes. Thus the piston-liner thermal path has been included in the steady-state conduction model. However, the effect of the cyclic temperature transients on these surfaces also needs to be accounted for. While the magnitudes of these swings are smaller than those on surfaces permanently exposed to gas, they affect piston-liner heat transfer since the temperature difference between piston and liner surfaces is much smaller than the gas-wall temperature drop. The transients also affect the tribology of the piston-liner interface. The incorporation of the cyclic transient heat conduction model into the simulation allows the resolution of temperature transients on these surfaces. The implementation of the one-dimensional model to the liner and ring surfaces requires that all applied surface heat loads be accounted for in a correctly time-resolved form. The procedure used to accomplish this is described below.

Liner temperature transients. For liner surfaces, the one-dimensional model is driven by inputs from gas convection and radiation models when a surface is exposed to gas; however, while they are covered by the piston and traversed by the rings, the thermal load is calculated based on piston and ring temperatures and ring-liner/piston-liner heat transfer coefficients, as well as friction heat generated by ring-liner and piston-liner friction. The piston-to-liner and ring-to-liner heat transfer coefficients are inputs and assumed to be constant. When ring transients are being solved for, the instantaneous ring temperatures are used for the definition of part of the instantaneous heat transfer rate on the liner.

The instantaneous heat transfer rate to liner zone i is,

$$q_{liner,i} = q_{gl,i} + \sum_j q_{pl,ij} + \sum_j q_{rl,ij} + q_{fl,i}$$

where the subscripts are defined as: (gl = gas-liner)
(pl = piston-liner)
(fl = friction heat)
(rl = ring-liner)

The subscripts j for piston and rings indicate piston side zone (there are 5 in IRIS) and the ring number (up to 4; j=1 is the top compression ring). Piston side-zones and rings are shown in Figure 2-39).

Substituting for the first three terms on the right hand side the equation becomes

$$q_{liner,i} = h_{gi}A_i x_{gi}(T_{gi}-T_{wi}) + \sum_j h_{pj}A_i x_{pij}(T_{pj}-T_{wi}) + \sum_j h_{rj}A_i x_{rij}(T_{rj}-T_{wi}) + q_{fl,i}$$

x_{gi}, x_{pij}, x_{rij} are instantaneous area of exposure fraction ($0 \leq x \leq 1$) to gas (g), piston (p) and rings (r). T_{pj} and T_{rj} are temperatures of piston zones and rings, and h_{pj} and h_{rj} denote the heat transfer coefficients for heat exchange between piston zones and liner, and rings and liner. They are assumed to be constant, but the current implementation allows time variation (e.g., for h_{rj} due to changes in oil film thickness and transition to boundary lubrication).

Time-averaging the above equation, one obtains the mean heat transfer to liner zone i

$$\bar{q}_{liner,i} = \int h_{gi}A_i x_{gi}\,[T_{gi}-T_{wi}] + \sum_j \int h_{pj}A_i x_{pij}[T_{pj}-T_{wi}] + \sum_j \int h_{rj}A_i x_{rij}[T_{rj}-T_{wi}] + \bar{q}_{fl,i} \qquad (2\text{-}6)$$

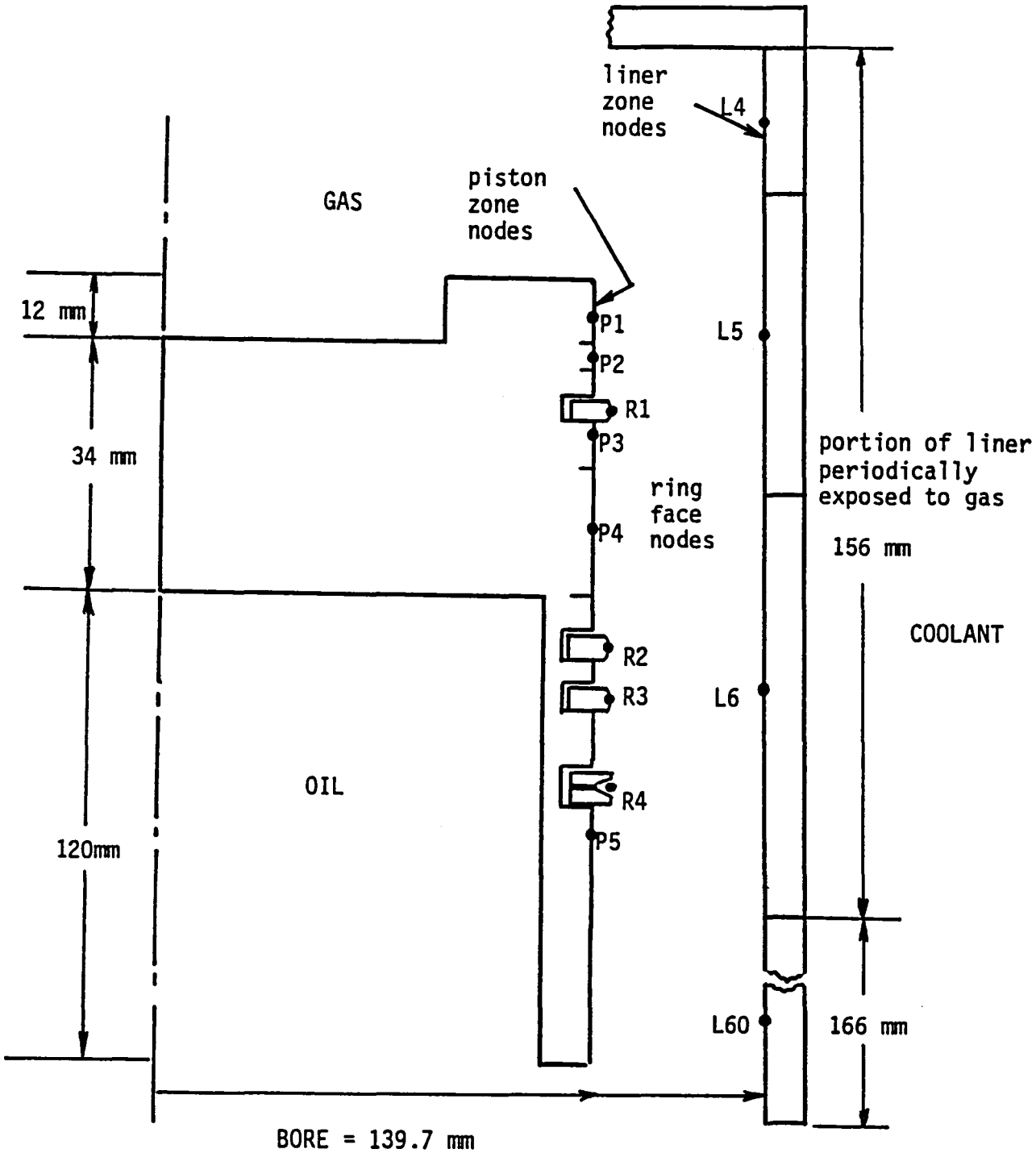

Figure 2-39 Configuration of network piston and liner zones at the piston-liner interface. Also shown are ring positions and ring face nodes.

The above equation can be rewritten as

$$\bar{q}_{liner,i} = h_{gi,eff} A_{gi} [T_{gi,eff} - \bar{T}_{wi} - C'_{lgi}]$$
$$+ \sum_j h_{pj} A_{pij} [T_{pj} - \bar{T}_{wi} - C'_{lp,ij}] \qquad (2\text{-}7)$$
$$+ \sum_j h_{rj} A_{rij} [\bar{T}_{rj} + C'_{rl,ij} - \bar{T}_{wi} - C'_{lr,ij}] + \bar{q}_{fli}$$

where piston surfaces were assumed not to have temperature swings (i.e., $\bar{T}_{pj} = T_{pj}$), (−) and (') denote mean and deviation from mean for temperatures, and the following quantities have been defined:

$$A_{gi} = A_i \int x_{gi}; \qquad h_{gi,eff} = \frac{\int h_{gi}\, x_{gi}}{\int x_{gi}}; \qquad T_{gi,eff} = \frac{\int h_{gi}\, T_{gi}\, x_{gi}}{\int h_{gi}\, x_{gi}}$$

$$A_{pij} = A_i \int x_{pij}; \qquad h_{pij,eff} = \frac{\int h_{pj}\, x_{pij}}{\int x_{pij}} = h_{pj}$$

$$A_{rij} = A_i \int x_{rij}; \qquad h_{rij,eff} = \frac{\int h_{rij}\, x_{rij}}{\int x_{rij}} = h_{rj}$$

$$C'_{lg,i} = \frac{\int h_{gi}\, T'_{wi}\, x_{gi}}{\int h_{gi}\, x_{gi}}, \qquad C'_{lp,ij} = \frac{\int T'_{wi}\, x_{pij}}{\int x_{pij}},$$

$$C'_{rl,ij} = \frac{\int T'_{rj}\, x_{rij}}{\int x_{rij}}, \qquad C'_{lr,ij} = \frac{\int T'_{wi}\, x_{rij}}{\int x_{rij}},$$

Thus, cycle-averaged heat transfer can be expressed with cycle averaged (effective) heat transfer coefficients, areas and temperatures, provided that second order correction terms $C'_{lg,i}$, $C'_{lp,ij}$, $C'_{rl,ij}$ and $C'_{lr,ij}$ are used to modify the mean temperature differences. All of these correction terms are calculated after the 1-D computations and are used in the boundary conditions to the steady-state conduction equations for liner nodes. Instantaneous liner surface temperatures are also used for

gas heat loss computation and as thermal loads for calculation of 1-D ring transients. An internal check to compare values of $q_{pl,ij}$ and $q_{rl,ij}$ computed from averaged quantities against the integrated ones is used to monitor the convergence of the coupled problem.

Ring Temperature Transients. In accordance with the above expressions, the instantaneous heat transfer to the face of ring j can be expressed as,

$$q_{ring,j} = \sum_i q_{lr,ij} + q_{fr,j} = \sum_i h_{rj} A_i x_{rij} (T_{wi} - T_{rj}) + q_{fr,j}$$

$$= \sum_i h_{rj} A_i x_{rij} (\bar{T}_{wi} + T'_{wi} - \bar{T}_{rj} - T'_{rj}) + q_{fr,j}$$

Mean heat transfer rate to ring face is then,

$$\bar{q}_{ring,j} = \sum_i \int h_{rj} A_i x_{rij} (\bar{T}_{wi} + T'_{wi} - \bar{T}_{rj} - T'_{rj}) + \bar{q}_{fr,j}$$

$$= \sum_i \int h_{rj} A_{rij} \left[\bar{T}_{wi} + \frac{\int T'_{wi} x_{rij}}{\int x_{rij}} - \bar{T}_{rj} - \frac{\int T'_{rj} x_{rij}}{\int x_{rij}} \right] + \bar{q}_{fr,j}$$

$$= \sum_i \int h_{rj} A_{rij} [\bar{T}_{wi} + C'_{lr,ij} - \bar{T}_{rj} - C'_{rl,ij}] + \bar{q}_{fr,j} \qquad (2\text{-}8)$$

The second order correction terms $C'_{lr,ij}$ and $C'_{rl,ij}$ are used to modify steady-state equations for nodes placed at ring faces. The ring face temperature histories obtained from the 1-D model for rings are used in defining the thermal load for the liner 1-D transient computation. The instantaneous ring face temperatures are also important for determining lubricant temperature and viscosity.

Frictional Heat Deposition. The heat generated by hydrodynamic and boundary friction at ring-liner contacts, skirt hydrodynamic frictional heat, and piston-liner boundary friction heat due to side-force-induced

rubbing of piston on liner, are calculated by an engine friction model described in Chapter III. Each of these components has temporal (and in the case of the liner, spatial) variation. The 1-D model for liner nodes uses one-half of the appropriate amount of each instantaneous frictional heat (rate) component as a driving thermal load for the transient computation. For the ring 1-D transient computations, the other half of each of the ring-liner frictional heat rate components is used as thermal load. Integrated averages of all friction heat rates form a part of the thermal load for the steady-state conduction computation.

The division of the frictional heat on a one-half basis to the two surfaces in the sliding contact is based on argument of physical plausibility. The local division of heat is not critical to the overall heat balance (on piston and liner) as long as the interface resistance remains smaller than the surrounding conductive and convective resistances.

The friction model is not sensitive to temperature or material composition. Hence, frictional heat generation and its variation is influenced only indirectly by changes in thermal conditions and materials (e.g., differences in coolant temperature or insulation strategy) through their effects on combustion chamber pressure, a parameter with significant effect on friction.

Cyclic transient temperature and piston-ring-liner heat transfer

Using the coupled steady-state and cyclic transient heat transfer methodologies described above, results for temperature histories of various surfaces were obtained. Simultaneously, the heat transfer rates at liner and ring surfaces and their breakdown into individual components (gas convection, gas radiation, friction heat, heat from piston and rings to liner) were computed. Runs were carried out for the turbocharged Cummins NH engine developing 350 HP at 2100 rpm and full load, with three materials configurations:

1. Baseline engine with metal thermal properties: aluminum piston, iron head and liner, steel valves and rings.

2. Insulated engine with piston, liner, head and valves coated with a 1.5 mm thick layer of plasma sprayed zirconia (PSZ; k = 0.6 W/mK, ρc = 1.1 MJ/m^{3}K).

3. "Superinsulated" engine with all components except rings made of a hypothetical low conductivity material, k = 0.01 W/mK; ρc = 3.1 MJ/m^3°K).

The thermal resistance network methodology was utilized for steady-state conduction computations. Baseline coolant/oil heat transfer coefficients used were set at levels producing component temperatures consistent with current design practice. Coolant heat transfer coefficients were then decreased by 30 to 90% for the insulated configurations.

Cyclic transients on piston and head. Figures 2-40 (a,b,c) show cyclic temperature variation on piston surfaces for baseline (metallic), insulated and "superinsulated" engines. As insulation is increased, temperature swings rise, up to 560K for the "superinsulated" conditions. Also wall temperatures approach gas temperature and their profiles increasingly resemble that of the gas temperature (note especially the decrease after IVO). Variations between different surfaces are due to differing effective gas temperatures, heat transfer coefficients and radiation heat fluxes applicable to each individual surface. The valve and firedeck surface temperature profiles are quite similar to those shown here, except for differences magnitude and shapes, produced by differences in applied heat loads and material properties.

Transients on exhaust port surfaces. Figures 2-41 (a,b,c) show cyclic variations of temperature on surfaces in the exhaust port. They are representative of those found on port walls near the valve (port 1), walls of port closer to exhaust manifold (port 2) and of the rear surface of the valve. Since port surfaces are thermally loaded mainly while the exhuast valve is open, their temperatures rise during that

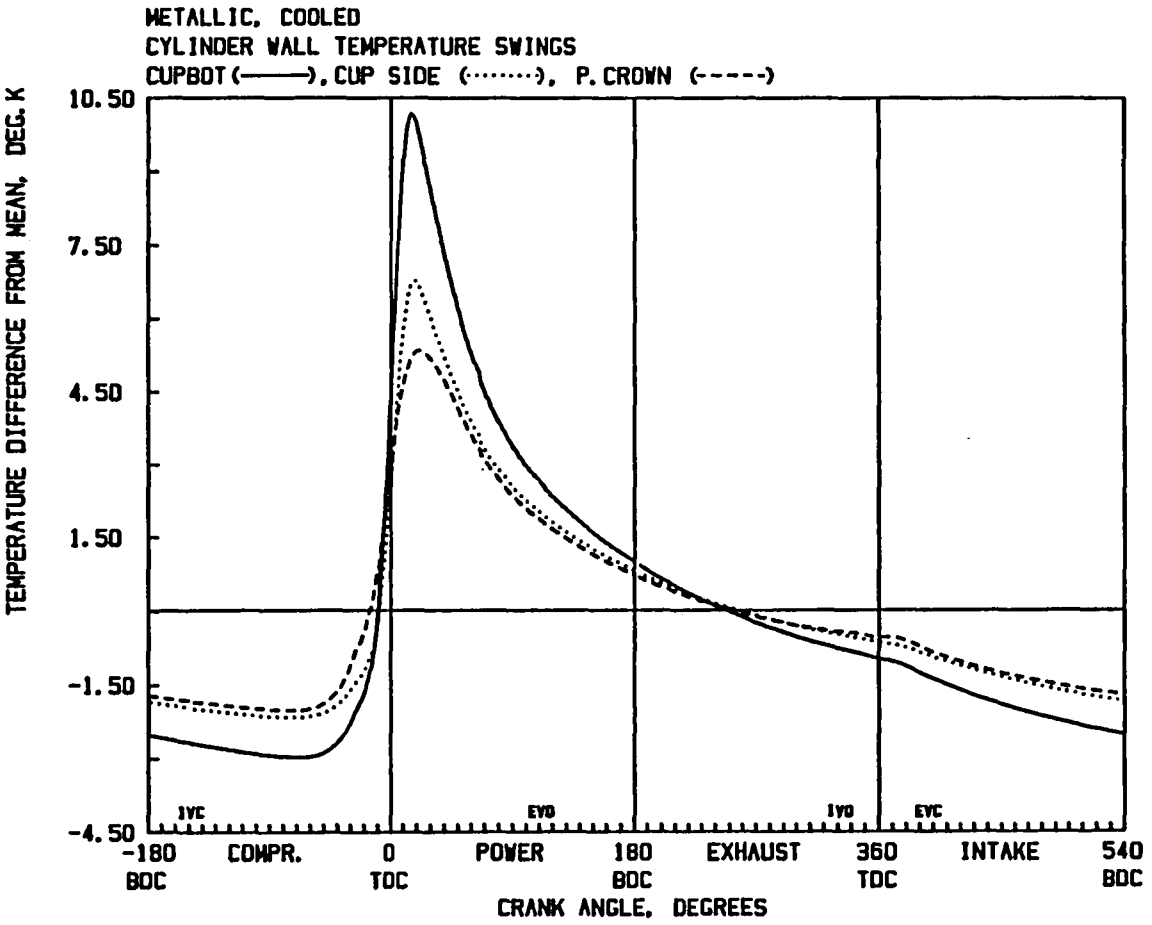

Figure 2-40a Cyclic temperature variation on piston surfaces: metallic engine.

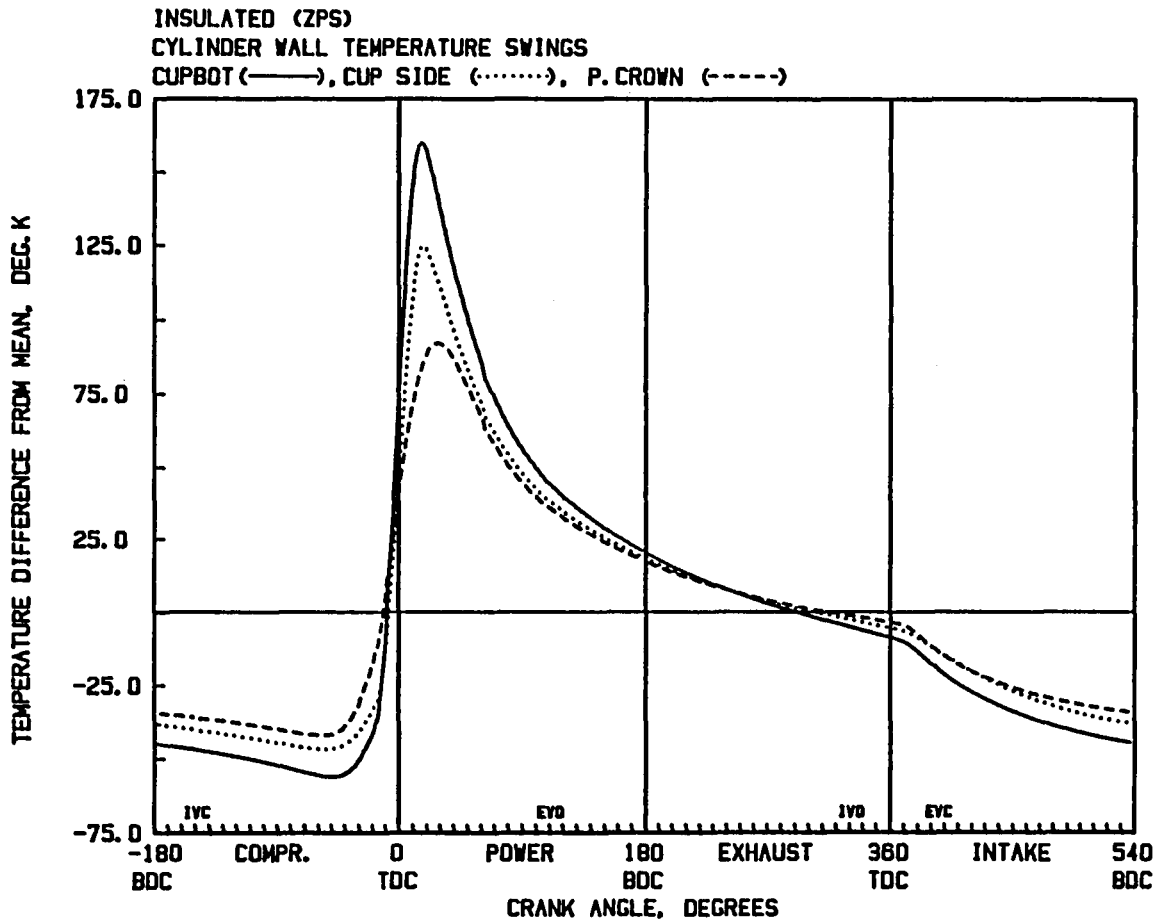

Figure 2-40b Cyclic temperature variation on piston surface: insulated (ZPS coated) engine.

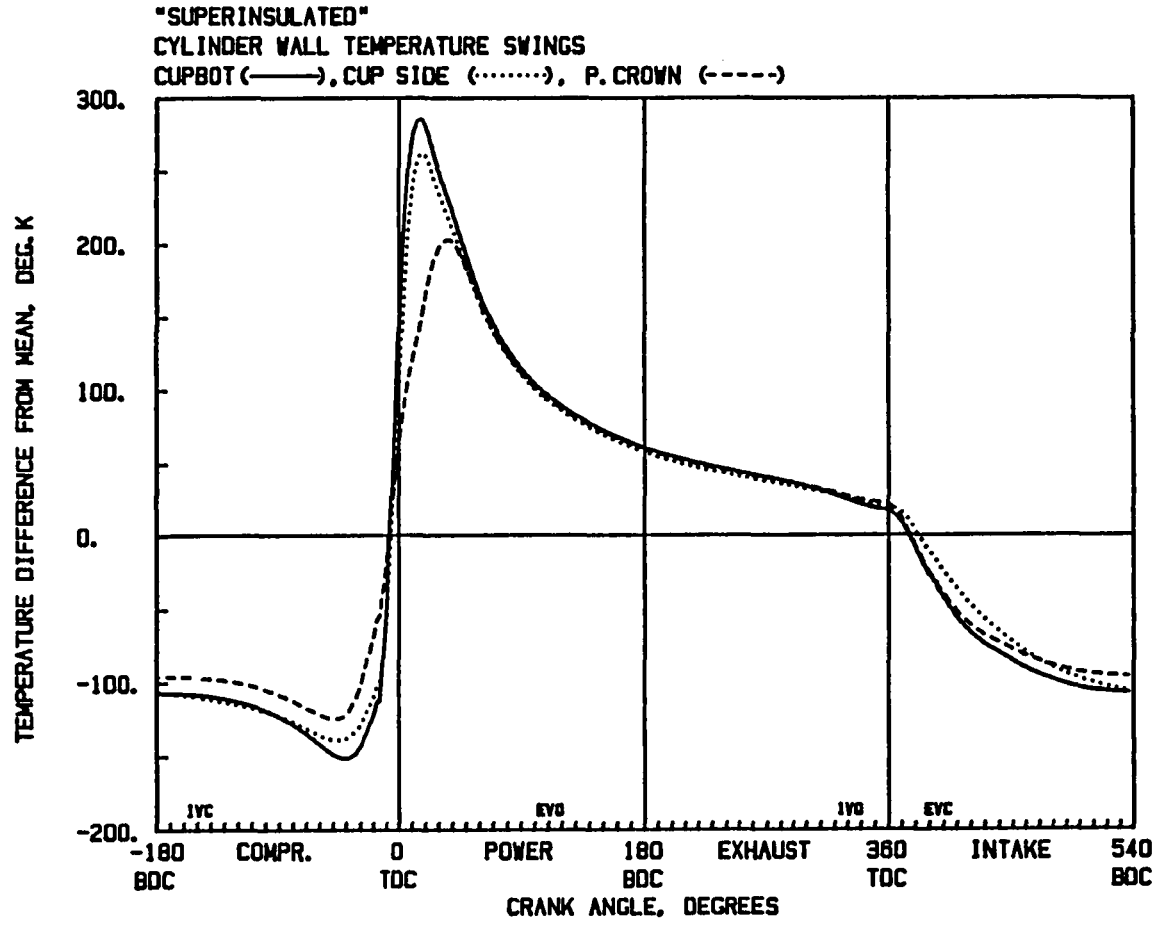

Figure 2-40c Cyclic temperature variation on piston surface: "superinsulated" engine.

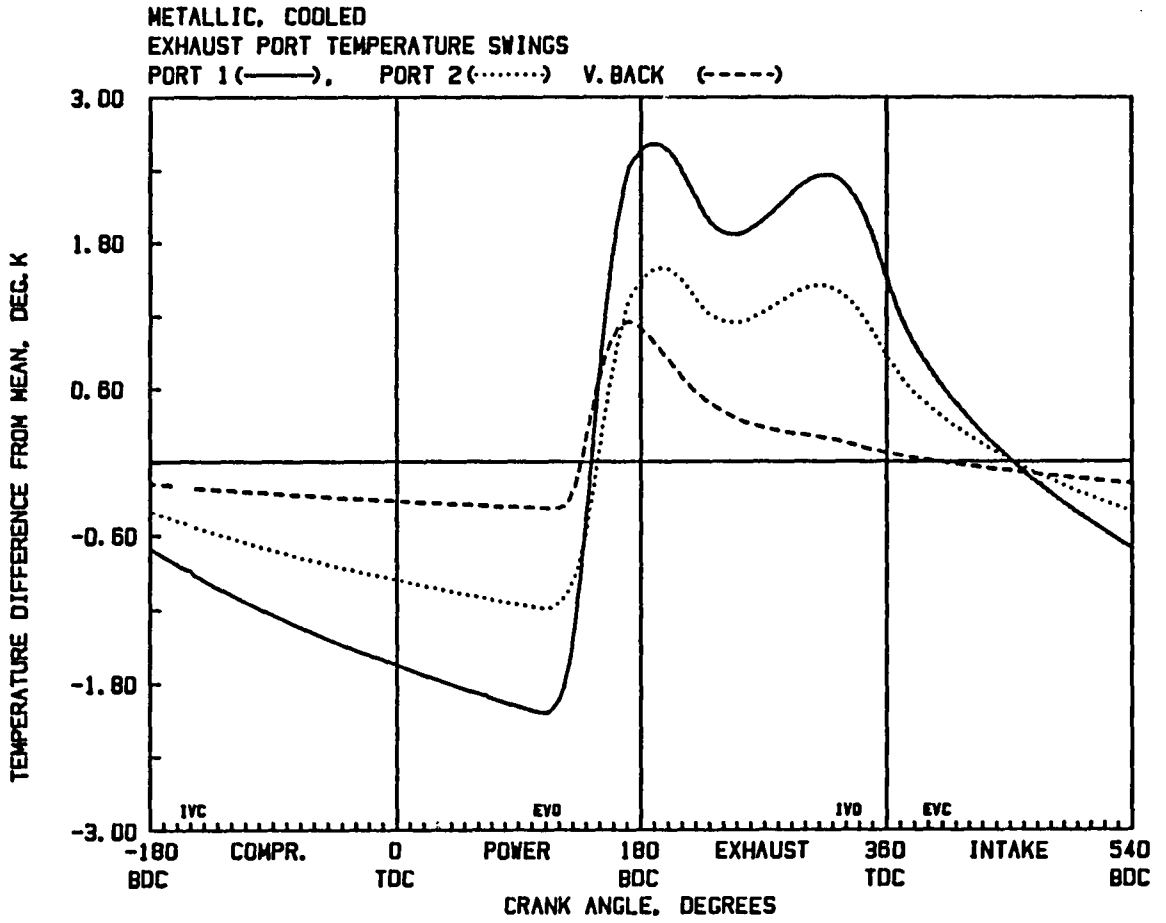

Figure 2-41a Cyclic temperature variation on exhaust port surfaces and back of exhaust valve: metallic engine

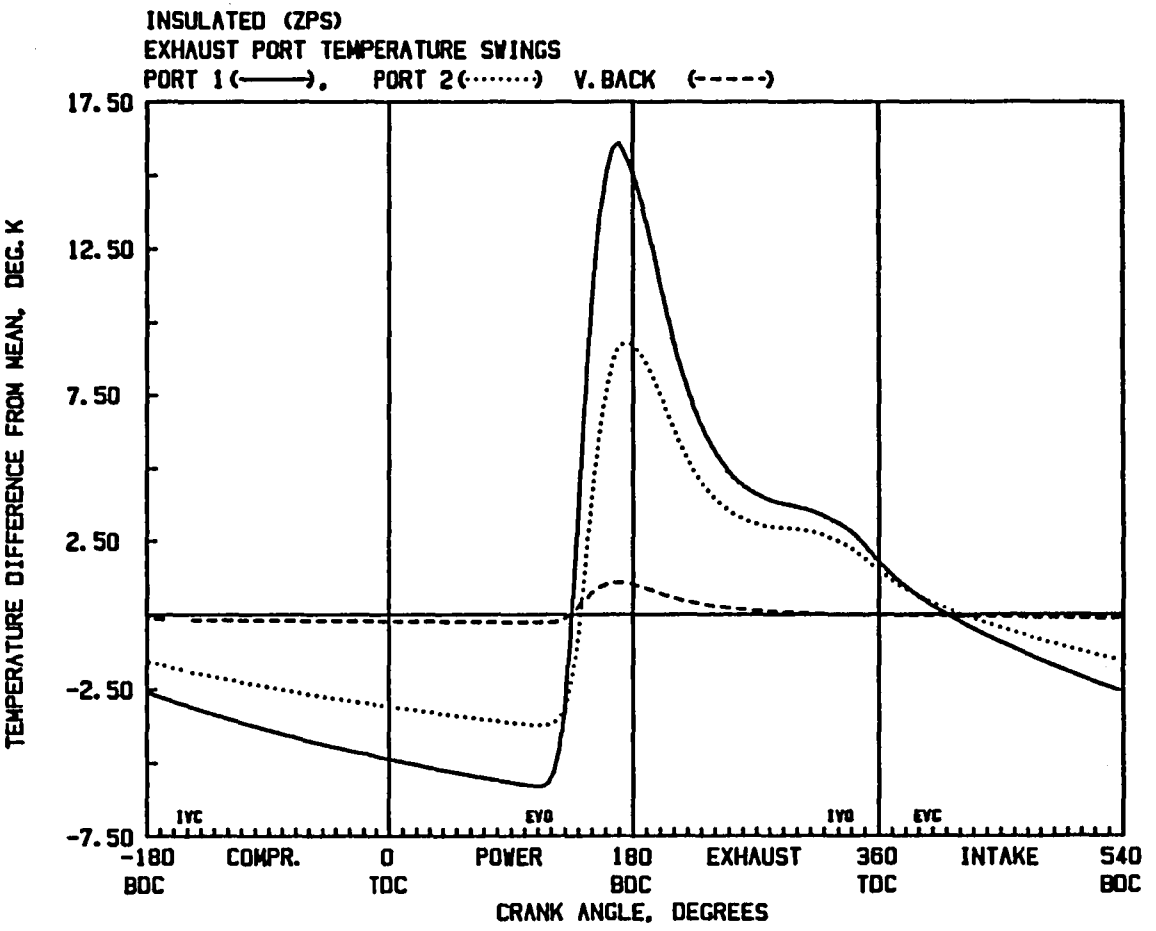

Figure 2-41b Cyclic temperature variation on exhaust port surface and back of exhaust valve: insulated (ZPS) coated engine.

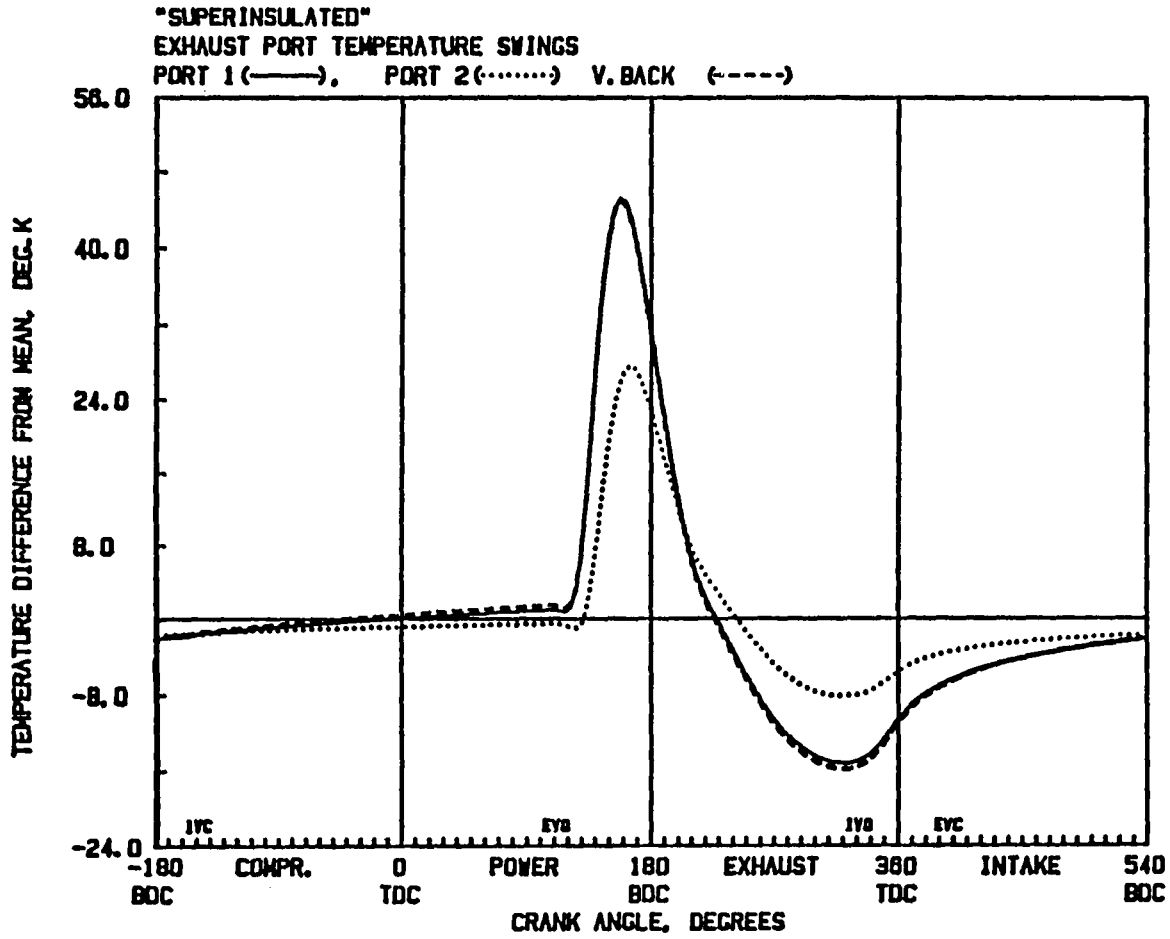

Figure 2-41c Cyclic temperature variation on exhaust port surface and back of exhaust valve: "superinsulated" engine.

period. For the metallic case, the variations of port surface temperatures follow the pattern of port flow (and therefore heat transfer coefficient) consisting of blowdown and a piston-induced exhaust pulse. The swings are only a few degrees and diminish in the downstream direction. The valve is hotter than the port surfaces and heat transfer to it is dominated by the high velocity of the flow through the valve rather than slower, averaged port velocity. This explains the single hump for the valve back temperature history after EVO, compared to the two humps for the port walls.

In the insulated case (2-41b), the magnitudes of the swings are much higher due to the different material properties. The exception is the valve back, which was not insulated. Another noticeable change is the reduced magnitude of the second pulse which is due to the higher port temperatures. For "superinsulated" conditions (2-41c) the exhaust gas temperature falls during blowdown below those of the port surfaces, thus cooling them, resulting in an altogether different shape in the transients. Although higher than for the baseline case, the port surface swings of the insulated cases are still much smaller in magnitude than those of the in-cylinder surfaces, reaching 65K for the superinsulated case and only 20K for plasma sprayed zirconia.

Liner transients. Cyclic temperature variations on liner zones are shown in Figure 2-42 (a,b,c). The shape of these profiles is quite complex and is the result of the many interactions between the liner and piston and rings. The overall configuration is that shown in Figure 2-39. The magnitude of swings is the largest on the top liner zone, where it reaches about 30% of the magnitude found on the piston surfaces. The liner surface temperatures clearly show the effect of shielding by piston, and each zone has a temperature peak during its exposure to gas. The magnitude of the peak decreases for the lower zones, and all peaks have lower magnitudes than those for permanently exposed surfaces. The effects of heat deposited by piston zones and frictional heat generation by the traversing rings are manifested as secondary peaks during the periods when liner zones are covered. These are best discernible for all three liner surfaces when valves are open

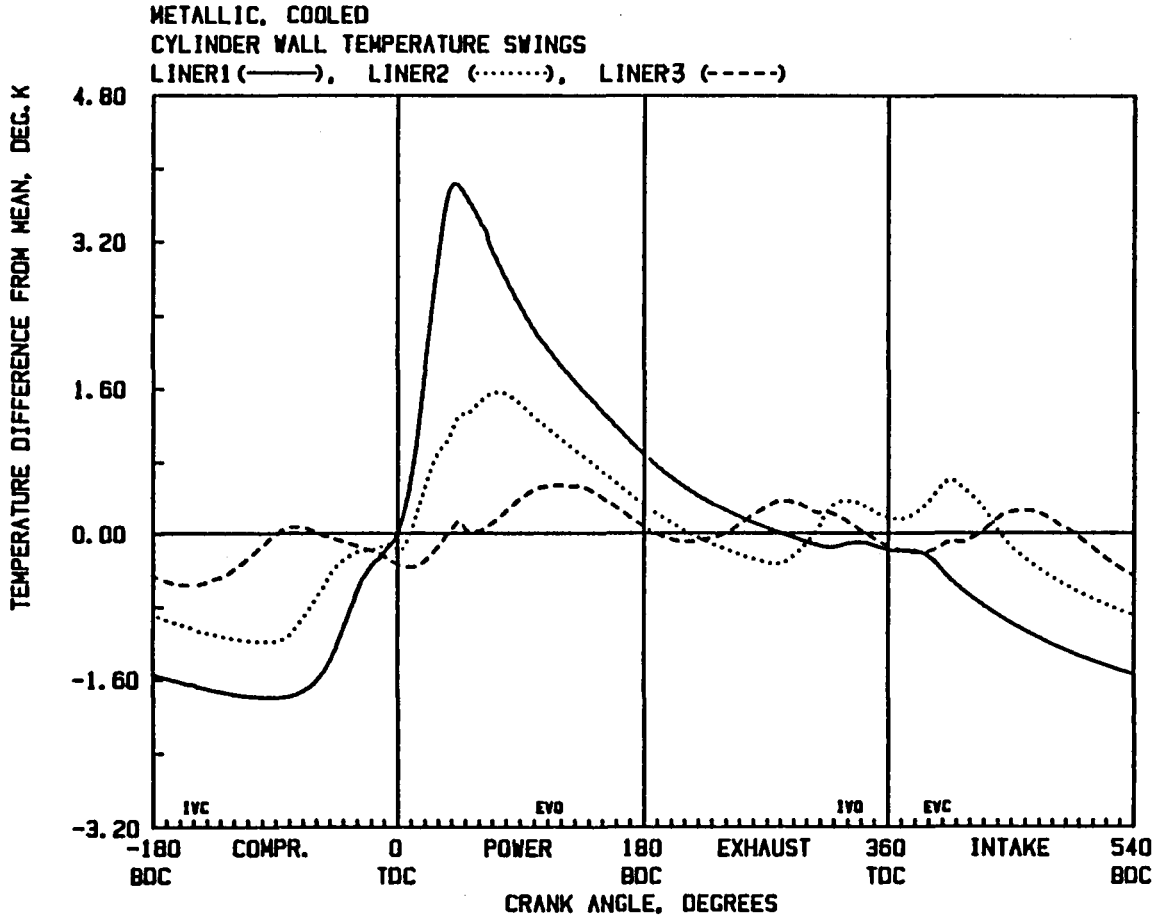

Figure 2-42a Cyclic temperature variation on liner surfaces: metallic engine.

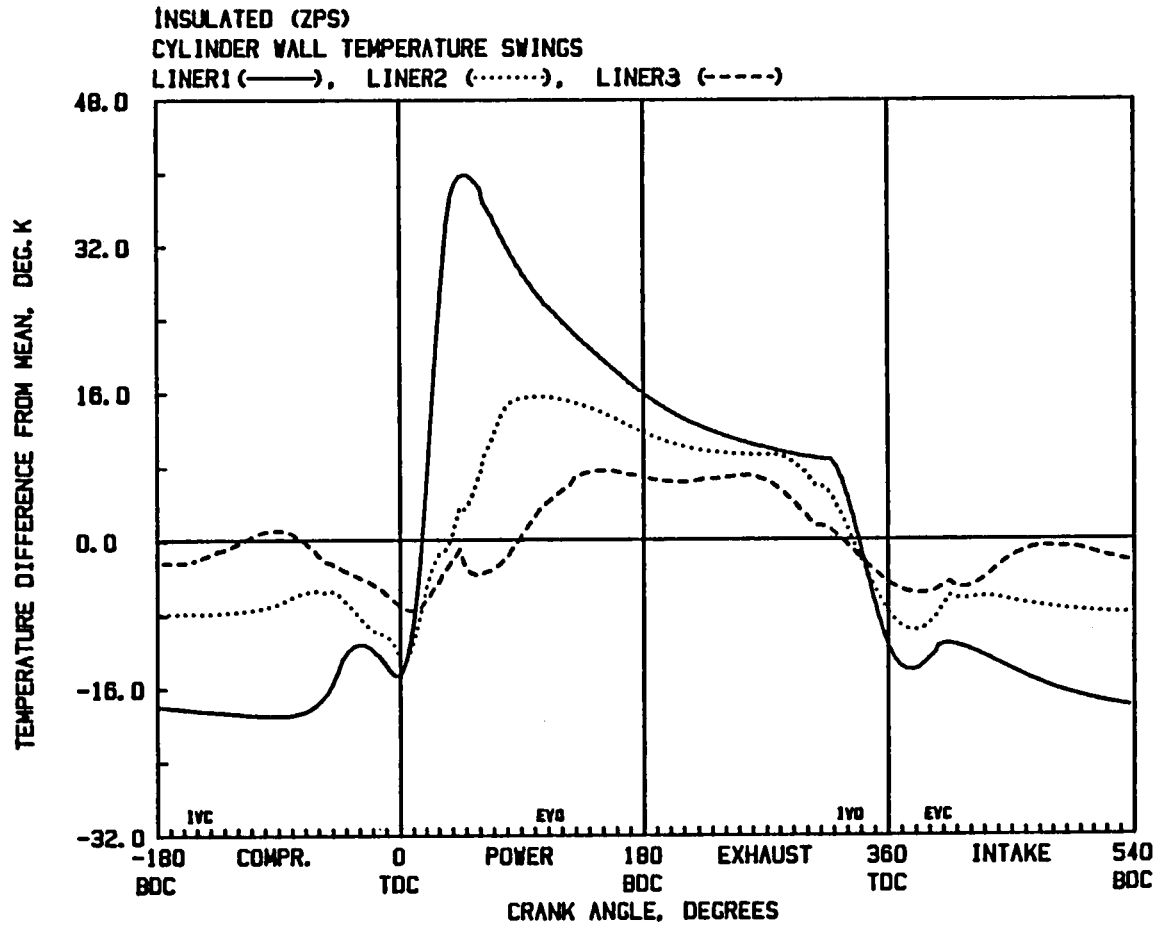

Figure 2-42b Cyclic temperature variation on liner surface: insulated (ZPS coated) engine.

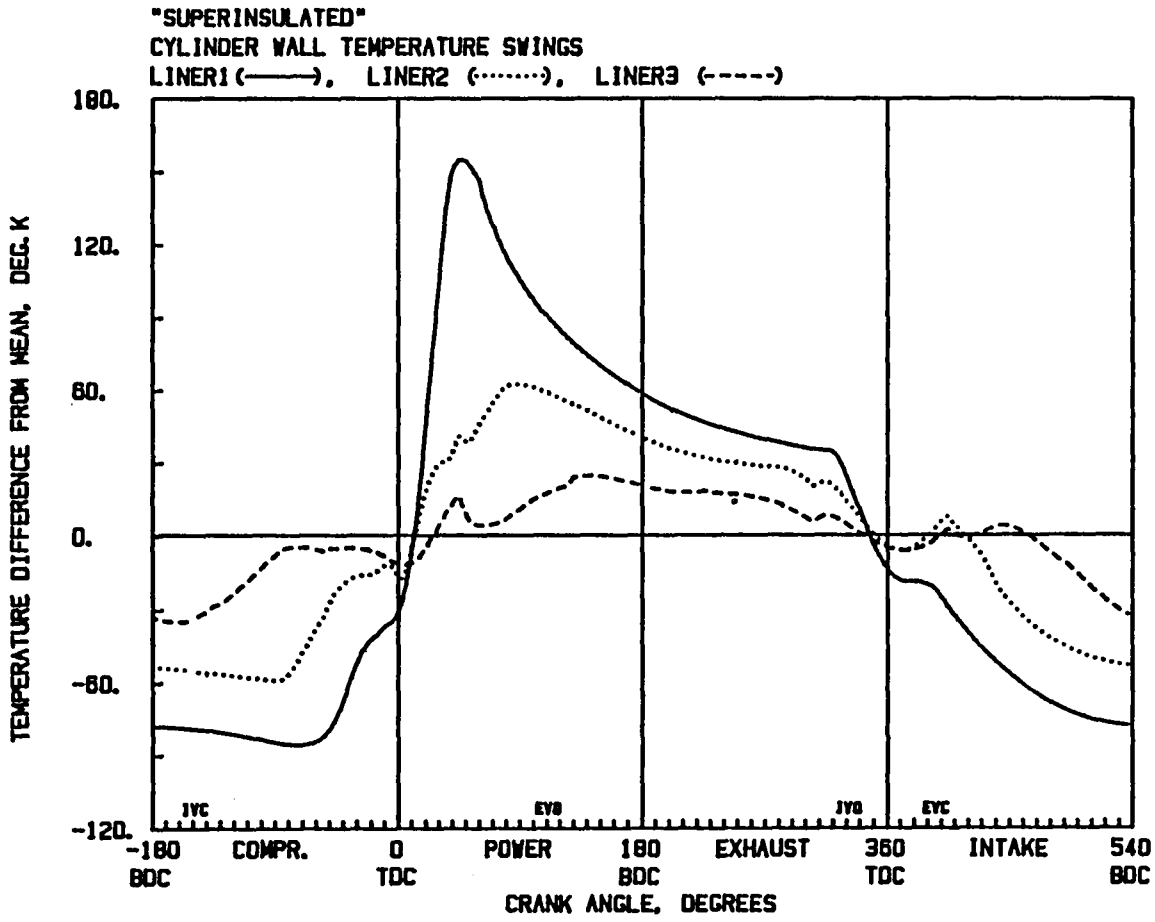

Figure 2-42c Cyclic temperature variation on liner surface: "superinsulated" engine.

and the gas heat transfer is low. Peaks on both sides of valve-open TDC indicate temperature increases resulting from convection and frictional heat being deposited on the liner surfaces due to contact with the hottest top piston zone. Smaller and sharper fluctuations occur at initiation or termination of contact between liner and piston zones or rings. These underestimate to some degree the magnitude of the local liner temperature peak under the face of a ring, since they are computed for each liner zone in a lumped sense. A finer liner division into a larger number of zones such as available with FEM conduction model, would be required to resolve these with a greater accuracy.

Predictions such as the above are an important input for studies of lubrication, friction and wear at piston-liner and ring-liner contacts. They can be used as the basis for asperity contact or "flash" temperature calculations, as well as evaluation of surface materials and lubricant thermal, mechanical and chemical properties.

Piston-liner heat transfer. The detailed treatment of the piston-liner interface including the effect of cyclic transients allows prediction of instantaneous heat transfer between piston and liner. Figure 2-43 (a,b,c) shows cyclic variation of piston-to-liner heat transfer for metallic, insulated and superinsulated configurations. For the metal engine, the heat flow is always positive (in the piston to liner direction). It is reduced near TDC, where piston contacts the hottest liner zones and the mean temperature drop between the two components decreases.

For the insulated configurations with cooled piston underside, the net heat transfer is actually from the liner to the piston, i.e., the heat deposited on the liner during exposure to gas and by friction, is transferred to piston. Instantaneous heat transfer becomes positive for short intervals on both sides of each BDC when piston is in contact with coolest portions of liner. For the superinsulated case, the cyclic variation of piston-liner heat transfer is similar, but the transferred heat consists mainly of frictional heat deposited on liner, since the gas-to-wall heat transfer has been significantly reduced.

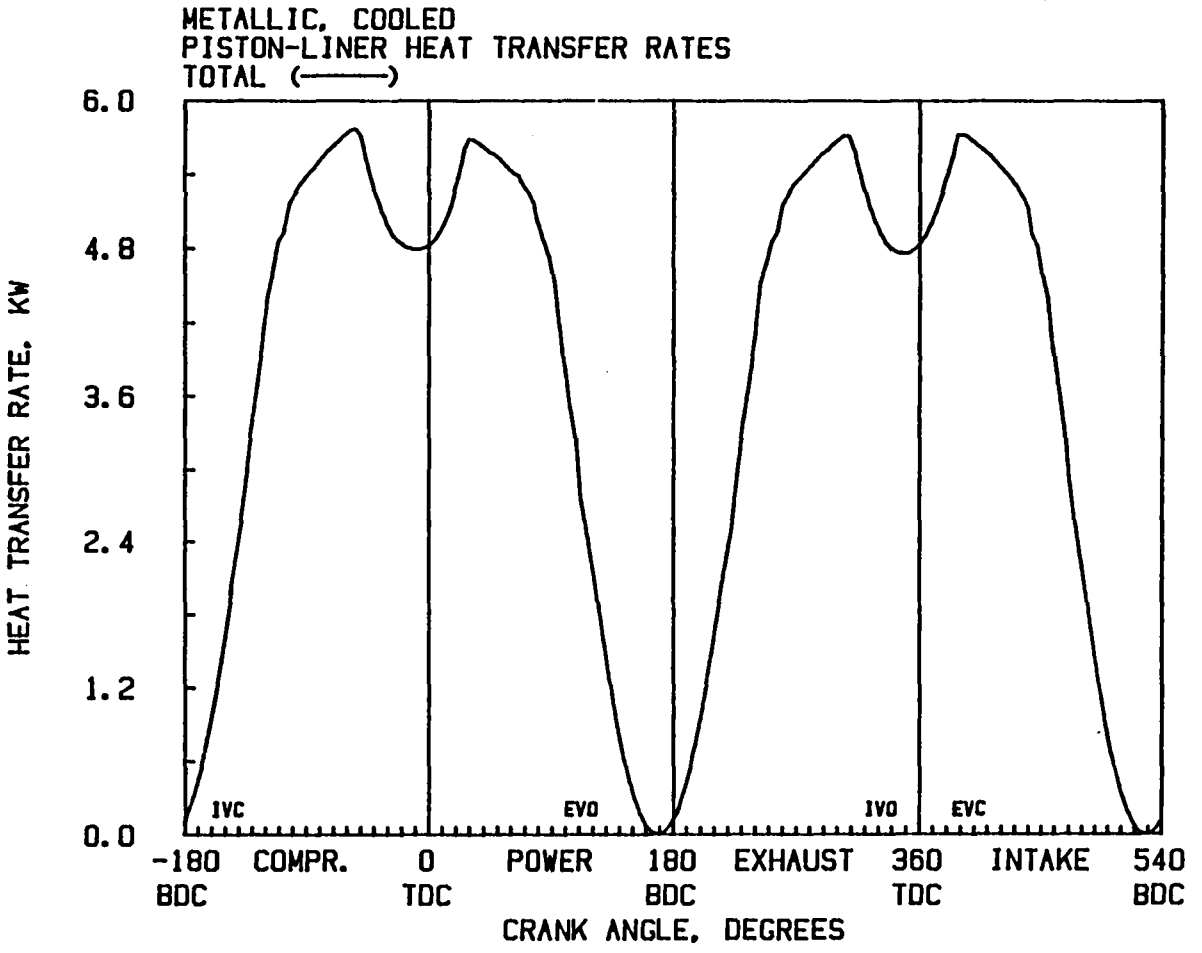

Figure 2-43a Cyclic variation of piston-to-liner heat transfer: metallic engine.

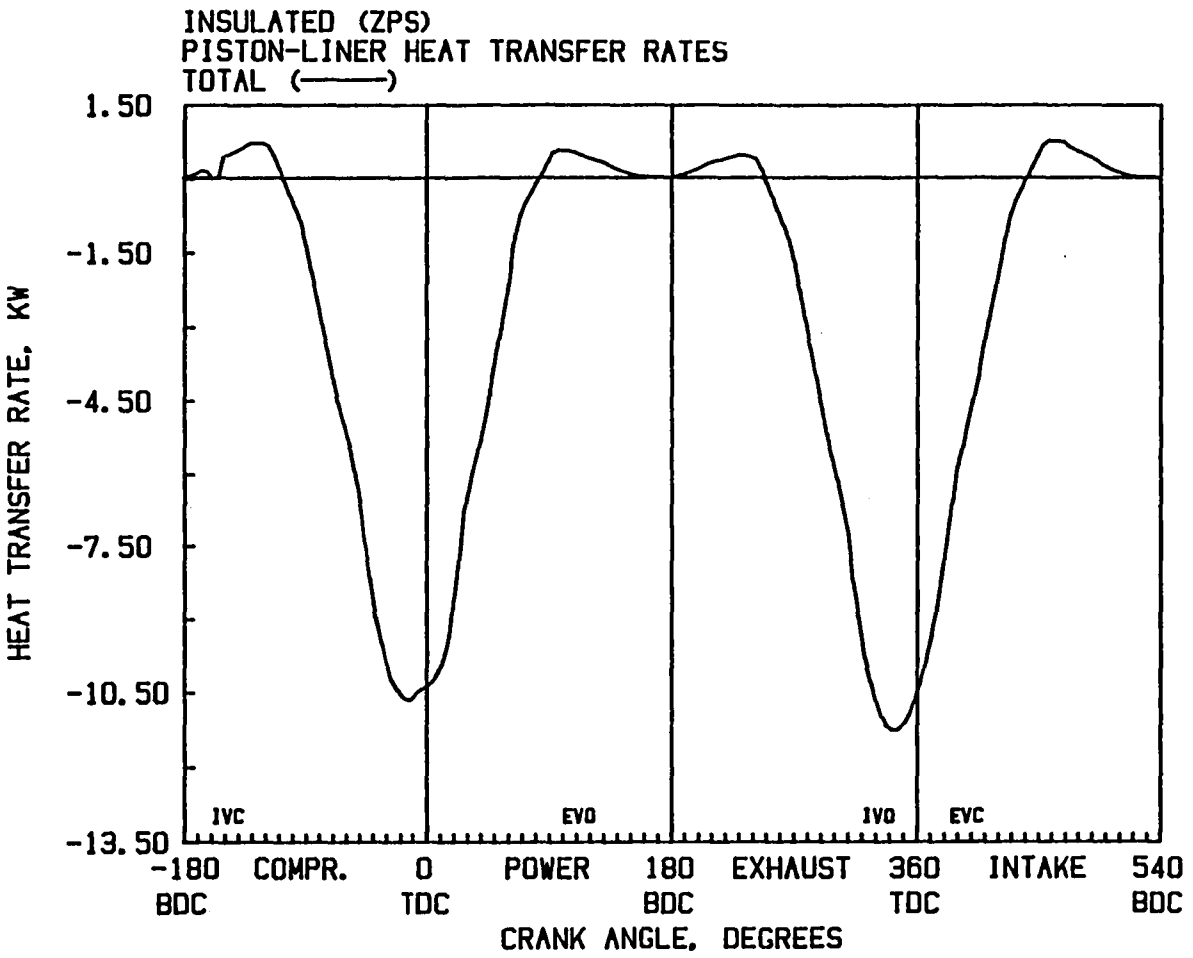

Figure 2-43b Cyclic variation of piston-to-liner heat transfer: insulated (ZPS coated) engine.

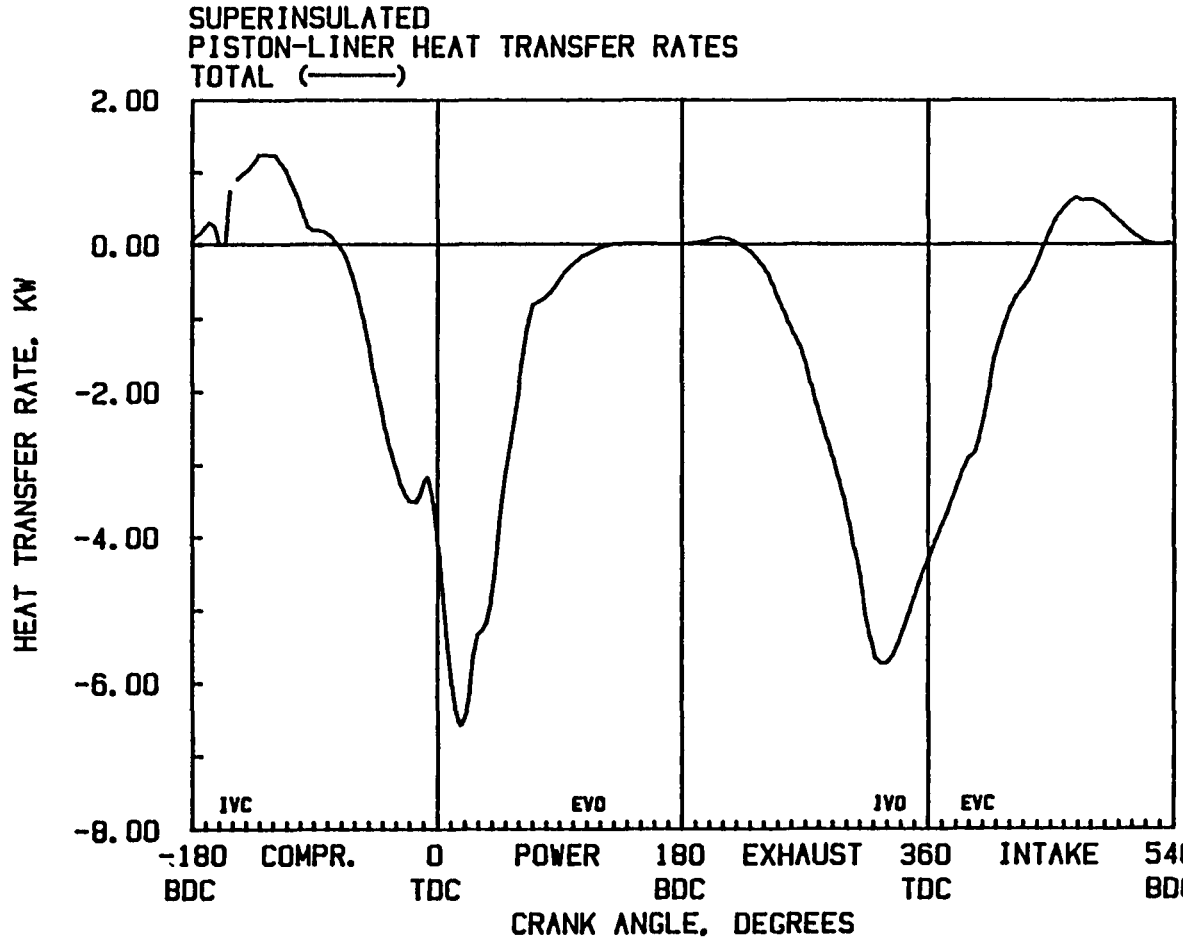

Figure 2-43c Cyclic variation of piston-to-liner heat transfer: "superinsulated" engine.

Figure 2-44 (a,b,c) amplifies on the above distinctions between the metallic, insulated and superinsulated configurations, and it indicates major heat paths and heat balances on piston and liner. The major heat paths for these three cases are as follows:

Metallic:	gas-piston-oil
	gas-piston-liner-coolant
	gas & friction-liner-coolant
Insulated:	gas & friction-liner-piston-oil
Superinsulated:	friction-liner-gas
	friction-liner-piston-liner-oil

For the insulated engine, the piston collects most of the heat deposited on the insulated liner as it travels upstroke. Most of that heat is rejected to oil. The superinsulated case is characterized by two heat paths. First, the temperature of the exposed portion of the liner is elevated to the extent that net convective heat transfer is negative (from liner to gas) and exceeds the positive contribution of radiation, implying that some of the friction heat is also rejected to the gas. Second, since both piston and liner are non-conducting, frictional heat is transported downward by being temporarily stored in surface layers. It is first stored in the piston and then transferred to and stored in the lowest liner zone from where it is rejected to oil. The superinsulated result thus serves to graphically demonstrate the heat path along the moving piston/liner interface. As a result of this path, the effectiveness of the liner insulation as a thermal barrier is reduced, as some of the heat is removed and carried away by the piston.

Effects of neglecting transients. To quantify the effects of not fully coupling surface cyclic transients to the steady-state methodology, (i.e., neglecting 2nd order correction terms), the computations were repeated for the metallic, insulated and "superinsulated" configurations, but the 1-D transient conduction model was suppressed, thus setting all correction terms (to steady-state boundary conditions) in

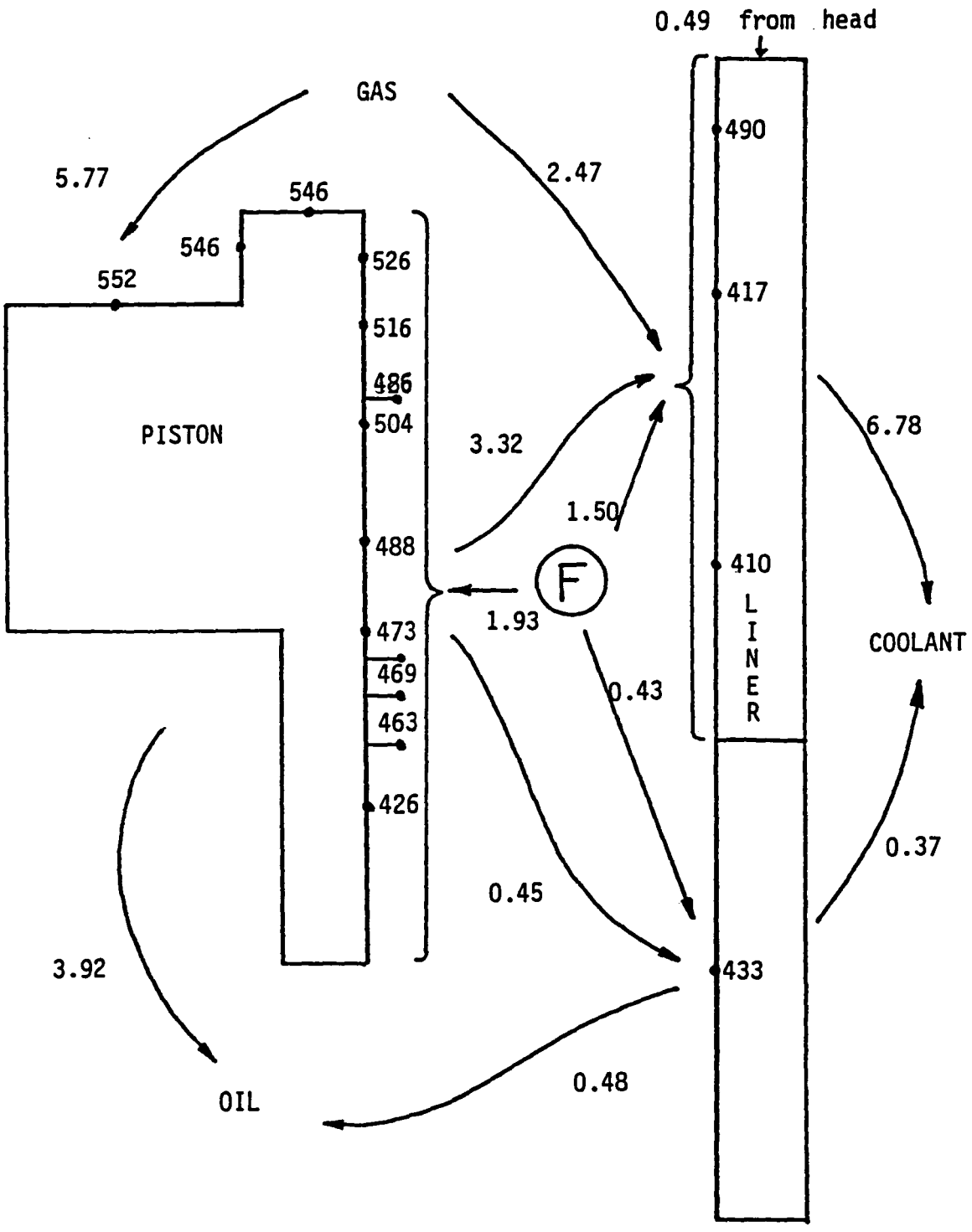

Figure 2-44a Temperatures (deg K), heat paths and heat transfer rates (fraction of fuel energy) at the piston-liner interface: metallic engine.

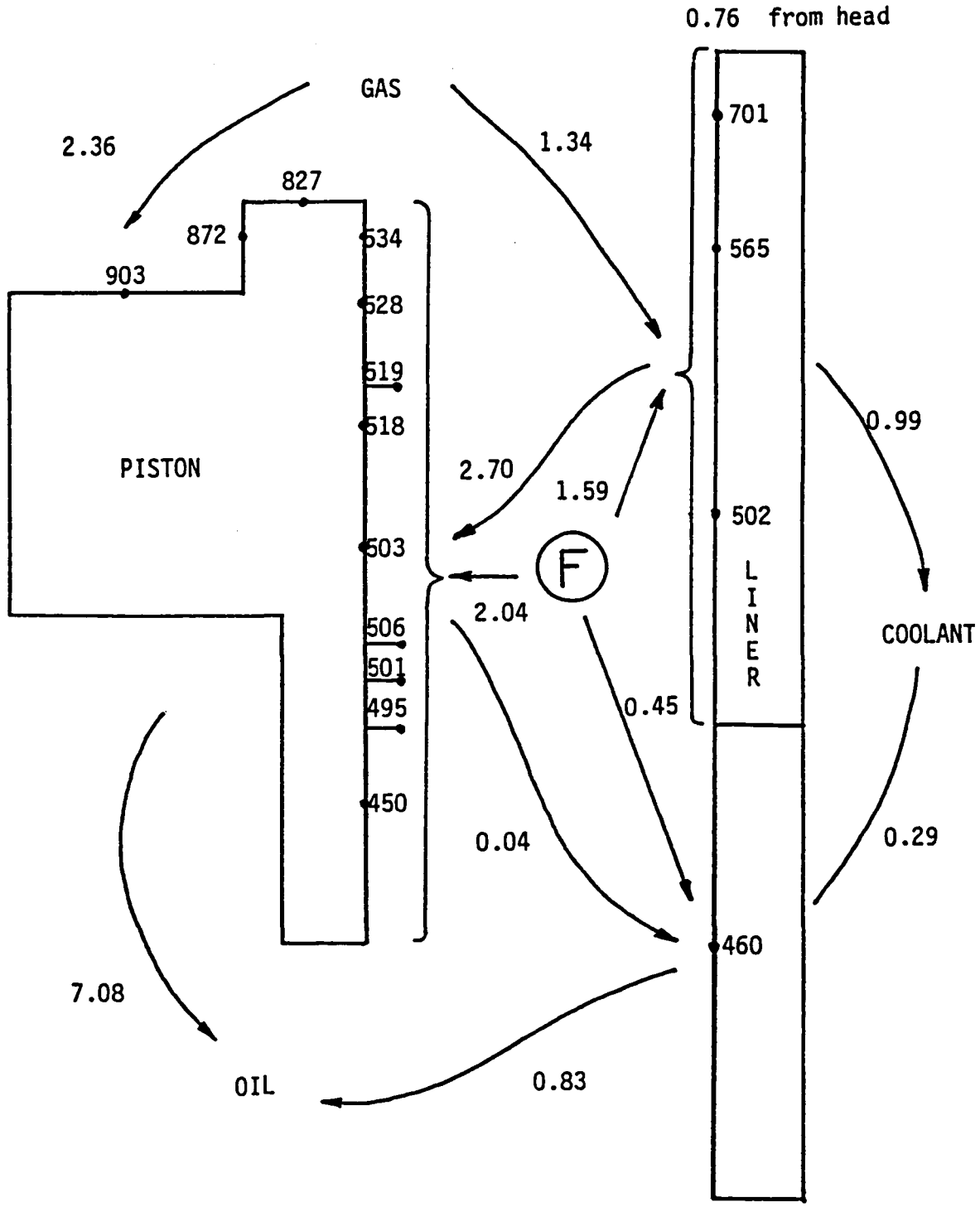

Figure 2-44b Temperatures (deg K), heat paths and heat transfer rates (fraction of fuel energy) at the piston-liner interface: insulated (ZPS coated) engine.

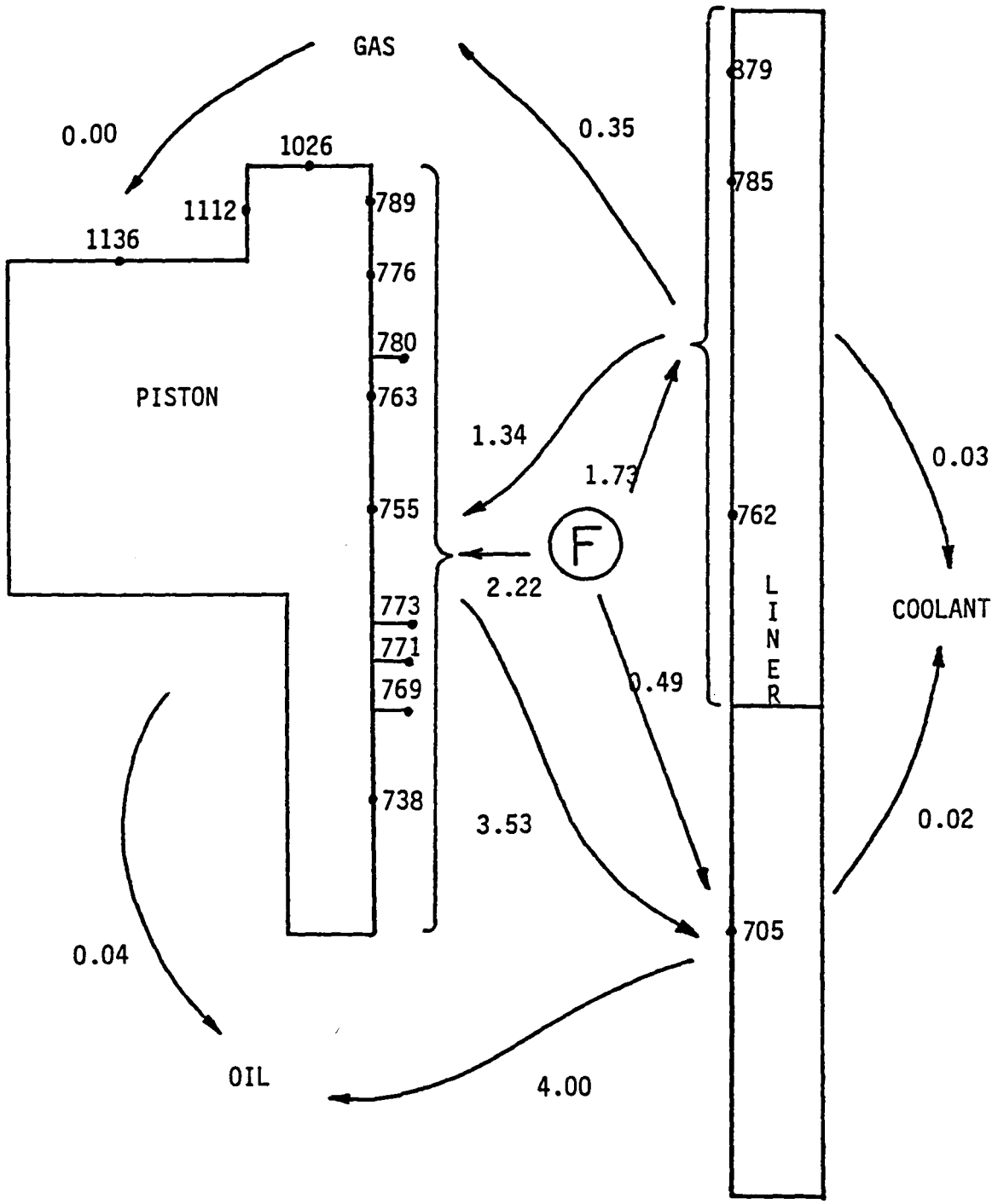

Figure 2-44c Temperatures (deg K), heat paths and heat transfer rates (fraction of fuel energy) at the piston-liner interface: "superinsulated" engine.

eqs. (2-4) (2-6) and (2-7) to zero. Predicted steady-state temperatures and heat transfer rates with and without the inclusion of the effect of cyclic transients were compared.

Almost no differences were found in the metallic case, which is not surprising in view of the small magnitude of the swings for this case. For the insulated configuration, total cylinder heat transfer was over-predicted (5.34 vs. 5.05% of fuel energy) by neglecting transients, with overpredictions of heat transfer rate to individual components by up to 7.2% and mean component temperatures by up to 38^{o}K. For the hypothetical superinsulated engine, component heat transfer rates and temperatures were overpredicted by up to 22% and 122^{o}K respectively, although total cylinder heat transfer (which is negative and occurs mostly when the liner temperature is higher than the gas temperature) was not affected. The above results indicate that there is a loss of accuracy in mean temperature and heat transfer predictions when effects on cyclic transients on mean thermal load on components are neglected. The relative errors increase with increasing insulation due to the increasing amplitude of the swings. The effect of the heat loss error on engine performance predictions is small. More important are the effects of neglecting transients on surface temperature prediction, both on the mean and the peak values, and consequently on predictions of thermal stresses generated in the structure and safety margins with respect to peak allowable material temperatures.

SUMMARY

1. A steady-state finite element heat conduction methodology was developed for use with a thermodynamic I.C. engine simulation code in a coupled solution procedure. Such a procedure makes possible design-stage studies of engines, to determine accurate peak component temperatures and temperature distributions simultaneously with detailed engine performance predictions. The methodology has been fully coupled to the convective, radiative and gas heat transfer and friction computations as well as to a transient conduction model. Exercising the model requires the pre-processing

of finite element structural (geometry, properties) data into a generic and compact packet of information (consisting of global conductance matrix, ordering array, and boundary element directory) which is then input into the thermodynamic cycle code. This can be accomplished with most existing general-purpose finite element software.

2. An important contribution is the rigorous mathematical procedure developed within the context of above conduction models, which is an essential element required for correct treatment of the piston-liner interface, accounting for the motion of the piston and the periodic gas-liner, piston-liner and (crankcase) oil-liner thermal interactions and the effect of cyclic transients.

3. An existing network steady-state heat conduction model, less computationally demanding than the FEM model, was used to carry out parametric studies to quantify and document effect of speed, load and progressive insulation on average component temperatures, heat transfer rates and heat paths. Significant differences were documented between surface temperatures of various components (piston, liner, firedeck, valves) forming the combustion chamber. These variations generally increase with load and insulation. The study of insulation effects has shown the increasing effectiveness of insulation at higher loads and has identified variations in heat transfer reduction (due to insulation) among different combustion chamber surfaces. Most notably different is the liner, which differs from the other components by being only partially exposed to gases, and by the presence of piston-liner interactions. The hypothetical case of "superinsulated" components was also used in the study to establish limits in temperatures and heat transfer rates and demonstrate the changes in heat path patterns with insulation strategy. A separate study was carried out of effects of progressive insulation on cyclic transients, with an emphasis on piston-liner thermal interactions and effects of neglecting transients. The errors stemming from neglecting cyclic transients were shown to affect the predicted heat transfer and steady-state temperatures for insulated configurations.

4. Using COSMIC/NASTRAN, finite element representations of a Cummins NH series engine combustion chamber components were constructed. NASTRAN axisymmetric, 3-D elements and scalar elements were used to model the geometry. Thermal interactions at the piston-ring, ring-liner piston-liner and valve-seat interfaces were included in the representations. The NASTRAN code was used to obtain the global conductance matrix, ordering array and a boundary element directory for the engine FEM model.

5. The FEM steady-state heat conduction methodology was exercised in a parametric study of effects of load at rated speed using the FEM models of Cummins NH engine geometry. Variations of peak temperatures as well as differences between FEM and network temperature results, with load, were documented. Effect of load on detailed component temperature distributions were also obtained. Results support experimentally established information on peak temperature locations and "hot spots" (e.g., firedeck between exhaust valves, exhaust valve face and neck). In addition, effects of specific features of the analyzed engine design (conical protrusion in piston cup, in-port coolant channels etc) were observed. Detailed results on liner surface heat flux distribution including effects of load and various heat paths, were obtained as a result of the capability to rigorously treat the piston-liner thermal interface.

REFERENCES

Borman, G. L., "Mathematical Simulation of Internal Combustion Engine Processes and Performance Including Comparisons with Experiment", Ph.D. Thesis, University of Wisconsin, 1964.

Li, C. H., "Piston Thermal Deformation and Friction Considerations", SAE Paper 820086, 1982.

Holtman, R. L., Layne J. L. and B. Schecter, "An Investigation of Enhanced Capability Thermal Barrier Coating Systems for Diesel Engine Components", NASA report Contract No. DEN 3-326, 1984.

McDonald, P. S., and Purnell D. J., "Methodology for Finite Element Based Thermal Analysis of Low Heat Rejection Diesel Engine Combustion Chamber", SAE paper 850507, 1985.

Woschni, G., "Prediction of Thermal Loading of Supercharged Diesel Engines", SAE paper 790821, 1979.

Kao, T. K. and Wallace F. J. "A New Approach to the Prediction of Heat Flow and Temperature in Engine Pistons with Special Reference to Thermal Barriers", I. of Mech. Eng. Sci., Vol. 23 pp. 647-657, 1981.

III. EXAMINATION OF SOME OF THE KEY ISSUES IN LOW HEAT REJECTION ENGINES

INTRODUCTION

METHODOLOGY

DESIGN ANALYSIS MATRIX

RESULTS

- Turbocharged Intercooled Engine
  - Exhaust Heat Recovery
  - Total Heat Rejection
  - Liner Insulation
  - Reduced-Cooling Engine
  - Liner Temperatures
- Effects of Intercooling
- Summary of Benefits for an Optimum Insulated Truck Engine
- Turbocharged Automotive DI Diesel with Swirl Combustion

COMPARISON TO PREVIOUS PREDICTIONS

CONCLUSIONS

III. EXAMINATION OF SOME OF THE KEY ISSUES IN LOW HEAT REJECTION ENGINES

INTRODUCTION

Improvement in engine thermal efficiency by reduction of in-cylinder heat transfer has received much attention. The objective is to retain within the cylinder (ie., conserve) the fuel energy normally lost to heat transfer to increase the work done on the piston, as well as to provide a higher temperature exhaust stream for downstream energy recovery. Experimental programs are underway, which are attempting to develop durable low heat rejection engine components and also to demonstrate the potential benefits of this concept in practical prototype hardware.

The issues facing the engine designer are diverse and complex. They include key questions concerning application of insulation within the engine such as:

1) which materials to use,
2) what are the preferred locations within the combustion chamber;
3) how thick a layer is needed;
4) application methods (coatings, brazing, interference fit, etc.);
5) what temperatures and stress levels will exist in the insulating materials within the envelope of operating conditions; and
6) what thermal and mechanical properties these should have to insure the desired benefits and life.

These questions serve only to highlight issues that, in reality, are highly interactive and must be addressed in a coupled way in order to optimize the design. From the point of view of benefits, the questions one needs to ask relate to:

1) conversion efficiency, i.e. the split between the conserved heat that flows directly to piston power and that which flows into exhaust energy;

2) magnitude of benefits for a turbocharged engine with no exhaust energy recovery;
3) comparison of turbocompounding to Rankine cycle bottoming;
4) desirability of intercooling under insulated conditions;
5) effects of insulation on volumetric efficiency and engine power;
6) thermal efficiency and heat rejection benefits of liner insulation in relation to increased tribological challenge and reduced volumetric efficiency;
7) temperature levels in the liner/ring/piston interface; and
8) benefits of insulation for smaller automotive DI diesels.

In the present work we have applied the engine analysis code IRIS, described below, to address the above issues, and have outlined and carried out parametric studies to derive insights and answers for the posed questions.

METHODOLOGY

The methodology employed in this work is driven by the fact that the issues involved in low heat rejection engine design are largely coupled and require an integrated systems approach. To enable such approach, a comprehensive engine systems computer code IRIS has recently been developed. Among its unique features are detailed heat transfer models representing convective and radiative gas phase heat transfer, steady state heat conduction in the engine structure, and cyclic heat transfer thermal transients in the surfaces surrounding the combustion chamber. These models have been described in the Phase I report as well as in individual publications dealing with convective heat transfer (Morel and Keribar, 1985), cyclic transients (Morel et al, 1985b) and heat radiation (Chapter I of this report) and they are briefly summaried below.

Convective Heat Transfer Model. The convective heat transfer model is based on an in-cylinder flow model which computes swirl, squish and turbulence as a function of crank angle. It has a degree of spatial dependence, in that it divides a bowl-in-piston geometry into three flow

regions (squish region above piston crown, cup volume, and region above the cup), and solves in each differential equations for swirl and turbulence. Its main features are: (1) the inherent dependence on actual flow velocities, which drive the convective heat transfer, and (2) the spatial resolution, which this allows, including the capability to treat reentrant piston bowl shapes.

Radiation Heat Transfer Model. Due to soot formation during diesel combustion, thermal radiation from gases to surrounding combustion chamber surfaces is a significant component of heat transfer for diesel engines. Instantaneous and mean levels of heat radiation are functions of the volume and distribution of burning gas, amount of soot present in the burning gas, combustion chamber geometry, and also of surface emissivities and temperatures. The heat radiation model incorporated in IRIS takes into account all of these dependencies. The soot concentration levels are calculated using a kinetic model, which provides rates for soot formation and subsequent burnup as a function of engine parameters and crank angle. The spatial distribution of the heat radiation can be calculated from the volume and shape of the burned zone. The burned zone volume is calculated from the cycle thermodynamic simulation, and its shape and location are obtained from an empirically based geometric model. All soot is assumed to be contained within the burned gas. The spatial distribution also includes the effects of chamber geometry through calculation of the actual optical thicknesses seen from one surface when viewing another, or when viewing the burned zone. This is accomplished through the use of a zonal radiation model, which divides the combustion chamber surface into seven individual subsurfaces. This model also represents the attenuation of radiation from one surface to another, as it passes through the absorbing burned zone, and accounts for multiple reflections of incident radiation from one surface to another.

Steady State Conduction. Steady state conduction through the engine structure is calculated in all of the present studies via a thermal resistance network model which approximates the engine by discretization into 158 elements. As shown in Chapter II, this representation provides

a realistic representation of the structure at a level of detail sufficient for analysis of general issues such as those addressed here. It allows for the simulation of laminated structures composed of layers of materials with various thermal properties, as is essential in studies of different insulation strategies. IRIS also has the capability to represent the structure by a finite element model for detailed design studies of specific engine geometries, but that option was not exercised in this study.

Cyclic Temperature Transients. The heat flux from the gas to the wall is highly transient, with high flux levels occurring during combustion followed by low heat flux periods. This pattern produces temperature transients in thin layers adjacent to the gas-side surfaces. The surface temperature swings are on the order of 20K for iron or aluminum surfaces, but for low conductivity coatings it can reach several hundred degrees Kelvin. IRIS analyzes the surface temperature dynamics by a transient one-dimensional model which interacts, in a spatially resolved way, directly with the steady state conduction model.

Mechanical Friction. The mechanical friction model is used to calculate the brake performance quantities and also to provide the frictional heat loads at the piston/liner interface. The model simulates the piston-connecting rod dynamics, which together with gas forces provides the total piston-liner contact force. Then, solving for ring hydrodynamic lubrication, the instantaneous friction at the ring-liner interface is calculated for hydrodynamic, boundary and mixed conditions.

Exhaust Heat Recovery Devices

One of the exhaust recovery devices considered in this study was the power turbine similar to that used by Cummins in their advanced turbo-compounding work (Hoehne and Werner, 1982). A 16.42 gear ratio was assumed between the power turbine and the crankshaft, producing over 31,000 turbine rpm at the rated speed. Since the power turbine produces a significant back pressure, which affects the operation of the turbo-charger, the entire engine/turbocharger/power-turbine combination has to

be treated as a coupled system. An iterative procedure is imbedded in IRIS, which accomplishes this coupling and allows a realistic simulation of the system.

The other recovery device considered is an organic Rankine cycle bottoming (RCB) machine operating on RC-1 organic fluid. The efficiency data describing the operation of this device were taken from the work DiNanno et al (1983), dealing with a Thermo Electron Corporation design study of RCB for adiabatic diesels. The system selected was an advanced but realistic high-pressure system with turbine inlet pressure of 35 bar (500 psi) and turbine inlet temperature of 670 K (750 ^{o}F). This RCB machine produces shaft work from the exhaust energy with an overall enthalpy conversion efficiency (referred to ambient conditions) of 12-17 percent over the range of typical engine exhaust temperatures of 600-1050 K. (Higher efficiencies could be obtained with less conservative RCB designs with turbine inlet pressure up to 70 bar (1000 psi).) In calculation of the work produced by the engine-RCB system it was assumed that the exhaust pressure drop across the RCB is very small and that it does not affect the operation of the basic reciprocator.

The results presented in the Phase I report and in Morel et al (1985a) were based on the same methodology as used here, but at an earlier stage of development. The recently developed zonal heat radiation model has replaced the simple mean-beam length model used previously and this changed the overall level of calculated heat transfer, especially at lower loads. An important addition to the scope of the systems model and to the simulations has been the representation of the exhaust heat recovery devices as described above.

DESIGN ANALYSIS MATRIX

The main emphasis of this study was on a state-of-the-art heavy-duty highway diesel engine as represented by the Cummins NH engine, which is a 14 liter six-cylinder engine. The engine was simulated in the following configurations:

- turbocharged, intercooled (TCI)
- turbocharged (TC)

Each of these two configurations was run as

- standard engine
- with exhaust power turbine
- with Rankine cycle bottoming

Each of these in turn was run at the following conditions

- rated (1900 RPM, A/F = 28, compressor pressure ratio = 2.5)
- peak torque (1400 RPM, A/F = 24.5)
- part load (1900 RPM, 1/2 fuel rate, A/F = 41)

Finally, each of the above configurations were run under seven different heat rejection strategies:

- metallic baseline with conventional liquid coolant and oil cooling;
- metallic with reduced cooling; no liquid coolant in liner and head, enhanced piston cooling with oil gallery;
- zirconia plasma spray (ZPS) coated on all in-cylinder surfaces, except on liner below top ring reversal point, with a layer 1.5 mm thick and conductivity of 0.6 W/mK, equivalent to conductance of 400 W/m^2K. The liner below top ring reversal point was made of steel. Conventional cooling was applied to the liner. Ports were lined with a 5.5 mm of alumina titanate with conductivity of 0.5 W/mK (case Z1);
- ZPS coated -- same as Z1, but with liner below top ring reversal point insulated by monolithic zirconia 5 mm thick and conductivity of 2.0 W/mK, equivalent to conductance of 400 W/m^2K (case Z2);
- superinsulated with a thin coating of near zero conductivity applied to all in-cylinder and port surfaces, except the liner below the top ring reversal point, which was made of steel and was conventionally cooled (case S1);
- superinsulated -- all components, including liner, made of solid material with near zero conductivity (case S2);

- o zero heat transfer -- in-cylinder and port heat transfer set to zero.

In the zirconia cases, coolant side heat transfer coefficients were reduced so that the metal substrate temperatures remained below 575K.

In the superinsulated cases above, the net (time-averaged) heat transfer to any of the insulated surfaces, except the liner, was very close to zero. However, on an instantaneous basis, there were periods of high heat flux into the surfaces during the combustion and exhaust periods, followed by heat flux from the wall to the gas during intake and compression periods. By contrast, in the case of zero heat transfer there was no heat flux between the gas and the wall for all of the in-cylinder and port surfaces both on the instantaneous and time-average basis.

In total, 126 different engine data points were run to develop the insights and conclusions to be presented in this study. In addition to the above design analysis matrix concerning heavy duty highway DI diesel engines with quiescent combustion systems, a smaller matrix was run with a automotive size diesel engine. This engine was selected to be a 2.8 liter 5-cylinder in-line configuration, with a direct injection and swirl combustion system (swirl ratio of 2.3 at BDC). Turbocharged with pressure ratio of 1.8, it delivers 96 HP at the rated speed of 3600 RPM. The in-cylinder geometry of this engine differed from the truck diesel engine by bowl shape, which was deep as is typical for swirl combustion systems, and by a higher compression ratio of 17.5:1.

The design analysis matrix for this engine involved only the basic turbocharged reciprocator with no exhaust heat recovery, and it considered only two operating conditions:

- o rated (3600 RPM, A/F = 25.5)
- o part load (3600 RPM, 1/2 fuel rate, A/F = 40)

At each of these two operating conditions, simulations were run for the same seven heat rejection strategies used for the NH engine. These operating conditions may not be the most meaningful ones for typical

automotive applications, but they were selected to allow comparison with the truck engine results, thereby highlighting the effects of speed, displacement and combustion system.

Engine Adjustments at Rated Conditions

In execution of the design analysis matrix, an effort was made to ensure that the comparison of the various heat rejection configurations was as realistic as possible, i.e., that none of the configurations is put at an advantage or disadvantage with respect to the others. To this end, the peak pressure and A/F ratio at rated conditions were kept the same for all configurations. This required adjustments in the boost levels and in the fuel flow rate; these adjustments were quite small, and did not exceed, for the turbocharged intercooled engine, a reduction by seven percent in the flow rate and a reduction by 0.13 bar in the boost pressure. Another adjustment was the rematching of the turbocharger turbine, whose volute volume was increased as exhaust temperature increased. This was done to take the full advantage of the increased exhaust energy and to reduce the reciprocator backpressure. All of these adjustments were made only at the rated conditions, and the follow-up runs at peak torque and part load were simulated with the hardware unchanged.

As far as engine friction is concerned, it was assumed that for each configuration an appropriate lubricant would be used whose viscosity, at the liner temperature levels found in that configuration, would be equal to that of current oils at the operating conditions which exist in conventional engines.

RESULTS

In the presentation of the results, we shall first concentrate on the turbocharged intercooled (TCI) engine and discuss the various heat-rejection strategies and also the effectiveness of the exhaust heat recovery devices. This discussion will then be followed by presentation of results for the non-intercooled engine and for the automotive diesel.

Most of the plots are presented with in-cylinder heat transfer expressed in percent of fuel energy along the abscissa, rather than the usually used percentage of baseline heat transfer. We believe this to be a preferable approach, highlighting the level of in-cylinder heat transfer which is available for insulation purposes.

Turbocharged Intercooled Engine

The thermal efficiency of the entire engine system is shown in Figure 3-1. This figure, and a number of others that follow, has three parts a, b and c; these always refer to rated conditions, peak torque and part load, respectively. The abscissa shows the in-cylinder heat transfer for each of the heat rejection configurations, expressed in percent of fuel energy. It may be seen that as in-cylinder heat transfer decreases, the thermal efficiency increases; as could be expected, it reaches maximum values for zero heat transfer. Expressed in terms of percentage fuel efficiency improvement above the baseline turbocharged/intercooled engine with conventional cooling, Figure 3-2, one finds that reduction in heat rejection, coupled with exhaust heat recovery, can produce very significant benefits.

Exhaust Heat Recovery. The benefits seen in Figure 3-2 may be divided between those generated by insulation and those produced by exhaust heat recovery. It may be seen that even in the absence of heat recovery devices, the turbocharged intercooled engine benefits by insulation, its efficiency rising for the Z1 configuration by 5 percent at rated condition, by 5.4 percent at peak torque and by 4 percent at part load.

The exhaust heat energy, which depends on the engine load and on the level of in-cylinder heat rejection, may be used to provide further significant benefits when exhaust heat recovery devices are used. This energy is characterized in Figure 3-3 by the turbocharger turbine exit temperature. These additional benefits are illustrated in Figure 3-4, which shows the percentage improvement in thermal efficiency with respect to turbocharged/intercooled baselines with the same heat rejection configuration. It may be seen for the Z1 the additional

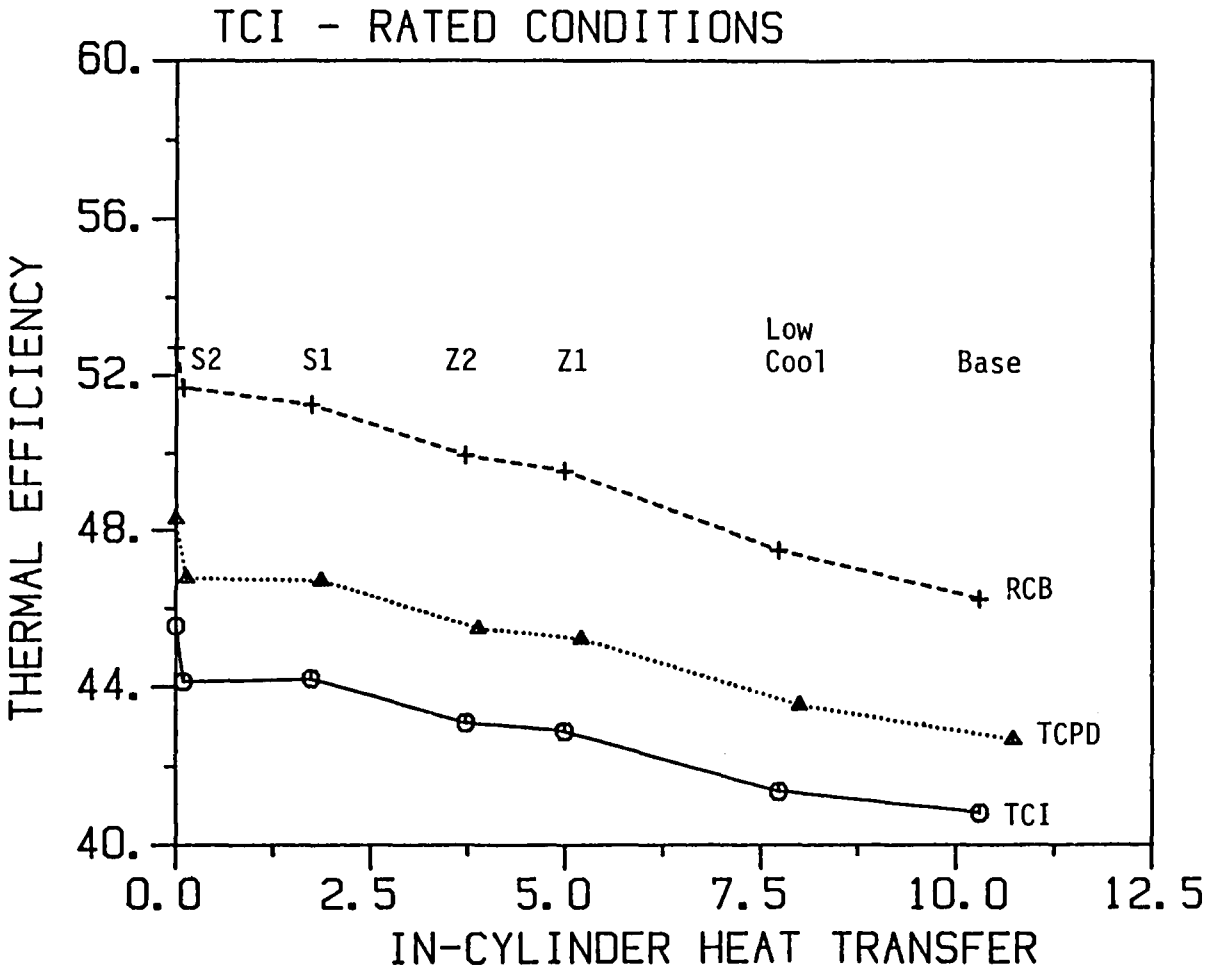

Figure 3-1a Thermal efficiency of a turbocharged intercooled truck engine under various heat-rejection strategies. Rated conditions. The in-cylinder heat transfer is expressed here and in all remaining figures in percent of fuel energy.

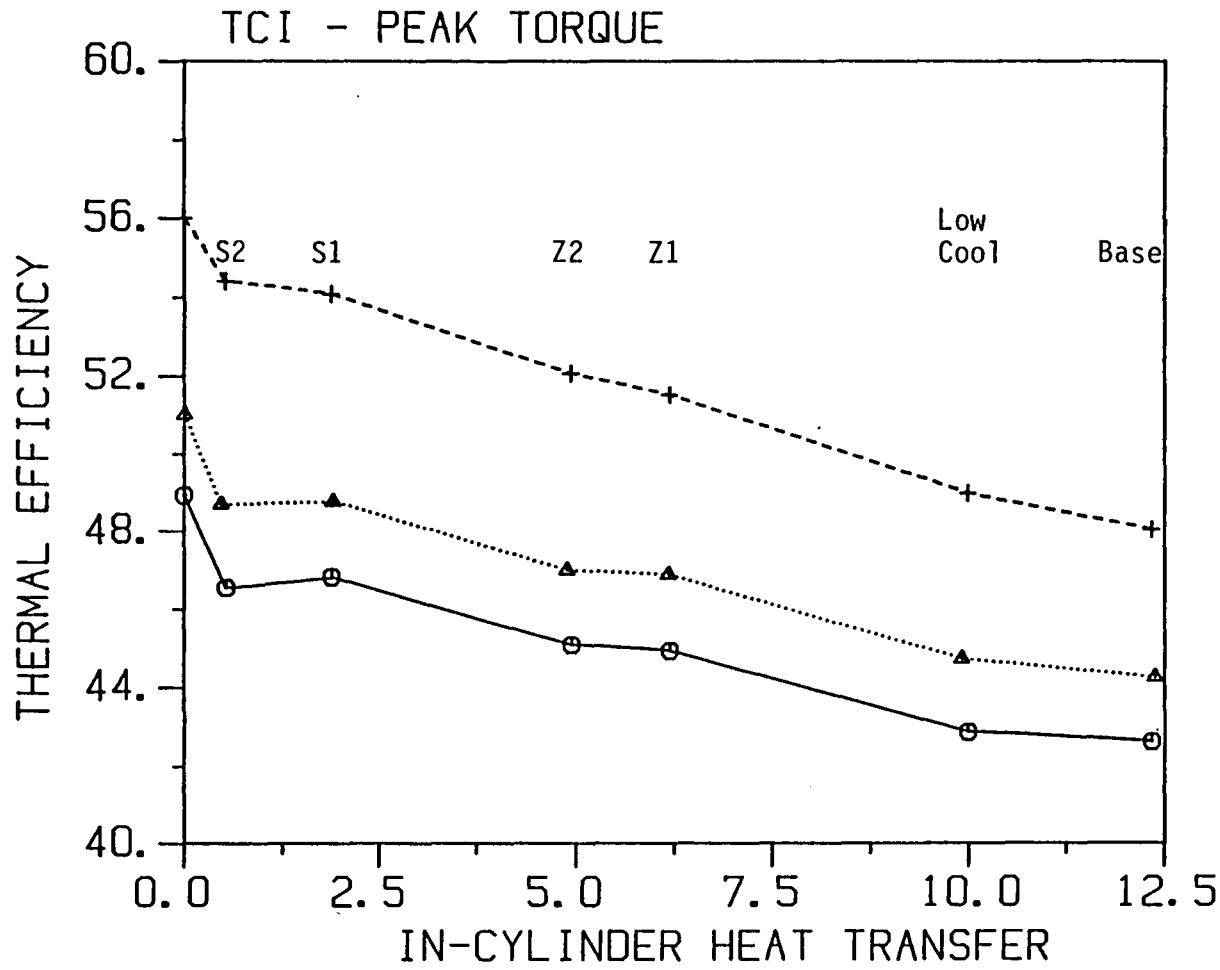

Figure 3-1b Thermal efficiency of a turbocharged, intercooled truck engine under various heat-rejection strategies. Peak Torque.

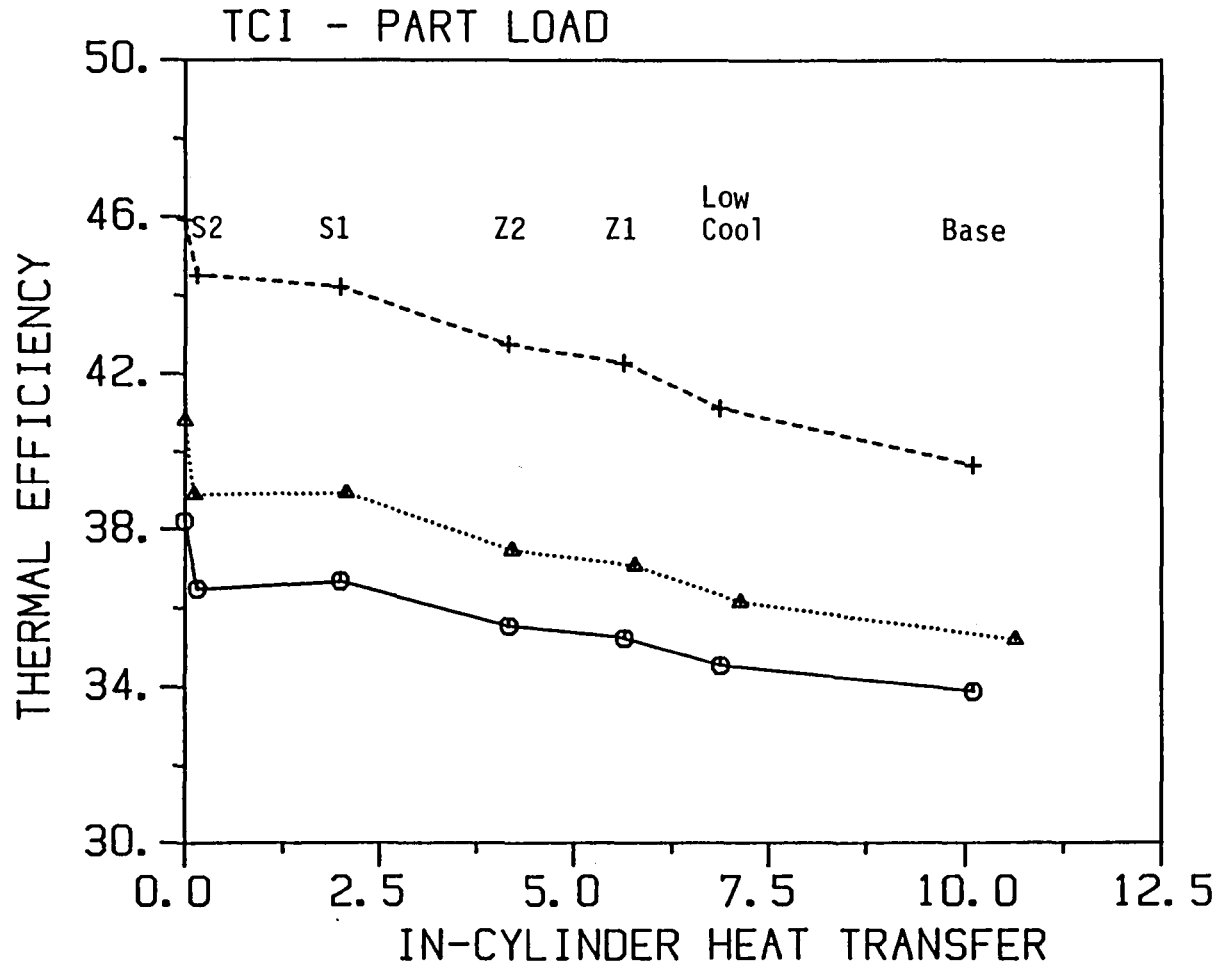

Figure 3-1c Thermal efficiency of a turbocharged, intercooled truck engine under various heat-rejection strategies. Part Load.

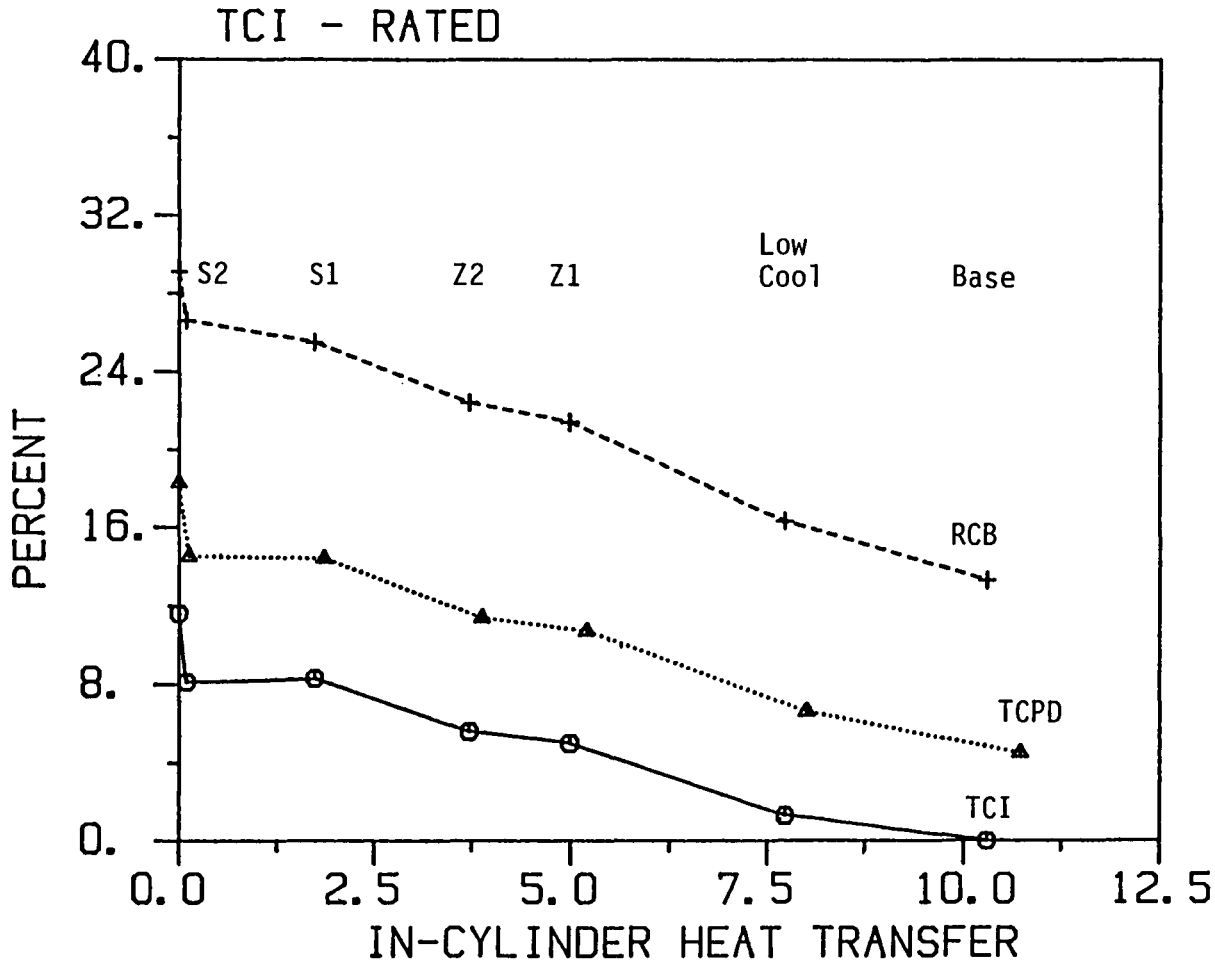

Figure 2a Percentage improvement in brake thermal efficiency of an intercooled engine with respect to cooled TCI engine. Rated conditions.

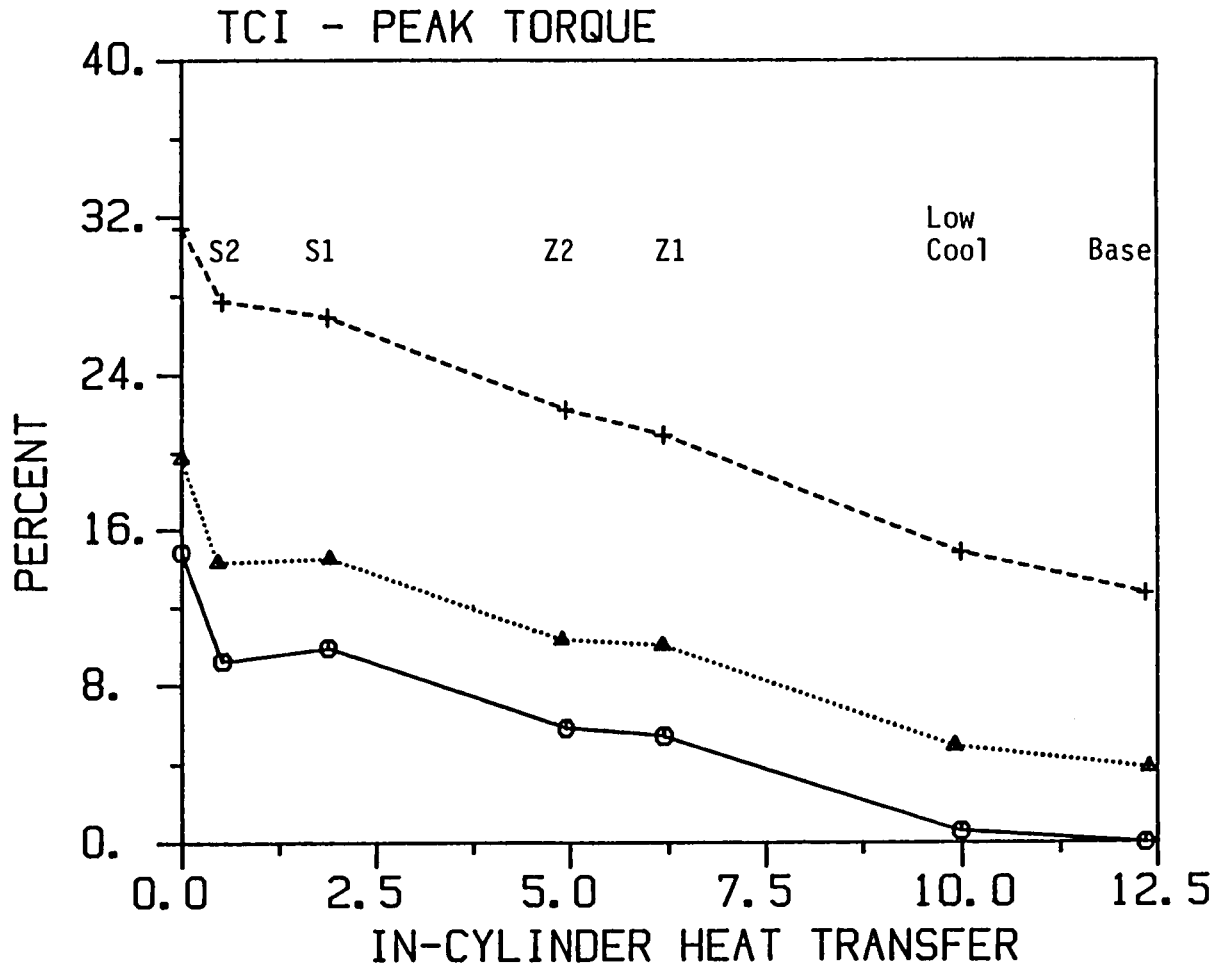

Figure 3-2b Percentage improvement in brake thermal efficiency of an intercooled engine with respect to cooled TCI engine. Peak torque.

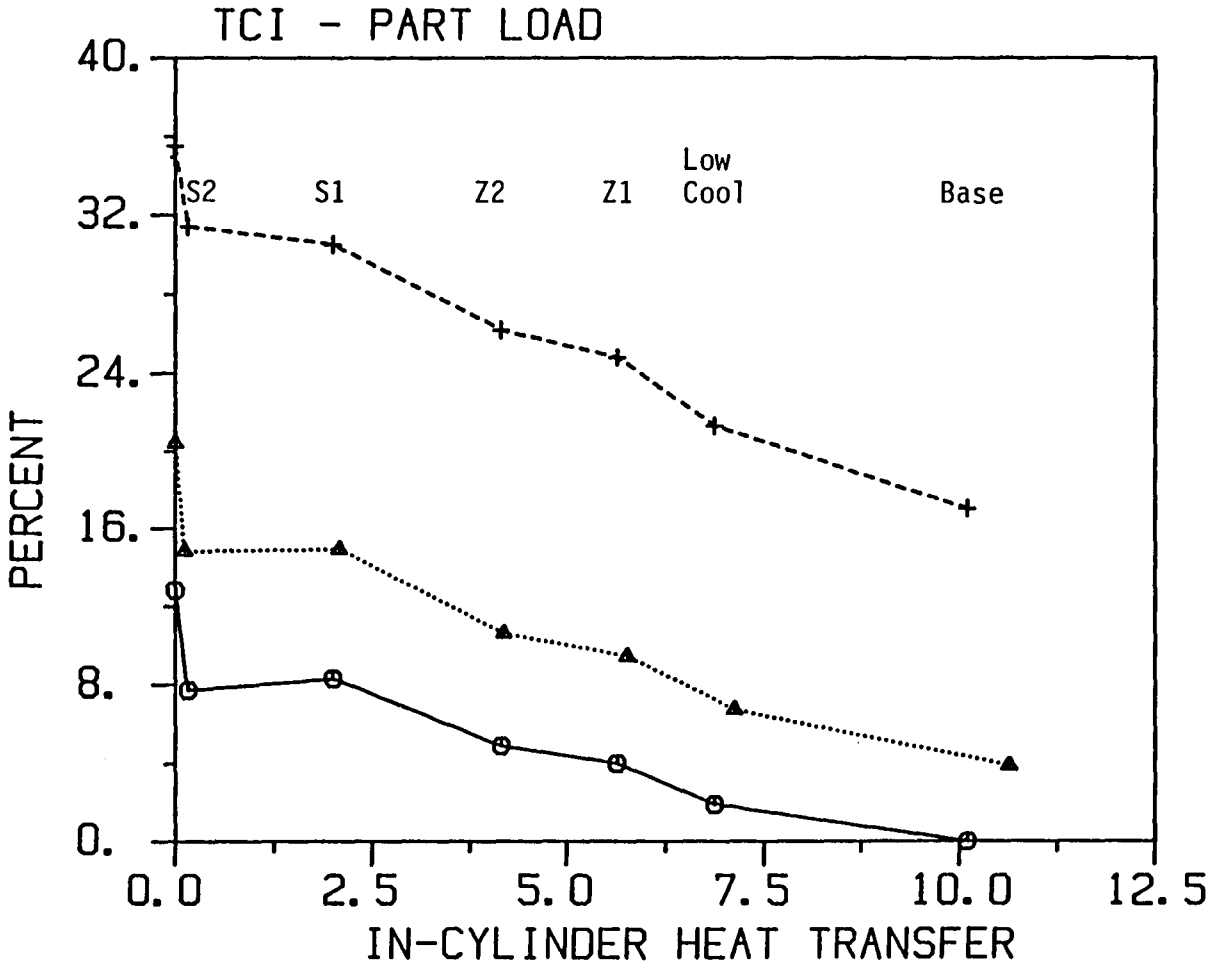

Figure 3-2c Percentage improvement in brake thermal efficiency of an intercooled engine with respect to cooled TCI engine. Part load.

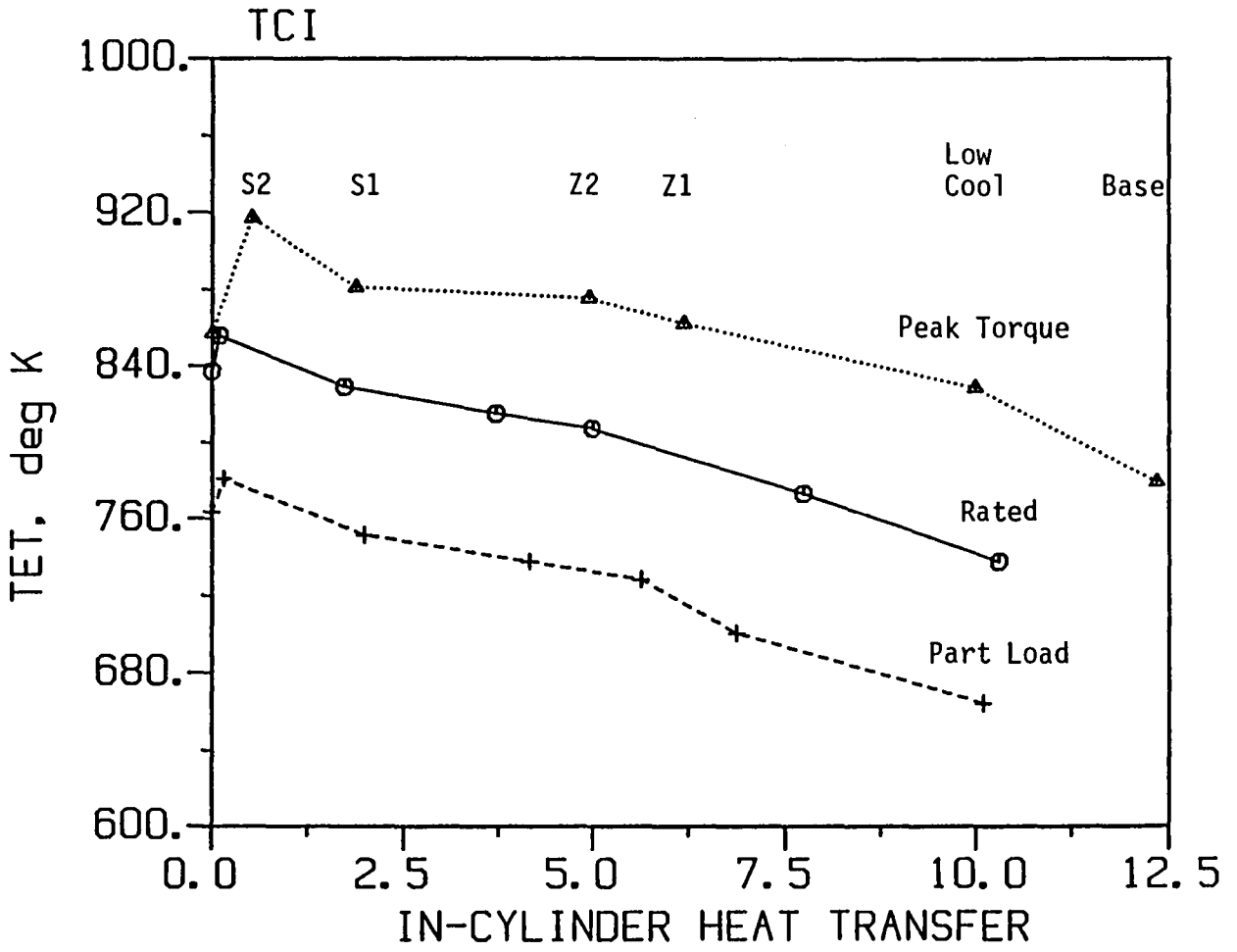

Figure 3-3 Exhaust temperatures downstream of turbocharger, intercooled engine.

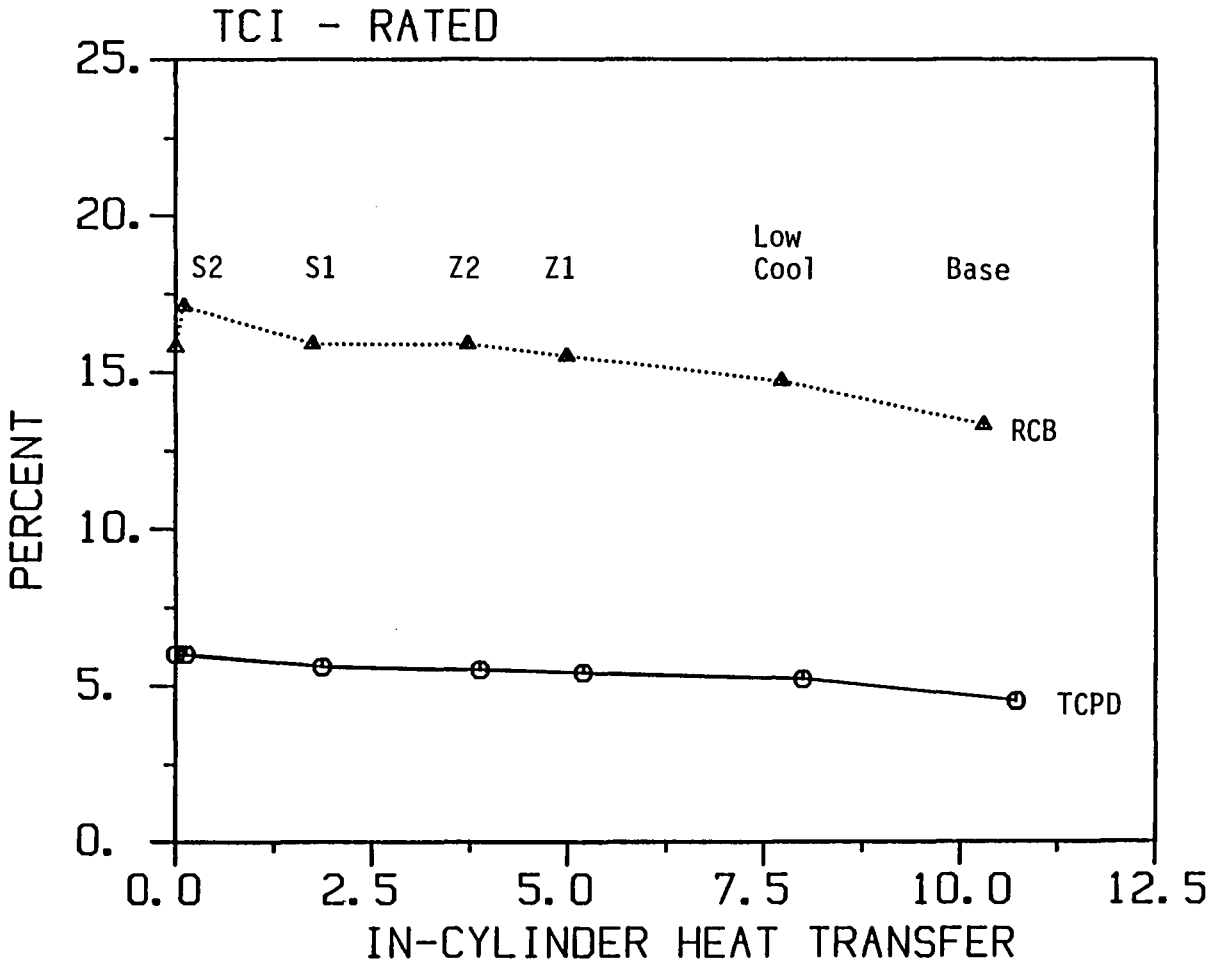

Figure 3-4a Percentage improvement in thermal efficiency due to exhaust heat recovery. Rated conditions.

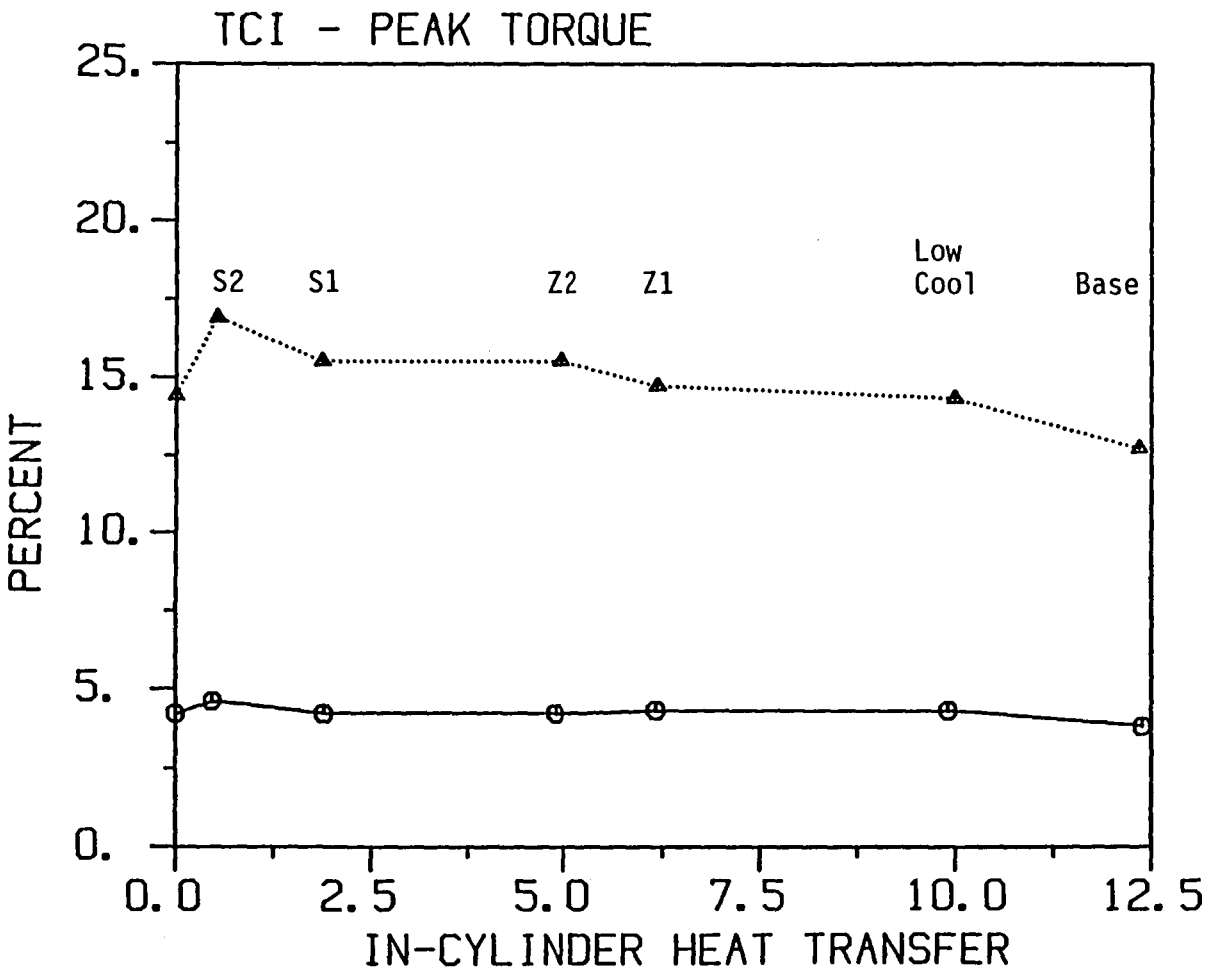

Figure 3-4b Percentage improvement in thermal efficiency due to exhaust heat recovery. Peak torque.

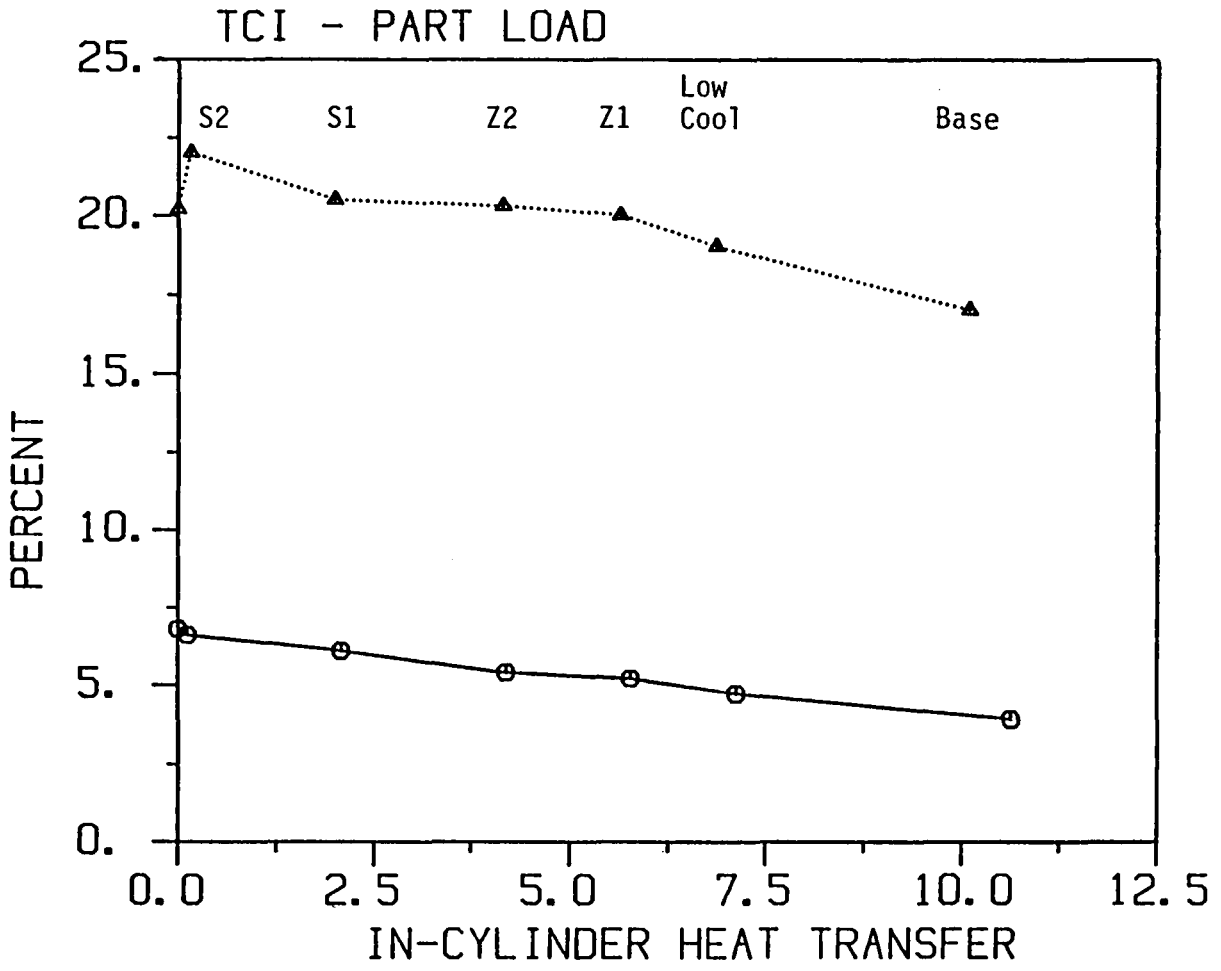

Figure 3-4c Percentage improvement in thermal efficiency due to exhaust heat recovery. Part load.

benefit of turbocompounding is 5.4% at rated conditions, 4.3% at peak torque, and 5.2% at part load. The benefits are somewhat lower for the baseline cooled engine which has a cooler exhaust, but they still amount to 4.5, 3.8 and 3.9%, respectively. Substantially higher benefits are realized with the RCB system, providing improvements for the Z1, of 15.5, 14.7 and 20.0 percent, respectively. The benefits obtained with the RCB system for the baseline cooled engine were only modestly lower.

It is clear from the previous discussion that much of the additional benefits of the exhaust heat recovery devices are available even for the conventionally cooled baseline case. The reason for this is seen in Figure 3-3, which indicates that although the exhaust temperature increases downstream of the turbocharger as in-cylinder heat rejection is decreased, it does not increase in an overwhelming way, and this is reflected in the moderate trends seen in Figure 3-4.

To examine these observations in a finer detail, one can address the question of efficiency with which the energy conserved in the cylinder gases by insulation is converted into useful work. This may be measured in terms of a ratio of the differential between the thermal efficiency (brake) of the lower heat rejection configuration and that of the baseline cooled engine, to the differential in in-cylinder heat transfer, i.e.,

$$RHCE = (\eta_t - \eta_{t,cooled})/(h.t._{cooled} - h.t.)$$

where RHCE stands for retained-heat-conversion-efficiency.

This efficiency includes the effects of

- o direct improvement in indicated work,
- o improvement in pumping loss due to rematched TC turbine,
- o work produced by the heat recovery device,
- o decrease in port heat transfer losses due to insulation done parallel to in-cylinder insulation, and
- o decrease in relative importance of engine friction with increase in BMEP.

The conversion efficiency is plotted in Figure 3-5 for the three engine operating conditions. (Note that since the conversion efficiency is calculated with respect to the cooled baseline, the baseline engine conversion efficiency is undefined.) It shows that some 37 percent of the conserved heat is converted directly into piston work at all three engine operating points. The exception is the reduced-cooling concept where the conversion into piston work is substantially lower; this aspect will be discussed in a later section.

Turbocompounding increases the conversion efficiency by about 6 percentage points (less at peak torque, more at part load). The Rankine cycle machine increases the conversion efficiency by about 22 percentage points, raising it to a level approaching 60 percent. A combined TCPD/RCB exhaust heat recovery increases the conversion efficiency to around 65 percent. This is a very high overall efficiency for converting saved thermal energy into work (even though some of it is due to extraneous effects such as changes in port heat transfer and engine friction).

Total heat rejection. One of the driving forces behind the insulated diesel is the reduction of the total heat rejection to coolant, and eventual elimination of the coolant. The total heat rejection to coolant and to the environment is composed of several elements:

in-cylinder heat transfer,
port heat transfer,
friction heat (piston, bearings, pumps), and
intercooler

Most of this heat (for a liquid-air intercooler) is rejected to the coolant, and only a smaller portion radiated and convected from the engine system outer structure goes directly to the environment. As seen in Figure 3-6, the total heat rejection decreases monotonically with decreasing in-cylinder heat transfer, and in fact it decreases faster than the in-cylinder heat transfer due to the accompanying effects of port insulation.

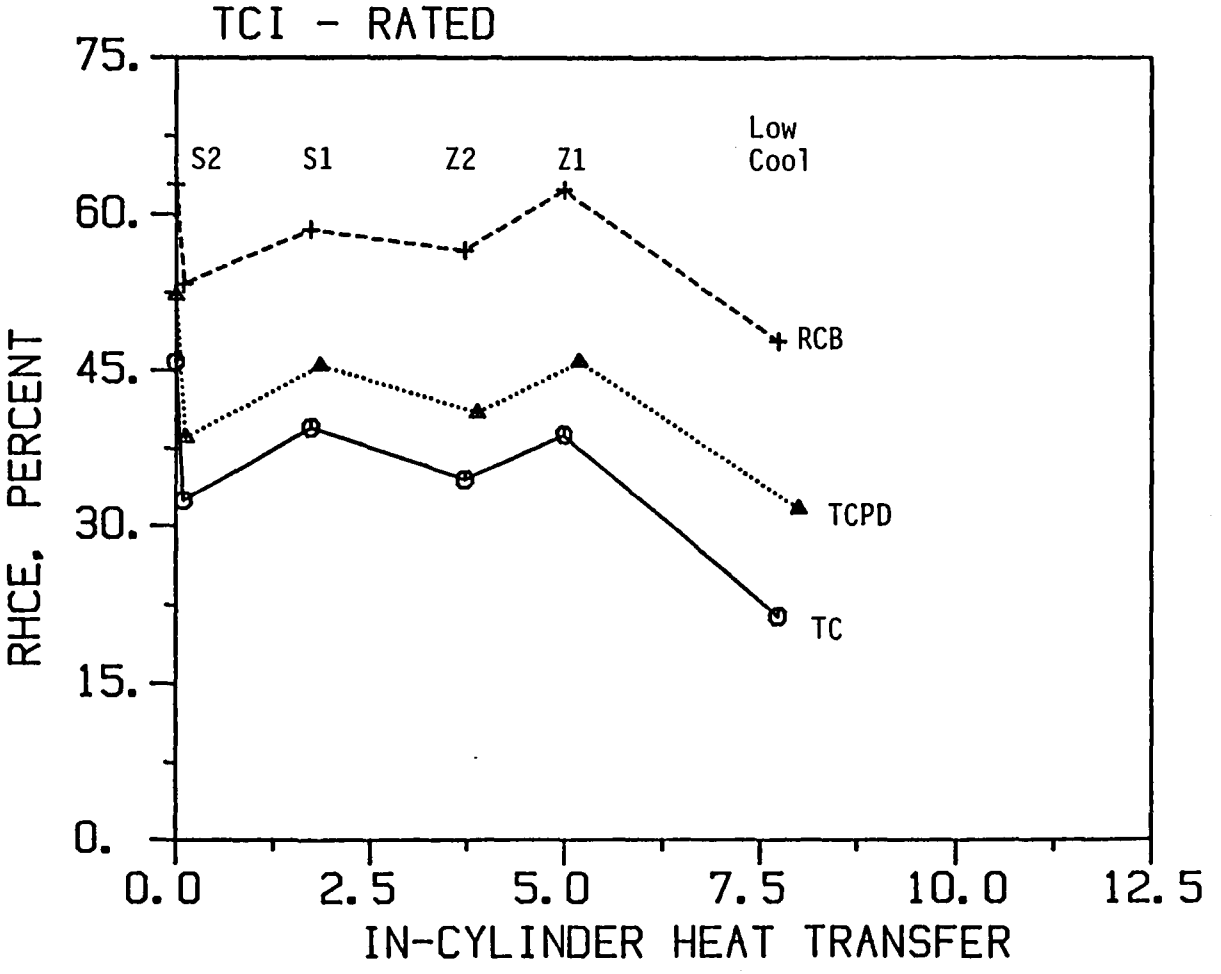

Figure 3-5a Retained heat conversion efficiency, intercooled engine. Rated conditions.

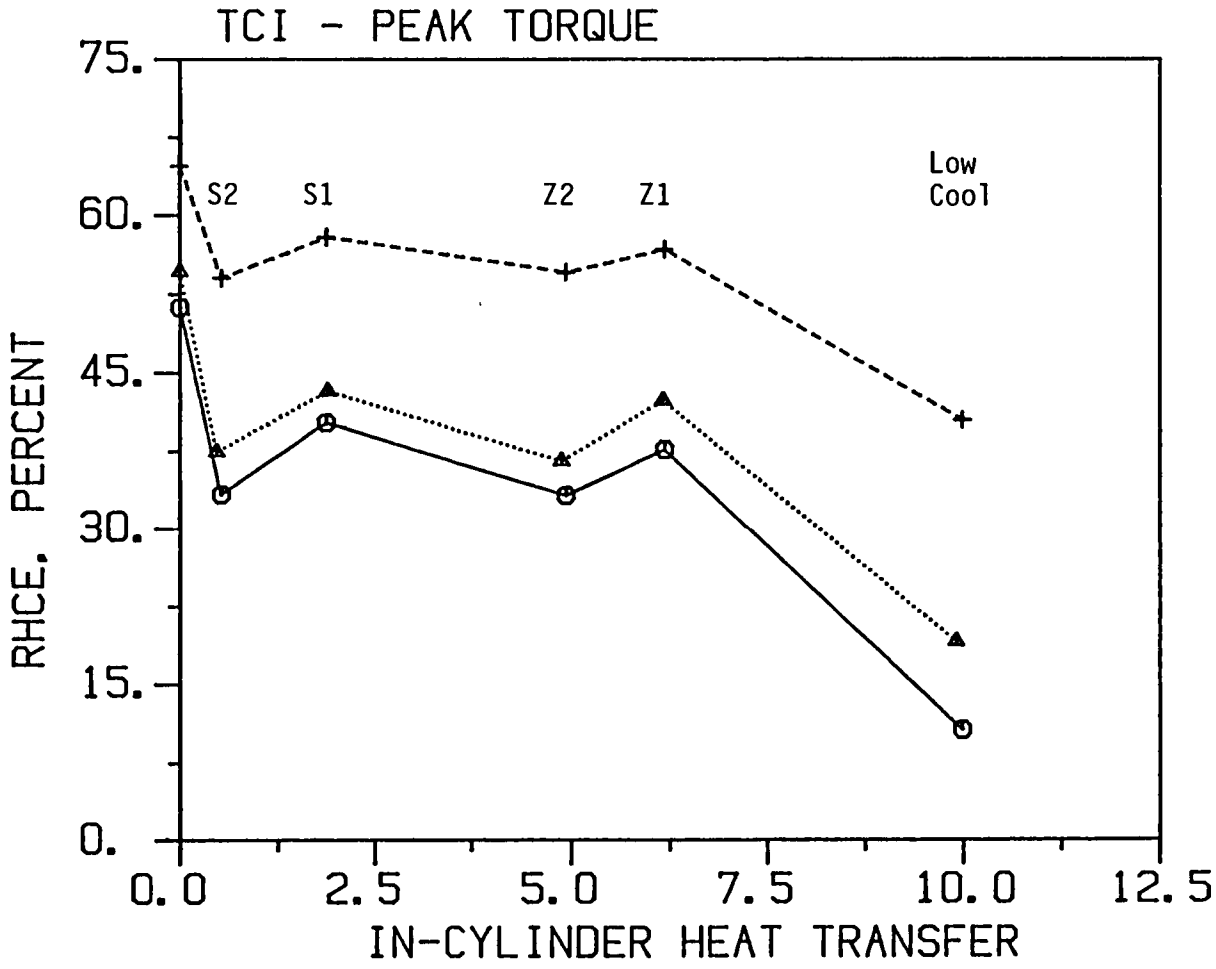

Figure 3-5b Retained heat conversion efficiency, intercooled engine. Peak torque.

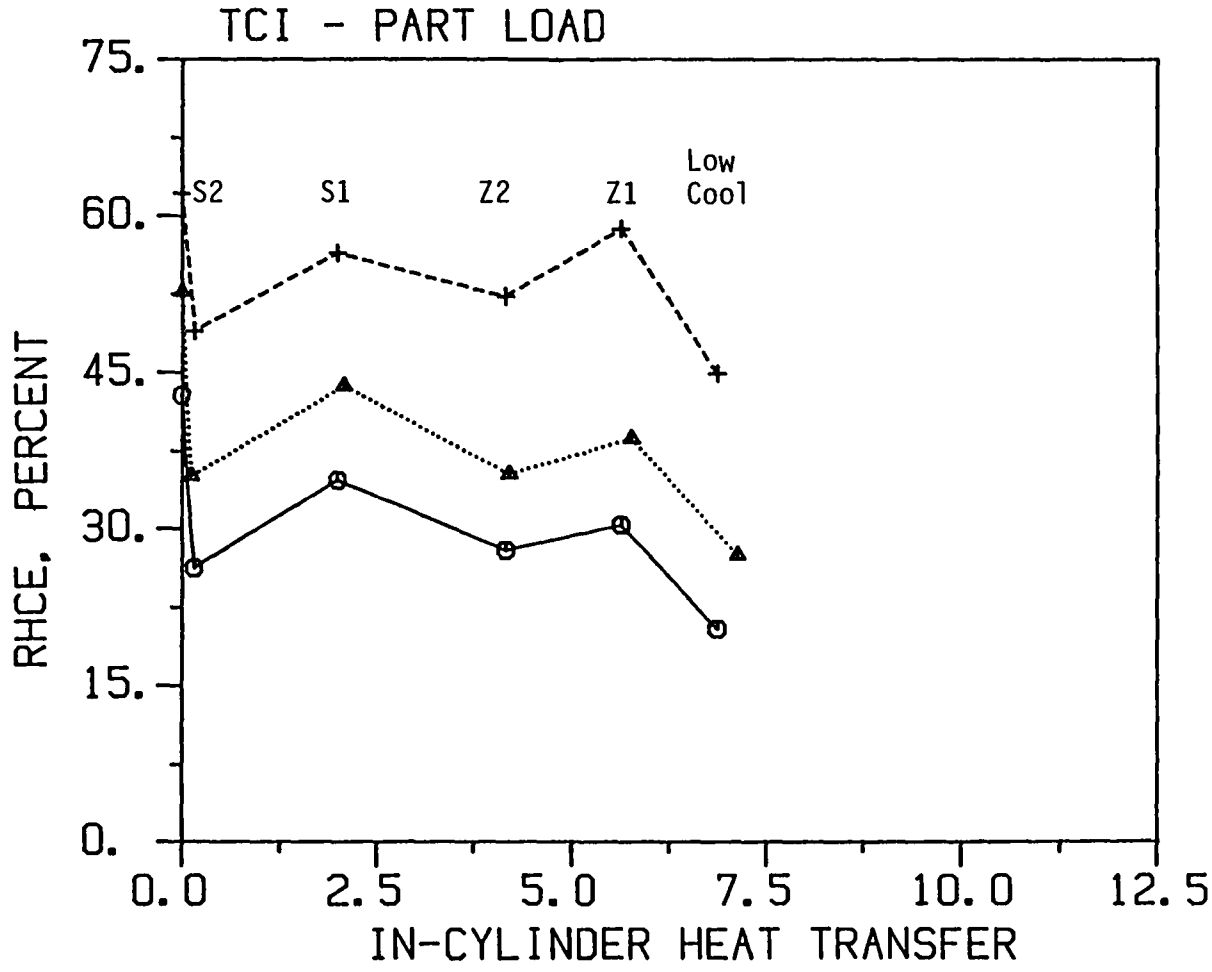

Figure 3-5c Retained heat conversion efficiency, intercooled engine. Part load.

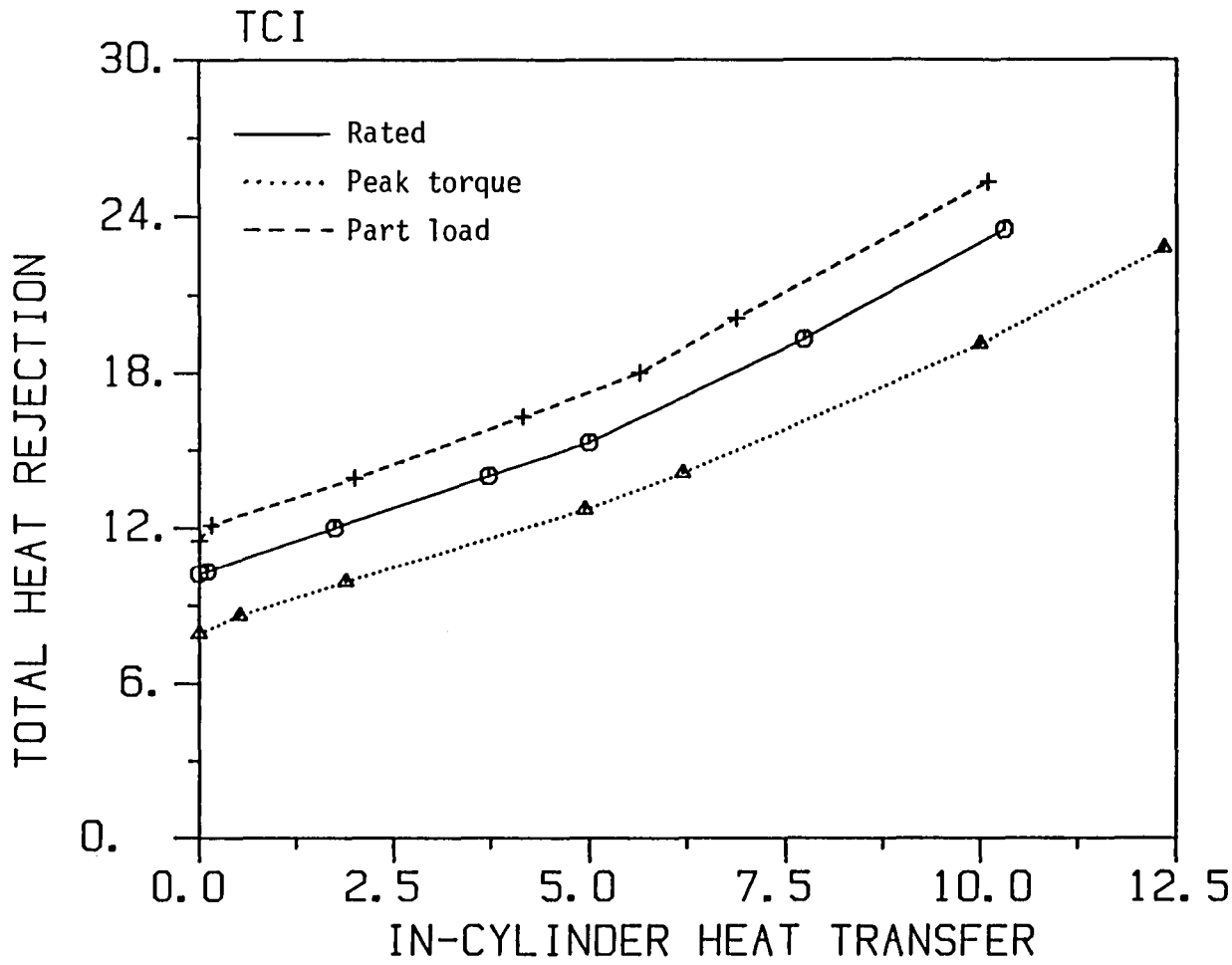

Figure 3-6 Total heat rejection to coolant oil, intercooler and environment, intercooled engine.

The most striking result that can be deduced from Figure 3-6 is that even with zero in-cylinder and port gas-to-wall heat transfer, the total heat rejection is only 56% lower than for the conventionally cooled engine (at rated conditions). This is due to heat rejected in the intercooler and friction-generated heat, and it indicates that some type of cooling will be required even for highly insulated engines.

Liner insulation. One of the important questions arising in the development of insulation strategies concerns the liner insulation. Insulating the liner brings some benefits and some problems, which have to be assessed and weighed with regard to a particular engine application. The most important of these are:

Benefits	Problems
lower in-cylinder heat transfer	lower volumetric efficiency
no liner coolant	higher piston/ring/liner temperatures
lower total heat rejection	engine power
higher exhaust energy level	
higher thermal efficiency	

The degree of reduction of in-cylinder heat transfer by liner insulation may be seen in Figure 3-1: 1.3 percent of fuel energy for a zirconia design, and 2.0 percent of fuel energy for a superinsulated design. The accompanying increase in thermal efficiency is seen to be quite small (Figure 3-2) and it has to do with the lower conversion efficiency of conserved in-cylinder heat which occurs when the liner is hot (Figure 3-5). It may be noted by referring to Figure 3-5 that all of the lower conversion efficiency points correspond to configurations with uncooled liner: i.e., reduced cooling, Z2 and S2. By contrast, the configurations with a cooled liner have more favorable conversion efficiencies. The lower conversion efficiency is related to the "pumped heat", i.e., heat that is absorbed by the combustion chamber surfaces during combustion and expansion, and which heats up the fresh charge during intake and compression. As seen in Figure 3-7, the pumped heat is larger for the configurations with insulated liners, and this negates to

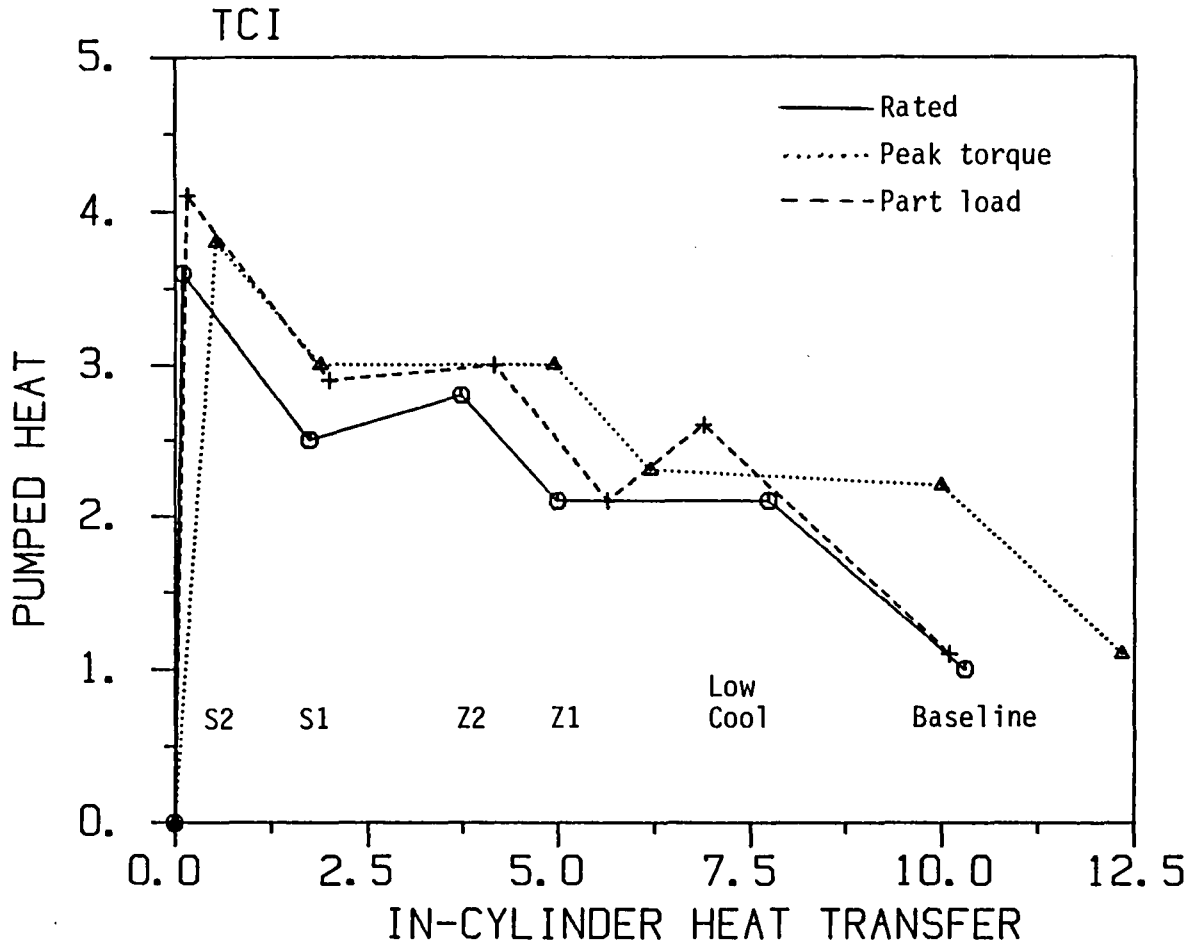

Figure 3-7 Pumped heat expressed in terms of percent of fuel energy, intercooled.

a large degree the benefits of the lower net heat transfer. Another way of looking at this is that the energy conserved through the use of an insulated liner is saved when the available expansion ratio is small and thus produces less piston work.

Liner insulation also has an effect on the volumetric efficiency (Figure 3-8). Volumetric efficiency values are the highest for the zero heat transfer, because there is no heat transfer to the incoming air in the ports nor inside the cylinder. Next highest is the baseline cooled case. The insulated cases all have lower volumetric efficiency; their volumetric efficiency would be even lower if it were not for the decrease in exhaust plenum back pressure, which comes about due to the possibility of rematching of the turbocharger turbine to take advantage of the higher exhaust temperature. The volumetric efficiencies are higher for all three cases with cooled liner: baseline, Z1 and S1, while the insulated designs are 1.5-2 percent lower.

Engine power is impacted negatively by liner insulation, as may be seen in Figure 3-9. This is a result of the lower volumetric efficiency and lower heat conversion efficiency, which are only partly offset by the increased exhaust temperatures. (Note that the boost pressure and fueling rate were being adjusted from configuration to configuration to limit the peak pressure and maintain constant air/fuel ratio, as described above.)

The effects of liner insulation on total heat rejection are not large (Figure 3-6). They represent only 1.3 percent of fuel energy for the ZPS design (ZPS2 vs. ZPS1) at rated conditions, which amounts to only about 8.5 percent of the total heat rejection.

In summary, the benefits of liner insulation are only modest: a small increase in thermal efficiency and a moderate decrease in total heat rejection. These have to be balanced against the lower volumetric efficiency, lower power, and substantially higher piston/ring/liner

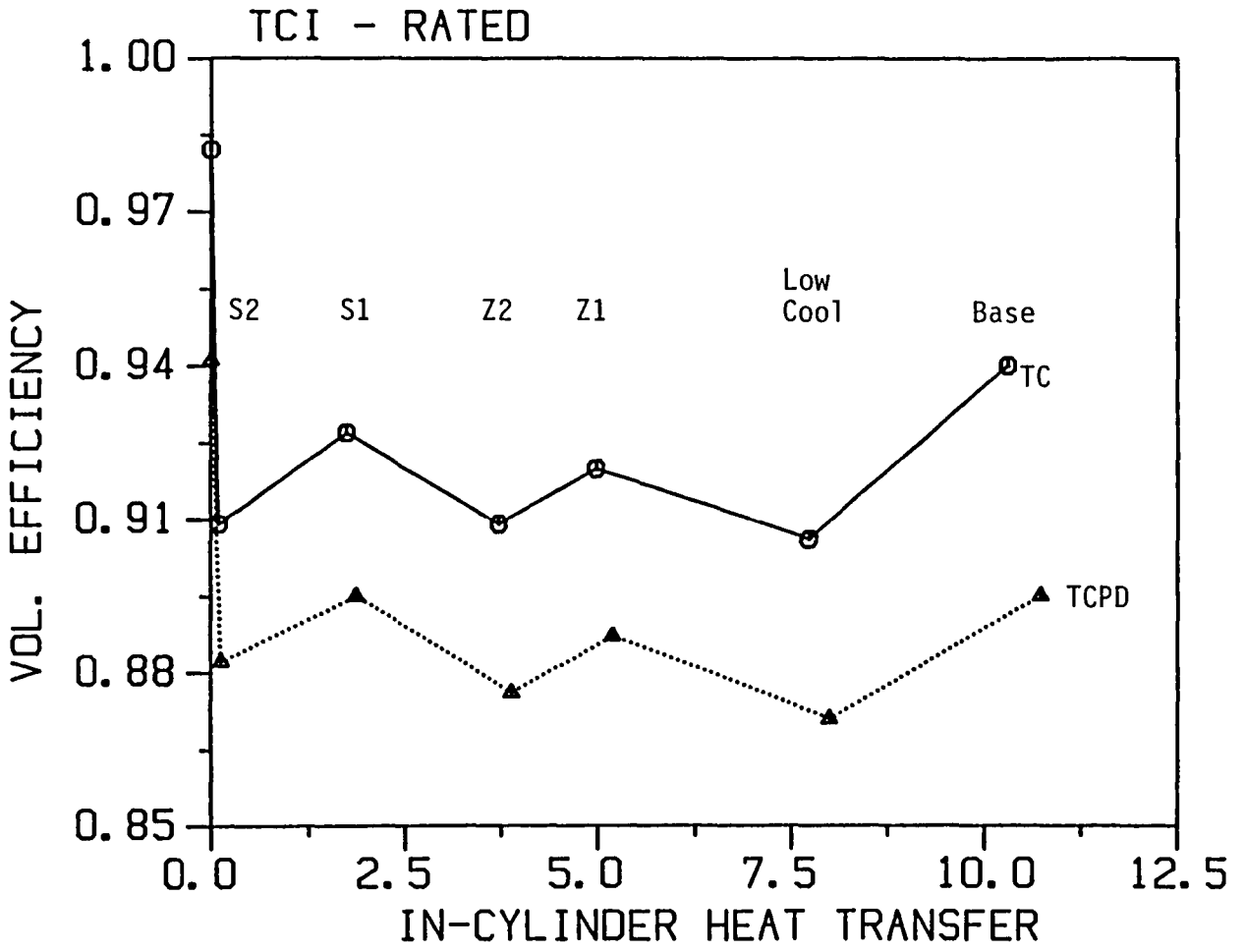

Figure 3-8 Volumetric efficiency, intercooled engine.

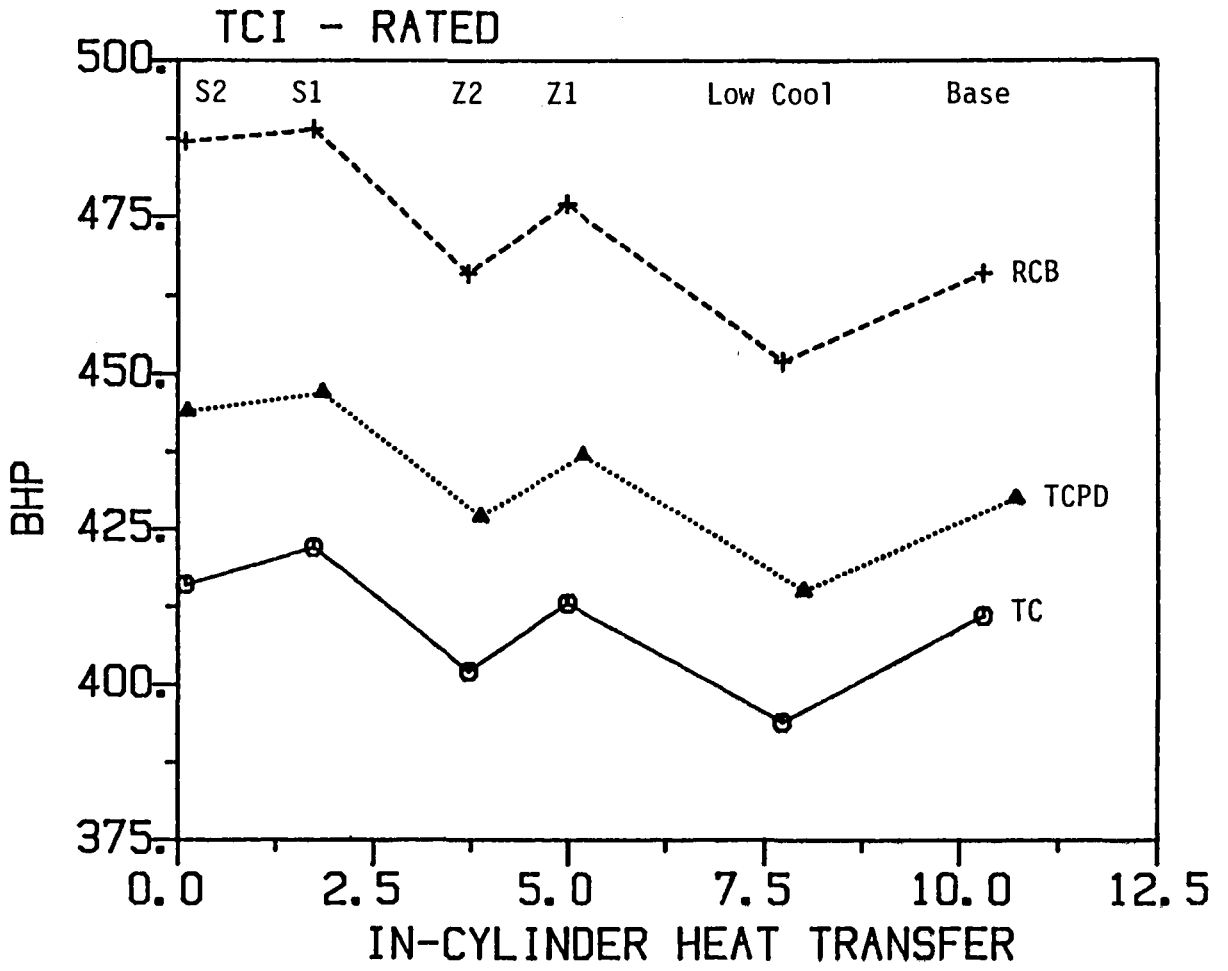

Figure 3-9 Engine system brake power, intercooled engine.

temperatures (see below), which adversely affect lubrication, friction and wear, and may require exotic lubricants and/or tribological designs.

Reduced-cooling engine. One of the low heat rejection concepts that has been proposed in the literature is the reduced-cooling engine (sometimes referred to as "uncooled engine"). This is essentially a conventional engine with no coolant (it is simply drained). The main modification is an enhanced-cooling piston design (typically with positive cooling through an oil gallery). The reason for this modification is that in a conventionally cooled engine the liner provides a significant heat path for the heat absorbed by the piston from the gases and for the heat generated at the piston/liner interface. When the coolant is drained, this path is significantly restricted and most of the heat has to be channeled through the piston to the oil, and this necessitates enhanced piston cooling to keep the piston temperatures low enough to maintain material integrity.

Unfortunately, this simple approach to low heat rejection provides only relatively small benefits. Thermal efficiency increases only by about 1-2 percent (Figure 3-2) and total heat rejection is reduced by 18 percent (Figure 3-6). On the negative side, the volumetric efficiency is reduced, and component temperatures (discussed below) are substantially increased, leading to difficulties with durability and lubrication. In addition, engine power is reduced as a consequence of the lower volumetric efficiency and also due to exceptionally low retained heat conversion efficiency (RHCE) of this configuration compared to the others (Figure 3-5).

Liner Temperatures. The level of liner temperatures has very important impact on tribological issues covering lubrication, friction and wear. It depends strongly on liner insulation and cooling strategy, and varies widely from configuration to configuration. This is seen in Figure 3-10 which presents temperatures at two different liner locations at peak torque operating conditions. Peak torque was chosen because it is near this condition that the temperatures reach the highest levels. The two locations chosen refer to points located at one-twelfth and one-third of

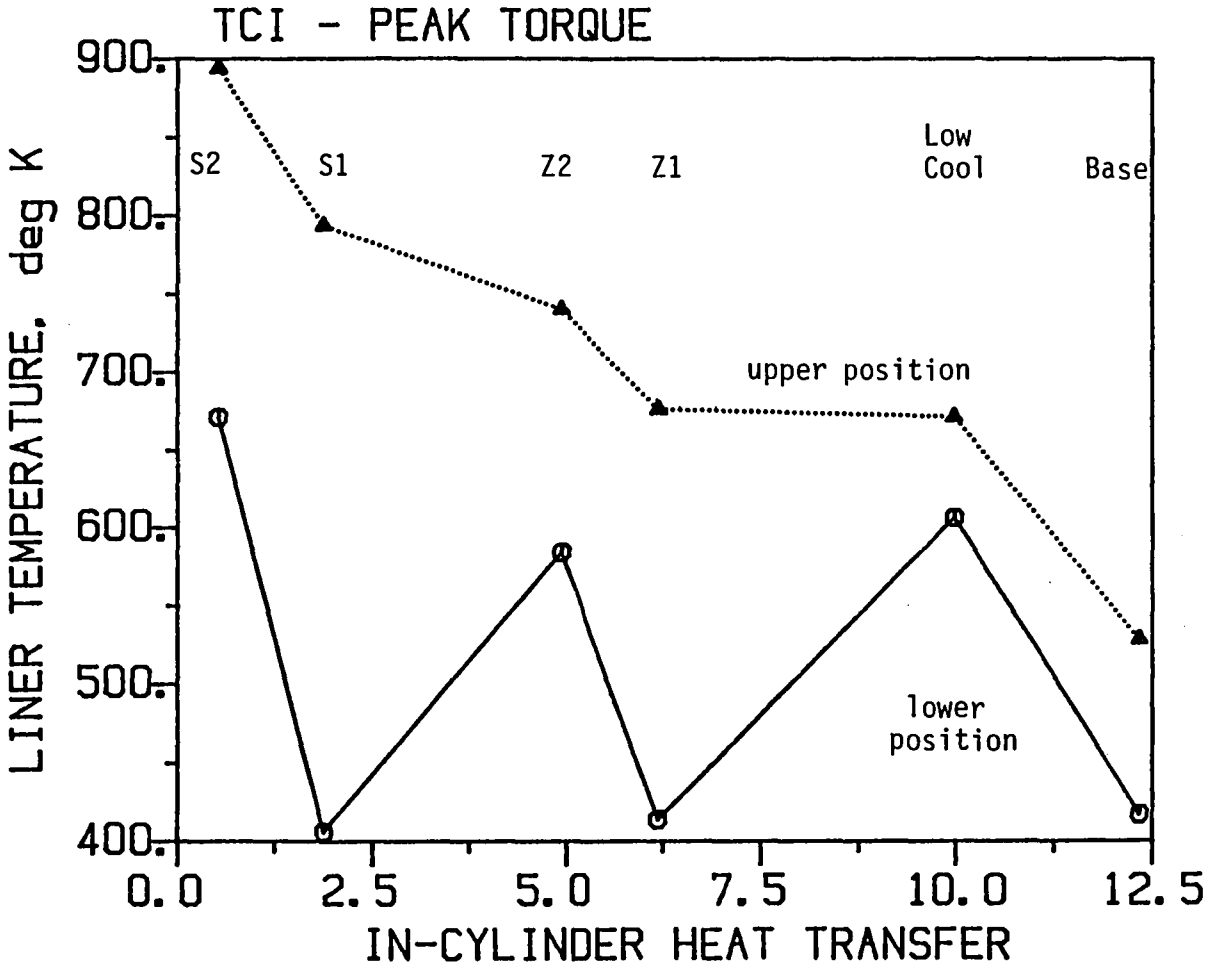

Figure 3-10 Liner surface temperatures at one twelfth and one third the distance from head to piston at BDC. Upper position insulated in Z1, Z2, S1 and S2 configurations, lower position insulated only in Z2, S2.

the distance from the head to the piston crown at BDC position. The higher of these points lies above the top ring reversal point, i.e., in the area which is insulated in the ZPS and superinsulated designs 1 and 2. The lower one is on the part of the liner which is cooled in designs 1 and in the baseline configuration, while it is uncooled in designs 2 and in the reduced cooling configuration. It should be realized that, due to the limited resolution of the structural model used, this is not the highest temperature on the ring/piston interface. To determine the maximum temperature of the ring/liner contact, which lies near the point of top ring reversal, and in fact the details of the entire thermal environment in the interface area, one needs to use a higher liner resolution attainable with a finite element calculation. While IRIS can carry out a coupled thermodynamics/heat transfer/finite element calculation, this was not done in the present study, utilizing instead the simpler network approach. Thus, we simply use the temperature at the lower of the two locations to represent the temperatures of surfaces in sliding contact for the purposes of comparison of the various configurations and elucidation of the more global trends.

The temperatures shown in Figure 3-10 are the time average values; the peak cyclic temperatures are even higher due to surface temperature swings, particularly so for the upper liner location. The results show that liner insulation, and/or coolant removal, both increase the liner temperatures very significantly, well above the range of current lubricant capabilities. A subtle point not elucidated in Figure 3-10 is that the temperature of uncooled liners depends strongly on piston cooling. Removal of oil cooling, or substantial reduction in oil cooling effectiveness, can substantially increase the liner temperature above the levels shown.

Effects of Intercooling

The non-intercooled engine was studied in the same detail as the intercooled engine discussed above, and the same type of plots were generated to display the trends with insulation configurations, operating conditions and heat recovery devices. The results obtained

are similar in trends and in magnitude to those obtained for the intercooled engine. Thus, only an abbreviated discussion of these results is presented, which concentrates on the differences between the two data sets, all of which may be ascribed to intercooling.

The removal of the intercooler raised the intake plenum temperature by 80, 70 and 45 K, for the rated, peak torque and part load conditions, respectively. The baseline non-intercooled engine was found to have a substantially larger in-cylinder heat transfer (by 20-32 percent depending on operating conditions), which was due to the higher intake temperatures. At the same time, the thermal efficiency of the non-intercooled baseline engine was lower, by 1.6 absolute percentage points at the high load conditions, and by 0.6 absolute percentage points at the part load condition. Thus the non-intercooled engine was starting at a worse baseline, but, it had an advantage in that its larger initial heat transfer promised greater benefits obtainable from combustion chamber insulation.

Simulating the same insulation configurations as for the intercooled engine confirmed that the non-intercooled engine does indeed derive greater incremental improvement in efficiency as a result of insulation, catching up with the intercooled engine at high levels of insulation and RCB heat recovery (Figure 3-11). This is further reinforced by Figure 3-12 which displays the percentage increase in thermal efficiency with insulation and heat recovery, which is higher than for the intercooled engine. Comparing the effectiveness of exhaust heat recovery alone (Figure 3-13), one observes that it is higher than for the intercooled engine, and this is due to the higher energy content of the exhaust stream (Figure 3-14). The efficiency of conversion of the conserved in-cylinder heat to work is about the same as for the intercooled engine (Figure 3-15), but since the in-cylinder heat transfer levels are higher to begin with, the incremental improvement in thermal efficiency is greater.

The total heat rejection from the engine to the coolant and to the environment starts at a level close to that of the intercooled engine

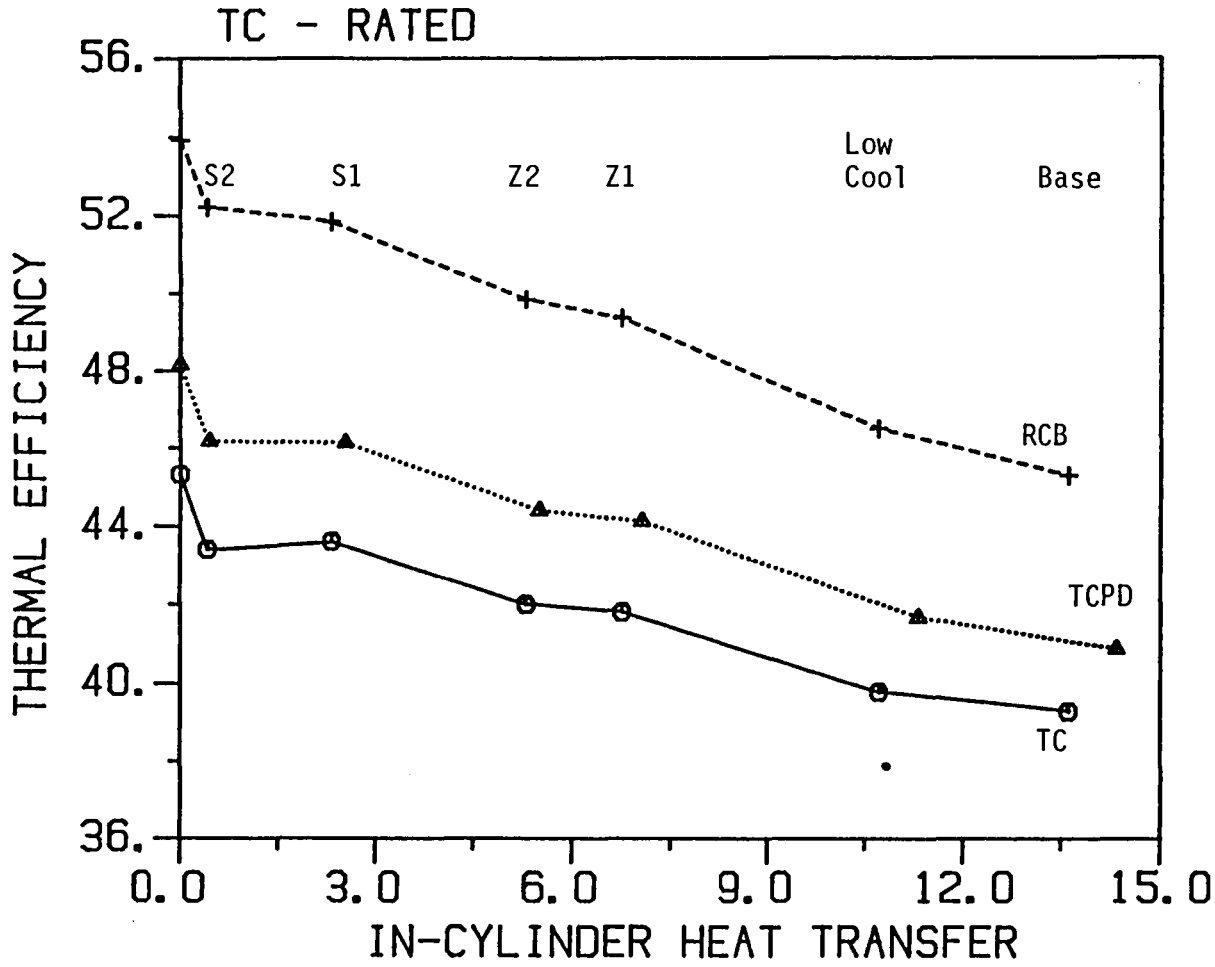

Figure 3-11a Thermal efficiency of a turbocharged non-intercooled engine under various heat-rejection strategies. Rated conditions.

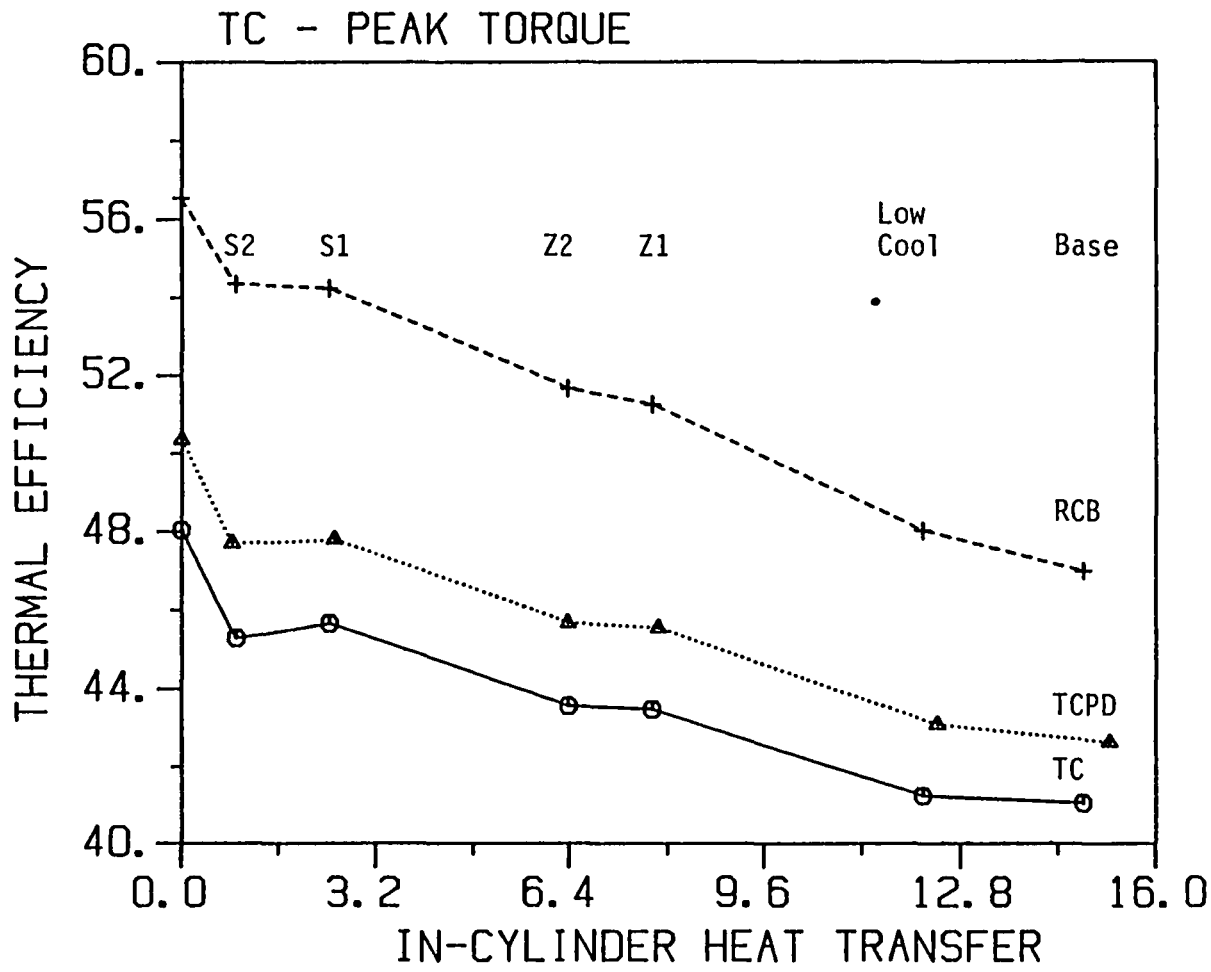

Figure 3-11b Thermal efficiency of a turbocharged non-intercooled engine under various heat-rejection strategies. Peak torque.

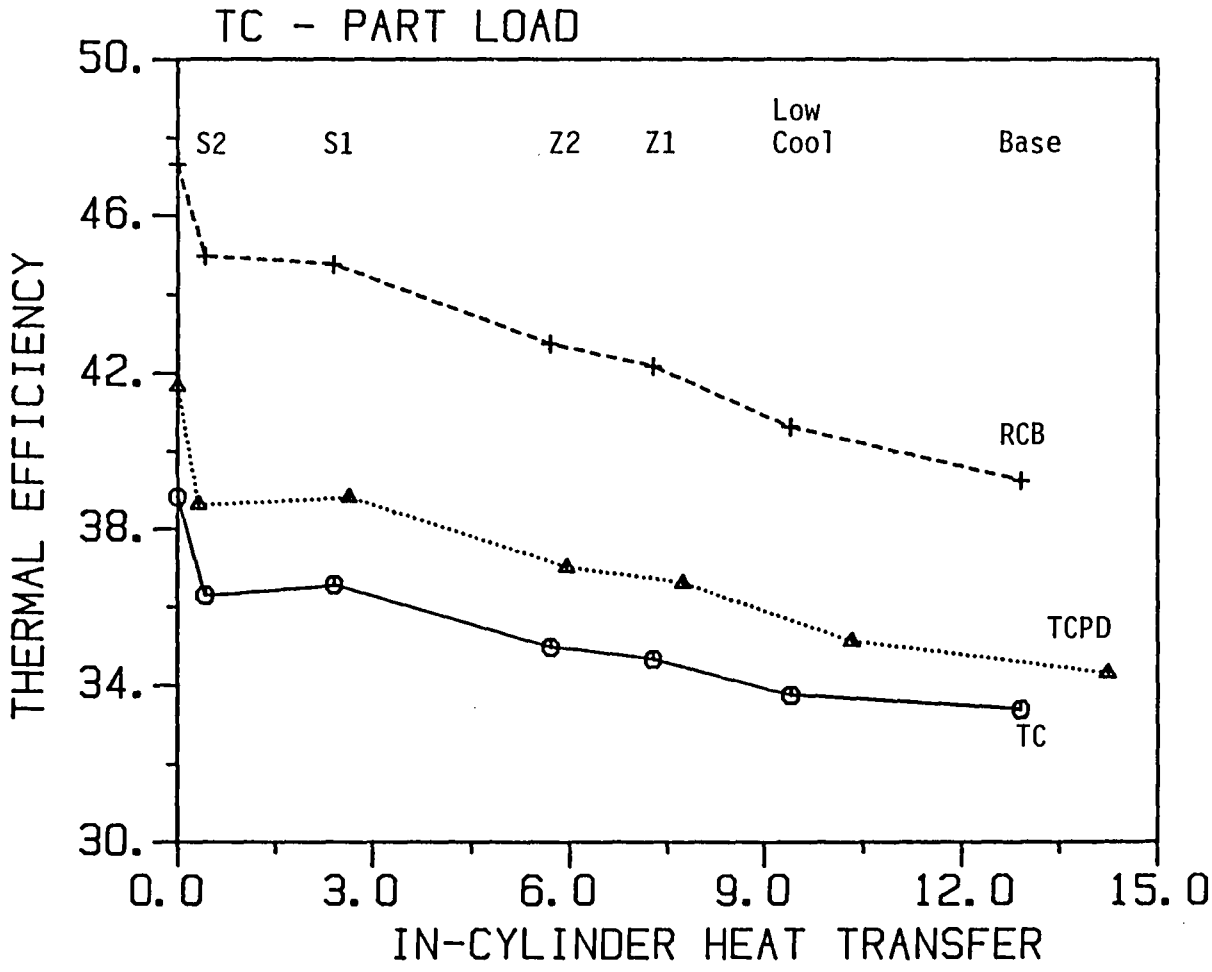

Figure 3-11c Thermal efficiency of a turbocharged non-intercooled engine under various heat-rejection strategies. Part load.

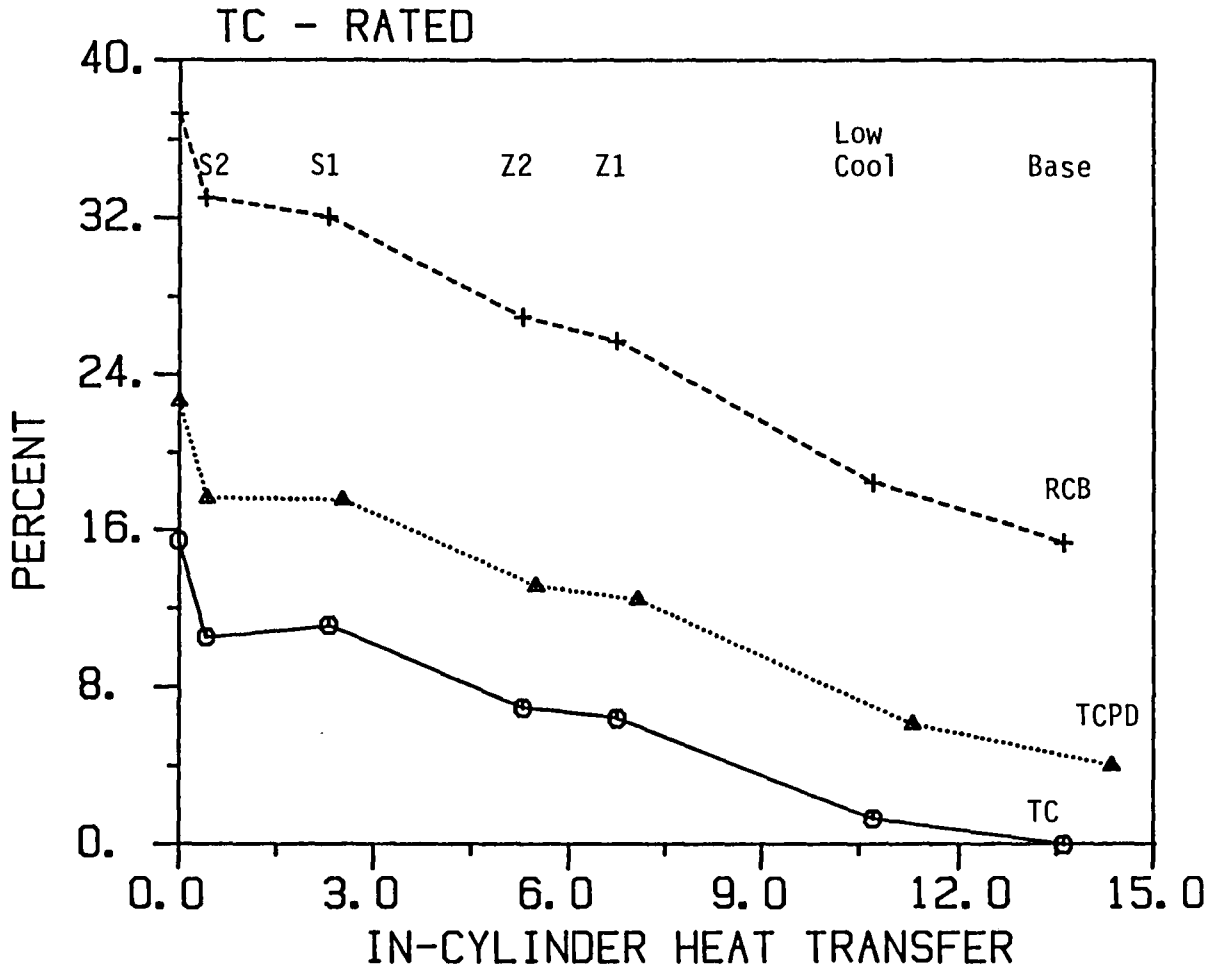

Figure 3-12a Percentage improvement in brake thermal efficiency of a non-intercooled engine with respect to cooled TC. Rated conditions.

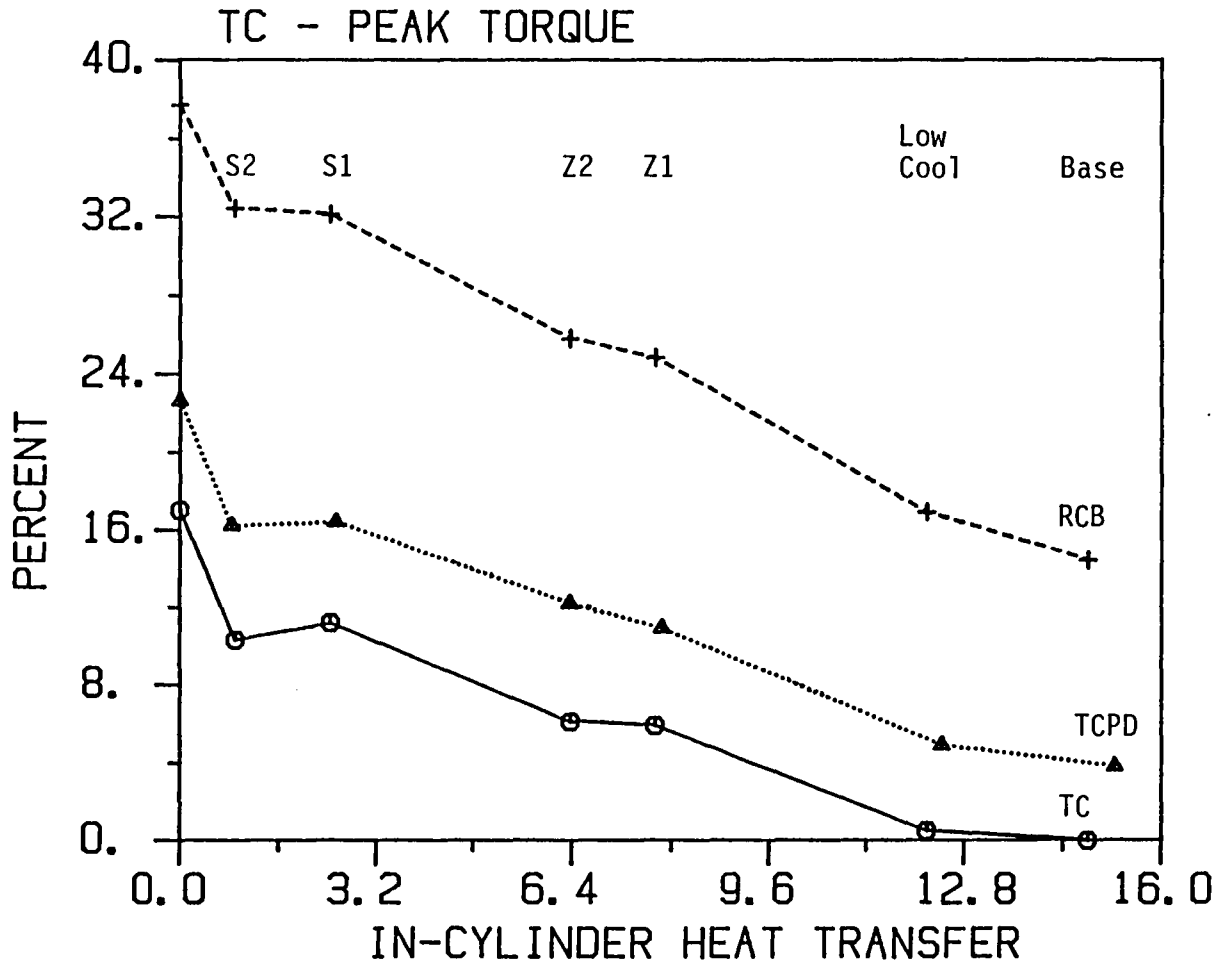

Figure 3-12b Percentage improvement in brake thermal efficiency of a non-intercooled engine with respect to cooled TC. Peak torque.

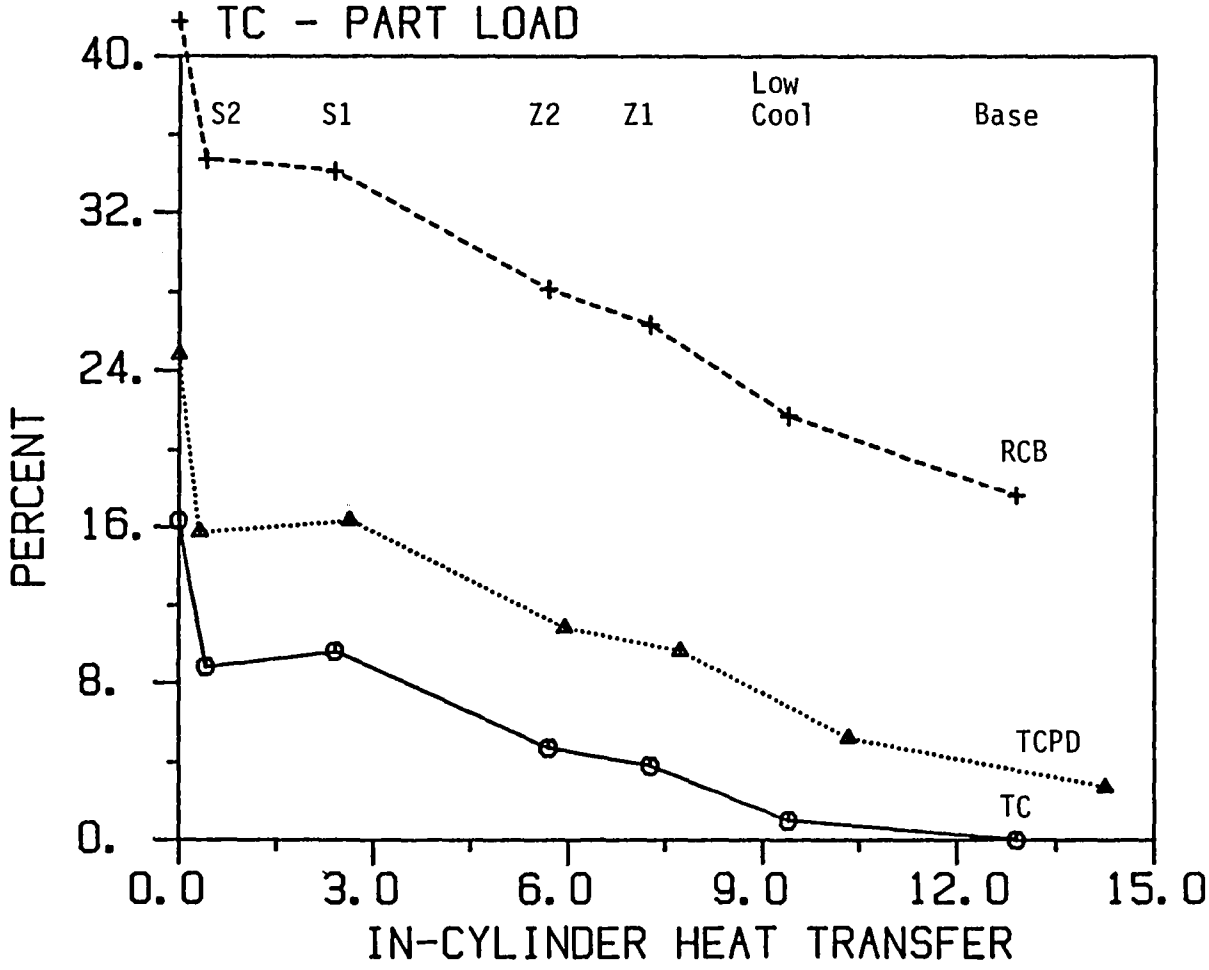

Figure 3-12c Percentage improvement in brake thermal efficiency of a non-intercooled engine with respect to cooled TC. Part load.

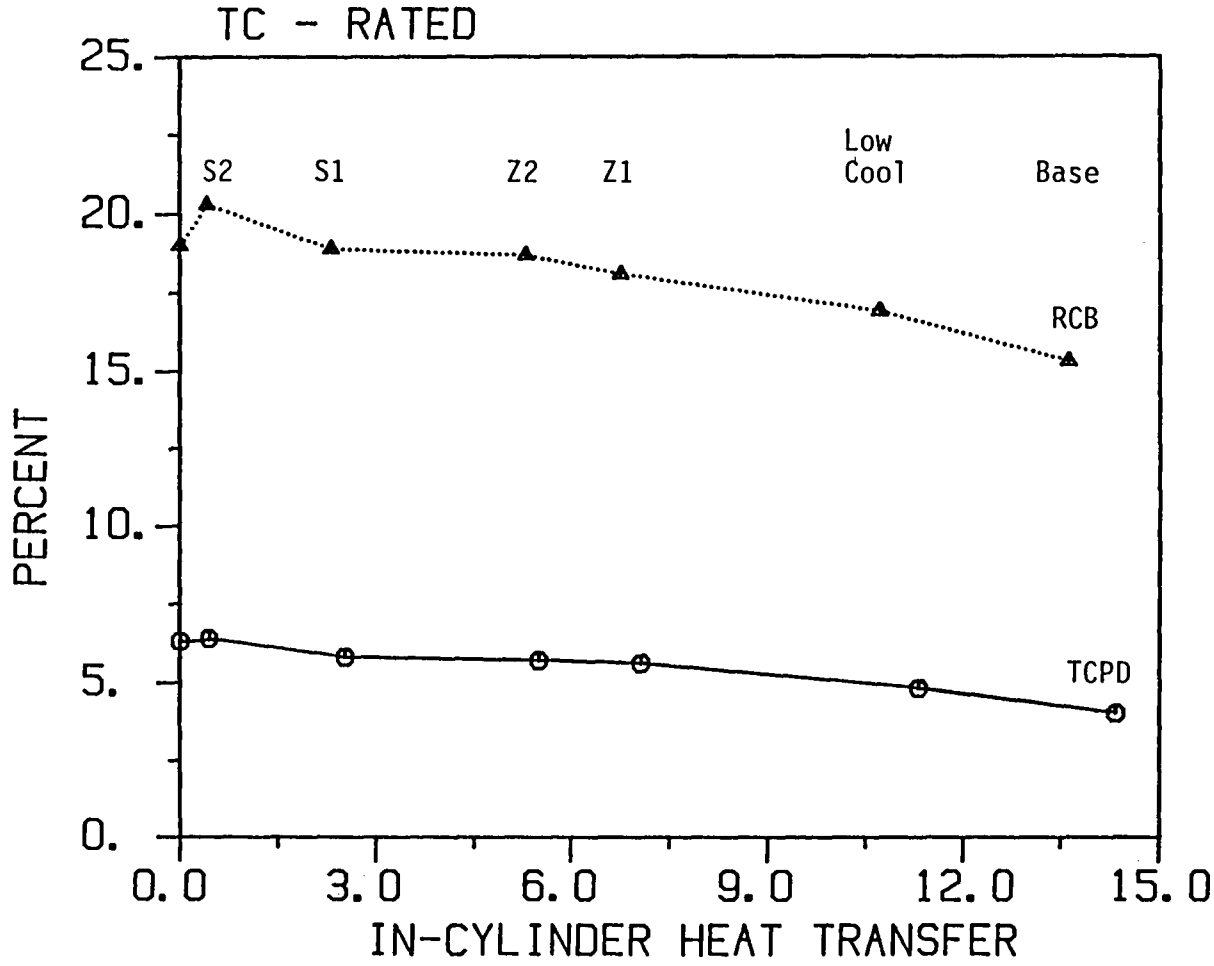

Figure 3-13a Percentage improvement in thermal efficiency due to exhaust heat recovery. Rated conditions.

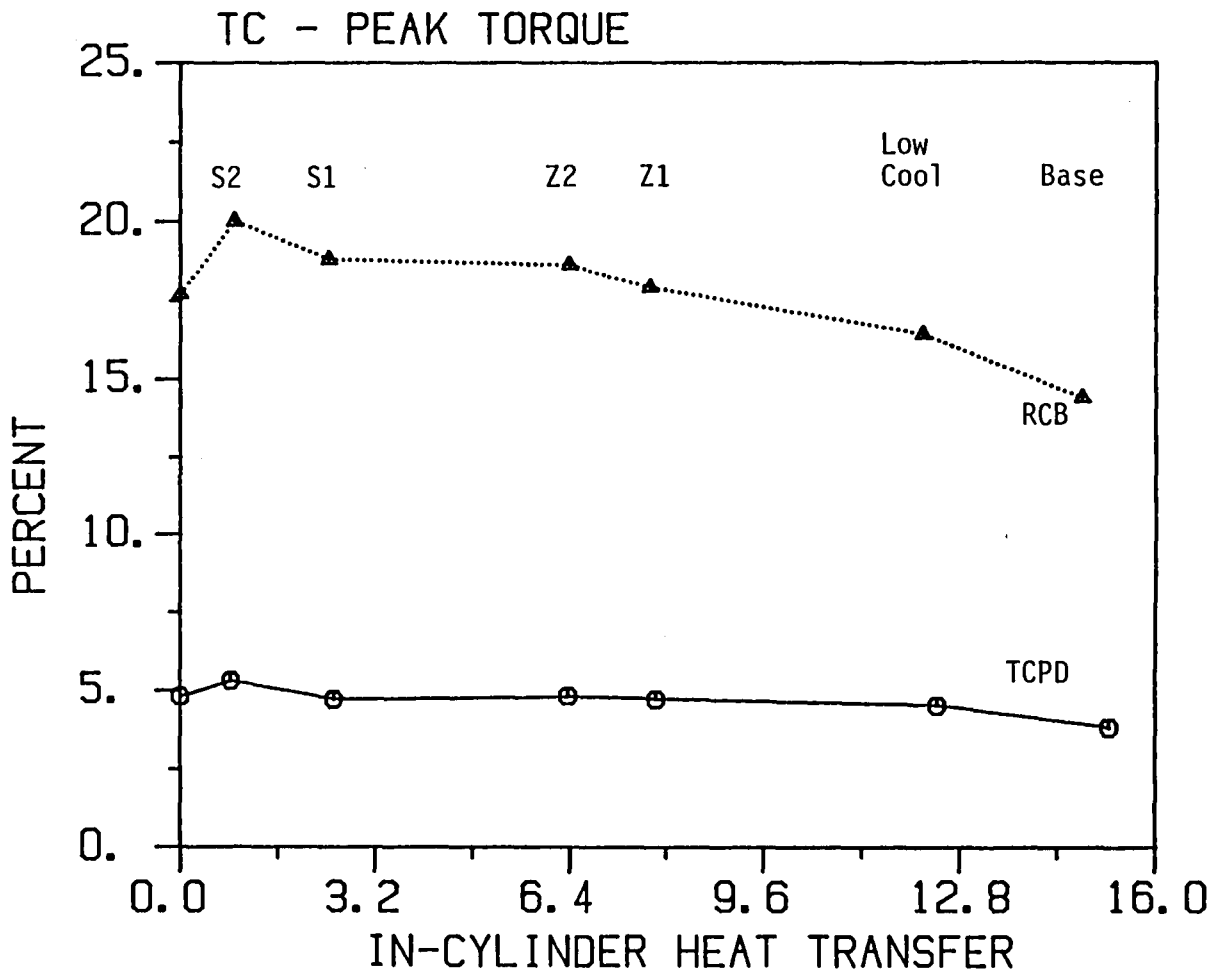

Figure 3-13b Percentage improvement in thermal efficiency due to exhaust heat recovery. Peak torque.

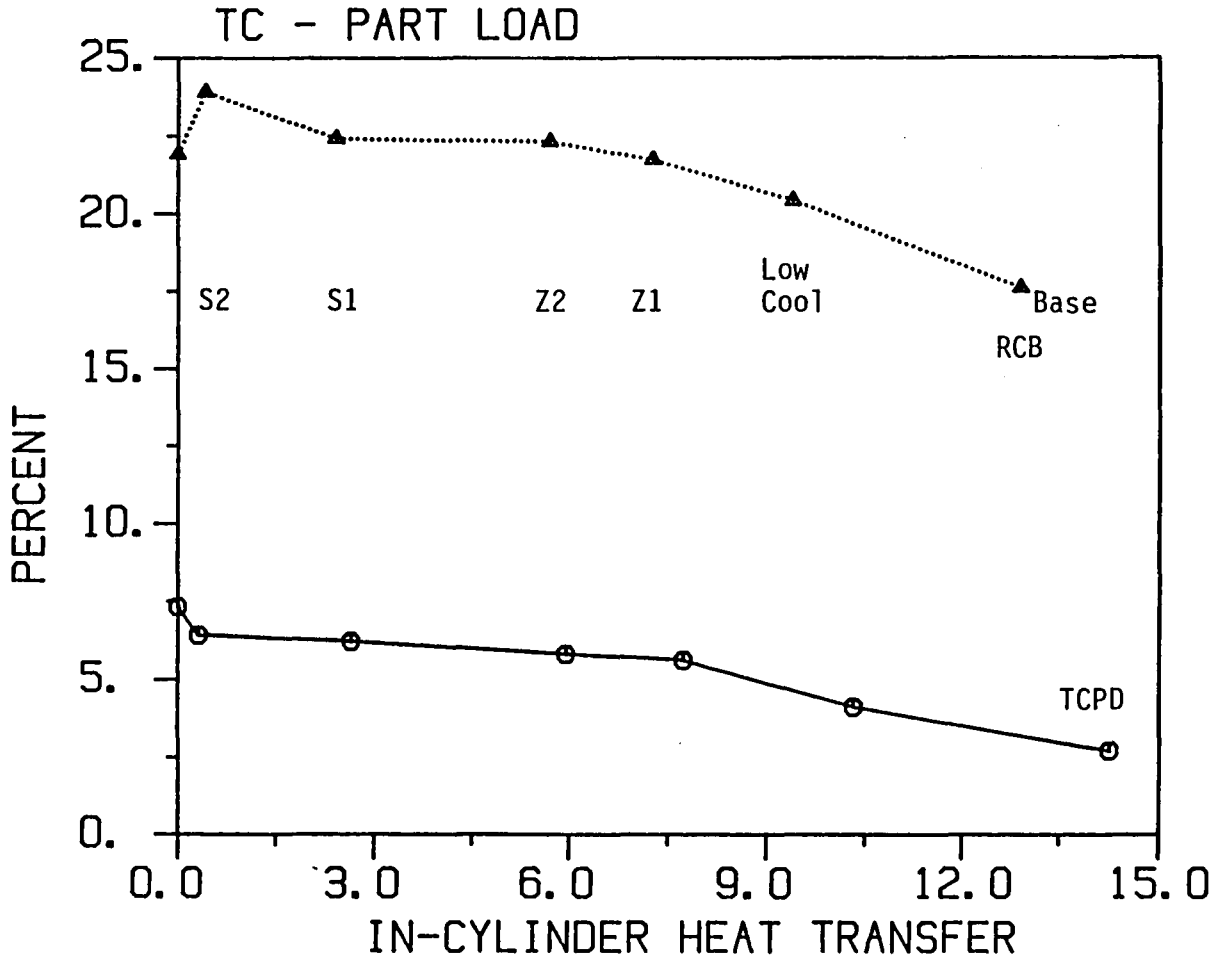

Figure 3-13c Percentage improvement in thermal efficiency due to exhaust heat recovery. Part load.

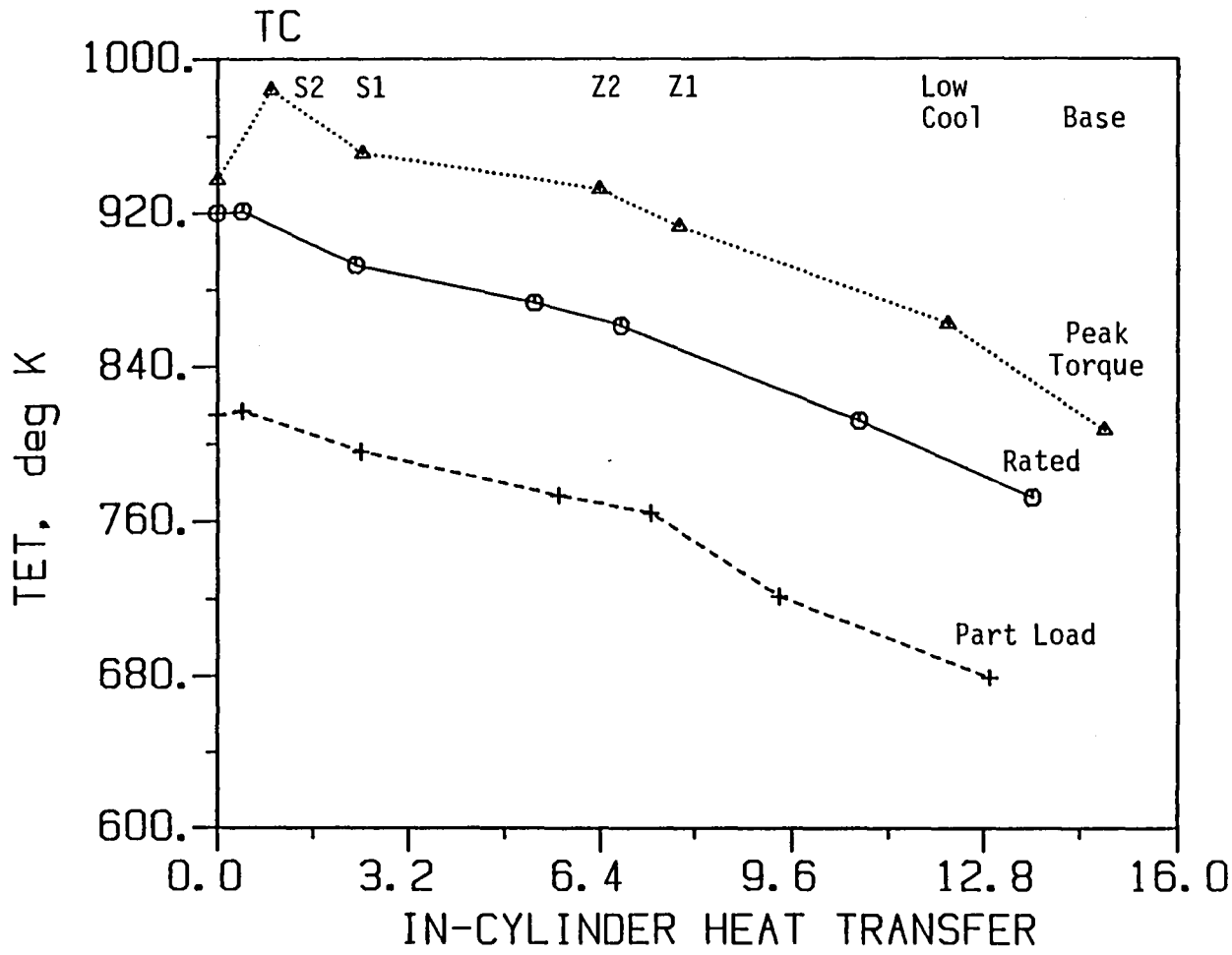

Figure 3-14 Exhaust temperatures downstream of turbocharger, non-intercooled engine.

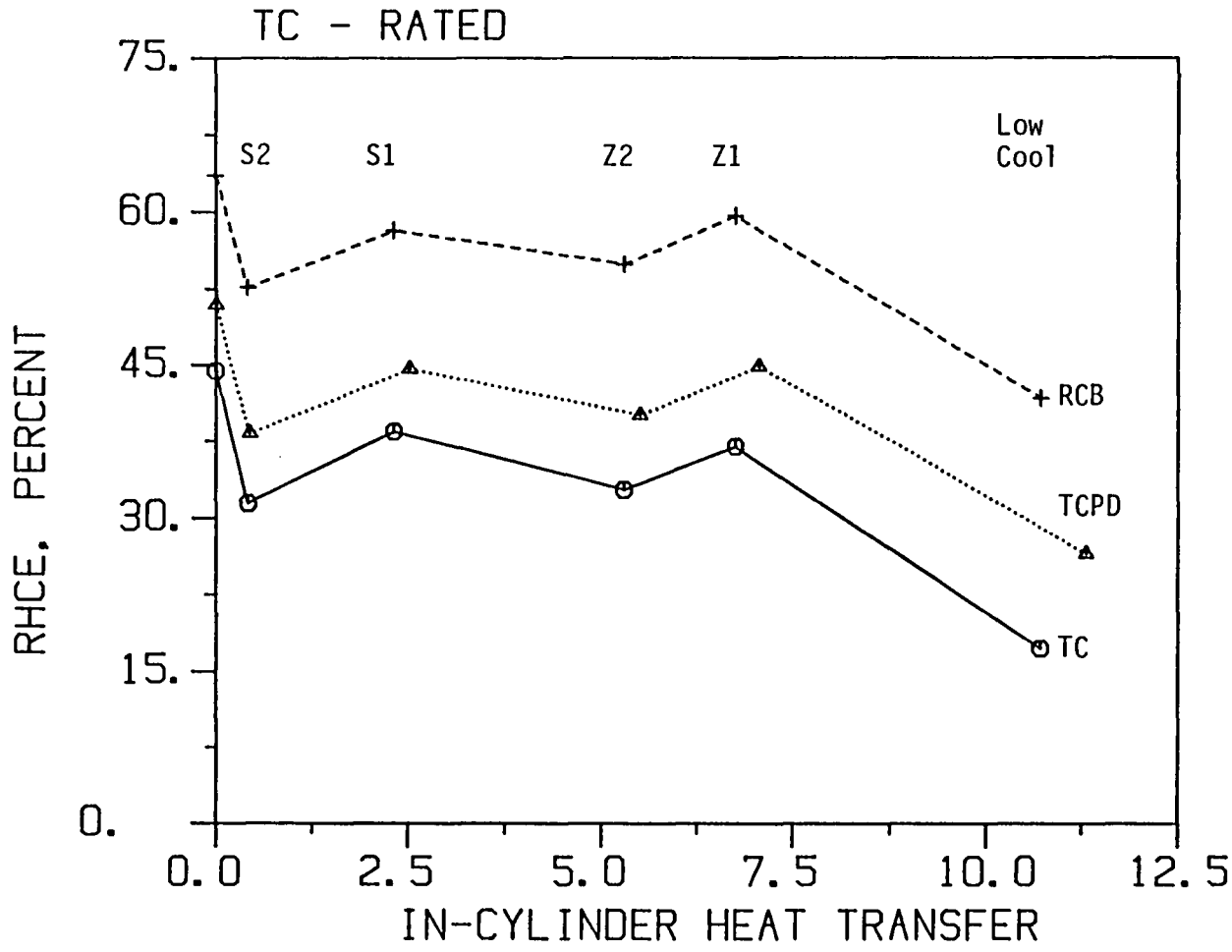

Figure 3-15a Retained heat conversion efficiency, non-intercooled engine. Rated conditions.

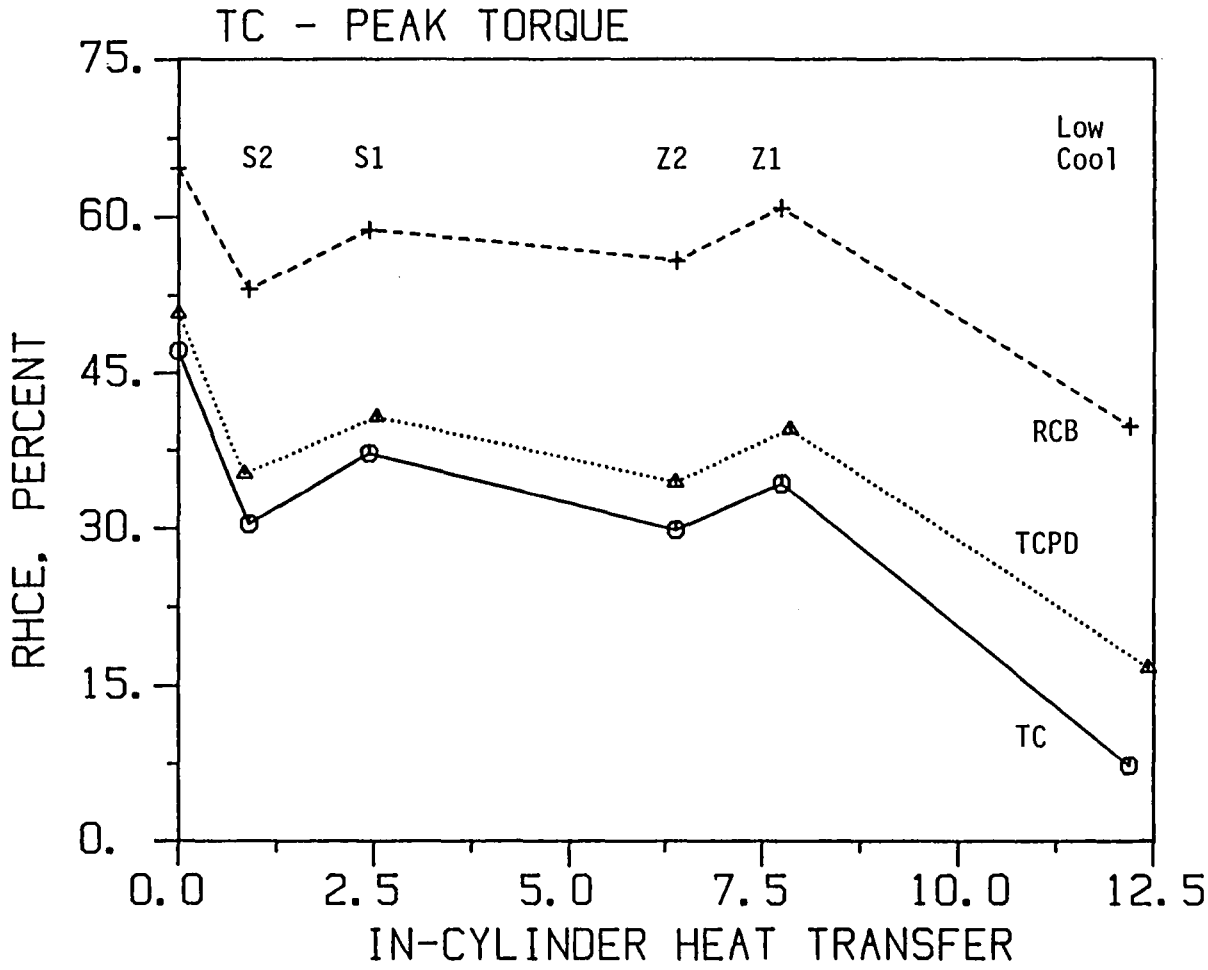

Figure 3-15b Retained heat conversion efficiency, non-intercooled engine. Peak torque.

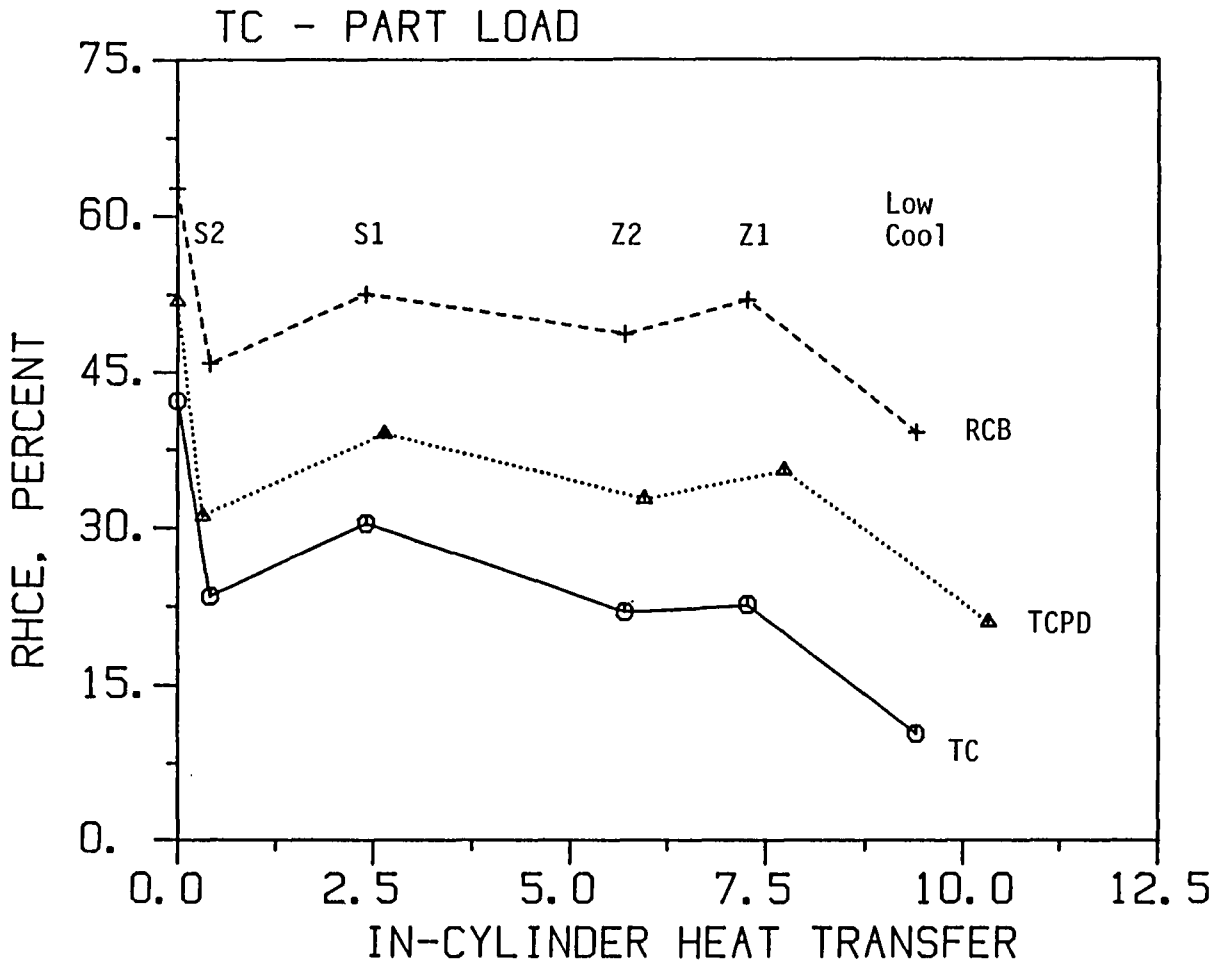

Figure 3-15c Retained heat conversion efficiency, non-intercooled engine. Part load.

(Figure 3-16). However, it decreases faster with insulation, reaching levels of only 28 percent of the baseline value for the superinsulated case at rated conditions. This is still short of the zero heat rejection goal, but some of this level is likely to be rejected to the environment directly by the hot engine structure rather than through a cooling system.

The pumped heat is lower for the baseline case as a result of the higher gas temperatures, but is about the same for the insulated configurations (Figure 3-17). The volumetric efficiency (relative to plenum conditions) is slightly higher (Figure 3-18) due to the higher intake air temperature, which is closer to the wall temperatures than in the intercooled case and so less heat is transferred from walls to fresh charge. However, the total air flow is substantially lower than in the intercooled case. A separate reason is the lower Mach number of the incoming air, which is due to the higher speed of sound of warmer air. The brake horsepower of the non-intercooled engine was substantially below the intercooled levels for all insulation configurations (Figure 3-19), and so intercooling has a lot to offer in this area even under insulated conditions.

In summary, non-intercooled engines show larger incremental improvements in efficiency when insulated than intercooled ones, and this finding agrees with the conclusions drawn by Bailey (1985). The reason for the greater improvement lies in the substantially larger heat transfer levels in the baseline non-intercooled engines, i.e., a greater potential that one can draw on. Starting at an initial disadvantage in thermal efficiency the non-intercooled engines, as they are insulated, narrow down the gap and at very high insulation levels and efficient exhaust heat recovery typical of RCB machines they match the intercooled engines. An advantage of non-intercooled engines is a lower overall heat rejection to coolant, especially at high insulation levels. The disadvantages are the lower power level of non-intercooled engines, which persists under insulated conditions, and expected higher NO_x emissions.

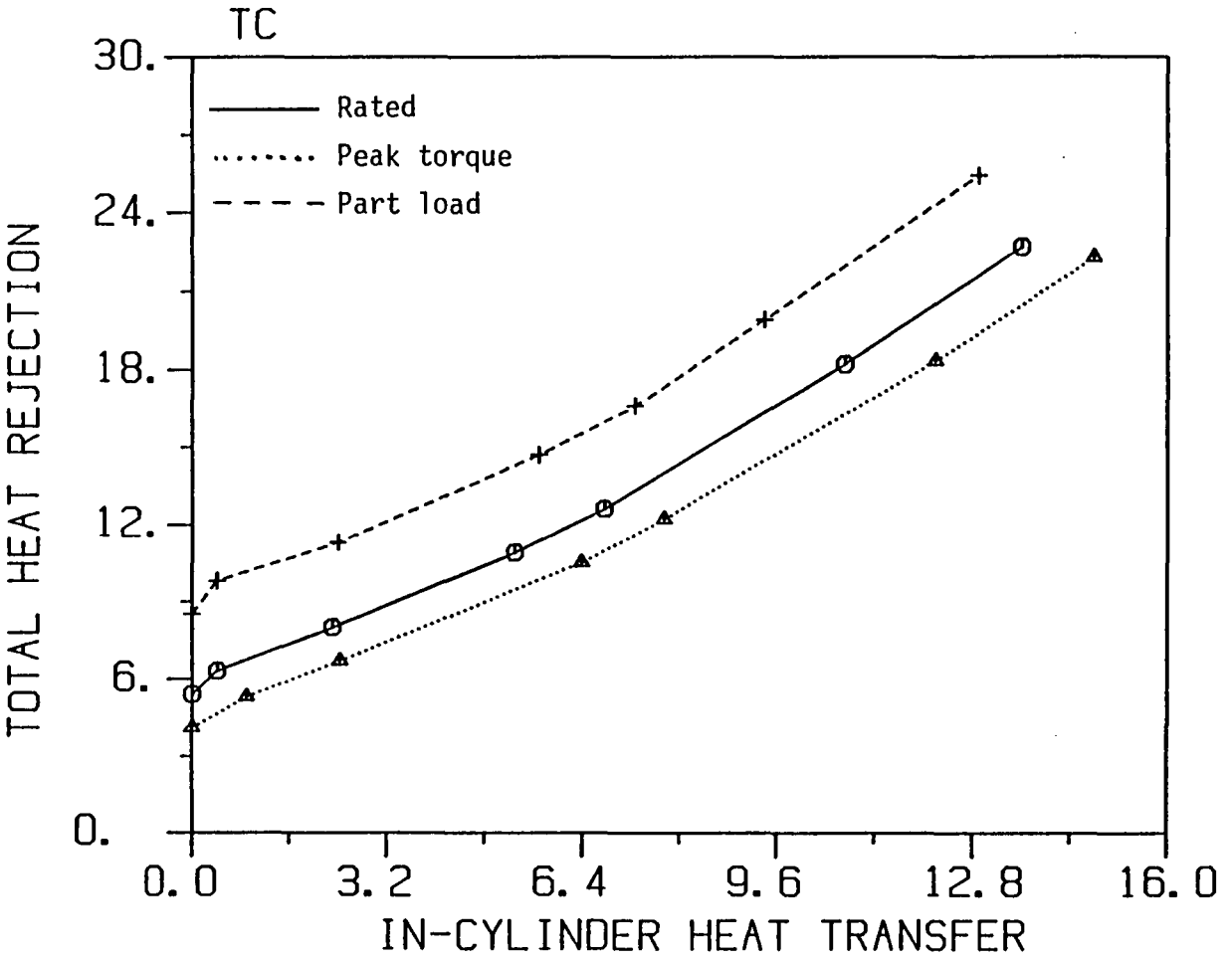

Figure 3-16 Total heat rejection to coolant, oil and environment, non-intercooled engine.

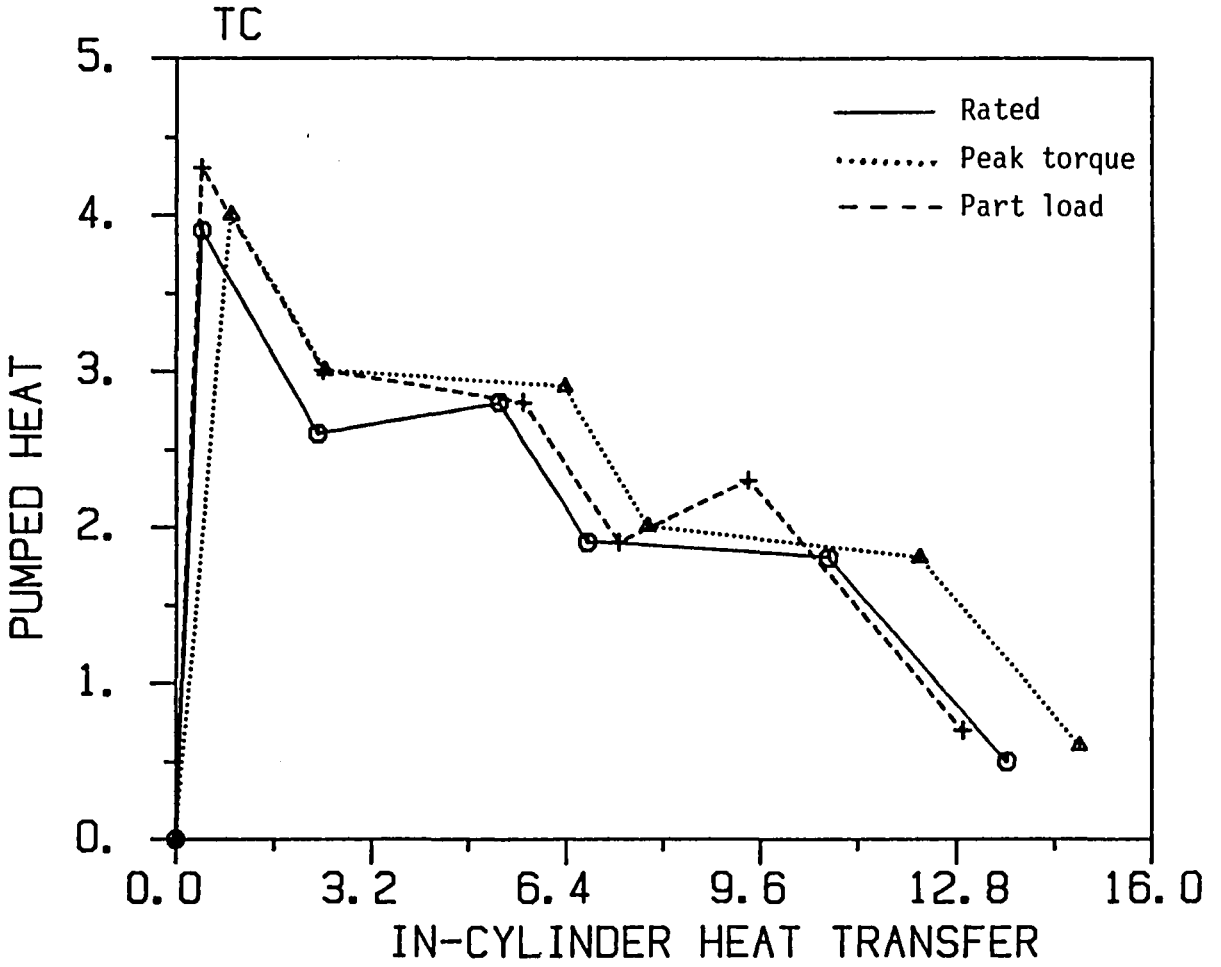

Figure 3-17 Pumped heat expressed in terms of percent of fuel energy, non-intercooled engine.

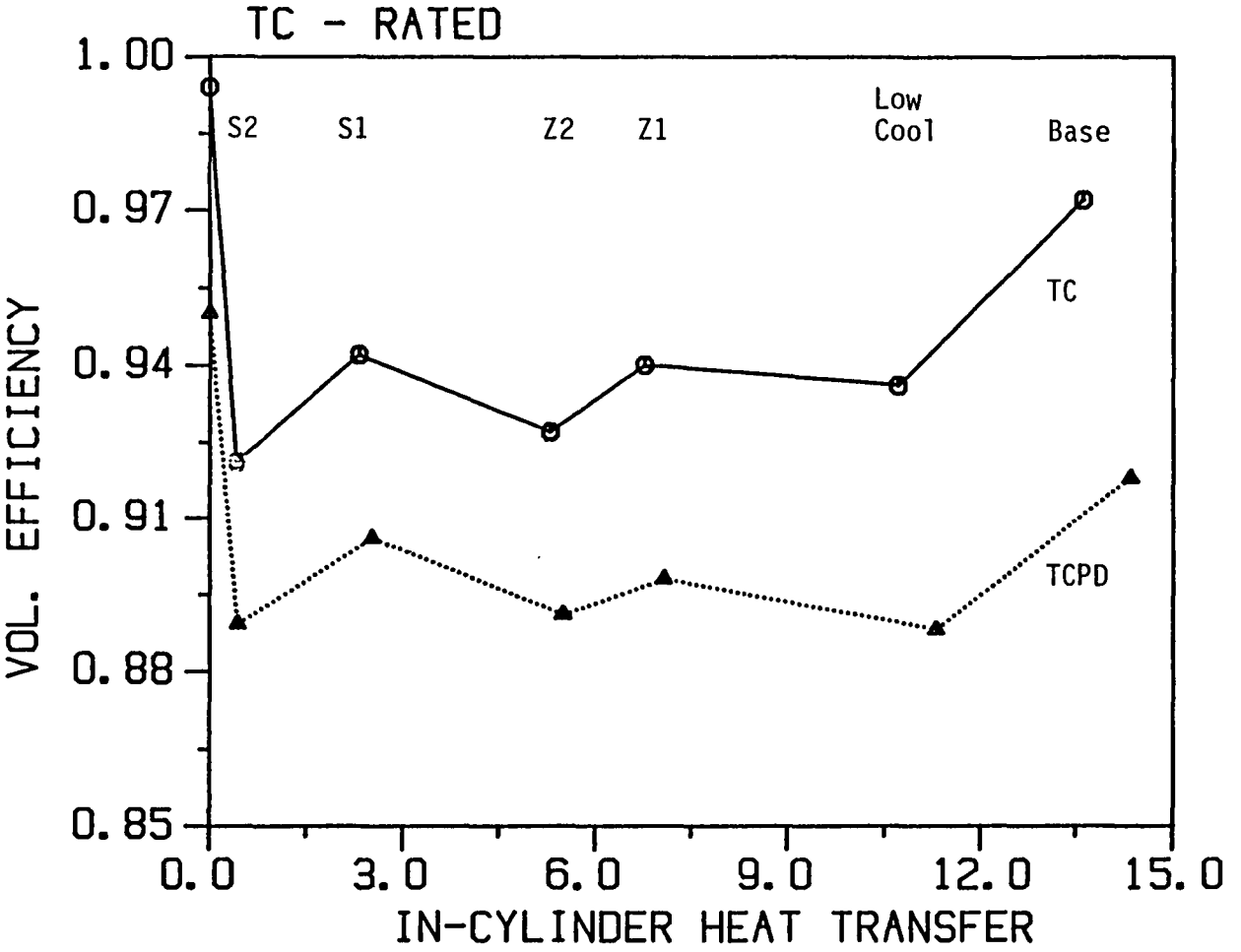

Figure 3-18 Volumetric efficiency, non-intercooled engine.

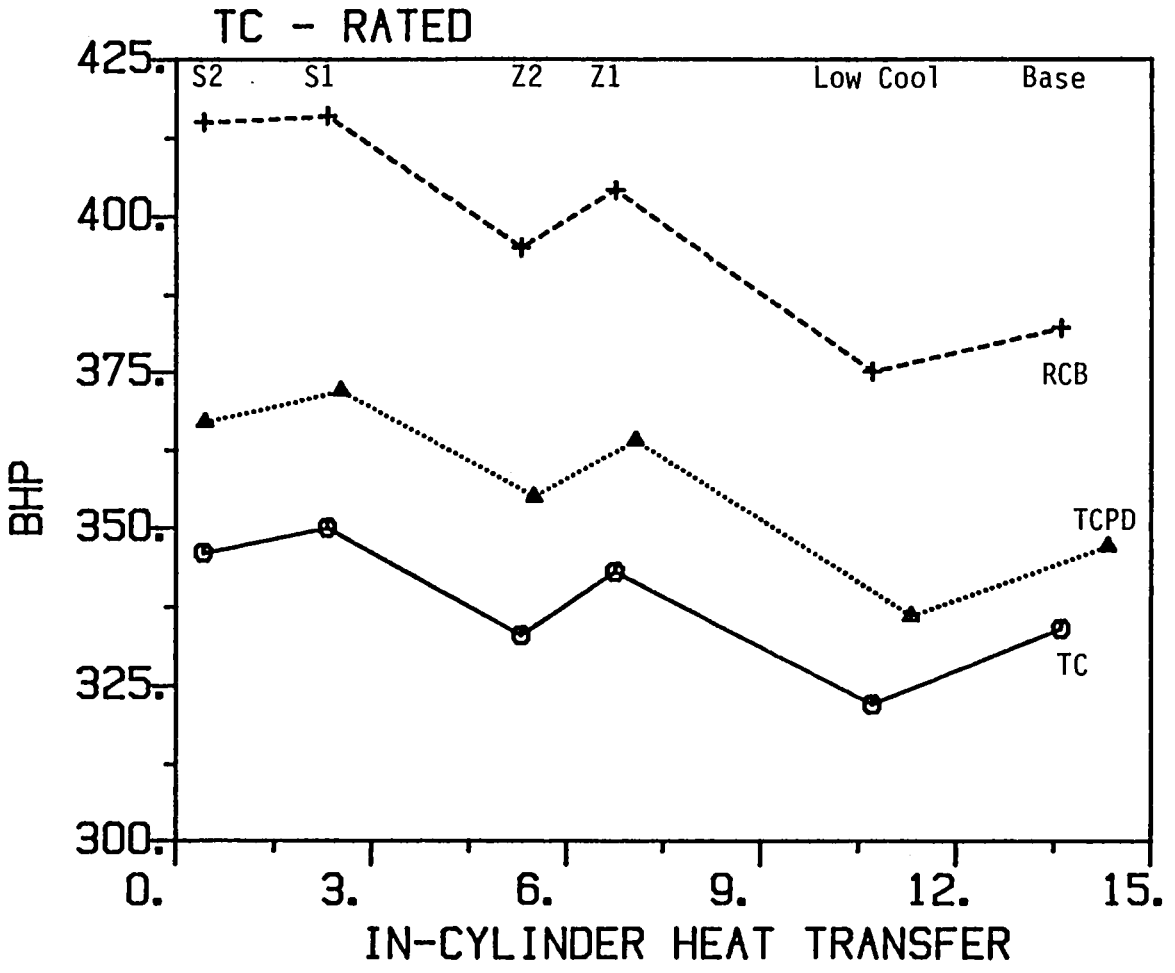

Figure 3-19 Engine system brake power, non-intercooled engine.

Summary of benefits for an Optimum Insulated Truck Engine

Based on the results presented above, one can make some observations on the optimum total package for a low heat rejection version of the baseline engine considered in this study. The zirconia coatings used here provide reductions in heat rejection (55%) which are typical of what is considered achievable in insulated diesels. The simulated port insulation, intake and exhaust, is achievable with cast-in-place ceramic components. The main remaining issues in choosing the engine system strategy are then

- liner insulation,
- intercooling, and
- heat recovery devices.

In the case of the first two items, the choice revolves around the issues of thermal efficiency, engine power, total heat rejection, tribology and emissions. These are graphically shown in Table I. The table shows that liner insulation brings small benefits in thermal efficiency and lower heat rejection, at a cost in lower power, possibly higher NO_x emissions; however the main penalty is in increased tribology problems due to high liner/piston temperatures. Intercooling provides much higher engine power and much lower NO_x emissions. It also lowers the liner temperature, thus alleviating the tribology problems. On the negative side, intercooling increases the total heat rejection, but the increase is quite small. As far as thermal efficiency is concerned, a well insulated engine with exhaust heat recovery has about the same thermal efficiency both with and without an intercooler.

In view of these trends, one concludes that if thermal efficiency, engine power and emissions are the main objectives, as they would be for a highway truck engine, the best configuration should have a cooled metal liner below the top ring reversal point, and it should be intercooled. If the main objectives are thermal efficiency and low total heat rejection and fuel flexibility, as it may be for a military engine, it may be advantageous to follow the opposite strategy of liner insulation and no intercooling.

Since the main focus of this work is the highway truck engine, let us consider in more detail the cooled liner/intercooling strategy, and explore the benefits of heat recovery. These are summarized in Table II for a turbocompound engine, Rankine cycle bottoming, and for a combination of both. The TCPD+RCB combination provides the highest thermal efficiency, with BSFC levels as low as 0.260 lbm/bhp-hr at peak torque conditions. The maximum improvements over a turbocharged/intercooled baseline are 26.5% at rated conditions, 24.6% at peak torque and 28.6% at part load (these relative improvements would be greater for a non-intercooled engine which starts with a lower efficiency in the baseline configuration). Of the four increments between the baseline and the TCPD+RCB, the first, second and third are fairly equal each accounting for less than 20 percent of the total improvement. The largest single improvement is that of RCB alone over TCPD alone, accounting for over 40 percent of the total. The addition of RCB to TCPD-equipped engine generates somewhat lower benefits than when added to an engine alone, which is not surprising since the exhaust gas temperatures of the TCPD engine are lower due to temperature drop across the power turbine; the benefits of the two devices are thus somewhat less than fully additive.

The separate benefits of insulation and heat recovery are highlighted in Table III. It is seen that the thermal efficiency improvements due to insulation start with 5.1 percent for the TCI, and they increase up to 7.9 for the same engine equipped with TCPD & RCB. This means that even though heat recovery does reinforce the thermal efficiency benefit of insulation, insulation alone brings respectable efficiency increases. If no heat insulation were used, the calculations show that at rated conditions TCPD alone brings 4.5 percent improvement, RCB brings 13.3 percent and TCPD & RCB brings 17.2 percent. If the base engine were insulated the benefits should be greater: 5.4, 15.4 and 20.4 percent, respectively. The last column shows the combined thermal efficiency benefits of insulation and heat recovery already discussed in the previous paragraph.

	thermal efficiency	engine power	total heat rejection	tribology	emissions
liner insulation	+	-	+	---	-
intercooling	0	+++	-	+	+++

Table I. Relative merits of liner insulation and of intercooling

Configuration	Rated Conditions BHP	BSFC (lb/bhp-hr)	η_t	Peak Torque BSFC	η_t	Part Load BSFC	η_t
Baseline	411	0.339	40.8	0.325	42.6	0.408	33.9
Insulated	411	0.323	42.9	0.308	44.9	0.393	35.2
Ins. + TCPD	437	0.306	45.2	0.295	46.9	0.373	37.1
Ins. + RCB	477	0.279	49.5	0.269	51.5	0.327	42.3
Ins. + TCPD + RCB	499	0.268	51.6	0.260	53.1	0.318	43.6

Table II. Thermal efficiency of an insulated engine with heat recovery devices, at three operating conditions. Zirconia plasma spray on all components except liner below top ring reversal point.

	Percentage Gain* due to Insulation	Percentage Gain due to Heat Recovery**		Percentage Gain due to Insulation and Heat Recovery***
		Cooled Engine	Insulated Engine	
TCI	5.1	--	--	5.1
TCPD	6.0	4.5	5.4	10.8
RCB	7.1	13.3	15.4	21.3
TCPD + RCB	7.9	17.2	20.4	26.5

* With respect to same engine/heat recovery system with no insulation

** With respect to turbocharged/intercooled baseline conventionally cooled and insulated, respectively

*** With respect to conventionally cooled turbocharged/intercooled baseline

Table III Percentage gains in brake efficiency in a turbocharged/intercooled truck engine due to insulation and heat recovery devices at rated conditions.

Turbocharged Automotive DI Diesel with Swirl Combustion

In addition to the studies involving the heavy-duty highway truck engines, a shorter study was made of the benefits that insulation can provide for turbocharged automotive DI diesels. These smaller DI diesels are currently among the most intensely researched and developed automotive powerplants, promising high fuel efficiency even in the conventional cooled form. Therefore, the benefits that insulation could provide to these engines are of interest, and are addressed in this section.

The engine simulated here is meant to represent an advanced powerplant with high pressure injection and a well-developed combustion system. Even so the engine thermal efficiency lags behind that of the larger engines (Figure 3-20). This is partly due to the higher heat transfer, augmented by the swirl and larger in-cylinder surface-to-volume ratio, which is about twice as large as that in the intercooled highway diesel. By the same token, the high baseline heat transfer indicates that this engine may benefit greatly from insulation. Indeed, the results shown in Figures 3-20 and 3-21 show that the relative benefits of insulation are about twice as large as those for the quiescent highway diesel.

The insulation increases the exhaust temperatures, shown in terms of turbine inlet temperature in Figure 3-22. Part of the conserved in-cylinder heat goes, as desired, into the piston work. The value of RHCE (Figure 3-23) is around 30 percent, except for the reduced-cooling configuration where it is much lower than that. It may be noticed that the conversion efficiencies are somewhat lower than for the highway truck diesels. This is due to the different crank angle distribution of the in-cylinder heat transfer: the swirl engine has a larger heat transfer during the latter portions of the expansion stroke, which, when conserved by insulation, produces less work because of limited expansion.

Volumetric efficiency of this engine is affected strongly by the insulation, as may be seen in Figure 3-24, decreasing by up to nine percentage points for the superinsulated design 2, and by about six

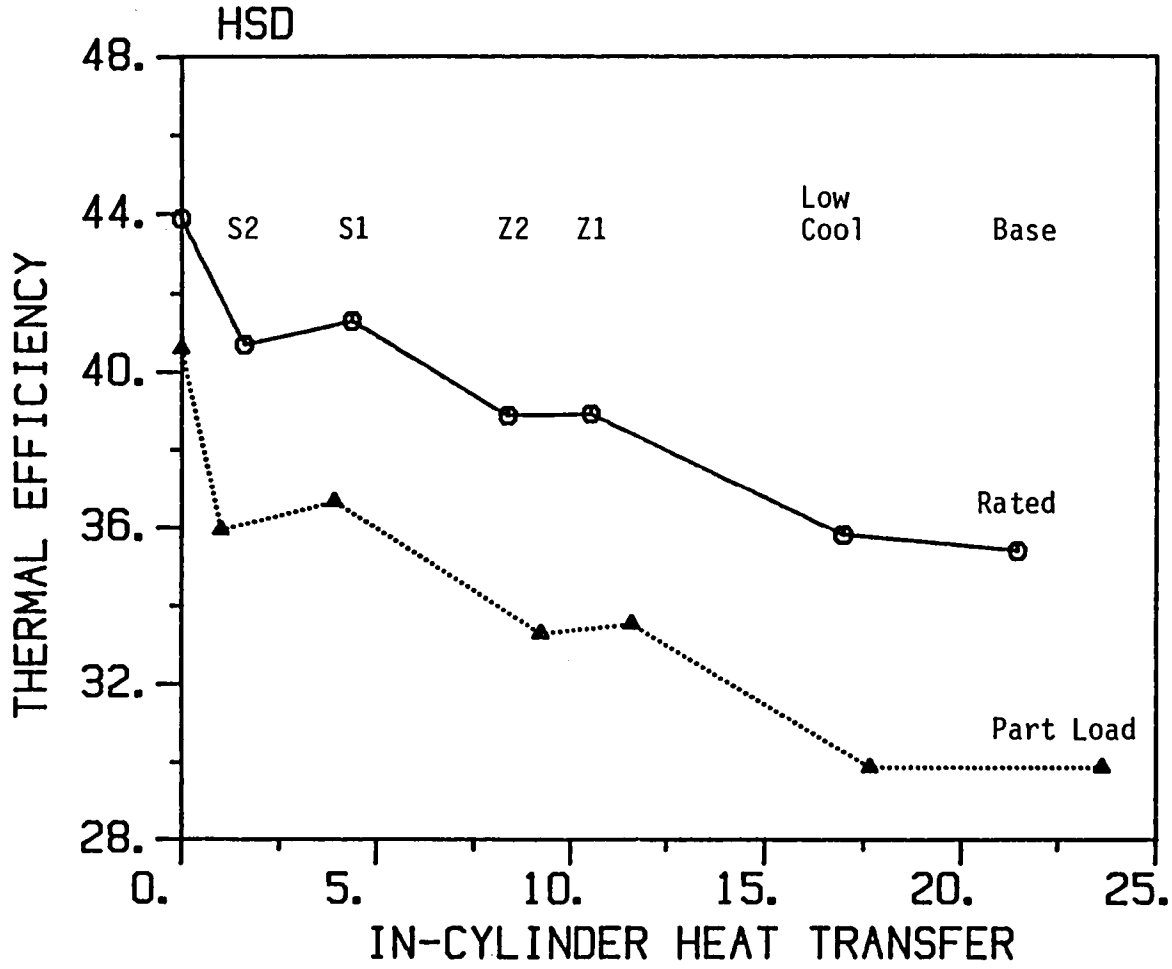

Figure 3-20 Thermal efficiency of a high speed DI diesel.

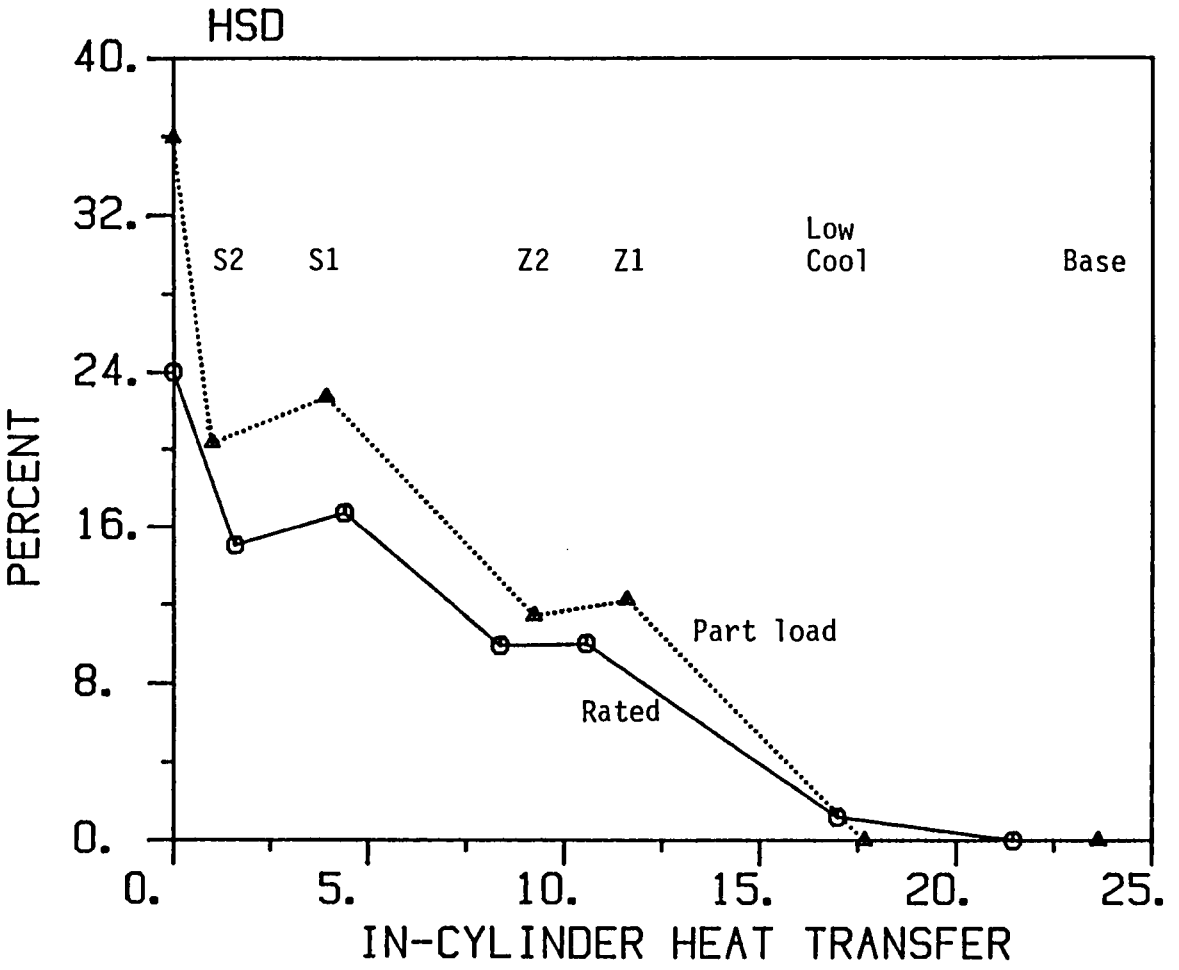

Figure 3-21 Percentage improvement in brake thermal efficiency of an automotive DI diesel with respect to the cooled baseline.

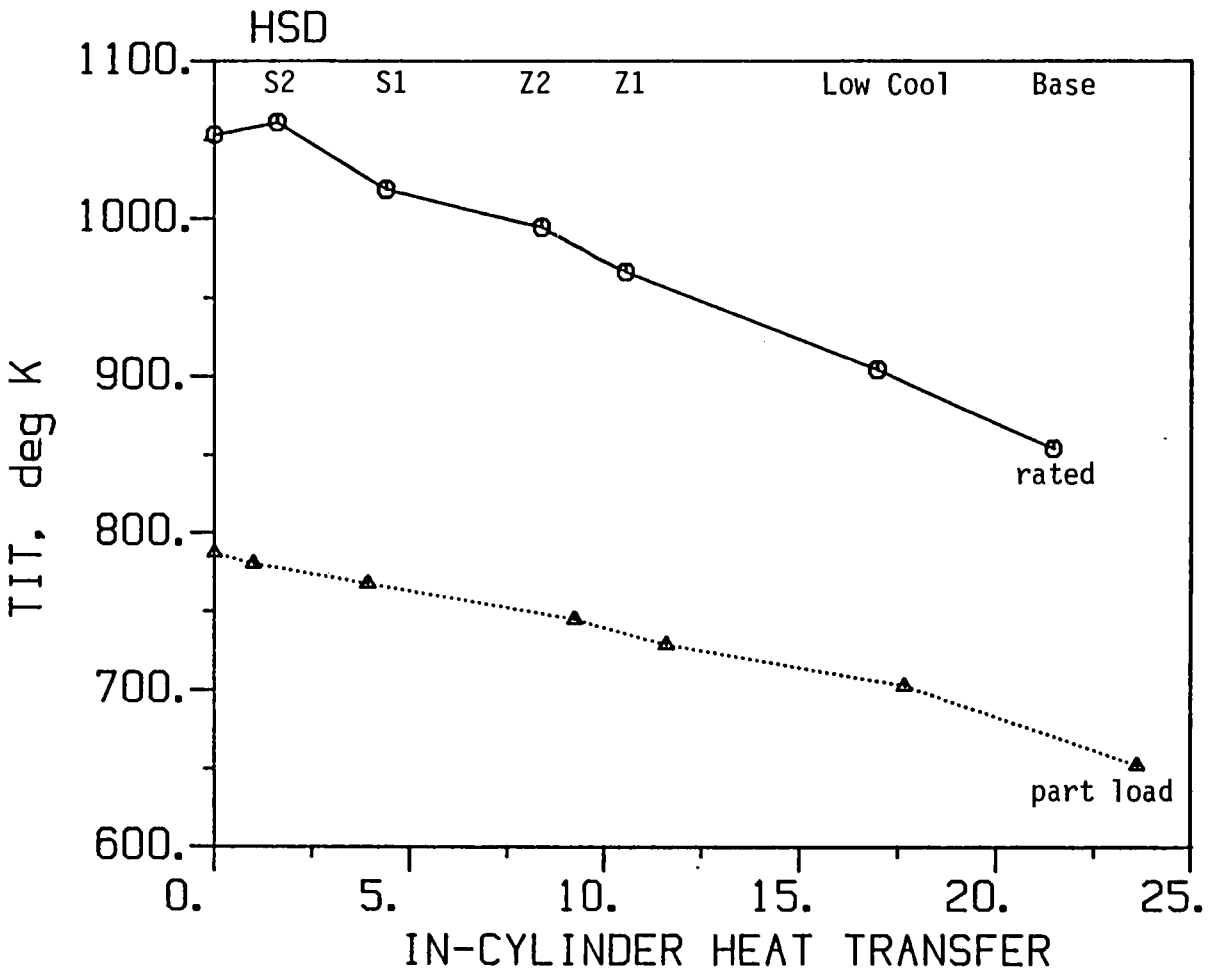

Figure 3-22 Turbine inlet temperatures, automotive DI diesel.

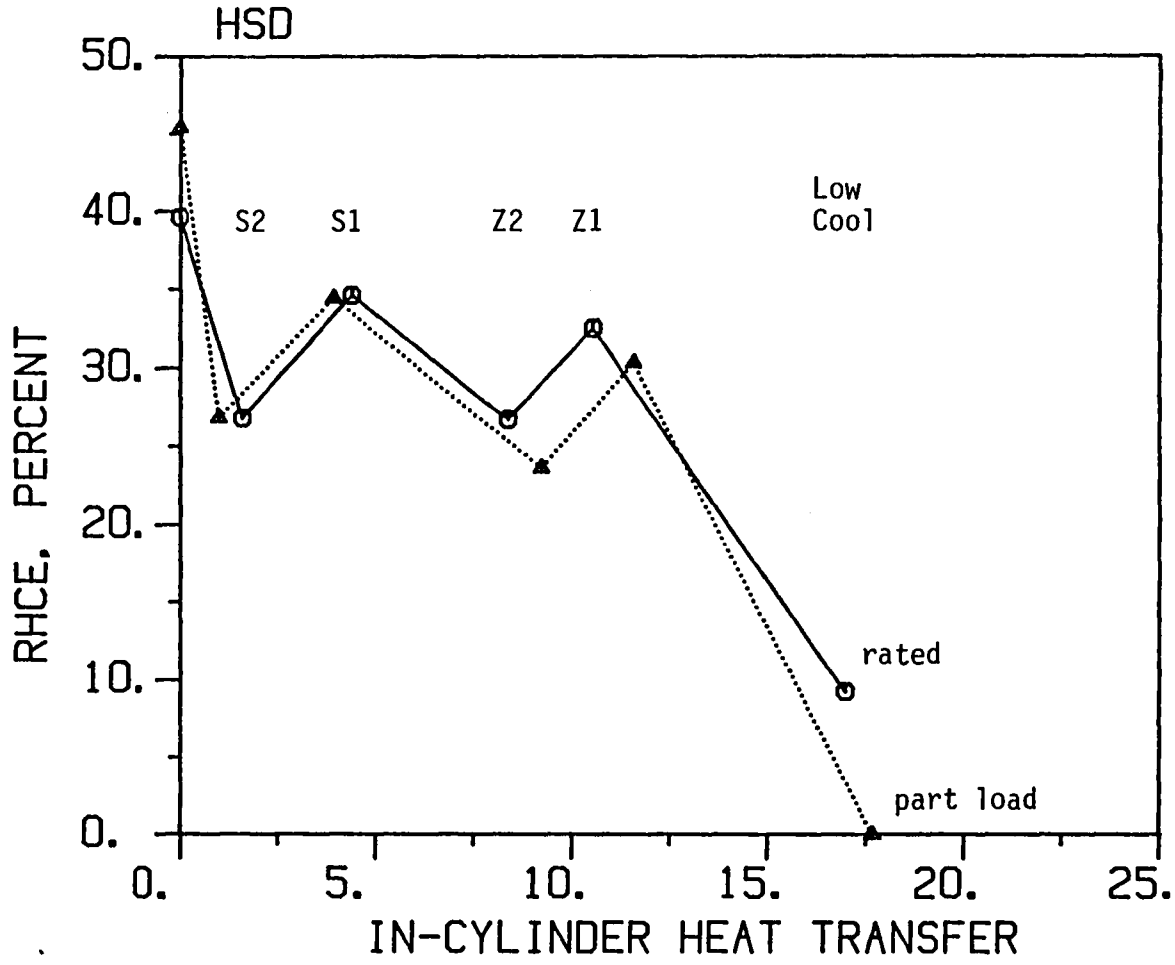

Figure 3-23 Retained heat conversion efficiency in an automotive DI diesel.

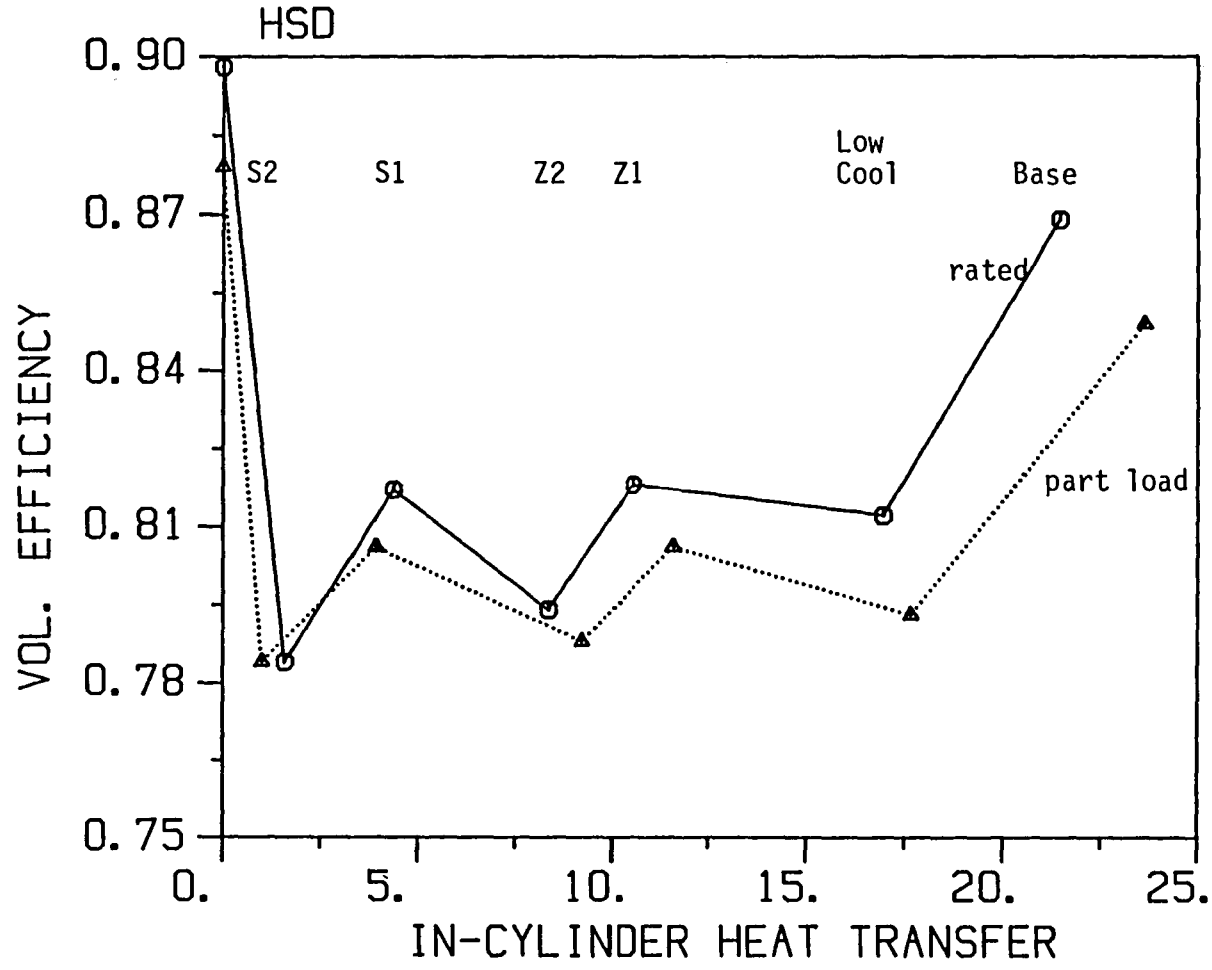

Figure 3-24 Volumetric efficiency of the automotive DI diesel.

points for the Z1. The pumped heat levels of all designs are about the same as for the truck engines (Figure 3-25), which appears surprising in view of the higher overall heat transfer, but this is again due to the differences in the crank angle distribution of the heat transfer. The engine power shows no benefits of insulation, Figure 3-26, in consequence of the lower volumetric efficiency and due to imposed constraints on peak cylinder pressure.

The total heat rejection, Figure 3-27, starts with quite high levels of around 30 percent of fuel energy for the baseline cooled configuration. The heat rejection drops very sharply with insulation, reducing to one half with ZPS insulation.

In summary, there are very significant benefits in brake efficiency, on the order of 10 percent for rated and 12 for part load conditions, achievable with practical ZPS coatings. These benefits are the direct result of the high heat transfer of the baseline cooled engine. Associated with the insulation are large penalties in volumetric efficiency, which offset the thermal efficiency gains and as a result the engine power is not increased. Liner insulation does not provide any advantages, and in fact it decreases thermal efficiency and engine power.

COMPARISON TO PREVIOUS PREDICTIONS

In a number of earlier publications, engine simulation codes were used to address some of the same issues studied here. The results of several relevant papers will be briefly reviewed below, comparing their predictions to the present ones. It will be seen that there are significant differences between the previous and the present results. The main differences lie in the predicted RHCE with which the conserved in-cylinder heat is converted into piston work, which our results show to be higher than shown by any of the previous studies. An important difference is also in the predicted effect of insulation on volumetric efficiency, which our results show to be less pronounced than some of the previous studies have indicated.

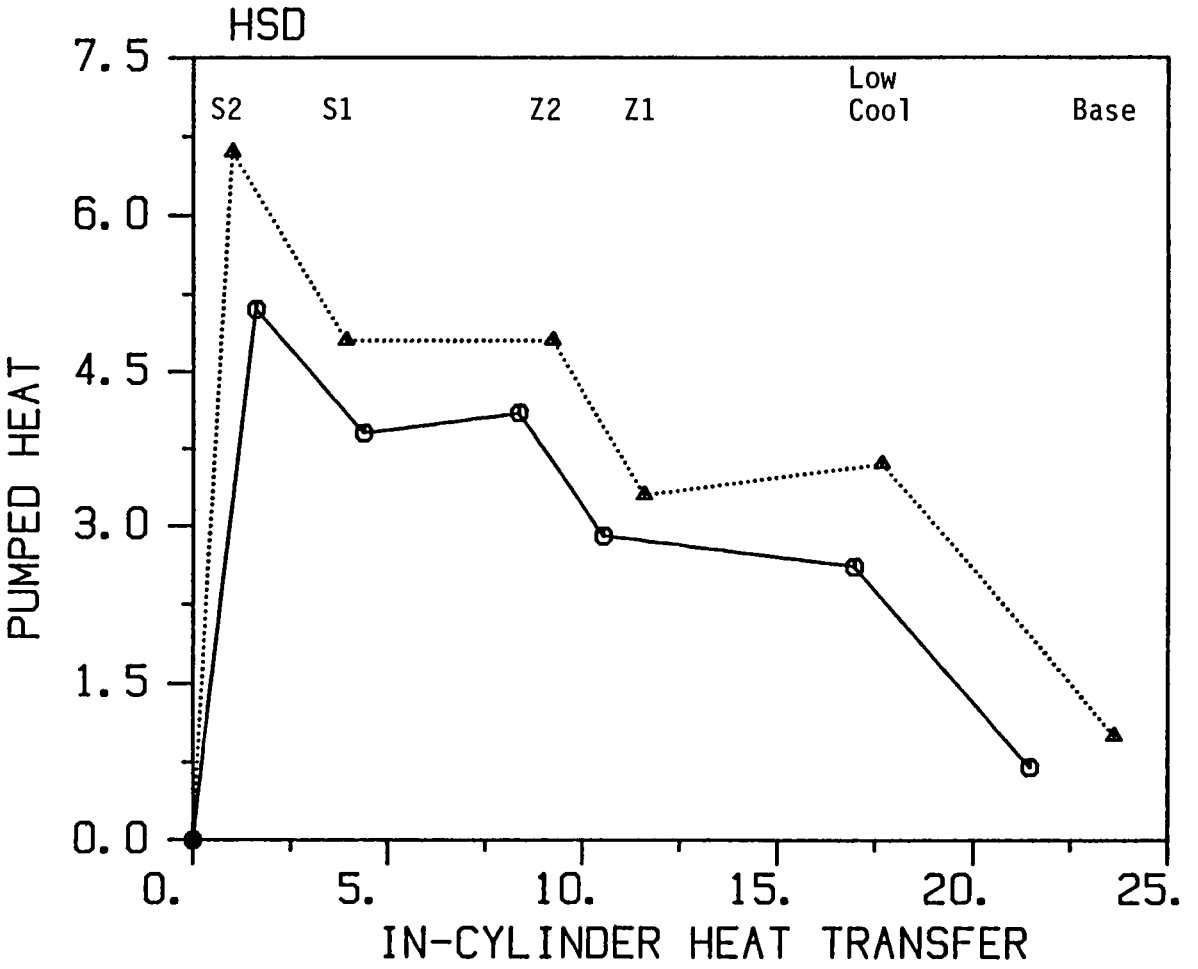

Figure 3-25 Pumped heat expressed in percent of fuel energy, automotive DI diesel.

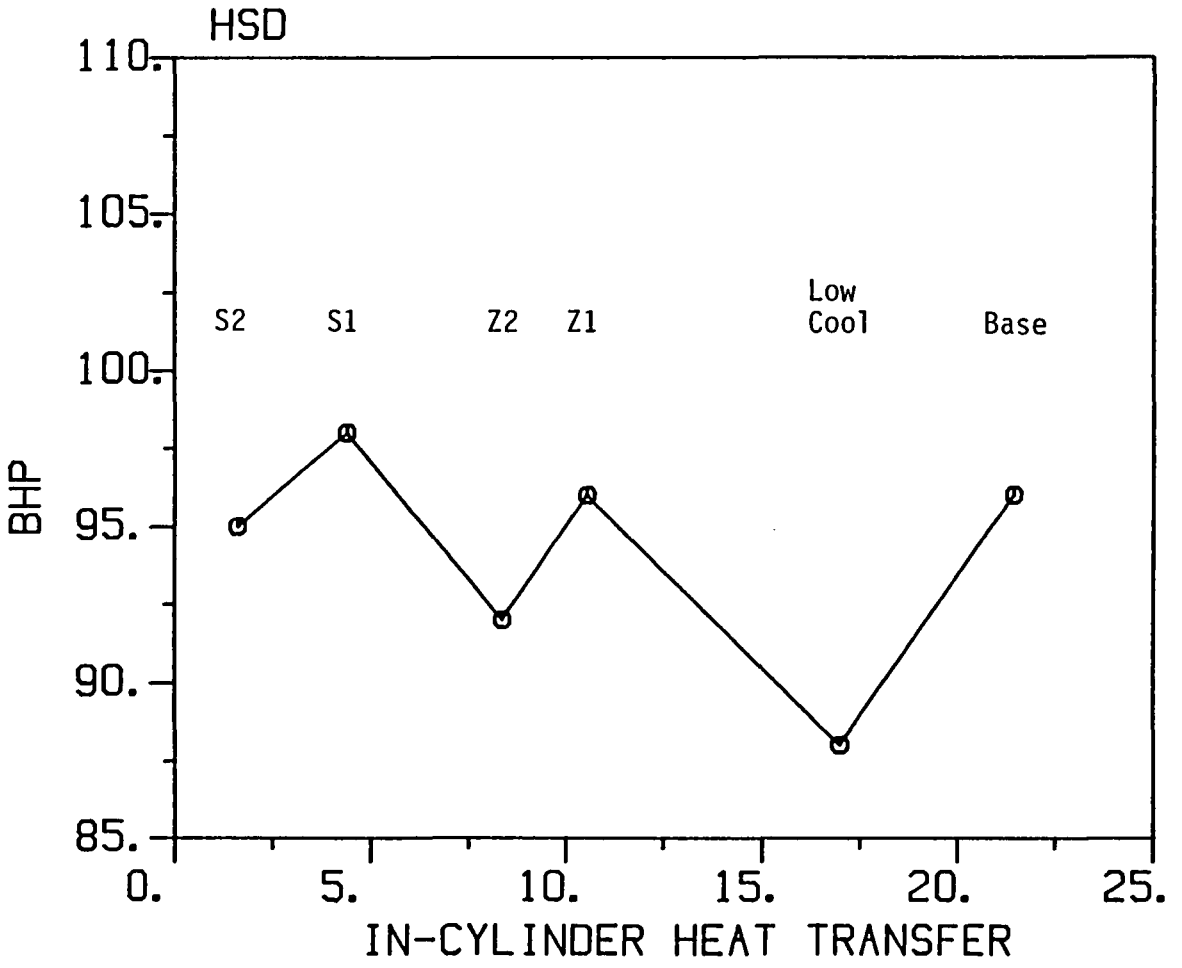

Figure 3-26 Engine brake power, automotive DI diesel.

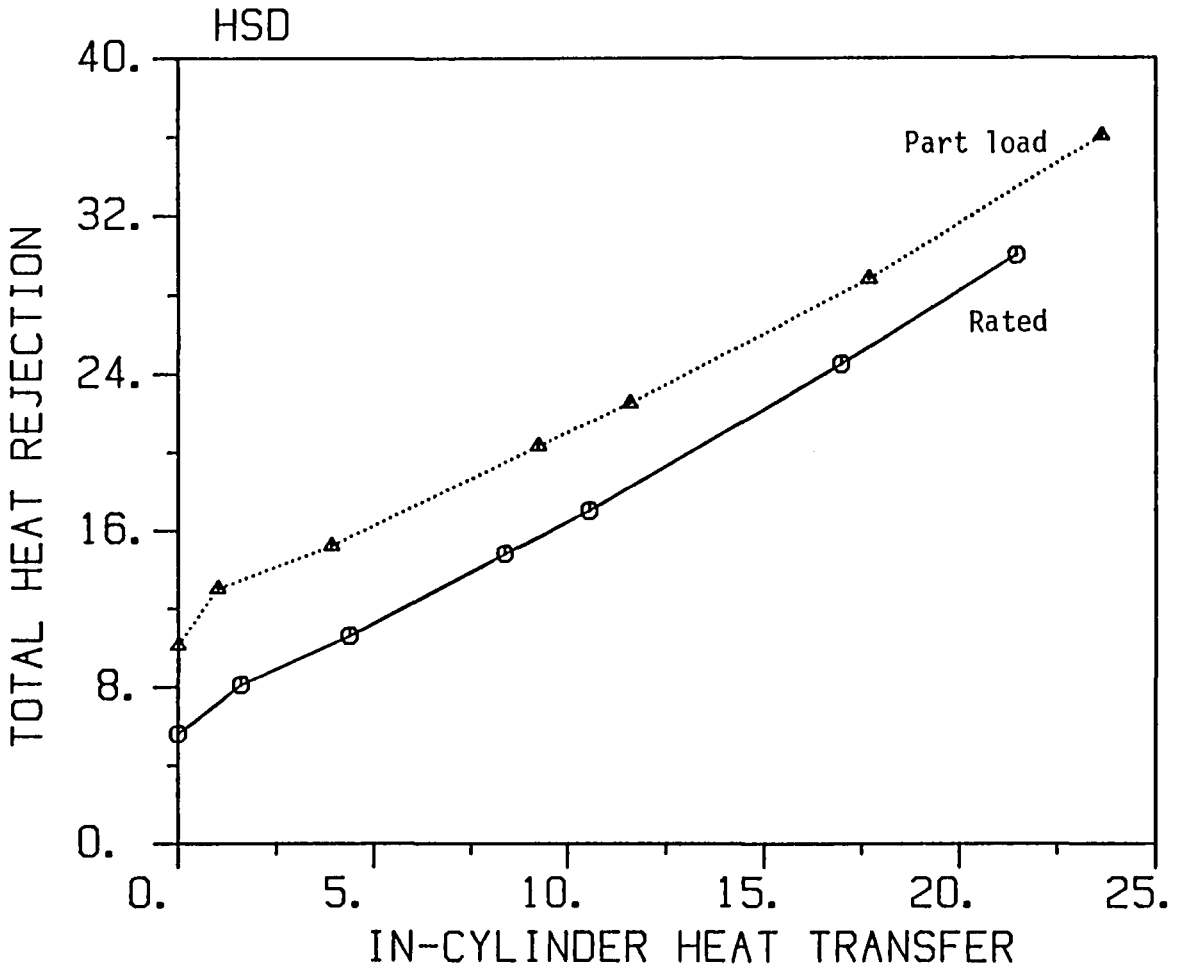

Figure 3-27 Total heat rejection to coolant, oil and environment, automotive DI diesel.

In order to understand these differences, our methodology was modified to permit incorporation of some of the assumptions used in other codes, and calculations were made to determine the effects of these assumptions. It was found that the reasons for the differences in predictions were due to:

- differences in gas-phase heat transfer models, specifically the relative magnitudes of heat transfer during the four strokes of the engine cycle,
- methods used to determine temperatures in the engine structure and the resulting predicted surface-to-surface temperature variations in the combustion chamber, and
- surface temperature swings, which were neglected in all previous simulations.

The previously used gas-phase heat transfer models had much less variation in heat fluxes with crank angle than the present model, which is flow based and accounts for variations in gas velocities. This particular difference, discussed in Morel and Keribar (1985), was analyzed in more detail and the results are presented below. The structure temperatures used in previous studies were either guesses or estimates, or were obtained by a simplified conduction scheme decoupled from the cycle calculation. However, the use of correct wall temperatures obtained by proper balancing of all heat loads and heat paths is quite important, and has an effect on the calculated trends of RHCE and especially on the volumetric efficiency.

To study the effect of gas-phase heat transfer models as used in some of the previous papers discussed below, the flow-based convection model was replaced by Annand's model (Annand, 1963), and the heat radiation model was deactivated. On the conduction side, the use of the network model was continued, but the surface temperature swing calculation was suppressed. Simulation was run for the turbocharged intercooled engine at rated conditions over six configurations: baseline, reduced cooling, Z1, Z2, S1 and S2. The constant of the Annand's model was adjusted to produce the same cycle averaged heat transfer as obtained with the flow

model at the rated conditions in the baseline engine. All other cases were then run with the same constant. The results for the baseline case showed a heat split between the piston, head and liner of 38/24/38, compared to a very different split obtained with the flow model 48/32/20, and this difference is directly attributable to the very different temporal and spatial variation of the heat transfer during the 720 crank angle degrees.

While the heat rejection was matched at the baseline conditions, the heat rejections calculated for the other configurations were different than calculated with the flow model. This is shown in Figure 3-28, which shows the difference between the Annand-based and flow-based model predictions. It may be seen that the maximum differences are quite significant and that for configurations with the cooled liner the points tend to lie higher than for the uncooled liner cases; this is again due to the differences in temporal and spatial variation of the heat transfer.

One of the major differences lies in the RHCE (Figure 3-29), which is much higher for the present model than for Annand's model. This translates into differences in predicted thermal efficiency improvements (Figure 3-30) obtained with no exhaust heat recovery. The present model indicates that the direct efficiency benefits obtained in a turbocharged engine are quite significant. One of the reasons for the poorer benefits predicted with the Annand's model is that the pumped heat it calculates (Figure 3-31) is higher, and this pumped heat increases the proportion of conserved in-cylinder heat that leaves in the exhaust stream. It is interesting, in view of the differences observed in the engine work increments, that the differences in the exhaust temperature are quite minor, being of the order of 10-25°K.

Since the gas-phase heat transfer provides boundary conditions for structure temperature calculations, it is not surprising that the large differences in heat transfer distribution, produced by the two models, also have a strong effect on the calculated component temperatures, reaching up to 100°K difference on the top of the liner, with Annand's model giving the higher value. Volumetric efficiency decreases due to

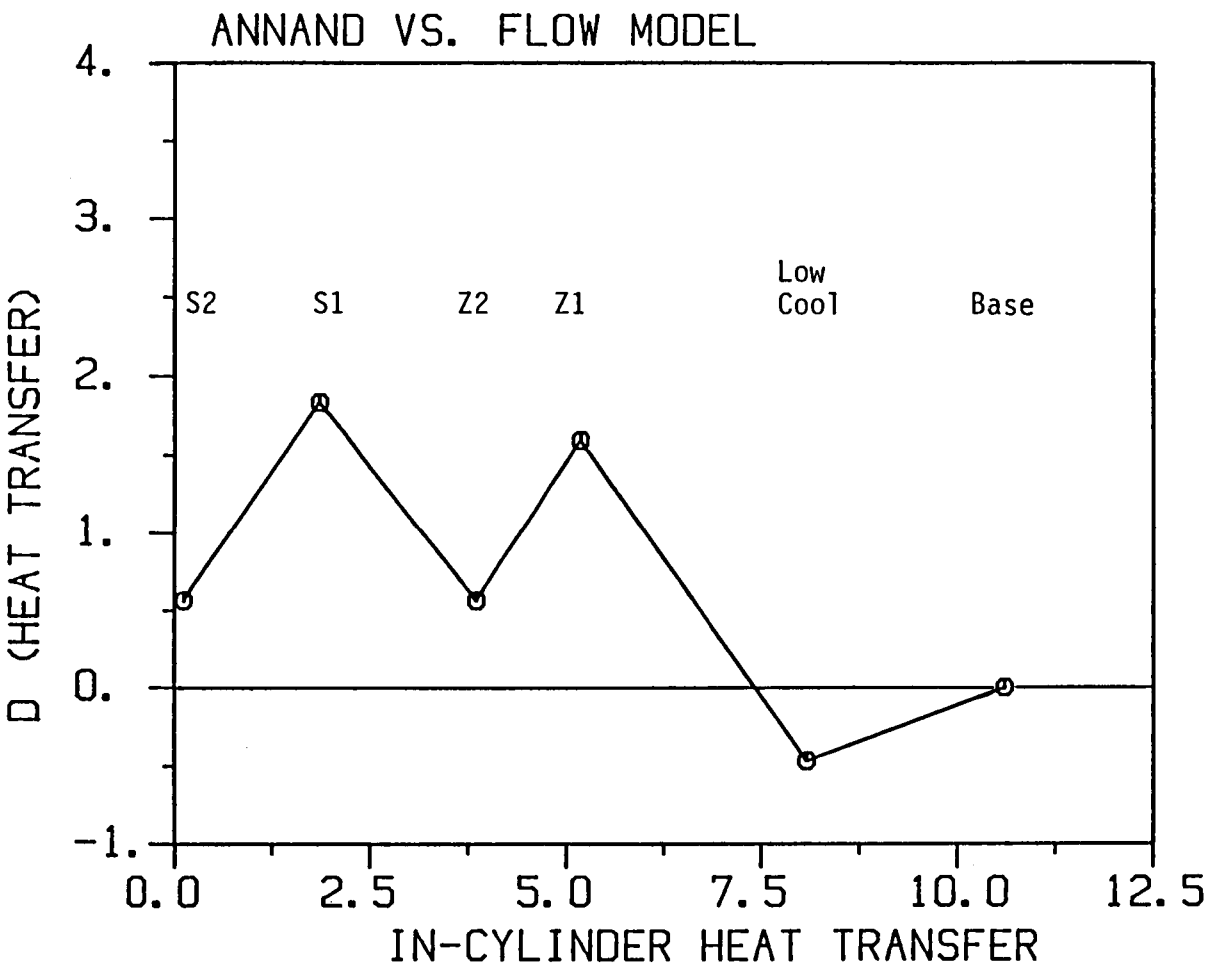

Figure 3-28. Difference between heat rejection predicted using the Annand model and that predicted by the present model. Turbocharged, intercooled engine.

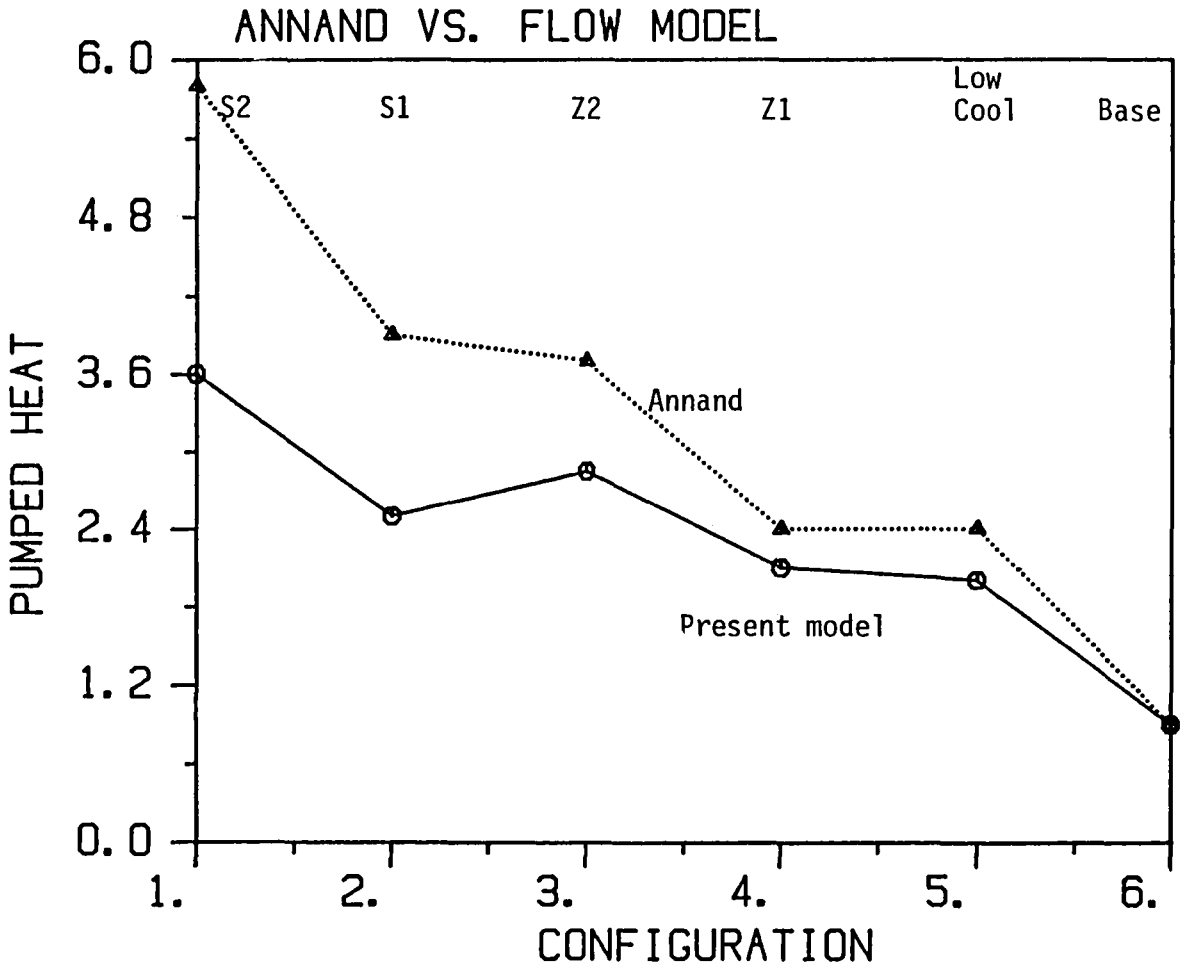

Figure 3-31 Pumped heat.

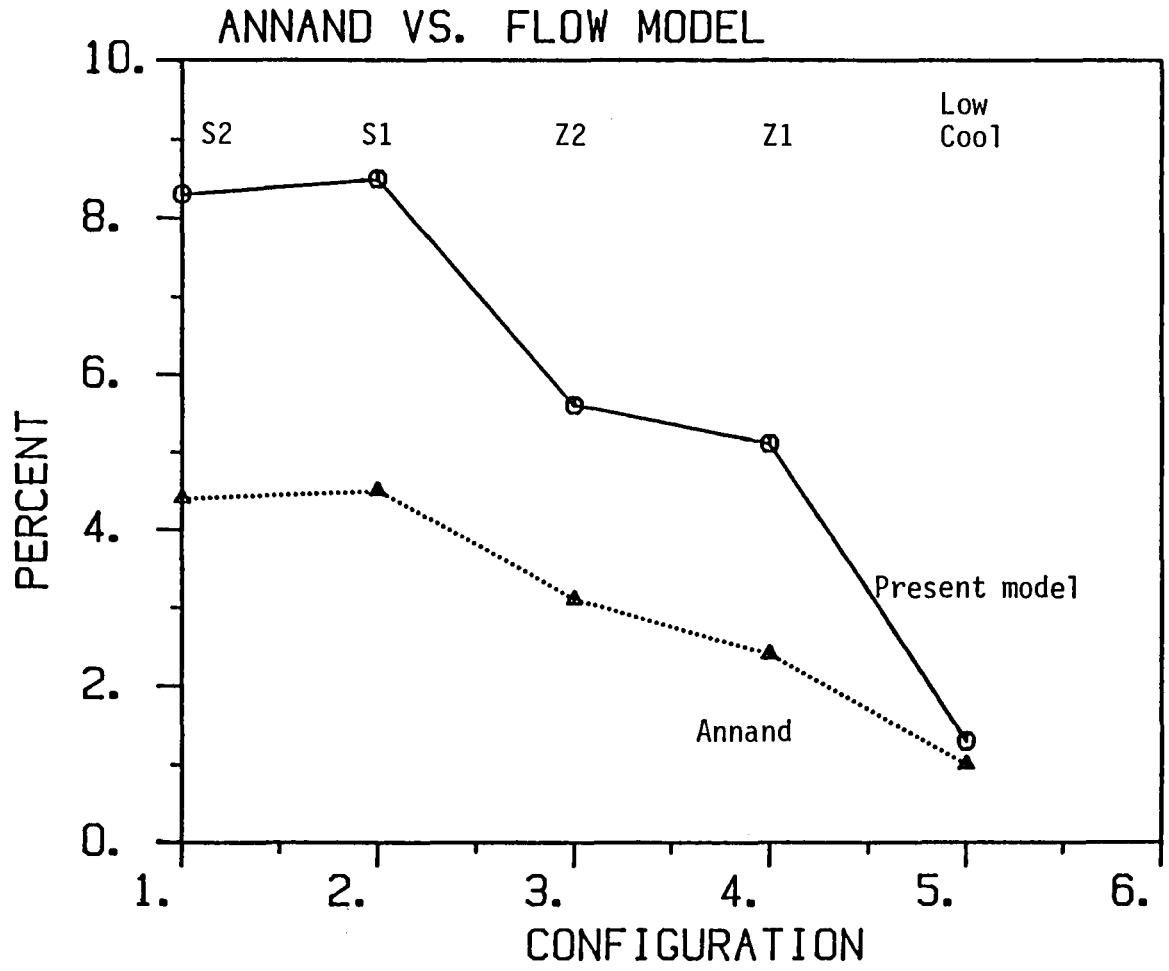

Figure 3-30 Thermal efficiency improvement produced by various insulation configurations compared to cooled baseline. Turbocharged, intercooled engine.

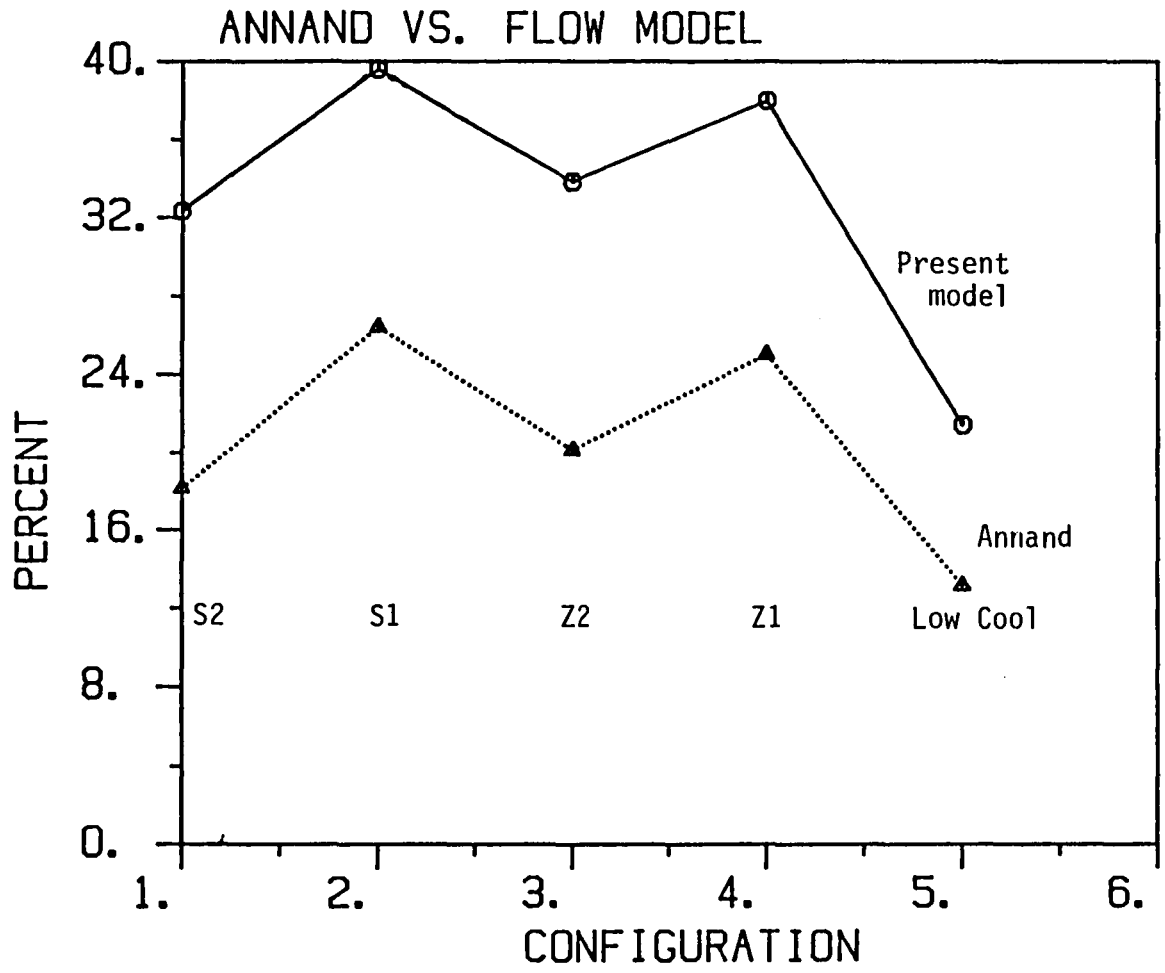

Figure 3-29 Retained heat conversion efficiency.

insulation predicted by the Annand-based model, are larger than for the present model, and the differences can become even much greater if instead of using the conduction network one uses certain prescribed wall temperatures used by previous investigators, e.g., Zapf (1975), as discussed below.

In the following brief summaries of the results obtained by the other investigators, description is given of the engine and insulation strategy studied, and then some selected results are presented. No direct comparisons could be made with the present results as the engines studied and insulation methods used were not the same as those used here. Nevertheless, the general trends in RHCE, heat rejection split and volumetric efficiency should be noted. They differ substantially from the present results, mainly due to differences in heat transfer models employed, in particular the use of Annand-like heat transfer correlations and the use of guessed wall temperatures.

One of the first papers dealing with insulated diesels was due to Zapf (1975). He looked at a naturally aspirated diesel, and simulated the effects of increasing wall temperatures. These were raised from 521 and 593°K on piston and head to 1523°K, and from 433°K on liner to 1103°K. This reduced in-cylinder heat transfer from 20.6 percent of fuel energy to zero, but indicated SFC decreased only by 4 percent. RHCE of the conserved heat was only 9 percent, far below the results obtained in the present work. Simultaneously, the volumetric efficiency decreased by 27 percent, which is a much larger decrease than we predict with our heat transfer models and calculated wall temperatures.

Griffiths (1976) analysed a turbocharged intercooled diesel, specifically the effect of raising piston and head surface temperature from 555°K to 889°K. The liner temperature was kept unchanged at 416°K. The heat rejection decreased from 13 to 8 percent of fuel energy, increasing thermal efficiency by 1.2 percentage points, giving RHCE of 24 percent. Heat rejection split between piston, head and liner for the cooled baseline was 39:30:31.

Kamo and Bryzik (1978) made calculations for a naturally aspirated and turbocharged engines. Their results showed very small benefits for the naturally aspirated case, reaching 0.5% BSFC improvement for zero heat rejection. In the turbocharged case they simulated zirconia insulated engine; the procedure used to calculate the resulting wall temperatures was not described. In one of the cases, they insulated piston and head and kept the liner cooled. This reduced the heat rejection by 41 percent and increased η_t by 1.4 percentage points, for RHCE of about 26 percent. When the liner was insulated as well, the heat rejection decreased by a total of 55 percent, but η_t went up only by 1.2 percentage points, for RHCE of only 17 percent.

Yoshimitsu et al (1982) simulated a turbocharged and turbocompound engines. They found that the turbocharged engine efficiency increased essentially linearly with insulation, reaching 4.3 percent improvement in BSFC with 60 percent reduction in heat rejection. The turbocompound engine efficiency increased faster, reaching 7.8 percent improvement in BSFC for the same level of heat rejection. Since the baseline heat rejection level was not given it is not possible to deduce their predicted RHCE. The piston/head/liner heat rejection split of the base cooled engine was 31:23:46. The high proportion of heat transfer going to the liner led them to the suggestion that the liner is the main component that should be insulated -- this is exactly contrary to the conclusions derived in this study.

Tovell (1983) studied a turbocharged high swirl diesel which had in-cylinder heat rejection of about 19 percent of fuel energy. Fully insulated with superinsulating material (zero conductivity) having no surface temperature swings, the heat rejection went to zero and BSFC was reduced by 7.5%. This indicates RHCE of about 17 percent. A more "practical" design of an insulated engine, utilizing high temperature alloys and zirconia, provided heat rejection reductions of 29%, reducing ISFC by 2.5 percent, i.e., with RHCE similar to the above.

Sudhakar (1984) calculated the performance of an insulated turbocompound engine, and found that insulation improved its BSFC by 4.8 percent at 60

percent reduction of heat transfer. This translates into RHCE of about 32 percent.

Hoag et al (1985) analyzed both a turbocharged and a turbocompound engines insulated with zirconia on all surfaces including the liner. They used a simplified heat conduction model to provide them with wall temperatures, and plotted improvements in BSFC against heat rejection. Their simulation for a case with heat rejection reduced to 50 percent indicated a 1.5 percent reduction in BSFC for a turbocharged engine and 3.7 percent for a turbocompound engine. This translates into RHCE of 11 and 30 percent, respectively. It may be noted that the turbocompound result agrees well with that obtained earlier by Sudhakar.

In summary, the previous investigations have produced results that consistently differ from the present ones in their predictions of the effects of insulation on RHCE, heat transfer split between engine components, and volumetric efficiency. These differences have been shown to be due to the differences in the gas-phase and structural heat transfer models used. The most significant impact of these differences is that the present model shows greater benefits of insulation than previously thought.

CONCLUSIONS

1. Thermal efficiency improvements due to combustion chamber insulation are proportional to retained-heat-conversion-efficiency, RHCE, i.e. the efficiency with which the in-cylinder heat retained in the gases by insulation is converted directly into work. It is also proportional to the in-cylinder heat transfer level of the baseline engine prior to insulation.

2. For a typical highway truck diesel engine at rated conditions RHCE is around 35-40 percent. These levels of RHCE are higher than those predicted by previous models, and this is due to the differences between the present gas-phase and structural heat transfer models, and those used in previous simulations. As a result, the

predicted thermal efficiency benefits of insulation are greater than previously reported by other investigators.

3. Insulation of the cylinder liner brings only small benefits in thermal efficiency and a moderate decrease in total heat rejection. These are offset by lower volumetric efficiency, lower power and substantially higher piston/ring/liner temperatures which adversely affect engine tribology.

4. A practical configuration, consisting of zirconia coatings on piston and head, and a cooled metal liner, provides an improvement of 5.1% in thermal efficiency for an intercooled turbocharged engine at rated conditions. Exhaust energy recovery by turbocompounding (TCPD) brings additional improvement of 5.4%, while Rankine cycle bottoming (RCB) adds 15.4%, and combined TCPD/RCB adds 20.3% (for a total of 26.5% over the baseline). The resulting BSFC for this insulated turbocharged intercooled engine with TCPD/RCB is as low as 0.260 lbm/bhp-hr at peak torque.

5. The percentage gains in thermal efficiency over the baseline are even greater for a non-intercooled engine. On an absolute basis, this engine starts at a lower thermal efficiency in the baseline configuration, but due to increased benefits it catches up with the intercooled one, and for the super insulated case and high exhaust heat recovery discussed above it achieves similar levels of BSFC. However, as in conventional engines, the engine power is substantially lower due to reduced charge density and NO_x emissions would most probably be higher.

6. "Reduced-cooling" engines (i.e., conventional engines with coolant-drained) provide only small BSFC benefits due to very low RHCE. There is a moderate reduction in total heat rejection, but these benefits must be weighed against durability and lubrication problems and lower engine power.

7. Contrary to results obtained previously by others, the thermal efficiency of a turbocharged engine benefits meaningfully from insulation even without heat recovery due to the RHCE values in the 35-40% range. In fact, the effects of exhaust energy recovery and insulation are to a large degree additive. This is an important conclusion which offers an additional choice in engine system selection i.e. an insulated engine without heat recovery. (A separate study, not discussed here, showed that even naturally aspirated engines can benefit from application of a well designed insulation package.)

8. A high-speed turbocharged automotive diesel with a swirl type combustion system shows very significant improvements in BSFC, on the order of 10% at rated and 12% at part load conditions, achievable with practical zirconia coatings. These high percentage improvements are the result of the high heat transfer of the baseline cooled engine caused by high swirl levels, providing a larger potential to draw on.

REFERENCES

Annand, W. D. (1963), "Heat Transfer in the Cylinders of Reciprocating Internal Combustion Engines," Proc. Instn. Mech. Engnrs., 1963, Vol. 177, No. 36, p. 973.

Bailey, M. (1985), "Comparative Evaluation of Three Alternative Power Cycles for Waste Heat Recovery from the Exhaust of Adiabatic Diesel Engines," NASA Lewis Report DOE/NASA/50194-43, NASA TM-86953.

DiNanno, L. R., DiBella, F. A. and Koplow, M. D. (1983), "An RC-1 Organic Rankine Bottoming Cycle for an Adiabatic Diesel Engine", NASA Contractor's Report NASA CR-168256.

Griffiths, W. J. (1976), "Thermodynamic Simulation of the Diesel Engine Cycle to Show the Effect of Increasing Combustion Chamber Wall Temperatures on Thermal Efficiency and Heat Rejection," Wellworthy Topics No. 63, Winter 1976-7.

Hoag, K. L., Brands, M. C. and Bryzik, W. (1985), "Cummins/TACOM Adiabatic Engine Program," SAE Paper 850356.

Hoehne, J. L. and Werner, J. R. (1982), "The Cummins Advanced Turbo-compound Diesel Engine Evaluation", NASA Contractor's Report NASA CR-168042.

Kamo, R. and Bryzik, W. (1978), "Adiabatic Turbocompound Engine Performance Prediction," SAE Paper 780068.

Morel, T., Fort, E. F., and Blumberg, P. N., (1985a), "Effect of Insulation Strategy and Design Parameters on Diesel Engine Heat Rejection and Performance," SAE Paper 850506, SAE Congress, Detroit, 1985.

Morel, T. and Keribar, R. (1985), "A Model for Predicting Spatially and Time Resolved Convective Heat Transfer in Bowl-in-Piston Combustion Chambers," SAE Paper 850204, SAE Congress, Detroit, 1985.

Morel, T., Keribar, R. and Blumberg, P. N. (1985b), "Cyclical Thermal Phenomena in Engine Combustion Chamber Surfaces," SAE Paper 850360, SAE Congress, Detroit, 1985.

Sudhakar, V. (1984), "Performance Analysis of Adiabatic Engine," SAE Paper 840431.

Tovell, J. F. (1983), "The Reduction of Heat Losses to the Diesel Engine Cooling System," SAE Paper 830316.

Yoshimitsu, T., Toyama, K., Sato, F. and Yamaguchi, H. (1982), "Capabilities of Heat Insulated Diesel Engine," SAE Paper 820431.

Zapf, H. (1975), "Grenzen und Moglichkeiten eines Warmedichten Brennraumes bei Dieselmotoren," VDI-Berichte Nr. 238, pp. 85-87.

IV. ENGINE INSTALLATION

At the end of the program's first year a Cummins NH single cylinder test engine had been installed on a dynamometer in Purdue's engine laboratory. Necessary supporting equipment such as a cooling system, a lubricating system and a fuel supply system also had been installed. One exception was the air supercharging and heating system required to simulate the charging conditions of a highly boosted truck diesel under normal highly loaded operation. System components had been ordered but not received.

During the early part of the program's second year components for the supercharging system were received and installed. In its designed configuration, ambient air is compressed and stored in two large high-pressure vessels located in a courtyard outside of the laboratory. This air is brought through high pressure piping into the engine test cell, where it is throttled, dried to near-zero absolute humidity, metered and heated (if required) before entering the engine intake plenum tank. With this arrangement, the single cylinder engine rig can duplicate intake air pressures and temperatures that exist at any full-scale engine operating condition.

Engine Modification for Test Purposes

In order to provide combustion chamber access ports for incorporating a pressure transducer, a fast response thermocouple probe and a radiation probe, several modifications to the engine cylinder head were necessary. Early in the program, Cummins had agreed to supply a special test head with a pressure transducer adapter sleeve installed. This head then would be modified in Purdue's shop to accept special mounting sleeves for the other two probes. Specific locations for the pressure/temperature/radiation probes were selected, following careful study of sectioned castings and prints, to present the best possible resolution of the normal conflict between adequate data requirements and practical access positions. All suitable locations were determined to lie in the cylinder head area.

For useful radiation measurements, the probe should view the main combustion zone. Also, since the probe is a line-of-sight instrument contained in a rigid sheath, its installed position must not interfere with valve gear, injector linkages or other head/rocker box components. In addition, there must be room to insert the protective window. Similarly, the surface thermocouple should be located in a position on the combustion chamber wall where the surface is flat, where there is coolant flow adjacent to that wall, and where the area is relatively free from interior support ribs that would interfere with one-dimensional heat flow. Pressure transducer installation requirements are less stringent, but its position should avoid direct flame impingement on the sensing diaphragm.

Locations finally selected took all of the above requirements into account. The radiation probe views the piston cup near the imaginary circle where its depth is greatest. By contrast, the surface thermocouple and pressure transducer are positioned on larger radii where flames do not impinge directly on their faces. The only significant engine modification that was required to mount the instrumentation at the selected points was the deactivation of one intake valve so that the radiation probe passes in a straight line down the center of the valve guide boss. Since the engine has two intake valves and breathes very freely, the lost air flow can be returned to normal levels through increased supercharger boost that is within the capacity of the air system. With the instrumentation mounted in the selected locations, data obtained should be adequate for model validation. Also, with all three transducers placed in non-interfering areas, it is possible to obtain data on heat radiation, heat conduction and cylinder pressure simultaneously at each engine test condition. In addition, the adapter sleeves for each probe have identical internal dimensions. This feature allows the probes to be interchanged for additional data verifications.

Although some delays were experienced in obtaining the test head from Cummins and in locating suitable materials for the modified components,

all of the probe mounting hardware has been fabricated and installed in the test head. New rocker arm components, including a special crosshead which slides freely along the radiation probe sleeve and which preserves the normal cam lift/valve lift relationship also have been fabricated and installed.

When the cylinder head supplied with the single cylinder engine was removed, prior to installing the test head, the piston was found to be of a design not intended for use with the test head configuration. The test head that Cummins chose to supply (due to considerations of most readily available hardware) had recessed valves while the piston had cutouts in its crown to accommodate protruding valves. This type of piston was unsuitable for two reasons: 1) the cutouts were located in the area where the optical proximeter was focused and thus would interfere with TDC determination, and 2) the combination of recessed valves and piston crown cutouts increased clearance volume enough to lower compression ratio below an acceptable value. Since the test head with recessed valves already had been extensively modified, the most practical correcting alternative was to obtain a flat-crown piston that was compatible with the engine. As a result, Cummins was asked to try to locate a suitable piston and was able to supply two useable types. Both had flat crowns but one produced a 17:1 compression ratio while the other showed 15.8:1. The 15.8 variant was judged to be the most suitable for program test purposes and consequently it was installed in the engine along with the modified test head.

During the installation sequence, compression ratio and valve lift characteristics were measured. In addition, a strain gaged fuel injector push rod for locating the start of injection was installed and the valve cover was modified to allow wiring from the test probes to exit without excessive oil leakage.

Towards the latter part of the second year the engine was run in test configuration with instrumentation installed to check out general operation and look for potential problem areas. During these runs the

sleeve that mounts the radiation probe became loose and required some additional modifications in order to hold it in place. Otherwise all checkout operation indicated satisfactory installation and modifications.

V. EXPERIMENTAL TECHNIQUES AND INSTRUMENTATION

During the Phase I of this program, a considerable effort was mounted at Purdue University to develop specialized instrumentation that could be used in the engine experiments. This instrumentation covered three areas:

1) heat radiation measurement,
2) total heat flux and wall temperature measurement, and
3) cylinder pressure measurement.

For the first of these measurements the plans called for the use of detector system placed behind a recessed window. For the total heat flux a fast response surface thermocouple is to be used. The cylinder pressure will be measured using a standard AVL pressure transducer, but the requisite accurate pressure-crank angle phasing will be assured by use of a unique TDC detector -- an optical proximeter.

The initial work done on these instruments in the first year of this program was described in the Phase I Report, and the reader is directed to that report for background information and for some of the technical details. In this report we summarize our additional experiences with the instrumentation.

Radiation Measurements

Methodology. There are two proved methods commonly employed for determining the temperature of a radiating gas: 1) the emissions absorption method, and 2) the multicolor method. The emissions absorption method involves measurement of a beam that passes through the gas in a direct line and thus requires two access ports. This constraint makes the absorption method impractical for use in the test engine. The multicolor method involves extracting a signal from the radiating gases through only one access port and therefore is a practical method for use in the test engine, as shown by the work of Flynn et al (1972). Thus, it is the method chosen for radiation measurements in this program.

In application, the multicolor method uses the measured radiation intensity at two or more wavelengths to determine an equivalent black body temperature. The actual temperature is obtained from an iterative solution based on three assumptions:

(1) the temperature of the gas is homogeneous over the area measured,
(2) gas concentration is homogeneous over the area, and
(3) radiation from the walls is small compared to that from the gas.

When this method is applied to engine combustion, two additional assumptions are made:

(1) soot is the dominant emitter (spectral peaks from gases can be neglected), and
(2) the intensity is independent of direction, which implies that the emission (E_λ) is directly related to the intensity (I_λ):

$$E_\lambda = \pi I_\lambda \tag{5-1}$$

The radiation intensity data obtained at two wavelengths ($I_{\lambda 1}$ and $I_{\lambda 2}$) are related to black body emission at the same temperature through the following relationship:

$$E_\lambda(T) = \pi I_\lambda = \varepsilon_\lambda E_{\lambda b}(T) \tag{5-2}$$

The emissivity (ε_λ) for soot particles is shown by Flynn et al and other to be well represented by:

$$\varepsilon_\lambda = 1 - \exp(kL/\lambda^\alpha) \tag{5-3}$$

where α is nearly unity in the near infrared wavelength region found in diesel combustion, and the product kL must be obtained by solution.

The measured emission can be described by an equivalent black body source at an apparent temperature (T_a). Thus:

$$E_\lambda(T) = E_{\lambda b}(T_a) \qquad (5\text{-}4)$$

By combining the above three equations and solving for the product of absorptivity coefficient and thickness (kL) at each wavelength, and setting them equal, the following relation can be iteratively solved for the actual temperature (T).

$$[1 - \exp(\frac{C_2}{\lambda_1}(1/T - 1/Ta_1))]^{\lambda_1^{\alpha}} = [1 - \exp(\frac{C_2}{\lambda_2}(1/T - 1/Ta_2))]^{\lambda_2^{\alpha}}$$

With the actual temperature known, the relation for the monochromatic emissivity can be generated by fitting the relationship (5-3) for soot to the measured points. Then, based on the emissivity relationship developed along with the temperature that has been calculated, the emissive power along a line of sight can be found by the integration:

$$E = \int_0^\infty \varepsilon_\lambda \, E_{b\lambda}(T) \, d\lambda \qquad (5\text{-}6)$$

where: $E_{b\lambda}$ is Planck's function for a black body, ε_λ is monochromatic emissivity, T is temperature and λ is wavelength of radiation.

From this expression it is apparent that the emissivity (ε_λ), temperature (T), and the important wavelengths must be established before emissive power can be determined. The wavelength range can be determined from the expected temperature and the shape of Planck's function. The temperature of the gas when radiative heat transfer is

most important is well over 2000 K. Based on this temperature level, the wavelength range should extend from 0.5 to 3.0 microns.

Radiation probe. The initial design for the radiation probe to be used in conjunction with the heated sapphire optical access port developed during year one, was originally based on a commercial six-color radiation photodetector manufactured by Judson Infrared. In this design, radiation from a point source in the engine combustion chamber would be transmitted to the Judson detector by an optical train that splits the signal into pertinent wavelengths and then focuses the resulting pattern onto the detector window. Figure 5-1 shows a system schematic drawing. Calibration would be carried out with the complete system, including the sapphire optical port.

In practical application, this proposed design proved unworkable. The detector never could be made to perform properly during bench experiments and contacts at Judson Infrared were not able to offer workable modifications. After several bench trials, it finally was decided that the instrument was much too sensitive to light intensity and to handling shocks to be used for engine test stand measurements. In addition, the design of a practical focusing and dispersion system for use around a vibrating engine proved to be much more difficult than anticipated. Bench experiments with a more rugged commercial detector manufactured by Spiricon, Inc. also proved to be unsuccessful, in that the detector was not able to respond in a predictable manner to the signal intensity expected from the engine sample train output.

As a result of the difficulties encountered with these two commercial photo detectors and their associated sample trains, development work was undertaken on an alternative radiation probe system. In this system a commercial paired fiber optics bundle, similar to the one used in the optical proximeter, gathers radiation which passes through the optical access port, and splits it into two beams. Each beam is filtered to pass only a specific wavelength on to photo detectors which then respond only to that wavelength. Figure 5-2 shows a schematic drawing of this

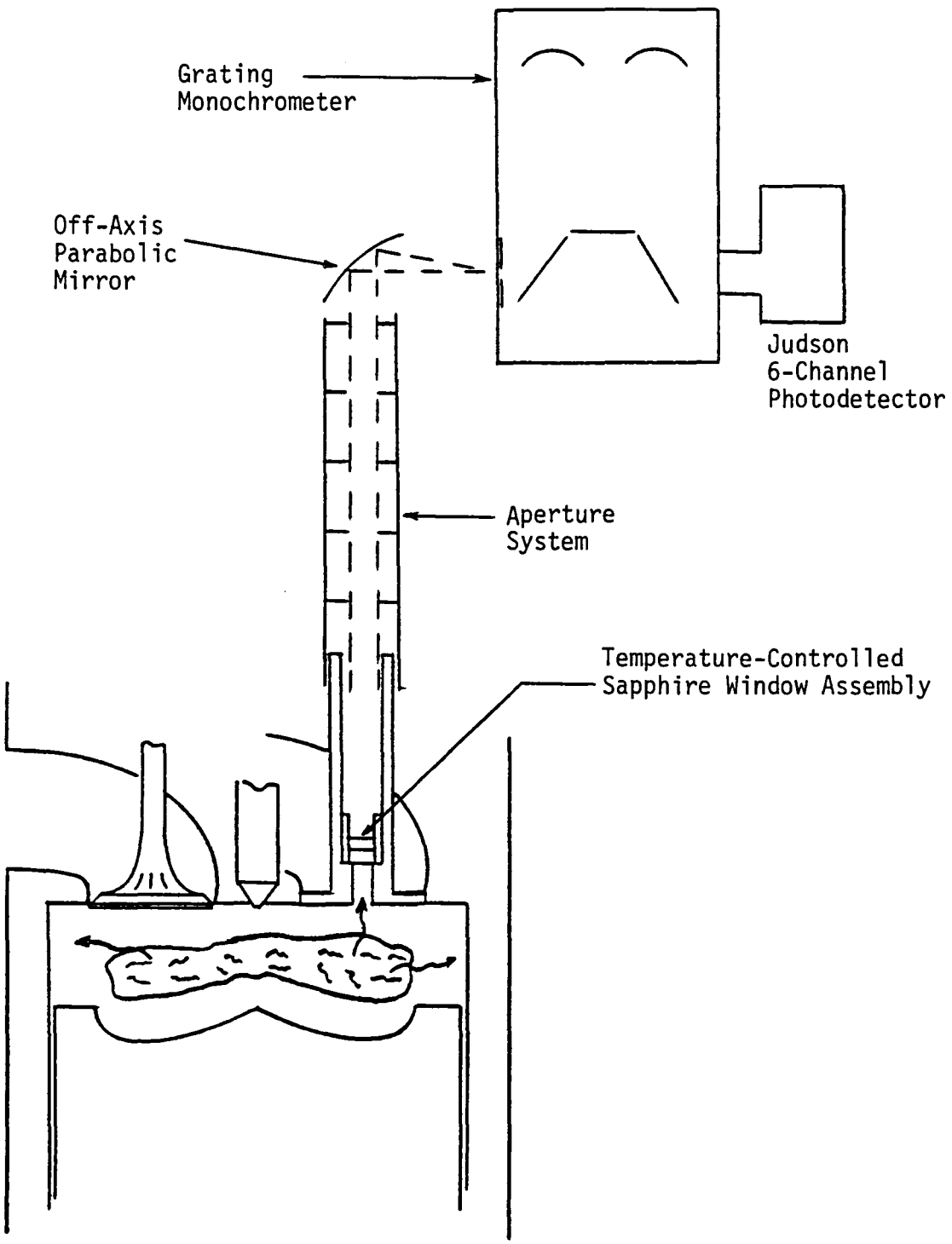

Figure 5-1 Originally Proposed Heat Radiation Probe System

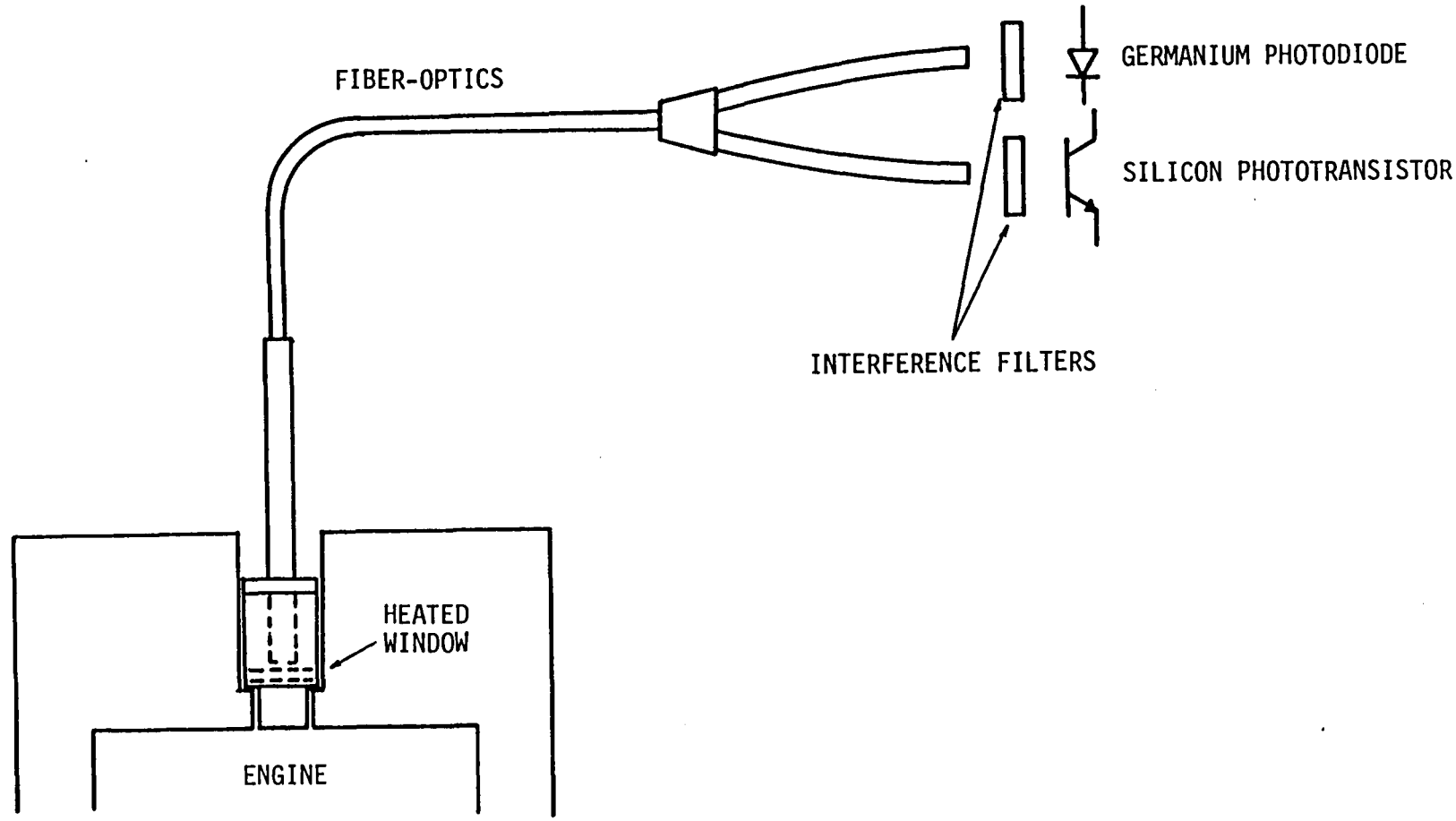

Figure 5-2 Measurement schematic utilizing fiber optic as a beam splitter, and combining interference filters with spectrally dependent components as monochromatic detectors.

alternative sampling system. As described earlier in this section, the intensity observed at two properly chosen wavelengths can be used to deduce source temperature and radiative heat transfer.

Two factors were determined to be of key importance in the practicality of this alternative system for engine radiation measurements: 1) the fiber-optic bundle and associated filters/detectors must operate at wavelengths that are useful and 2) the response time of the components must be fast enough to track combustion radiation in time. From consideration of the engine radiation spectrum observed by Flynn, shown in Figure 5-3, measurement at wavelengths of 0.9 and 1.5 μm was selected as most desirable for calculation accuracy. The proposed system was found to satisfy both of the above requirements for wavelengths of 0.9 and 1.5 μm . In the case of wavelength compatibility, manufacturers data for the proposed optical bundle showed satisfactory operation up to wavelengths of 2 μm. Also, Germanium (1.5 μm) and Silicon (0.9 μm) photodiodes with appropriate filters for the wavelengths of interest were determined to be commercially available. With respect to response time, bench tests of a bread-board circuit showed a response of about 4 μs. This time corresponds to about 0.05 crank angle degree at 2100 rpm and therefore is satisfactory for time resolved combustion radiation measurements. Thus, work during the remainder of the second year concentrated on developing a practical system based on the alternative concept just described.

In the initial design stage for this concept, radiation was to be collected from a nearby point source in the combustion chamber by an optical system that would focus the energy from this point onto the fiber-optic bundle receptor. However, expected engine vibration and space restrictions imposed by the diameter of the sleeve installed in the cylinder head, along with a need for cooling to counter thermal interference effects, presented nearly insoluble problems in the design of any practical configuration. Consequently, a design which would incorporate signal collection from a small conical volume rather than a single point was considered. With this approach the fiber optic bundle

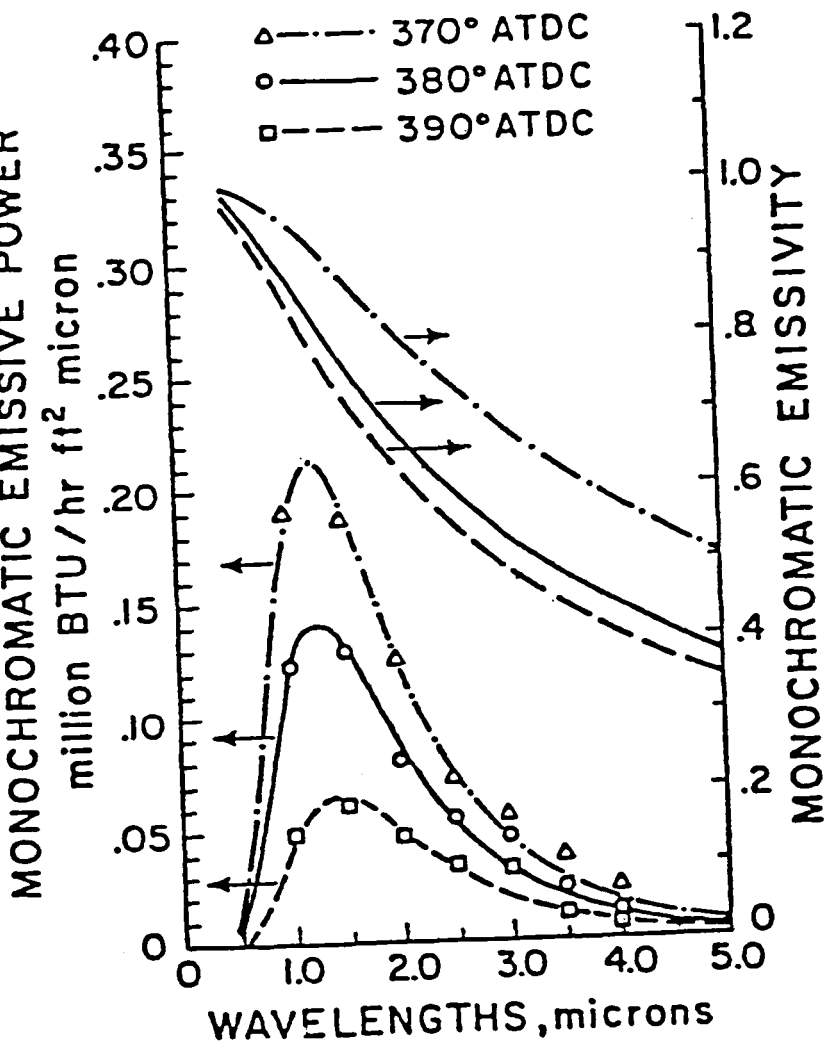

Figure 5-3 Engine radiation data collected by Flynn. (University of Wisconsin, 1971).

receptor end could be placed directly in back of the access window and all of the other optical focusing elements of the sample train as well as cooling would be unnecessary. After a detailed study of the effects of such a design configuration on radiation measurements, it was concluded that the advantages of simplicity of construction, ruggedness and speed with which working hardware could be assembled far outweighed the disadvantage of having to correct for small amounts of unwanted radiation from the access port walls.

Following this decision, hardware was designed and fabricated. In implementation it was found that detector stability could be improved markedly by mounting them in a constant temperature heat sink. As a result, a cooled heat sink was made a part of the final design configuration.

After assembly, the time response of the system was checked by monitoring the flash from a xenon flash lamp with a pulse time of about 20 μs. The pulse was viewed by both photodiode detectors and a photomultiplier tube. The xenon flash lamp provides a good radiation source since it produces a fast, wide spectrum flash. A photomultiplier tube was used as a reference, since the response of this photomultiplier is over 100 times faster than the expected response of the photodiode detectors. The results of this test were satisfactory in that the Silicon and Germanium photodiode detectors lag the photomultiplier response by only 6 μs and 2 μs respectively.

Preliminary engine measurements. Toward the end of the second year the complete radiation probe assembly, including the sapphire viewing window, was installed in the single cylinder test engine head for initial performance evaluation in a realistic environment. The engine was fired, naturally aspirated, at 500 rpm and the minimum fuel rate for steady operation. This condition approximates a "curb idle" during which relatively low pressures are produced and thus the probe was not overly stressed. This also is a condition which should produce a low signal level and thus serve to evaluate the probe sensitivity and re-

sponse in this minimum region. Based on the results of this test at minimum expected signal level, the response and sensitivity of the photodiode detectors were found to be more than adequate for radiation measurement at any useful speed or load. The data collected in this low load case was processed to determine the temperature, emittance and soot volume fraction by the technique described below.

Since the detector output is linear with intensity, the measured actual intensity can be equated to an apparent black body intensity:

$$V_m = K\,\varepsilon_\lambda\, I_{\lambda b}(\lambda,T) = K\, I_{\lambda b}(\lambda,T_a)$$

where:

T	soot temperature
T_a	apparent black body temperature
K	calibration constant
$I_{\lambda b}$	Planck's blackbody intensity
ε_λ	emittance of soot

Planck's black body function for intensity and the emittance of soot follows the relationships:

$$I_{\lambda b}(\lambda,T) = \frac{C_1/\pi}{\lambda^5\,[\exp(\frac{C_2}{\lambda T}) - 1\,]}$$

$$\varepsilon_\lambda = 1 - \exp(\frac{-(f_v L)\,A_\lambda}{\lambda})$$

where:

$(f_v L)$ soot volume fraction and characteristic length

A_λ constant dependent on complex index of refraction

Combining the above equations and solving for the soot volume fraction times the characteristic length, yields:

$$(f_v L) = -\frac{\lambda}{A_\lambda} \ln\left[1. - \frac{\exp(\frac{C_2}{\lambda T}) - 1}{\exp(\frac{C_2}{\lambda T_a}) - 1}\right]$$

Since $(f_v L)$ is independent of wavelength, the latter equation can be equated for the two different wavelengths. This yields one equation with one unknown (T):

$$-\frac{\lambda_1}{A_{\lambda_1}} \ln\left[1. - \frac{\exp(\frac{C_2}{\lambda_1 T}) - 1}{\exp(\frac{C_2}{\lambda_1 T_{1a}}) - 1}\right] = -\frac{\lambda_2}{A_{\lambda_2}} \ln\left[1. - \frac{\exp(\frac{C_2}{\lambda_2 T}) - 1}{\exp(\frac{C_2}{\lambda_2 T_{2a}}) - 1}\right]$$

$$\left[1. - \frac{\exp(\frac{C_2}{\lambda_1 T}) - 1}{\exp(\frac{C_2}{\lambda_1 T_{1a}}) - 1}\right]^{\frac{\lambda_1}{A_{\lambda_1}}} = \left[1. - \frac{\exp(\frac{C_2}{\lambda_2 T}) - 1}{\exp(\frac{C_2}{\lambda_2 T_{2a}}) - 1}\right]^{\frac{\lambda_2}{A_{\lambda_2}}}$$

The above equation must be solved iteratively for temperature. For this purpose, an objective function, below, is defined, where the solution exists at the zero crossing.

$$f = \left[1. - \frac{\exp(\frac{C_2}{\lambda_1 T}) - 1}{\exp(\frac{C_2}{\lambda_1 T_{1a}}) - 1}\right]^{\frac{\lambda_1}{A_{\lambda_1}}} - \left[1. - \frac{\exp(\frac{C_2}{\lambda_2 T}) - 1}{\exp(\frac{C_2}{\lambda_2 T_{2a}}) - 1}\right]^{\frac{\lambda_2}{A_{\lambda_2}}}$$

For a theoretical case where the actual temperature (T) is 2000°K and the emittance ($\varepsilon_{0.9}$) is 0.5, this equation produces the curves shown in Figures 5-4 and 5-5, for a range of temperatures around the correct temperature. It should be noticed that the slope approaches infinity at the highest apparent black body temperature (T_a), and approaches zero at temperatures just slightly above the actual temperature. These characteristics require that the first guess for temperature be fairly close. In the solution used, the temperature for the first iteration is chosen slightly higher than the highest black body temperature (T_a). The second method is then used to close in on the actual temperature.

To test the method outlined above, voltages were predicted for various combinations of (T) and ($\varepsilon_{0.9}$). This test required that a calibration of the detectors be performed and that an iteration program be written. Since a high-temperature calibration source was not readily available at the time, a low temperature calibration was performed with a black body, over a range of temperatures between 1000°K and 1400°K. When the iteration program was fed the theoretically predicted voltages, corresponding temperatures and emittances were reproduced with no appreciable error. This test provides confidence in the accuracy of the data reduction method.

Next, this data reduction method was applied to the 500 rpm, light load engine data described earlier in this section. Plots of detector output for one cycle are shown in Figures 5-6 and 5-7. Calibration data were extrapolated to temperatures of interest. For these engine data the resulting emittance at the wavelength of each detector, temperature and soot volume fraction times the characteristic length are displayed in Figures 5-8 through 5-11. The high fluctuations in apparent temperature beyond 60 degrees after TDC represent effects from operation near the low temperature resolution limit of the detector system. On first inspection, the temperatures and emittance values appeared low. In order to investigate this possibility further, a soot volume fraction was calculated for two cases. The characteristic length was defined as the distance from the engine head surface to the bottom of the piston

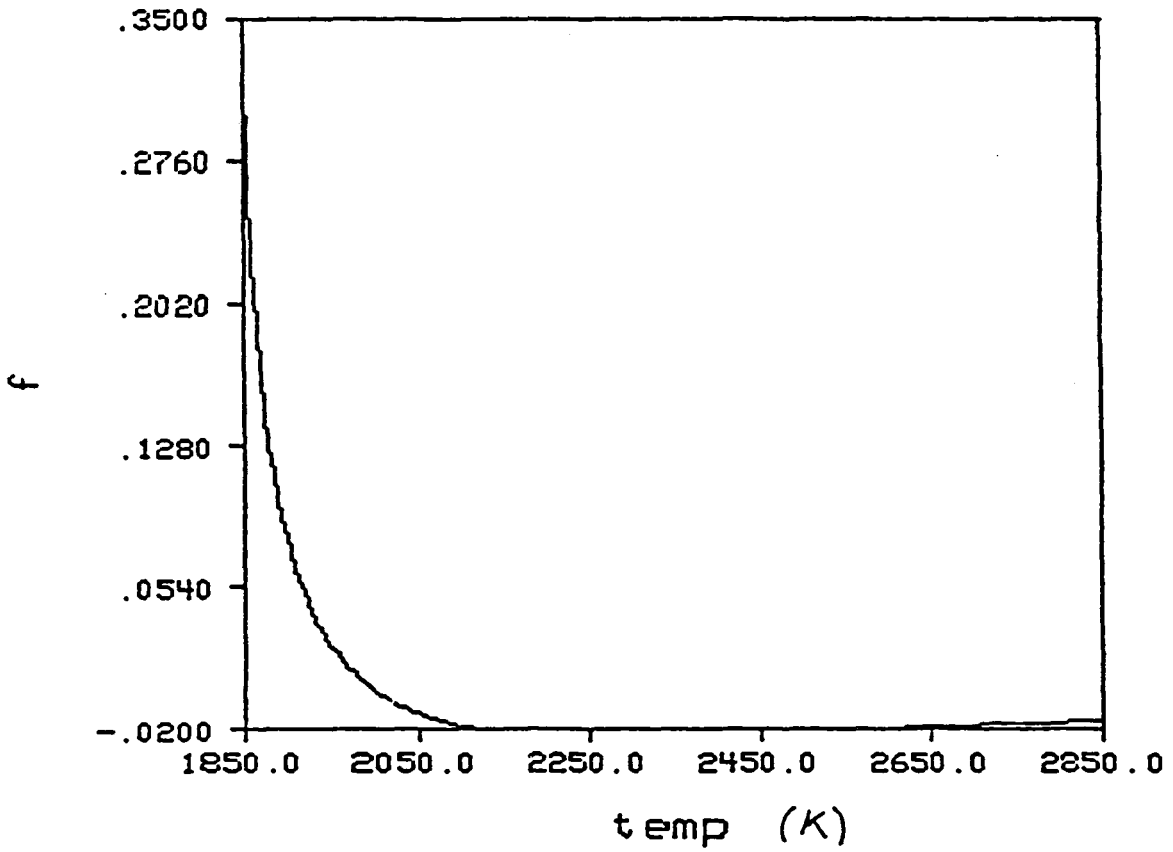

Figure 5-4 Objective function for a theoretical case where T=2000 K and $\varepsilon_{.9}$ = .5.

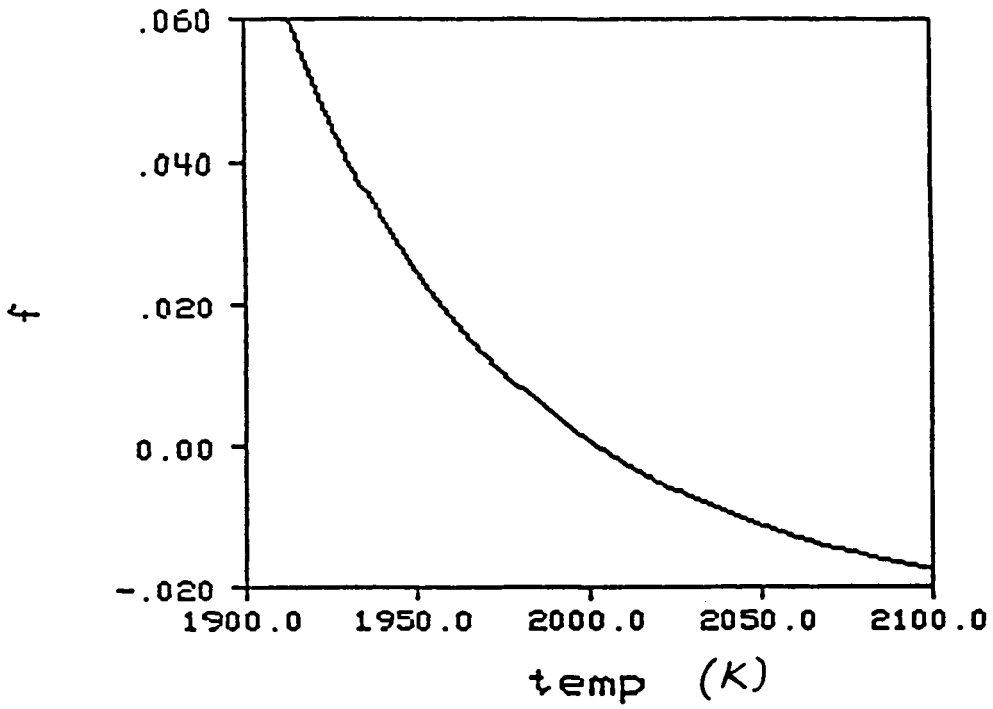

Figure 5-5 Objective function expanded near zero crossing (T=2000 K).

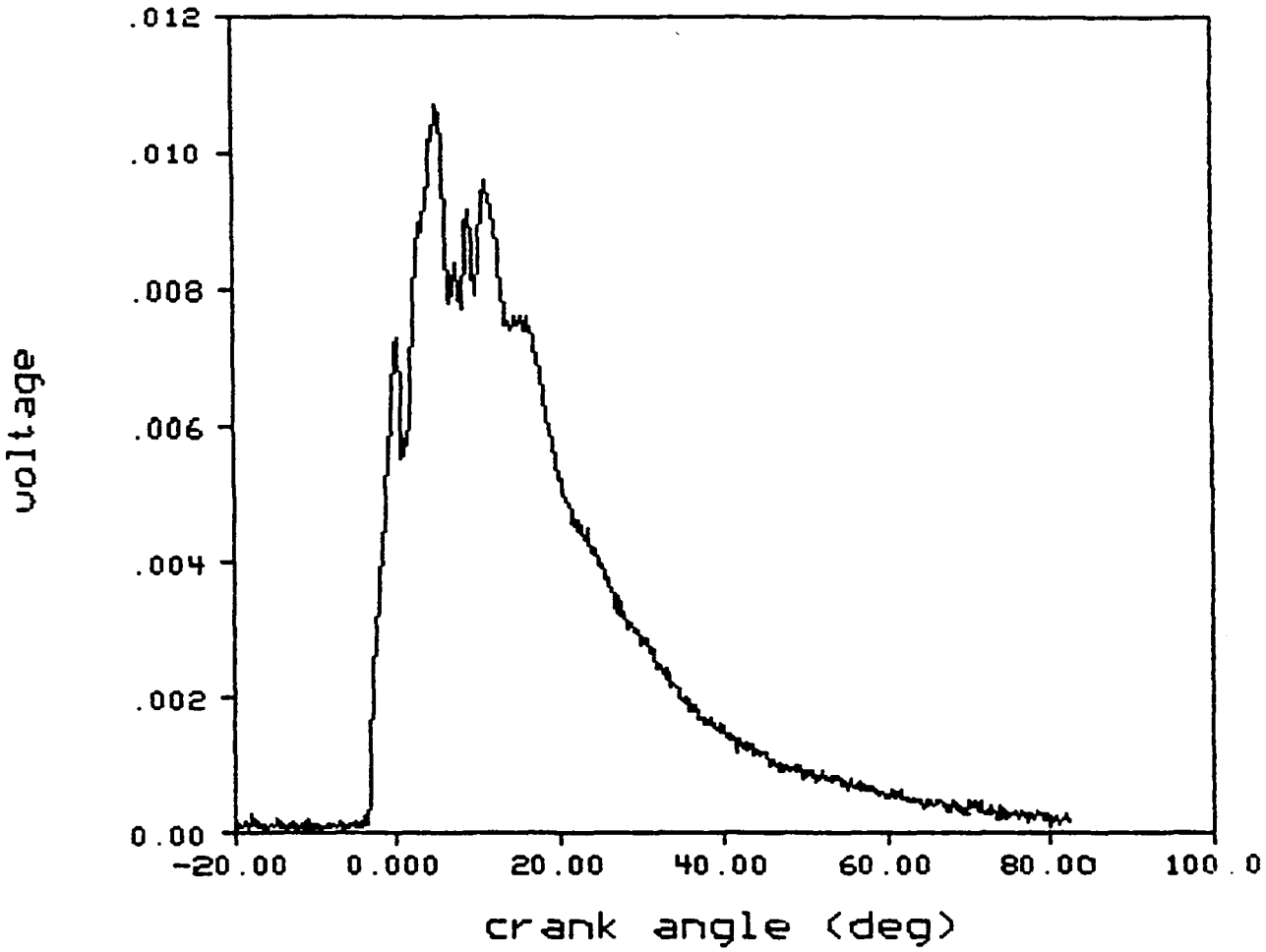

Figure 5-6 Voltage data from silicon detector with engine at 500 rpm and low load.

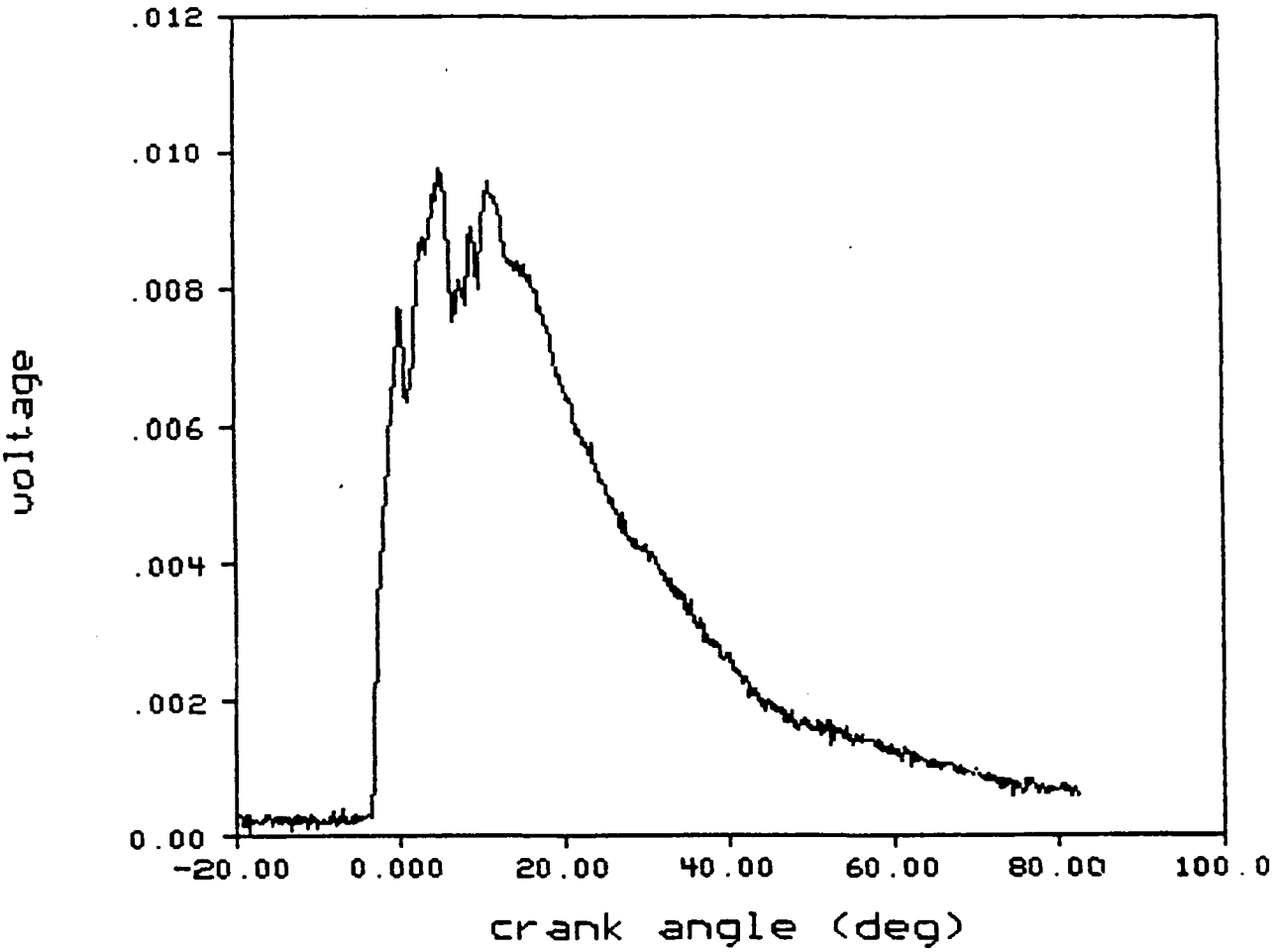

Figure 5-7 Voltage data from germanium detector with engine at 500 rpm and low load.

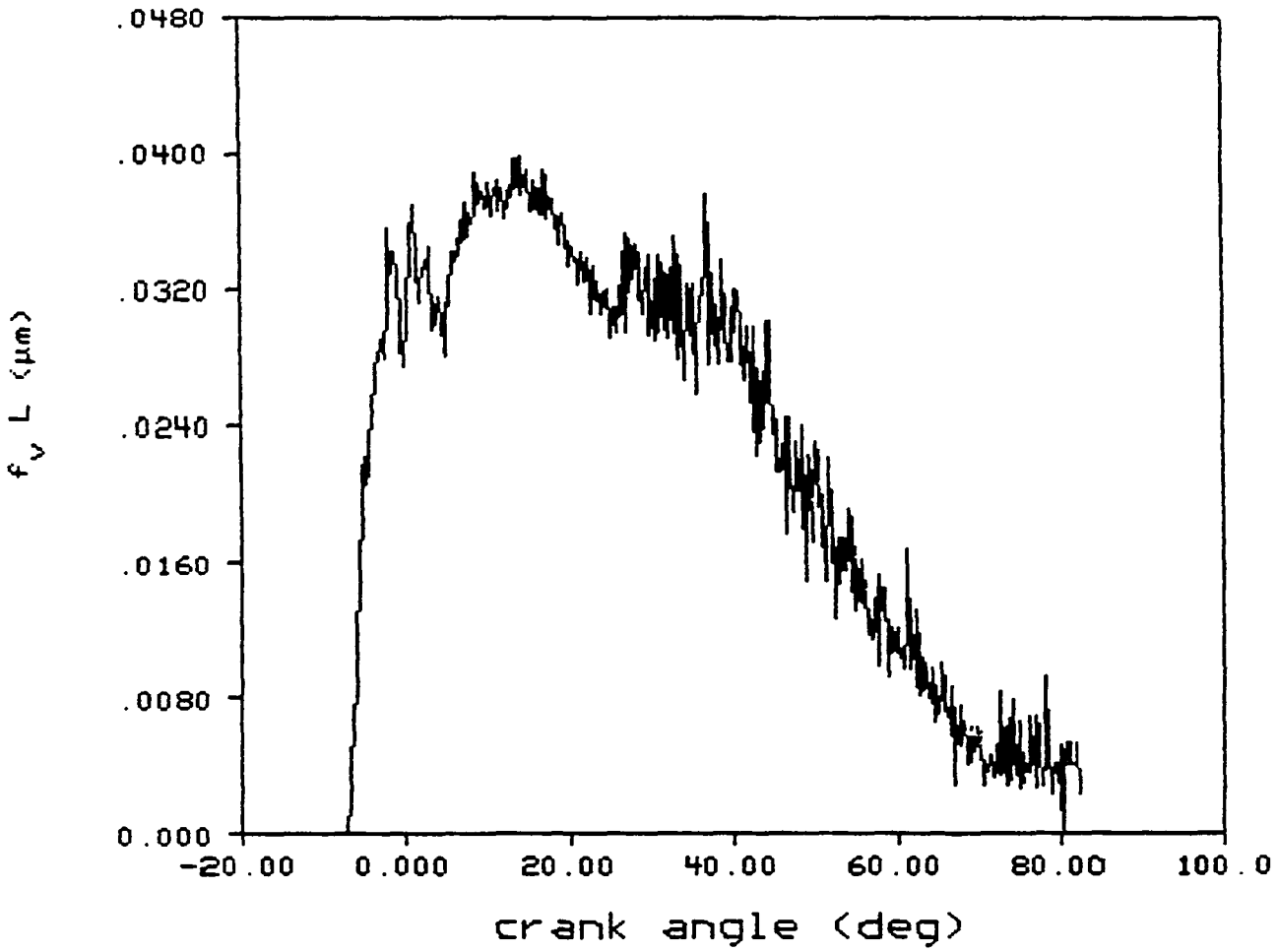

Figure 5-8 Deduced emittance at .9 µm.

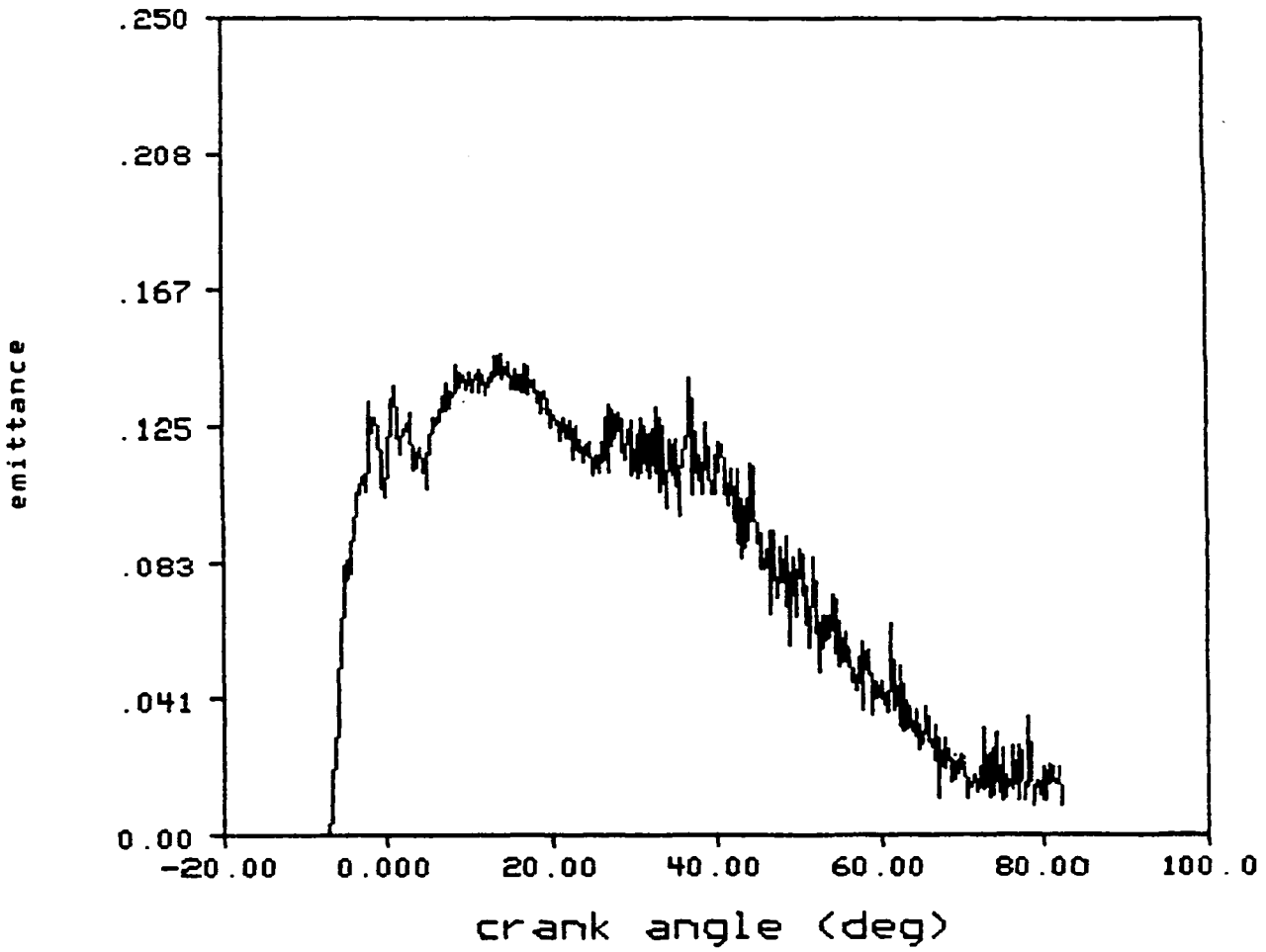

Figure 5-9 Deduced emittance at 1.5 μm

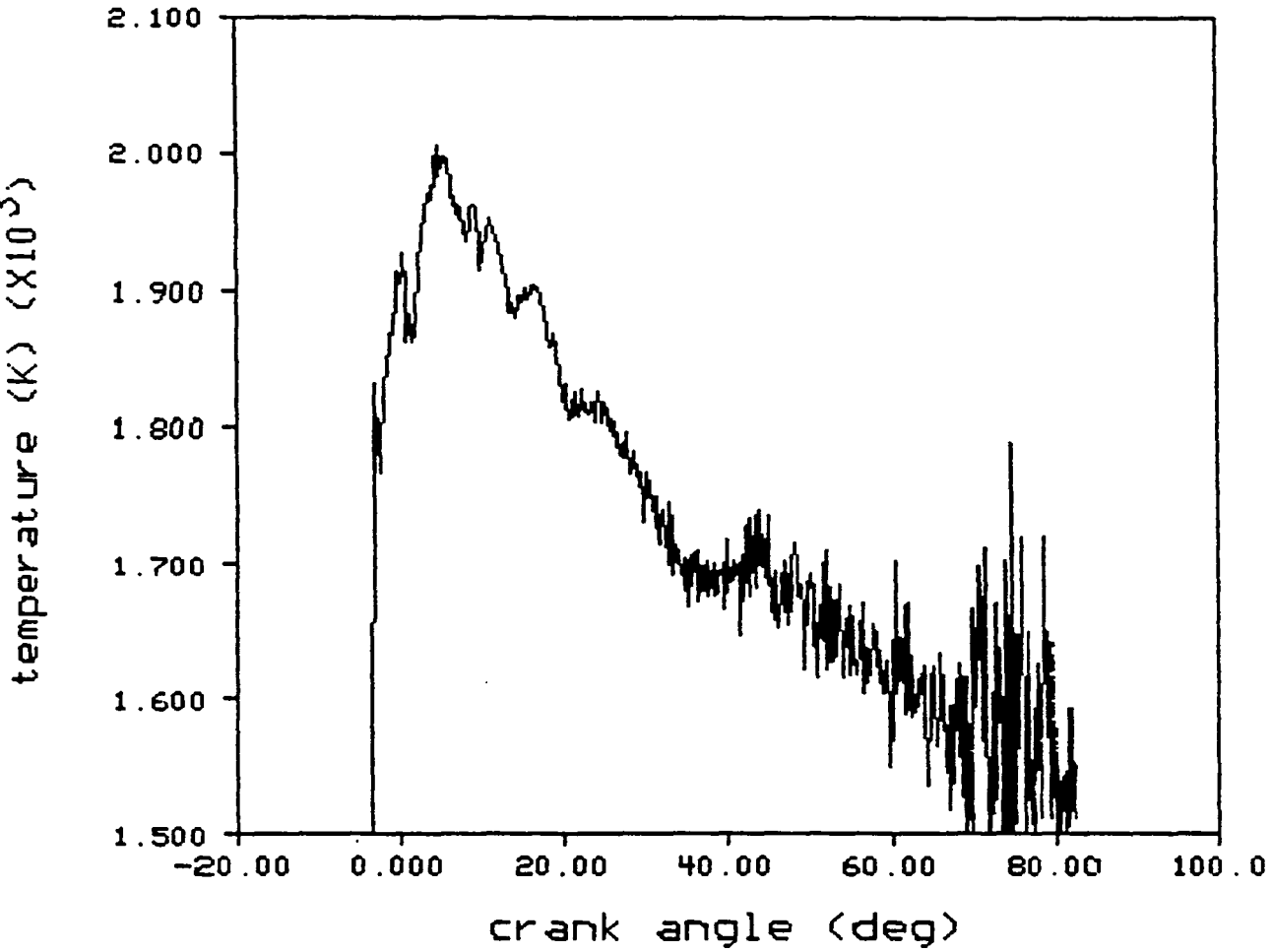

Figure 5-10 Deduced temperature.

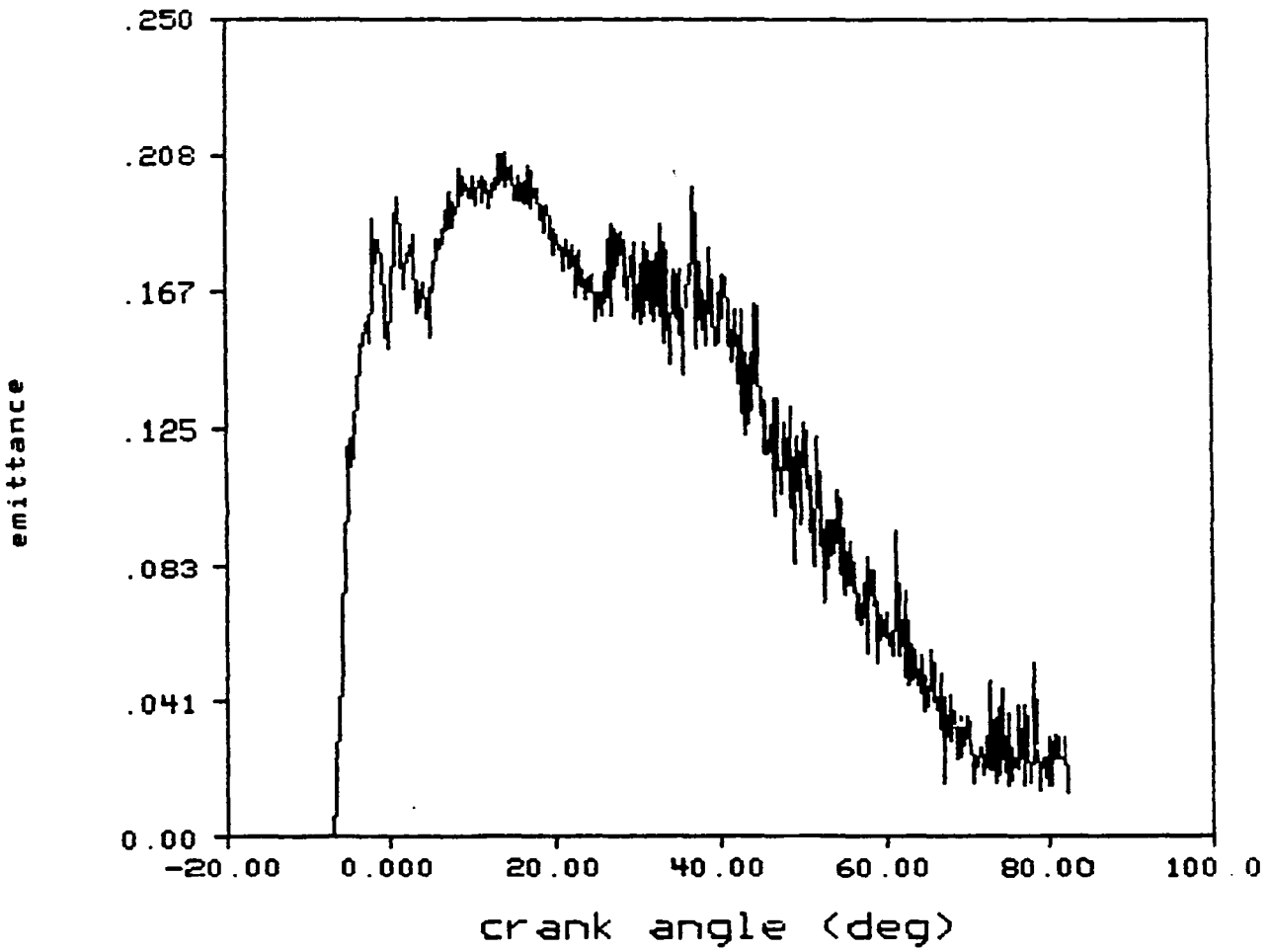

Figure 5-11 Deduced soot volume fraction times characteristic length.

cup. Based on this, $f_v(10°) \approx 1.5 \times 10^{-6}$ and $f_v(60°) \approx 4 \times 10^{-8}$. These values seemed reasonable, based on literature data.

Calibration of the detectors over the temperature range of interest in diesel combustion still is required, extending to 2700°K. An NBS-traceable black body which can achieve temperatures up to 2700°K has been located at a commercial facility and will be used for initial calibration. Later, in the third year of the program, a high-temperature furnace, to be made available by NASA-LeRC, will be installed at Purdue and be used for subsequent calibrations.

Fast Response Thermocouple

During the program's second year the fast-response-thermocouple design, tested in a low-temperature bomb experiment and described in the first year report, was applied to combustion surface temperature measurement in the single cylinder engine. A drawing of the design adapted for engine tests is shown in Figure 5-12. This design fits into any of the three access ports in the engine head, being interchangeable with either the pressure transducer or the radiation probe window assembly. During fabrication, a number of problems arose. Most were associated with lack of adhesion of the thin nickel plating that forms one leg of the iron-nickel junction. Others involved contamination of the film by impurities present in the plating system and delays due to breakdowns in the plating equipment which is not under the control of the automotive laboratory research group. Toward the end of the second year, three thermocouples with films that appeared quite sound at room conditions were fabricated and tested in the single cylinder engine. Two failed under motoring conditions due to the nickel film peeling off, very soon after being exposed to motoring operation. Another failed early in a firing run. Critical reappraisal of the design indicated that the nickel film had failed to adhere properly to the mica insulator that separates the nickel tape from the iron body and, with this failure as a starting point, rapidly peeled from all surfaces. The principal cause

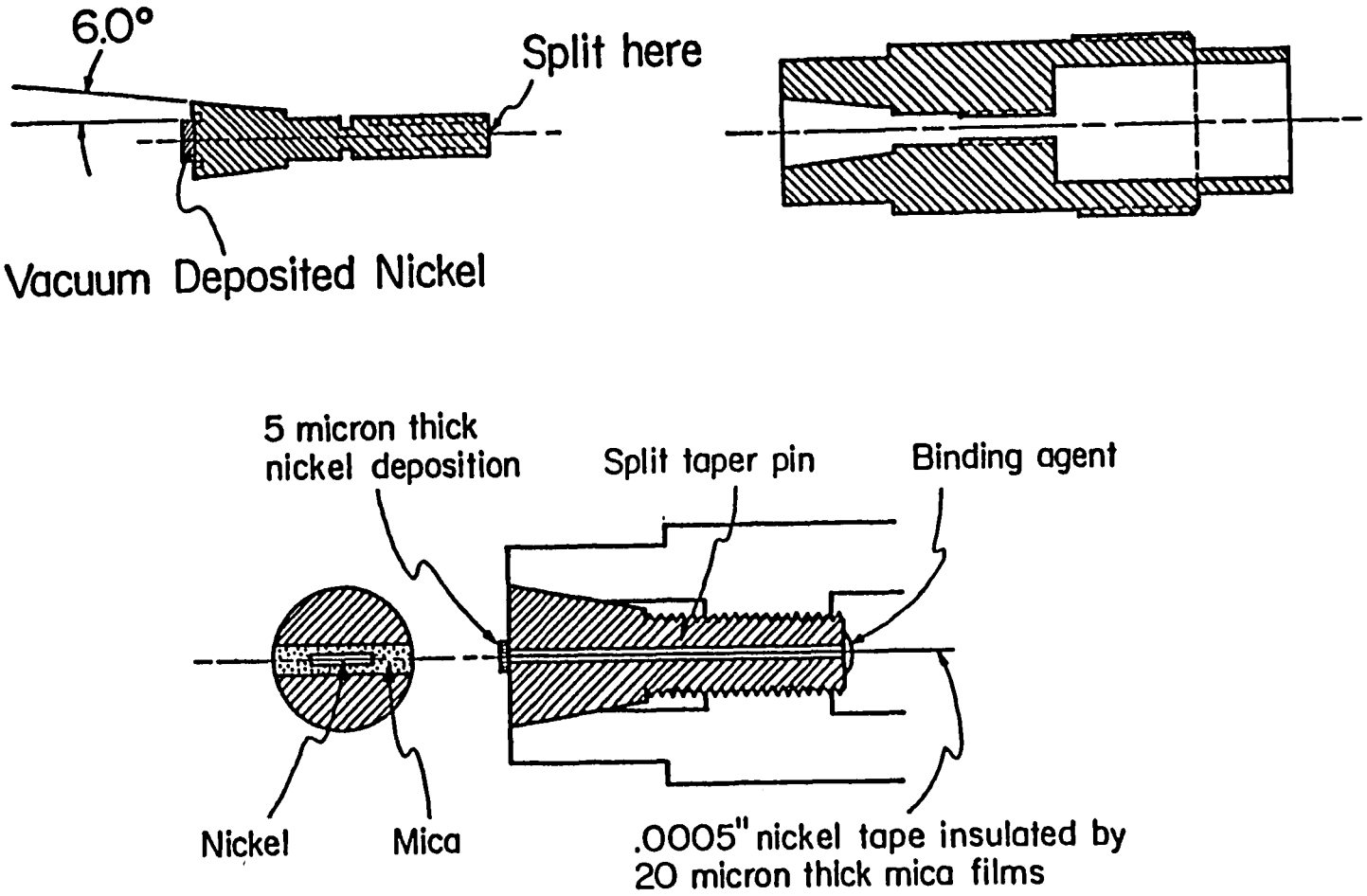

Figure 5-12 Schematic of the surface thermocouple design.

of the lack of film adherence appeared to be crumbling of the mica around the nickel tape, which resulted in surface gaps that the nickel film could not bridge successfully. This crumbling probably occurred during the polishing step prior to plating, possibly due to failure of the split taper pin in the body to clamp the mica tightly and prevent movement. Alternatively, the mica may have crumbled due to its brittle structure.

As a result of these failures, the thermocouple unit was redesigned to incorporate a round nickel center wire encased in a ceramic sleeve that, insulates it from the iron body, instead of using a nickel tape insulated by mica layers. A drawing of this new design is shown in Figure 5-13. The new design is believed to be more suitable than the original one in that the ceramic insulator should not crumble and thus should provide a solid surface to support the nickel plating. Fabrication of these units was begun during the last month of year two.

Because of the difficulties encountered at Purdue in developing a fast-response thermocouple that is durable in engine tests, commercial sources were investigated as part of a back-up plan. The only commercial source, located to date, that appears to have the expertise required is Medtherm Corporation of Huntsville, Alabama. Medtherm makes a comprehensive line of fast-response thermocouples, largely for military ordinance testing, but has supplied engine test units, that have worked successfully, to Cummins and Detroit Diesel. After discussions with Medtherm, an iron plug which fits the engine access ports and that will accept a standard Medtherm thermocouple was designed and submitted for quotation on the complete assembly. We plan to buy six of these thermocouple assemblies for metallic engine test work in the event that the revised Purdue design fails to satisfy program needs.

Optical Proximeter for Determination of TDC Location

During the first year of the experimental program, an optical proximity probe was designed and constructed for use in dynamically determining engine TDC. For proper phasing of acquired pressure data it is neces-

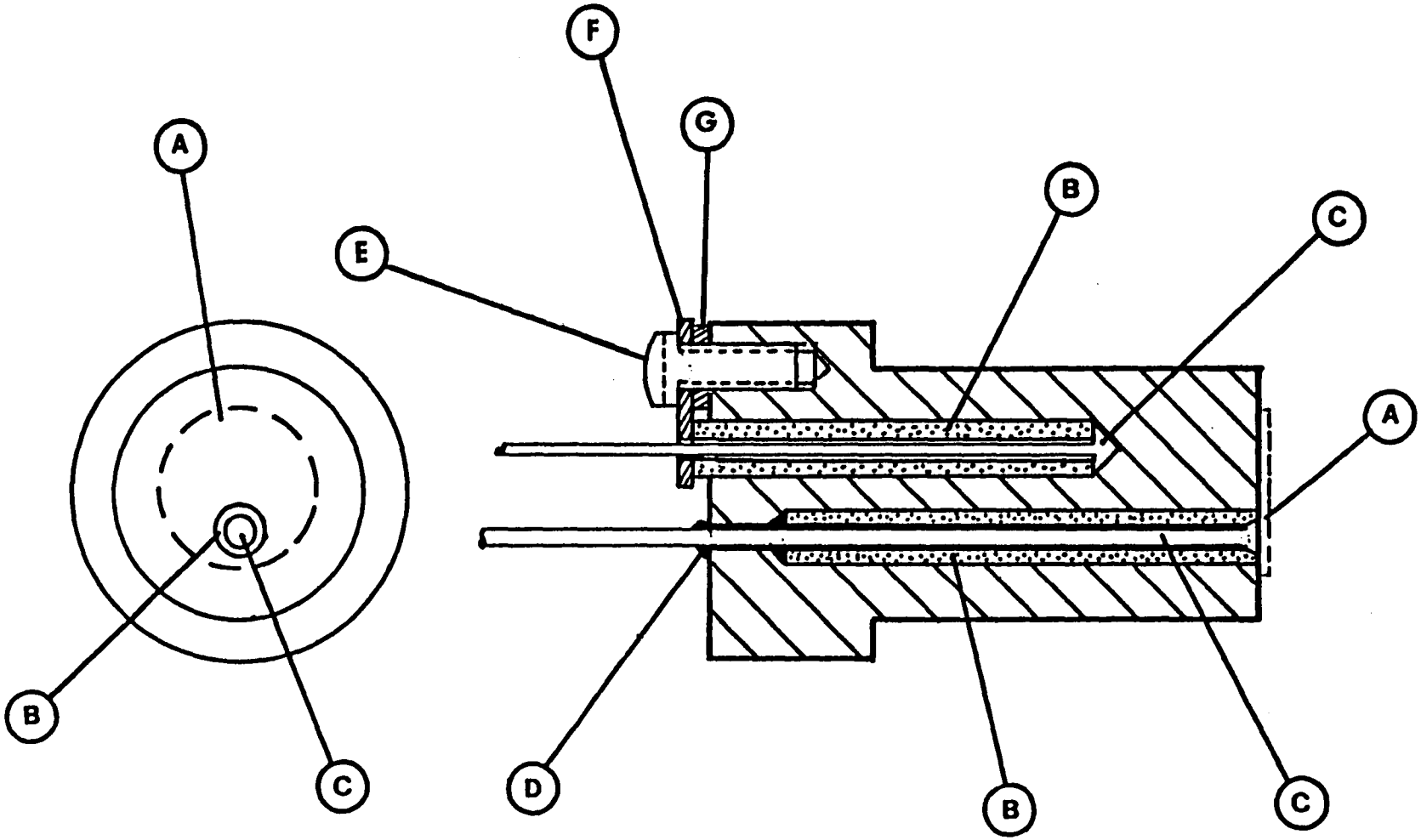

A - Vacuum Deposited Nickel Thin-Film
B - Ceramic Sheath
C - Nickel Wire
D - Ceramic Cement
E - Machine Screw
F - Flat Retaining Spring
G - Shim

Figure 5-13 Heat-flux transducer, internal parts.

sary to determine the location of TDC within 0.1 degrees of crank rotation. This requirement was established by analytical studies of the dependence of heat transfer calculated from engine pressure data on pressure-crank angle phasing. From initial tests performed with the proximity probe, it appeared the desired accuracy could be achieved using this device, and based on this a detailed research effort was mounted to develop it into a reliable instrument.

A detailed explanation of the design and operation of the proximity probe was presented in the Phase I Report, hence only a brief review will be given here. Figure 5-14 presents a schematic of the probe, illustrating the essential features of the device. The proximeter consists of two fiber optics bundles joined together at one end. Light is directed through the transmitting bundle and reflected off the work surface. The reflected light is collected by the receiving bundle and sensed by a photodetector. The intensity of the light sensed by the detector is a nonlinear function of the distance between the work surface and the probe face. Insertion of the probe into an engine in such a way that the piston crown becomes the work surface, results in the output signal near engine TDC shown in Figure 5-15. From this signal, the location of TDC can be determined, in principle, as the location of the signal minimum or the location of the midpoint between the two signal peaks (average of the peaks location). During the second year of the experimental program, the proximeter probe was exercised thoroughly over a wide range of engine speed in order to assess the accuracy of the technique. The experiences gained during that process, and the results obtained, are reviewed below.

Preliminary Proximeter Measurements and Data Analysis. During the preliminary use of the proximeter probe in the Cummins' single cylinder test engine, significant improvements were made to the probe hardware. Refinement of the probe circuitry reduced time delays associated with the use of the proximeter to an acceptable level. Problems with signal noise levels were eliminated by effective shielding of the probe circuitry and the use of a more powerful light source.

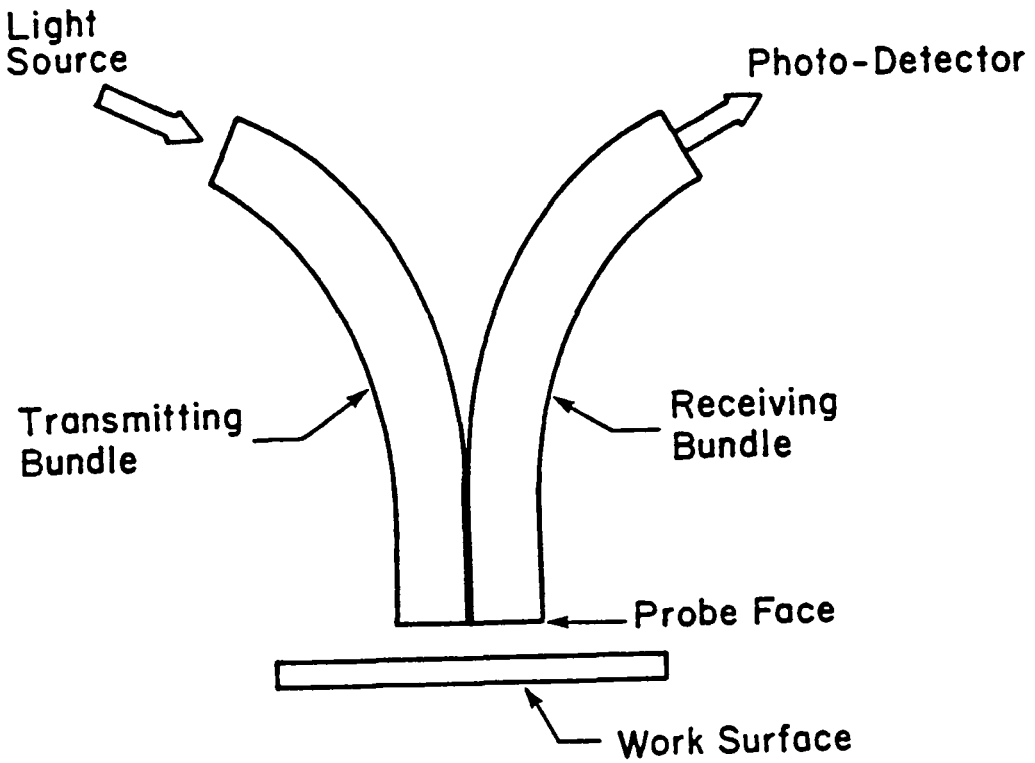

Figure 5-14 Schematic of fiber optic proximity probe sensing the distance to a surface.

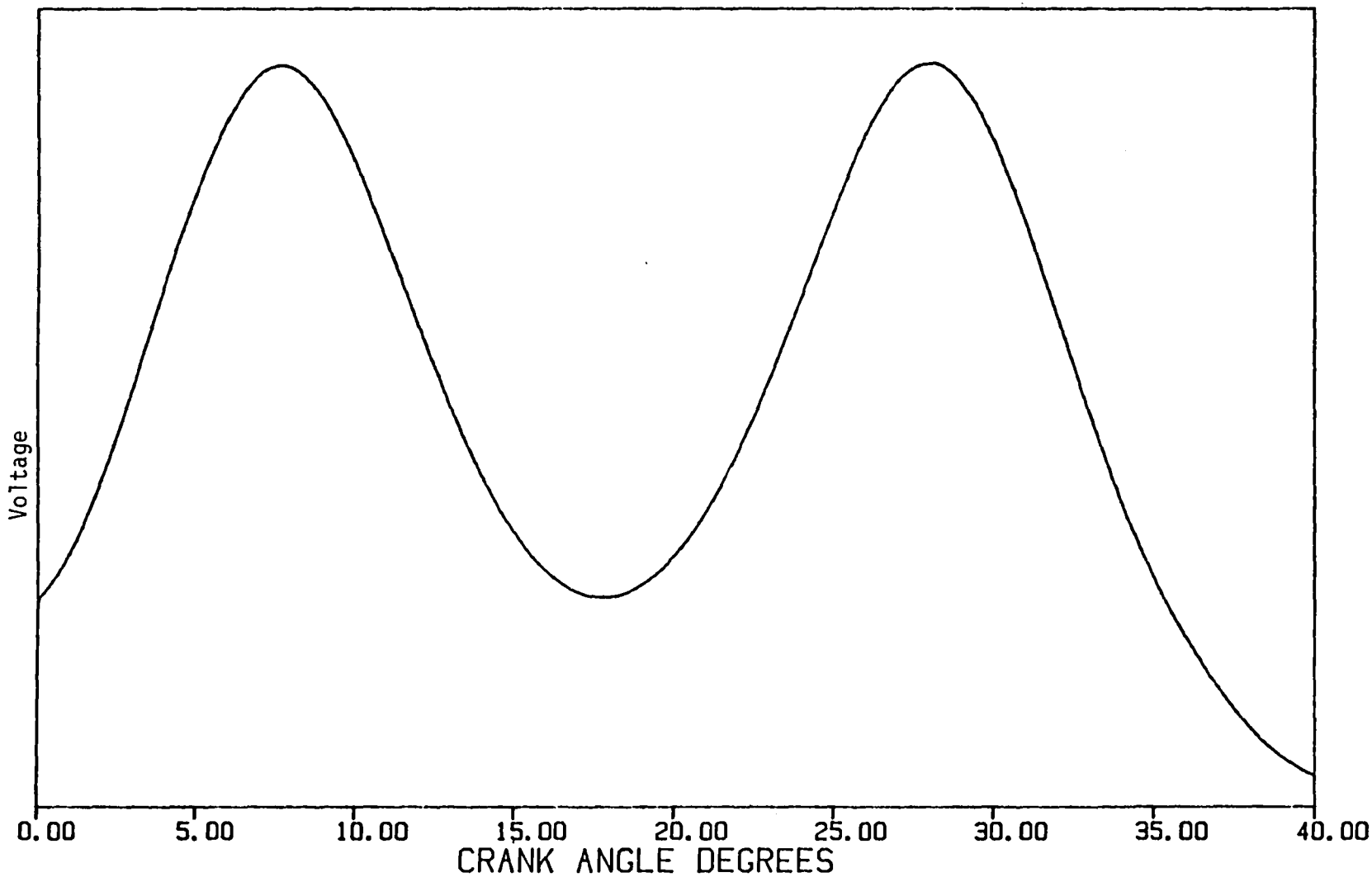

Figure 5-15 Optical proximity probe output generated from use in an engine with the piston crown as the work surface.

Using the proximeter data sets acquired during the initial period of proximeter use, computer data reduction techniques were developed and refined for determing the location of engine TDC from the probe signal. In all of the tests data were acquired at 0.2° intervals. The analysis of the data involved the following steps:

- smoothing of the probe signal near TDC, and
- locating the smoothed signal maximums and minimums.

Signal smoothing was accomplished by averaging the proximeter signals over a number of crankshaft revolutions and applying a sliding least squares curve fit to the result. The sliding least squares curve fit technique is a procedure which fits each data point to a polynomial of a specified degree using only the data points in the vicinity of the point being fit. The parameters involved in the application of the technique are the order of the polynomial and number of points used in the local fit and the number of times the data is curve fit. Single and double smoothing of the data is accomplished by curve fitting the data once and twice, respectively, after averaging is performed.

Signal minimum and maximum locations were determined by locating points of zero slope. The zero slope locations were first determined to the nearest data point using an exhaustive search. The coefficients of the polynomial associated with the curve fit through this point were then used to calculate a more exact location of the zero slope point.

A parametric study was performed on the smoothing procedure to determine the variation of the signal minimum and midpoint of the peaks (average of the peaks) locations at a given engine speed with the order of the polynomial and number of points used in the local fit and the level of smoothing applied to the data (single or double). The order of fit was varied from 2 to 5 and the number of points was varied from 35 to 75 (7.0 to 15.0 degrees of crank rotation) in increments of 10 points. A proximeter data set consisting of engine speeds of 500, 750, 1000, 1250 and 1500 RPM was used in the study. The results of the analysis indi-

cated that the total variation in the TDC location with number points fitted and order of fit was less than 0.06° at any given engine speed for both the compression-expansion and valve open periods, and both the minimum and average-of-the-peaks. A fourth order fit over 55 points using single smoothing was chosen for all future analysis. These particular parameters gave proximeter results which were close to the mean of the results obtained from the parametric study at all engine speeds.

Final Proximeter Data Analysis -- General Results. After several iterations on the development of the proximeter hardware and data analysis techniques, an updated set of proximeter data was collected at engine speeds between 1000 and 2100 RPM at 100 RPM increments. Data was acquired over 35 crankshaft revolutions at each speed. The proximeter signal minimum and average of the peaks locations were determined in the manner described above and the results are plotted in Figure 5-16 as a function of engine speed. The figure shows a sudden shift in the proximeter results during the compression-expansion period at 1600 RPM. This shift was apparent in all of the preliminary proximeter data sets collected. The magnitude of the shift is gradually reduced as engine speed increases to 2100 RPM. The valve-open period results are smooth over the range of engine speeds and do not show any shift.

A great deal of effort was spent in determining whether the shift in the proximeter results shown in Figure 5-16 was truly indicative of the actual TDC location. The basic assumption inherent in determining TDC from the proximeter signals is that the signals are symmetric about engine TDC. Given the nature of the proximeter operation and an entirely symmetric proximeter signal from an engine, the point of symmetry is the point at which the piston is closest to the probe face. Under these conditions, the minimum, average-of-the-peaks and TDC locations are all the same. An unsymmetric proximeter trace can be generated by a change in the orientation of the piston crown with respect to the probe face through a rocking or sideways motion of the piston near TDC. The result is a change in the amount of light col-

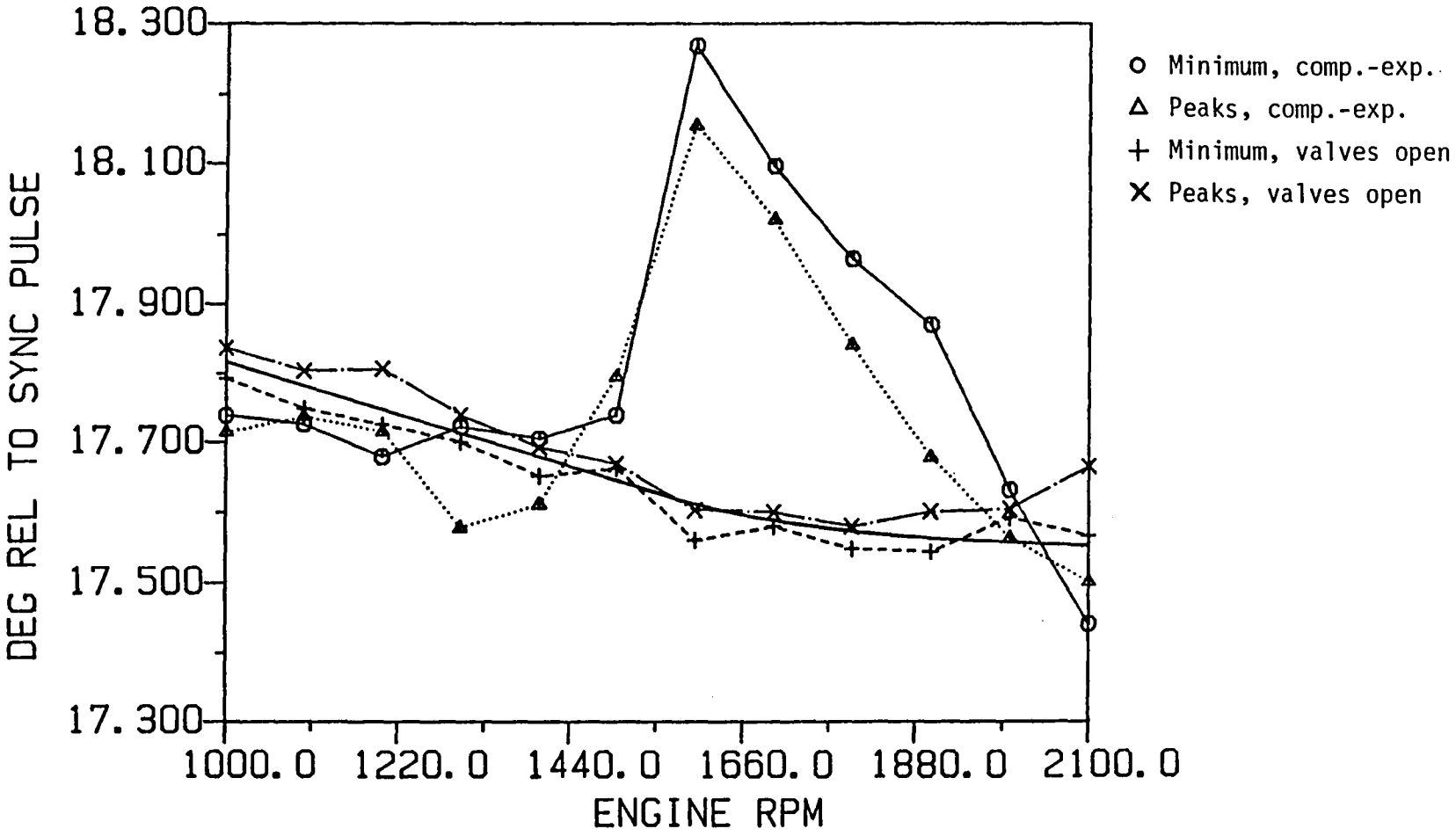

Figure 5-16 Optical proximity probe signal minimum and average of the peaks' location vs engine speed for the valve open and compression-expansion periods.

lected by the proximeter receiving bundle at a given position of the piston in the engine cycle. Hence, different output levels from the proximeter can be obtained at the same piston position, and the slope of the proximeter signal can be different on opposite sides of engine TDC. Due to the change in output level, the signal minimum is no longer assured to correspond to TDC and due to the change in slope the midpoint between the signal peaks is no longer assured to correspond to TDC. Thus, given a nonsymmetric proximeter signal from an engine, the minimum, the average-of-the-peaks and the TDC locations are not necessarily the same.

An examination of the symmetry of the proximeter signals near TDC is useful in assessing the validity of the results obtained after 1600 RPM during the compression-expansion period. Figures 5-17 and 5-18 show plots of the average probe signals at speeds of 1000, 1200, 1400, 1600, 1800 and 2000 RPM for the valve-open and compression-expansion periods, respectively. The signals are reasonably symmetric during the valve open period over the entire range of engine speeds. During the compression-expansion period, however, the proximeter signals become noticeably unsymmetric at engine speeds of 1600 RPM and above. As a result, the signal minimum and average-of-the-peaks locations for these speeds cannot be used as a reliable indication of engine TDC location.

Analysis of a companion set of motoring pressure data taken at the same engine speeds as the proximeter data provided further support for the rejection of compression-expansion results past 1600 RPM. The analysis showed that peak pressure location shifted smoothly and gradually with engine speed towards TDC and it did not change significantly past 1600 RPM. Thus, given this result, the unsymmetric shape of the proximeter signals, and the lack of a suitable physical explanation for the movement of engine TDC during the compression-expansion period in the manner shown in Figure 5-16, the proximeter results for the compression-expansion period were judged not to be indicative of the actual engine TDC location at 1600 RPM and above.

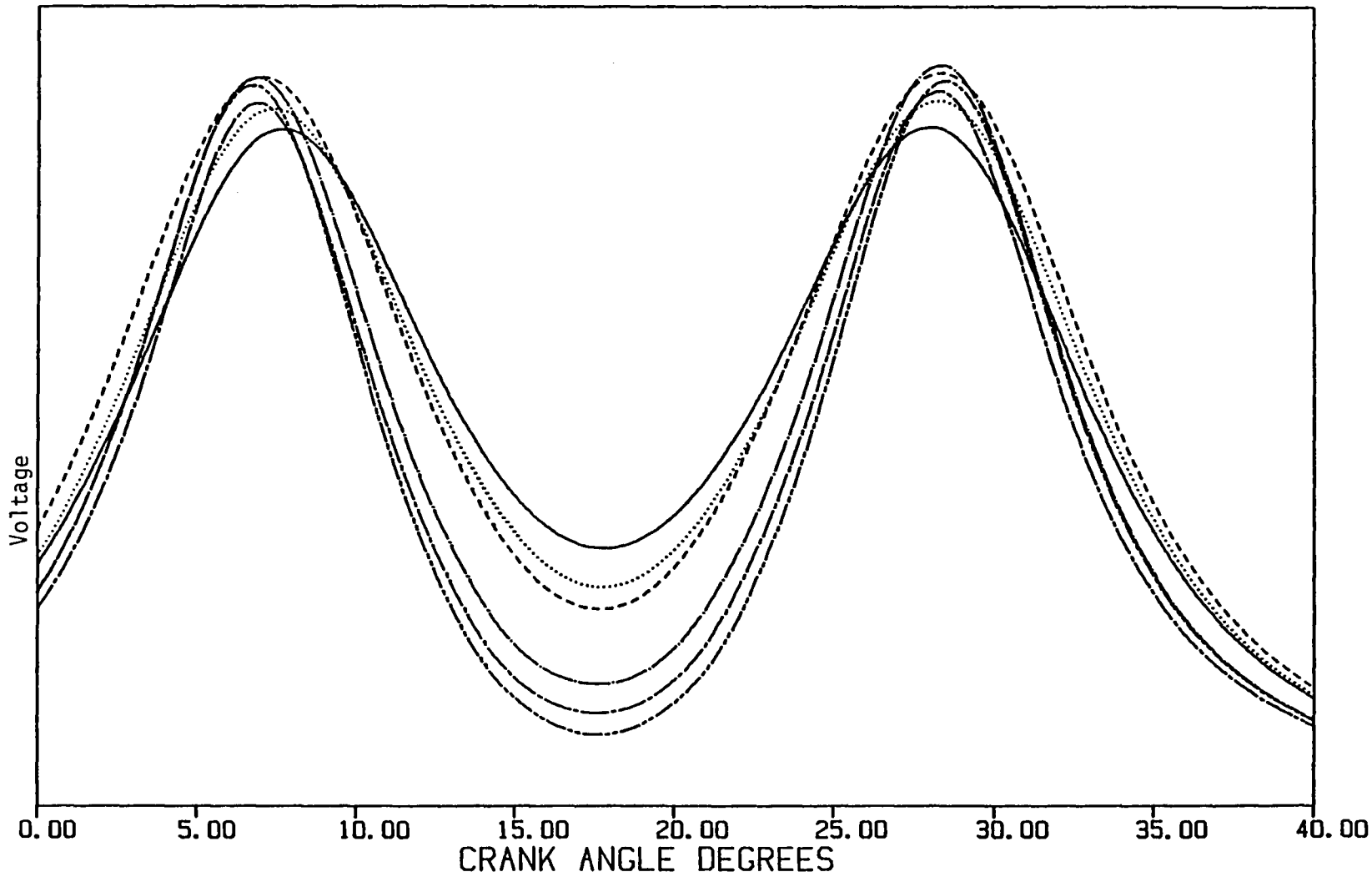

Figure 5-17 Average optical proximity probe signals constructed over 17 engine revolutions during the valve open period.

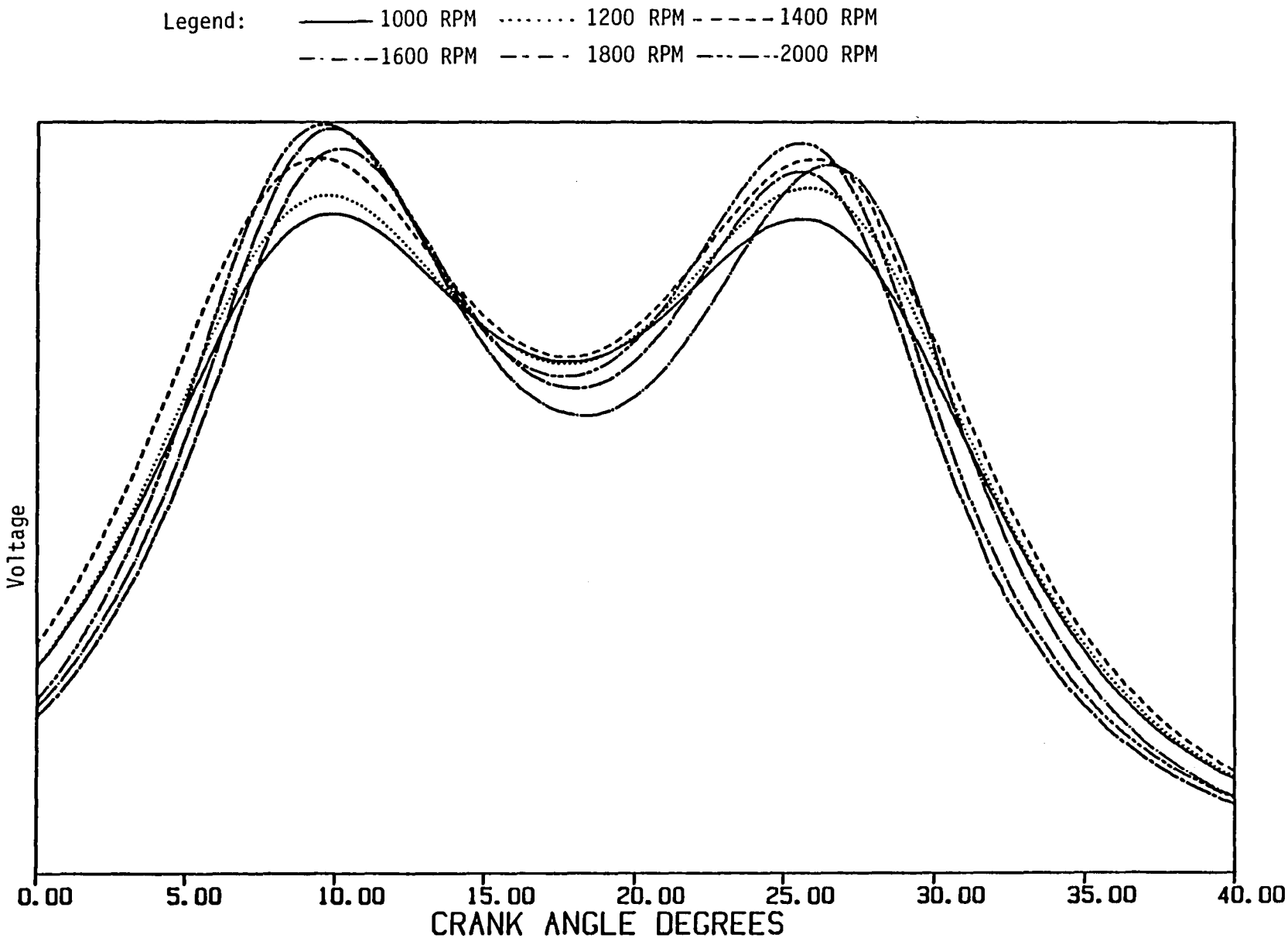

Figure 5-18 Average optical proximity probe signals constructed over 17 engine revolutions during the compression-expansion period.

Error Analysis. Using the updated set of proximeter data an assessment of the accuracy of the probe measurements was made. To address the question of accuracy, an evaluation of the errors associated with the use of the probe must be made. These errors can be grouped according to the following classifications:

- error due to cycle to cycle variation of the measurements, and
- error due to the assumed relation between engine TDC and the probe signal minimum and average-of-the-peaks locations.

The error associated with the repeatability of the measurements can be quantified in a straightforward manner using statistical analysis. The signal minimum and average of the peaks locations for each individual crank revolution from the proximeter data were determined for all engine speeds. From these results the 95% confidence intervals for the minimum and average-of-the-peaks locations were computed. The confidence intervals represent the error due to cycle to cycle variation resulting from use of the proximeter and the chosen techniques for smoothing the data and locating signal maximums and minimums. For the compression-expansion period this error is less than 0.05°, while for the valve open period it is less than 0.02°. The narrower confidence interval for the valve open results is attributable to less cycle to cycle variation in the secondary motions of the piston during this period in the absence of significant pressure forces. These error estimates are well below the desired 0.1 degree accuracy for locating engine TDC.

The error due to the assumed relation between engine TDC and the proximeter signal maximum and minimum locations is difficult to quantify. As discussed above, the relation is assumed to be valid only when the proximeter signal is symmetric. Thus, one way to quantify the error in the assumed TDC proximeter signal relation is to quantify the degree to which a given proximeter trace differs from an entirely symmetric trace. One global measure of this difference is the magnitude of the difference between the minimum location and average-of-the-peaks location for each proximeter signal. As can be seen in Figure 5-16, a maximum 0.19° and

0.10° difference exists for the compression-expansion and valve open periods, respectively. These numbers give some indication of the error in the assumption that the TDC location is related to the minimum and average-of-the-peaks locations.

The error values determined by the above analysis, give an indication of the total error associated with the use of the proximeter. Concentrating only on the valve open period data which are more consistent, a second order curve was fit to all the data for the valve open period between 1000 and 2100 RPM, including both the minimum and average-of-the-peaks data. This curve is shown in Figure 5-16 by a bold solid line. It displays a mild variation with engine speed, which amounts to 0.25° over the range of interest. This variation is most likely due to dynamic structural flexing, and it would not be detected with standard methods of TDC determination, which are essentially static.

In summary, a data reduction procedure was developed for the optical proximeter, which reduces and enhances the acquired data, and provides a consistent method for TDC determination very close to the desired $\pm$ 0.1° accuracy.

1. Report No.	2. Government Accession No.	3. Recipient's Catalog No.
NASA CR-175072		

4. Title and Subtitle	5. Report Date
Methods for Heat Transfer and Temperature Field Analysis of the Insulated Diesel Phase II Progress Report	September 1985
	6. Performing Organization Code

7. Author(s)	8. Performing Organization Report No.
Thomas Morel, Rifat Keribar, Edward F. Fort, and Paul N. Blumberg	778-34-12
	10. Work Unit No.

9. Performing Organization Name and Address	11. Contract or Grant No.
Integral Technologies Incorporated 415 East Plaza Drive Westmont, IL 60559	DEN 3-342
	13. Type of Report and Period Covered
	Contractor Report

12. Sponsoring Agency Name and Address	14. Sponsoring Agency ~~Code~~ Report No.
U.S. Department of Energy Office of Vehicle and Engine R&D Washington, DC 20585	DOE/NASA/0342-2

15. Supplementary Notes

Interim Report. Prepared under Interagency Agreement DE-AI01-80CS50194. Project Manager, James C. Wood, Propulsion Systems Division, NASA Lewis Research Center, Cleveland, Ohio 44135.

16. Abstract

This report describes work done during Phase II of a 3-year program aimed at developing a comprehensive heat transfer and thermal analysis methodology for design analysis of insulated diesel engines. The overall program addresses all the key heat transfer issues: (1) spatially and time-resolved convective and radiative in-cylinder heat transfer, (2) steady-state conduction in the overall structure, and (3) cyclical and load/speed temperature transients in the engine structure. These are all accounted for in a coupled way together with cycle thermodynamics. An experimental program is underway to produce data for validation of the methodology.

During Phase II, radiation heat transfer model was developed, which accounts for soot formation and burn up. A methodology was developed for carrying out the multi-dimensional finite-element heat conduction calculations within the framework of thermodynamic cycle codes. Studies were carried out using the integrated methodology to address key issues in low heat rejection engines. A wide ranging design analysis matrix was covered, including a variety of insulation strategies, recovery devices and base engine configurations. A single cylinder Cummins engine was installed at Purdue University, and it was brought to a full operational status. The development of instrumentation was continued, concentrating on radiation heat flux detector, total heat flux probe, and accurate pressure-crankangle data acquisition.

17. Key Words (Suggested by Author(s))	18. Distribution Statement
Diesel engine; Heat transfer; Transportation; Insulated engine; Fuel consumption; Adiabatic engine	Unclassified - unlimited STAR Category 85 DOE Category UC-96

19. Security Classif. (of this report)	20. Security Classif. (of this page)	21. No. of pages	22. Price*
Unclassified	Unclassified	317	A14

*For sale by the National Technical Information Service, Springfield, Virginia 22161

End of Document